Development of Novel Diagnostic Platforms Using Gold Nanoparticles and Spectroscopy

By

Xiaona Wen

Dissertation

Submitted to the Faculty of the

Graduate School of Vanderbilt University

in partial fulfillment of the requirements

for the degree of

DOCTOR OF PHILOSOPHY

in

Chemical Engineering

December 18, 2021

Nashville, Tennessee

Approved:

Rizia Bardhan, Ph.D.

Matthew J. Lang, Ph.D.

Marjan Rafat, Ph.D.

Bhuminder Singh, Ph.D.

Jacob Houghton, Ph.D.

ACKNOWLEDGEMENTS

It has been a challenging and precious experience working towards the Ph.D. degree. I would like to thank everyone who supported me in following my passion, leveraging my strength, and challenging my thinking in the added value of exploring and conducting research.

First, I would like to thank my advisor Dr. Rizia Bardhan for her invaluable help and guidance through all ups and downs during this long journey. I am deeply grateful to be a part of her team. Likewise, I would like to thank the members of my committee, Dr. Matthew J. Lang, Dr. Marjan Rafat, Dr. Bhuminder Singh, and Dr. Jacob Houghton, who provided a diverse range of expertise and insights without which this work would not have been possible.

I am immensely thankful to have Dr. Yu-Chuan Ou as my senior lab mentor. Her positive attitude and strong leadership have made working with her both enjoyable and productive. Many thanks to my other lab mates who number too many to list but are nonetheless greatly appreciated.

Last but not least, my most sincere thanks are extended to my family and friends for their unconditional love and support. To my dear mom Zhucui, no words can express the depths of my gratitude for the endless sacrifices she made in parenthood to fill my life with opportunities. Thank you for being a role model and providing anything and everything that I could ask for. To my dear sister Yudan, I am truly blessed to have a caring and loving sister in my life. Thank you for always letting me tag along and having my back. To all my friends, friendships we made along the way are the real treasure. Thanks for always being there for me.

TABLE OF CONTENTS

LIST OF TABLES

LIST OF FIGURES

Chapter 1

INTRODUCTION

1.1 Motivation

With the emergence of advanced molecular profiling approaches, the heterogeneous landscape of various diseases can now be accurately measured revealing that the "one-size fits all" approach to treatment is ineffective in understanding the complex pathophysiology of diseases.[1-4] Personalized medicine driven by each patient's unique molecular, physiological, and behavioral characteristics has led to a paradigm shift.[5] This new healthcare model allows for early detection of a prevalent disease, accurate prediction of disease progression, and monitoring of treatment responses, as part of an integrative framework defined by P4 (predictive, preventive, personalized, participatory) medicine.[6-8]

The success of personalized medicine highly relies on the continued identification and detection of biomarkers. The Food and Drug Administration (FDA) defines a biomarker as "a characteristic that is objectively measured and evaluated as an indicator of normal biological processes, pathogenic processes, or pharmacologic responses to a therapeutic intervention".[9] This definition implies that biomarkers can be classified into different categories depending on their (i) biology, (ii) measurement or read-out, and (iii) purpose. With regard to biology, different features such as molecular, physiological, and morphological characteristics can be used as biomarkers. Another characteristic for a biomarker is the possibility of trustable and actionable measurement which can be divided into qualitative (yes/no), semi-quantitative, and fully quantitative results in terms of interpretation. Biomarkers can be further subgrouped into diagnostic, prognostic and disease monitoring and surveillance markers, depending on the type of information that individual would like to obtain. Biomarkers can take many forms, and consequently a variety of strategies

have been adopted for their discovery and detection. The search for disease biomarkers has increased significantly with the recent development of high-throughput technologies that allows screening of thousands of biomolecules simultaneously in a given sample. However, FDA approval of novel biomarkers is limited, averaging 1.5 new proteins per year despite substantial investments.[10-12]

There are many factors that lead to the apparent discrepancy between efforts on the biomarker development and FDA approval. The main issues are technological in nature, including the need for measurements that are concurrently sensitive, quantitative, multiplexed and high-throughput, the need to have standard metrics for quality assurance and quality control that enable validation during technology transfer, and the need for integration of different sources of information to gain complementary understanding of results.[13] To address these challenges, we demonstrate versatile platforms to detect biomarkers *in vitro*, in biofluids, and *in vivo*.

1.2 Mass Spectrometry for Biomarker Detection

Over the past decade, mass spectrometry (MS)-based proteomics has evolved dramatically through the tremendous advancements in throughput, sensitivity, resolution, mass accuracy, and dynamic range of MS technology. For example, liquid chromatography coupled to tandem MS (LC-MS/MS) can be routinely used to identify thousands of proteins from complex biological samples (*e.g.*, cell lines and biofluids).[14,15] When combined with front-end enrichment methods, targeted quantitative MS approaches, such as selected reaction monitoring (SRM), or more recently, parallel reaction monitoring (PRM), can be highly sensitive at pg/mL level in blood plasma or serum.[16,17] With these enhancements, MS-based proteomics holds great promise for biomarker development. Yet, despite intensified interest and investment, few new biomarkers are

used in clinical practice.[18] This disjunction reflects the translational gap between the candidate discovery and clinical deployment. As a result, a better understanding of the overall process, especially the challenges and strategies inherent in each phase, would greatly increase the overall efficiency of biomarker development.

Phase	Aim	Method	Number of Candidates	Number of Samples
Discovery	Identify candidate biomarkers	Unbiased LC-MS/MS	100 – 1000	1 – 10
Verification	Verify expression level of candidate biomarkers	Targeted SRM, PRM	10 – 100	10 – 100
Validation	Perform large cohort validation for candidate biomarkers	Targeted Immunoassay	1 – 10	100 – 1000

Figure 1.1 Process flow for biomarker identification. *LC-MS/MS*, liquid chromatography tandem mass spectrometry; *SRM*, selected reaction monitoring; *PRM*, parallel reaction monitoring. Reproduced from Wu *et al.*[19] with permission from the Springer.

Current applications of MS-based proteomics in biomarker development can be divided into three phases: discovery, verification, and validation (Figure 1.1). In the first discovery phase, potential biomarker candidates are determined by comparing the differential expression between the normal and diseased samples.[20] At present, two distinct strategies are commonly used in the discovery stage, namely, top-down or bottom-up approaches.[21] The key difference between these two approaches lies in the use of pre-MS protein digestion. In the top-down approach, the intact protein is fractionated followed by mass measurements as well as dissociation to obtain sequence information, while in the bottom-up approach, proteins are first reduced, alkylated, and digested into peptides (*e.g.*, trypsin digestion) and further fractionated or enriched.[22] The resulting fractions or enrichment products are separated and further ionized into gas phase followed by the detection

of peptides *via* MS. Typically, a mass detector is first used to scan an intact peptide precursor to produce a full mass spectrum with accurate precursor mass-to-charge (m/z) ratio. Next, the isolated peptide precursor is fragmented to generate a spectrum (*i.e.*, by MS/MS) that contains significant peptide sequence-related backbone fragment information. The resulting MS data are then searched with protein sequence database (*e.g.*, Sequest and Mascot) for protein/peptide identification. However, within the identified candidates in this untargeted discovery step, some of them are false positives indicating that such proteins are not differentially expressed along the distinction of interest upon further testing.[23] A relatively high false discovery rate is expected at this stage, particularly for the lower-abundance proteins that have low frequency to be selected for peptide sequence analysis in complex proteomes, and produce signals at the lower limit of instrument dynamic range yielding occasional and artificial differences.

To advance in development, all biomarker candidates require verification. In verification, the assessment is extended to hundreds of samples, now including a wide range of controls and cases, which begins to incorporate the biological, genetic, and stochastic variation in the tested population.[24] The sensitivity of potential candidates is therefore confirmed and specificity begins to be evaluated. The expected output of this phase is a small number of highly credentialed candidates suitable for next stage. The historical lack of candidate verification is primarily due to reagent limitations.[25] In fortuitous scenarios where high-quality immunoassays already exist for newly described biomarker candidates, they can be used for verification. However, for many or most novel candidates, such assays are not immediately available, and their development is expensive and requires extensive time, presenting a significant bottleneck. An attractive alternative to immunoassays that avoids the need to develop paired affinity reagents for each candidate protein is SRM using a triple quadrupole mass spectrometer.[26] SRM measurements

typically start with ions of interest preselected with the first mass filter Q1 followed by fragmentation in Q2 by collisional excitation with a neutral gas in a pressurized collision cell. The resulting ions are further filtered by third quadrupole Q3 and transmitted to the detector.[27] This selection strategy enhances the lower detection limit for peptides by up to 100-fold by eliminating potential interference and allowing continuous monitoring exclusively for the specific ions of interest.[13] Although SRM provides a powerful strategy for candidate verification, its sensitivity remains constrained by sample complexity. Particularly for biomarker candidates with lower abundance where sufficient fractionation is unachievable by SRM, stable isotope standards and capture by anti-peptide antibodies (SISCAPA) provides a compelling alternative approach.[28] In SISCAPA, signature peptides are enriched with anti-peptide antibodies before SRM analysis. This immunoaffinity peptide enrichment allows measurement in complex matrices with little or no fractionation, thereby significantly improving sensitivity and throughput.[29] Further, high specificity is achieved by the fragmentation pattern of the affinity-captured peptides, enabling SISCAPA to act much like a sandwich enzyme-linked immunosorbent assay (ELISA) with MS/MS substituted for the secondary antibody. In contrast to targeted SRM analysis where one extra fragmentation step is needed and species are sequentially analyzed by only monitoring the predefined transitions, recent technical developments (*e.g.*, PRM) allowing multiple sets of ions to be selected for simultaneous MS/MS measurements are accelerated by the emerging capabilities for faster separations, higher MS resolution, more effective ion sources, and MS detectors with broader dynamic ranges.[30] With these advancements, the convergence of "untargeted/discovery" and "targeted/verification" is possible, speeding up overall process.

After verification, the list of biomarker candidates is substantially reduced, and each protein candidate has shown to have measurable differential expression between the states of

5

interest. The next phase of biomarker development is validation, which typically requires measurement of thousands of samples with single-digit measurement coefficient variation. At present, validation is usually performed by immunoassays (*e.g.*, ELISA). Many of the aforementioned problems inherent to immunoassays limit their use in biomarker validation. SRM-based quantitative assays offer many advantages over immunoassays.[31] For example, SRM assays can be multiplexed, rapid, and targeted for any protein and its multiple peptides. SRM assays are also not subject to interference caused by auto-antibodies or anti-reagent antibodies. However, other practical issues such as complex sample preparation and cost benefit still need to be better addressed. Overall, great strides have been made to use MS-based proteomics for biomarker identification in the past decade, but to date its contribution to the diagnostic armamentarium is not satisfactory. The combination of MS-based proteomics with other techniques providing complementary information has great potential to detect biomarkers in complex biological matrices in a cost-effective, sensitive, and high throughput manner.

1.3 Raman Spectroscopy for Biomarker Detection

In the pursuit of a sensitive and specific method for identifying and detecting biomarkers of diseases, in the past few years, Raman spectroscopy (RS) has gained overwhelming attention as a powerful state-of-the-art platform for disease diagnosis at the molecular level.[32-35] RS is a vibrational spectroscopic technique based on Raman scattering, in which incident light is inelastically scattered from a sample and shifted in frequency by the energy of excited molecular vibrations.[36] From a quantum-mechanical perspective, Raman scattering can be described as a two-photon scattering process on quantized vibrational energy levels (Figure 1.2).[37] When molecules are excited from a vibrational ground state into a short-lived virtual state, incoming

photons (v_0) can be elastically scattered back into the ground state (Rayleigh scattering) or inelastically scattered (Raman scattering) by an amount, v_m, which corresponds to the energy of a molecular transition in the molecule. In the case of Raman scattering, the scattered photons may have a lower energy than incident photons and be red-shifted (Stokes scattering, $v_0 - v_m$). Alternatively, the scattered photons may have a higher energy compared with incoming photons and be blue-shifted (anti-Stokes scattering, $v_0 + v_m$). As vibrational ground states are more populated than the vibrationally excited level, Stokes scattering has higher intensity than anti-Stokes scattering. As a result, the term Raman spectrum is often used for a Stokes vibrational Raman spectrum. More importantly, a Raman spectrum provides a unique fingerprint of materials, rendering RS attractive for identifying and quantifying molecules for diagnostic purposes.[38] Further, RS can be label-free and can nondestructively probe biological samples in their natural setting. Crucially, water is known to have a remarkably weak Raman scattering cross-section, enabling RS suitable for studies in aqueous environments.[39]
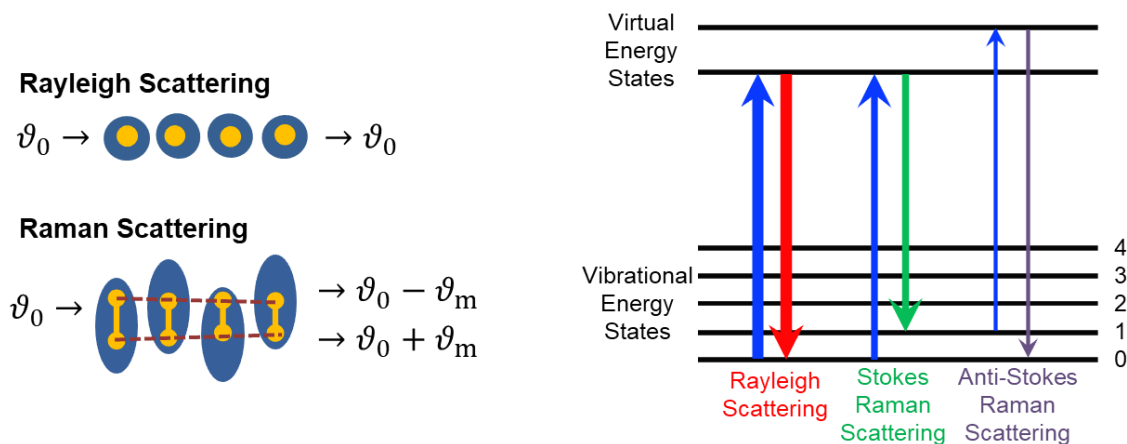
Figure 1.2 Electromagnetic radiation interacting with a vibrating molecule. When molecules are excited from a vibrational ground state into a shot-lived virtual state, incoming photons (v_0) can be elastically scattered back into the ground state (Rayleigh scattering) or inelastically scattered (Raman scattering) by an amount, v_m, which corresponds to the energy of a molecular transition in the molecule. In the case of Raman scattering, the scattered photons may have a lower energy than incident photons (Stokes scattering, $v_0 - v_m$). Alternatively, the scattered photons may have a higher energy compared with incoming photons (anti-Stokes scattering, $v_0 + v_m$). Reproduced from Moura[40] with permission from the Royal Society.

The development of powerful, narrow-bandwidth lasers, sensitive detectors, and efficient filters as well as the possibility to couple these optical components to modern microscopes has transformed RS into a promising analytical technique. Specifically, lasers are ideal excitation sources for RS because of their monochromatic and coherent emission, wavelength stabilization, and narrow bandwidths.[41] Nowadays diode lasers are commonly used for excitation, which are available for wavelengths from 405 to 1064 nm, and offer compact size, great cost effectiveness, and user-friendly operation.[42] When conducting studies, the laser intensity must be kept below the damage threshold to avoid carbonization and phototoxicity. The 785 nm laser is usually used for biological samples as it minimizes the fluorescence background and provides reasonable Raman scattering intensities.[43] Further, to register the Raman spectrum, charge coupled device (CCD) cameras are commonly used as multichannel detectors. The sensitivity of a CCD detector increases with high quantum efficiency defined as the number of electrons generated per photon and low dark signal formed by spontaneous generation of electron-hole pairs in the detector.[41] An optimum balance between low dark noise and sensitivity can be achieved by cooling to temperatures between -65 and -95 °C. To avoid condensation issues, the cooled CCD sensor is hermetically vacuum sealed. Moreover, Raman signals originated from inelastic scattering are several orders of magnitude weaker than elastic Rayleigh scattering.[44] As a result, dielectric long-pass filters or holographic notch filters are usually used to suppress the elastically scattered light and reduce the noise for better signal-to-noise ratios. Lastly, microscopes coupled to Raman systems allow high spatial resolution down to the diffraction limit. Especially, the high-numerical-aperture objective lenses built in microscopes render the maximum photon density for excitation and maximum photon collection. These advanced optical elements can increase Raman scattering,

but surface-enhanced Raman spectroscopy (SERS) offers a compelling alternative in various types of ultrasensitive sensing applications.[45,46]
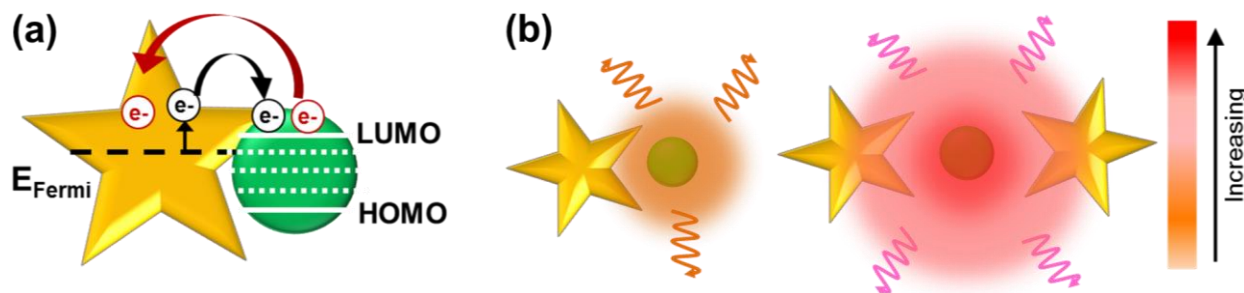
Figure 1.3 Schematics of (a) chemical and (b) electromagnetic enhancement in SERS. Here, *LUMO* and *HOMO* represent lowest and highest unoccupied molecular orbital, respectively.

SERS exploits metallic nanoparticles to enhance Raman signals.[47] This enhancement is mainly attributed to chemical enhancement and electromagnetic enhancement (Figure 1.3). In chemical enhancement, only molecules whose polarizability can be modified result in Raman scattering.[48] Particularly, molecules with a lone electron pair bound to metal surfaces by chemisorption where a charge transfer occurs. Depending on the structural and chemical nature of molecules, chemical enhancement can occur in different ways. In the first scenario, when a molecule is physisorbed onto the metallic nanoparticle surface, a small perturbation is induced and then results in a change in electronic distribution.[49] Afterwards, a change in polarizability occurs which affects Raman efficiency. In the second scenario, a molecule-metal complex formed by covalent bond (*e.g.*, thiol bond) or by indirect binding under the help of an electrolyte ion leads to a change in the intrinsic polarizability which in turn directs a change in Raman efficiency.[50] In the third scenario, when the excitation laser energy matches the differences in Fermi energy level of metallic nanoparticles and highest occupied molecular orbital (HOMO) or lowest unoccupied molecular orbital (LUMO) energies of a molecule, photo-driven charge transfer may occur. In particular, charge transfer from HOMO and unoccupied energy states above Fermi level or

between LUMO and unoccupied energy states just below Fermi level can occur, which causes a change in polarizability and hence SERS enhancement.[50]
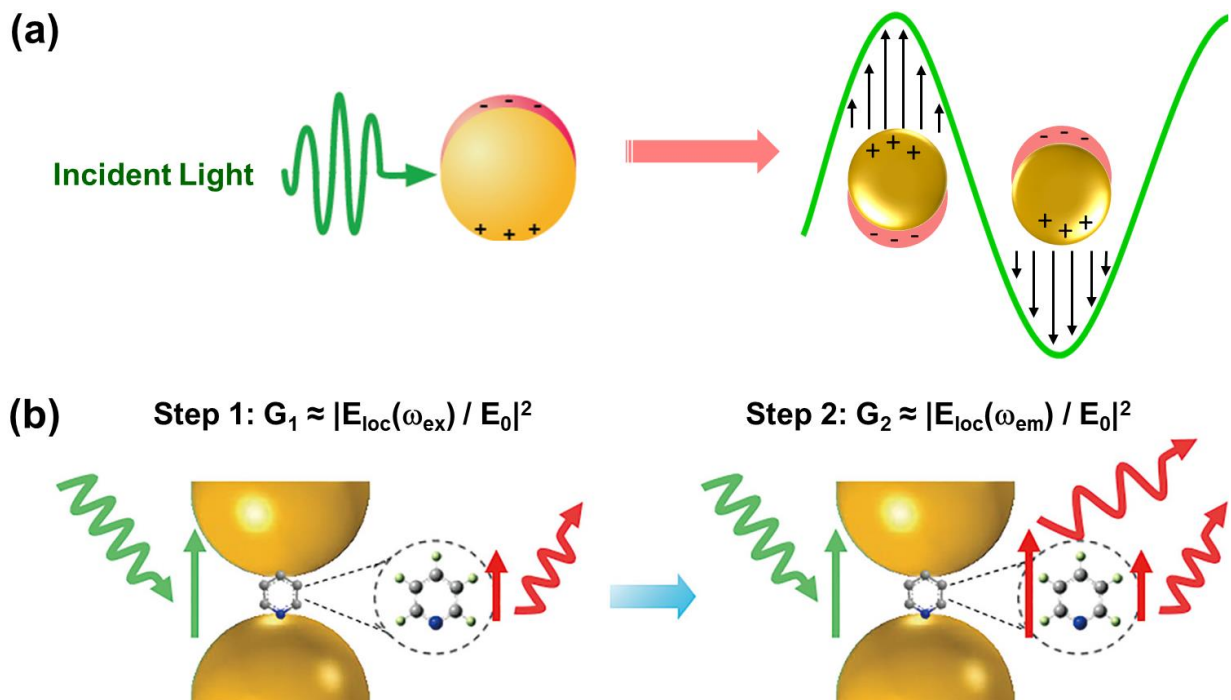
Figure 1.4 Schematics of (a) localized surface plasmon resonance (LSPR) and (b) electromagnetic enhancement mechanism in SERS including two-step processes. Reproduced from Zong *et al.*[46] with permission from the American Chemical Society.

On the other hand, electromagnetic enhancement is well accepted as the dominant contribution to SERS enhancement, which arises from the excitation of the localized surface plasmon resonance (LSPR). LSPR refers to the collective oscillation of conduction electrons at the interface of metallic nanoparticles (Figure 1.4a).[51] The nanoparticles that are able to generate a strong LSPR are called plasmonic nanoparticles. Electromagnetic enhancement can be viewed as a two-step process (Figure 1.4b).[46] First, local electromagnetic field enhancement occurs around the plasmonic nanoparticles at the exciting frequency (ω_{ex}): $E_{loc}(\omega_{ex}) = G_1 E_0$, where G_1 is the enhancement factor of the electromagnetic field in the near field at ω_{ex} and E_0 is the local electromagnetic field in the absence of nanoparticles. In this step, plasmonic nanoparticles serve

as a receiving optical antenna to transform the far field to the near field. Second, the enhancement arises from the Raman polarizability of the molecule-nanoparticle system. Here, plasmonic nanoparticles serve as transmitting optical antennae to transfer the near field to the far field at the Raman emission frequency (ω_{em}). The Raman signal is proportional to the enhanced local electric field: $E_{loc}(\omega_{em}) = G_2E_0$, where G_2 is the enhancement factor of the electromagnetic field at ω_{em}. Therefore, the overall electromagnetic enhancement is a function of both exciting and emitting electric field: $G \propto [E_{loc}(\omega_{ex})/E_0]^2[E_{loc}(\omega_{em})/E_0]^2 = G_1^2G_2^2$. When the incident and Raman scattered frequency are comparable, the SERS enhancement factor is approximately proportional to the fourth power of the enhancement of the local electric field. As the strength of the local electric field correlates to the distance (r) between the molecule and nanoparticles by $E(r) \propto (1 + r/a)^{-3}$, the electromagnetic enhancement may scale with r roughly by $(1 + r/a)^{-12}$, where a is the radius of nanoparticles.[52] This relationship indicates that vicinity molecules at the nanoparticle surface have the highest enhancement and sensitivity in the SERS measurements.

Strategies aimed at enhancing Raman signal of molecules have focused not only on the use of label-free SERS, but also on the introduction of small Raman tags to increase detectability. This labeled SERS is of particular interest in cases in which signals of molecules of interest are intrinsically weak and can be easily overwhelmed by other irrelevant molecules in complex biological systems, such as biofluids and *in vivo* conditions. Generally, Raman tags have the same role as fluorescent molecules. However, Raman tags possess the following advantages: (1) a powerful signal derived from the relatively large Raman scattering cross-section, (2) a strong affinity for nanoparticles to prevent photobleaching, (3) characteristic and well-assigned Raman peaks to avoid spectral overlapping during multiplex detection, (4) amenability to operate at near-infrared (NIR) with low autofluorescence interference, and (5) high biocompatibility.[53,54] Overall,

SERS inherits high sensitivity and rich fingerprint information that make it superior to other conventional spectroscopic techniques. To improve the performance of SERS for biomarker detection, an important prerequisite is to better understand physicochemical properties of metallic nanoparticles.

1.4 Gold Nanoparticles for Biomarker Detection

Among different metallic nanoparticles, gold nanoparticles (AuNPs) have emerged as an exceptional platform due to their unique physical and chemical properties.[55,56] Generally, for simple geometries such as spherical AuNPs, smaller sizes ($\leq$ 40 nm) are highly absorbing while larger sizes ($\geq$ 80 nm) are predominately scattering.[57] As the size of AuNPs increases, a red-shift in the LSPR is observed due to phase retardation effects. Phase retardation originates from the oscillations of the electron cloud around AuNPs. With increasing dimensions, the amplitude of the electron oscillation enhances which consequently increases the plasmon lifetime.[58] Afterwards, the frequency of the waves decreases which inversely red-shifts the plasmon wavelength. However, in complex anisotropic AuNPs, the absorption and scattering properties are mainly dependent on geometry rather than the size.[59] A spectral shift observed by altering the shape is due to the change in polarizability of AuNPs.[60] This polarizability is particularly dominant for AuNPs with highly branched geometries such as gold nanostars (AuNSs).[61] The polarizability of AuNSs is enhanced by increasing the numbers of protrusions with minimal changes in overall dimensions which gives rise to red-shifts in the plasmon resonances.[62] These tunable properties are of particular interest in biological applications as particles resonant in the NIR region (650 – 900) allow deep tissue imaging due to low absorption of NIR light by biofluids and greater photon penetration depth attained by NIR light with minimal tissue damage.[63] AuNSs with large

scattering cross-sections and high polarizability are thus extensively utilized as contrast agents for positron emission tomography (PET) and computed tomography (CT) which allow depth-resolved whole-body imaging with high resolution.[33] Further, the special geometry of AuNSs generates nanoantenna effect where the spherical core absorbs the incident light and then routes to the protrusions resulting unprecedented electromagnetic near-fields at the sharp tips. These near-field configurations of AuNSs amplify the signal of molecules of interest by $> 10^9$ in the SERS applications.[64-66]

The synthesis of AuNSs is straightforward and can be achieved by a one-step seedless approach using biological buffer HEPES (4-(2-hydroxyethyl)-1-piperazineethanesulfonic acid) as both capping and reducing agent.[67] The plasmon resonances of AuNSs can be tuned from the visible to NIR by modifying three parameters: concentration of HEPES, concentration of Au^{3+}, and pH of the buffer. First, by increasing the HEPES concentration, larger AuNSs with longer protrusions are formed. The number of HEPES molecules available during the nucleation and the weak adsorption of HEPES to Au along the $\langle 111 \rangle$ direction both attribute to the morphological evolution of AuNSs.[68] Initially, spherical gold nanoparticles nucleate in solution, and HEPES binds to the particle surface. At low [HEPES]/[Au^{3+}] ratio, fewer HEPES molecules are available to bind exposing the different facets of particles for further Au^{3+} reduction. As more Au^{3+} ions are reduced on the particle surface, spherical morphology with short protrusions is formed. As the [HEPES]/[Au^{3+}] ratio further increases, more HEPES molecules preferentially bind to $\langle 111 \rangle$ direction, and more Au^{3+} ions are reduced on the $\langle 111 \rangle$ crystal planes at higher [HEPES], resulting in the formation of AuNSs with longer protrusions. In addition to the HEPES concentration, the plasmon resonances of AuNSs can also be altered by modulating the concentration of Au precursor in the growth solution. When the [HEPES]/[Au^{3+}] is high, fewer Au nuclei are generated and a

13

higher [HEPES] binds to the nuclei. When the [HEPES]/[Au^{3+}] is low, a larger density of Au

nuclei is clustered together to block the binding sites for HEPES and also ⟨111⟩ crystallographic

direction, which gives rise to AuNSs with shorter and fewer protrusions. At significantly high

[Au^{3+}], more spherical-like AuNSs are formed. Moreover, the plasmonic tunability can be

achieved by changing the pH of reaction from 6.61 to 8.6 while keeping [HEPES] and [Au^{3+}]

constant. When the pH of reaction solution is less than the pKa of HEPES (pKa = 7.5), the acidic

solution facilitates the protonation of nitrogen atom in the tertiary amine in the piperazine ring in

a HEPES molecules. This protonation in turn decreases the binding affinity of HEPES for the

particle surface along both ⟨111⟩ and ⟨110⟩ directions. As a result, Au reduction occurs along all

facets of crystal leading to the formation of spherical particles with larger radius and shorter

protrusions. When the pH of solution is neutral or near the pKa, the piperazine ring is not

protonated giving rise to cationic free radical formation, preferred binding to the different facets

of Au except the ⟨111⟩ direction, and eventually AuNS formation. When the pH of solution is

greater than pKa of HEPES, the ethanesulfonic acid group in HEPES is deprotonated and becomes

negatively changed leading to the ionic strength increase of basic solution. It is well-known that

metallic nanoparticles tend to cluster together in high ionic strength solutions to balance the

charges and reach equilibrium.[69] Here, when the pH is slightly higher than pKa (pH 7.69 and 8.03),

AuNSs form higher-order clusters including dimers and trimers. A blue-shift in the plasmon

resonance is expected, which may be attributable to the charge-transfer plasmon among the closely

interacted particle clusters. However, when the pH is significantly high (pH 8.27 and 8.6), a red-

shift in the plasmon resonance occurs, which is due to the formation of large aggregates yielding

a plasmon shift to longer wavelengths, resonance broadening, and an increase in aggregate peak.

In addition to enabling the morphological and plasmonic tunability, HEPES-mediated AuNS fabrication also allows straightforward surface functionalization with a wide variety of molecules with diagnostic, therapeutic and imaging capabilities. For example, the surface of AuNSs can be functionalized with hydrophilic and biocompatible materials, such as polyethylene glycol (PEG).[70] Generally, when bare AuNSs contact a biological fluid, their surfaces can be easily covered with the protein corona leading to changes in their *in vivo* trafficking, uptake and clearance by the mononuclear phagocytic system (MPS). However, PEGylated AuNSs are able to render their stealth properties to reduce non-specific protein adsorption and prolong blood circulation time.[71] Further, AuNSs can be conjugated with antibodies to target specific antigens to reduce the non-specific accumulation in the body, enabling a lower dose of nanoparticles for the same therapeutic effects and lessening any nanoparticle-mediated toxicity.[72] Finally, AuNSs allow surface decoration with various imaging agents to detect and track biomarkers *in vitro* and *in vivo*.[34,73] Although unique physical and chemical properties make AuNSs extremely attractive in biomedical applications, the toxicity of particles must be scrutinized to expedite their clinical translation.[74] Especially, the lack of long-term toxicological and pharmacokinetic investigations of AuNSs in the living matter significantly hinders their use in diagnosis and therapeutics. As a result, a systematic evaluation at the preclinical level to elucidate fundamental questions about biodistribution and biocompatibility of AuNPs is important.

It is well-known that MPS is a major clearance route for AuNPs *in vivo*.[75,76] The MPS includes monocytes circulating in the blood and macrophages located in different organs, such as liver, spleen, and lung. Generally, macrophage precursor cells produced by hematopoietic stem cells in bone marrow are first released into circulation as monocytes.[77] These circulating monocytes then extravasate through the endothelium and migrate to tissues followed by

differentiation into various macrophage subsets, depending on their anatomical location and functional phenotype.[78] Kupffer cells in liver, alveolar macrophages in lungs, osteoclasts in bones and histiocytes in interstitial connective tissues are the major specialized tissue-resident macrophages. Other types of macrophages also exist in secondary lymphoid organs, including the macrophages residing in spleen marginal zones and subcapsular sinus macrophages in lymph nodes. In addition to MPS clearance, renal excretion is equally important. Particles undertaking renal filtration must pass through: (1) glomerulus endothelium, (2) glomerular basement membrane and (3) a slit diaphragm of podocytes.[79,80] The uptake and elimination of particles by these pathways are highly dependent on their hydrodynamic size, surface charge, surface functionalization and protein adsorption.[81] Therefore, each of these parameters must be carefully considered when designing particles in order to effectively control biodistribution, determine ultimate fate and minimize toxicity.

1.5 Point-of-Care Diagnostics

In resource-limited settings, it is estimated that about 32% of the disease burden is from communicable diseases such as malaria, respiratory infections and acquired immune deficiency syndrome (AIDS), while 43% of the burden comes from noncommunicable diseases including cardiovascular disease, neuropsychiatric conditions and cancer.[82] Laboratory-based assays such as cell-based assay, polymerase chain reaction (PCR) and enzyme-linked immunosorbent assay (ELISA) are usually used for diagnosis of these diseases. However, these conventional clinical methods require sample transportation, multiple preparation steps, expensive instruments, and well-trained personnel.[83,84] Lack of access to these high-quality diagnostics in resource-constrained settings further poses a staggering health burden. Therefore, developing diagnostic

platforms that meet ASSURED criteria (Table 1.1) is one of the top priorities for improving healthcare delivery.[85] Point-of-care (POC) diagnostic testing has the potential to alleviate this burden by decentralizing and making high quality diagnostics accessible to wider populations.[86,87] Especially, the integration of plasmonics and microfluidic technologies that exploit fluorescence detection, absorption, transmission and polarization measurements integrated on lab-on-a-chip (LOC) can lead POC diagnostics towards miniaturization, parallelization, automation and integration of complex procedures in a simplified tool.[88] Here, microfluidics enable the handling, transport and mixing of fluids within the smallest of space. Fluid volumes down to femtoliters not only reduce the reagent consumption, but also save the time required for analytical processes.[89] Further, incorporating a series of micropumps and/or microvalves in microfluidics facilitates the precise fluid control and thus improves the reproducibility of studies.[90] Cheap microchip fabrication also potentially allows mass production.[91] In addition, the synergistic integration of plasmonic nanoparticles into microfluidics has greatly enhanced the sensitivity of the platform. For example, the LSPR of metallic nanoparticles has allowed the observation of individual particles as small as 20 nm diameter for silver and 30 nm diameter for gold with dark-field microscopy.[92] Remarkably, a single 80 nm silver nanoparticle illuminated by white light can generate significant scattering flux equivalent to 5×10^6 fluorescein molecules or 10^5 quantum dots.[93] Further, the LSPR of metallic nanoparticles does not suffer from photo-bleaching, demonstrating superiority over conventional fluorophores for long-term monitoring. Due to these exceptional optical properties, metallic nanoparticles have extensively explored as spatial labels in imaging.[94-96] In order to translate molecular binding events into extinction changes for molecular detection, metallic nanoparticles have also widely used as transducers. As the refractive index of target molecules are higher than those of surrounding medium, the binding between

molecules and nanoparticles increases the refractive index and red-shifts the plasmon resonance.[97,98] The highly localized sensing zone of LSPR nanoparticles also enables the real-time monitoring of this refractive index changes upon binding.[99-101] Aside from outstanding properties of individual nanoparticles, the interaction between nanoparticles can lead to additional enhancements. When two plasmonic nanoparticles are placed in close proximity to one another (*e.g.*, edge-to-edge separations is less than one particle diameter), the plasmon resonances are coupled.[102] The coupling strength and peak shift are highly dependent on the interparticle distances. The coupling strength decays exponentially with an increasing interparticle spacing.[103-105] All of these properties have made the incorporation of metallic nanoparticles into microfluidics attractive for biomarker detection with high sensitivity.[106]

Table 1.1 The ASSURED criteria[85]

	Criteria	Description
A	Affordable	Cost-effective to end-users and health systems
S	Sensitive	Avoid false negatives
S	Specific	Avoid false positives
U	User-friendly	Simple to perform in few steps and require minimal training
R	Rapid and robust	Enable same-visit treatment and remain robust through varying supply chain and storage conditions
E	Equipment-free	Least use of special equipment
D	Deliverable to end-users	Available to end-users

1.6 Organization of Dissertation

This dissertation contains four main chapters.

Chapter 2 demonstrates a rapid, noninvasive, and label-free approach to evaluate treatment response to molecular inhibitors in breast cancer (BC) cells with RS. Metabolic reprograming in BC is probed with RS and multivariate analysis is applied to classify the cells into responsive or nonresponsive groups as a function of drug dosage, drug type, and cell type. Metabolites identified with RS are then validated with MS. Oncometabolites identified with RS

will ultimately enable rapid drug screening in patients ensuring patients receive the most effective treatment at the earliest time point.

Chapter 3 designs an innovative biodiagnostic sensor, portable reusable accurate diagnostics with nanostar antennas (PRADA), for multiplexed biomarker detection in small volumes (~50 µL) enabled in a microfluidic platform. PRADA simultaneously detects two biomarkers of myocardial infarction, cardiac troponin I (cTnI), which is well accepted for cardiac disorders, and neuropeptide Y (NPY), which controls cardiac sympathetic drive. In PRADA immunoassay, magnetic beads capture the biomarkers in human serum samples, and AuNSs "antennas" labeled with peptide biorecognition elements and Raman tags detect the biomarkers *via* SERS. PRADA is validated by testing cTnI in 11 de-identified cardiac patient samples of various demographics. Low-cost PRADA will have tremendous translational impact and amenable to resource-limited settings for accurate treatment planning in patients.

Chapter 4 evaluates the long-term (90 days) toxicity and ultimate fate of AuNSs. AuNSs are conjugated with a generic immunoglobulin G (IgG) antibody to explore untargeted biodistribution and radiolabeled with ^{64}Cu to enable PET imaging. Both *in vitro* and *in vivo* toxicities of this functionalized AuNSs (F-AuNSs) are evaluated. The biodistribution of F-AuNSs is assessed by (a) PET imaging, (b) gamma counts of ^{64}Cu radiolabeled F-AuNSs, (c) transmission electron micrograph (TEM) and (d) inductively coupled plasma mass spectrometry (ICP-MS) analysis of gold in tissues. Further, we assess the impact of cellular uptake and protein corona effect on the breakdown of F-AuNSs within tissues indicated from TEM images. Finally, Martini coarse-grained simulations are employed to understand the clearance of NPs as function of the shape, size and surface properties of broken NPs that are resulted from the degradation of F-AuNSs, and lipid membrane compositions. This in-depth study highlights the tremendous translational

potential of F-AuNSs and provides a great guidance for researchers to determine aspects needed to be considered when evaluating the biocompatibility of NPs.

Chapter 2

PROBING METABOLIC ALTERATIONS IN BREAST CANCER IN RESPONSE TO
MOLECULAR INHIBITORS WITH RAMAN SPECTROSCOPY AND VALIDATED WITH
MASS SPECTROMETRY

2.1   Summary

Rapid and accurate response to targeted therapies is critical to differentiate tumors that are resistant to treatment early in the regimen. In this work, we demonstrated a rapid, noninvasive, and label-free approach to evaluate treatment response to molecular inhibitors in breast cancer (BC) cells with Raman spectroscopy (RS). Metabolic reprograming in BC was probed with RS and multivariate analysis was applied to classify the cells into responsive or nonresponsive groups as a function of drug dosage, drug type, and cell type. Metabolites identified with RS were then validated with mass spectrometry (MS). We treated triple-negative BC cells with Trametinib, an inhibitor of the extracellular-signal-regulated kinase (ERK) pathway. Changes measured with both RS and MS corresponding to membrane phospholipids, amino acids, lipids, and fatty acids indicated that these BC cells were responsive to treatment. Comparatively, minimal metabolic changes were observed post-treatment with Alpelisib, an inhibitor of the mammalian target of rapamycin (mTOR) pathway, indicating treatment resistance. These findings were corroborated with cell viability assay and immunoblotting. We also showed estrogen receptor-positive MCF-7 cells were nonresponsive to Trametinib with minimal metabolic and viability changes. Our

findings supported that oncometabolites identified with RS will ultimately enable rapid drug screening in patients ensuring patients receive the most effective treatment at the earliest time point.

2.2 Introduction

Dysregulation of the mitogen-activated protein kinases (MAPK) pathway plays a critical role in the proliferation and progression of breast cancer (BC). This dysfunction is achieved by activating the extracellular-signal-regulated kinase (ERK) (or Ras/Raf/MEK/ERK) signaling cascade,[107] which has been associated with disease progression, metastasis, and treatment resistance in BC.[108,109] Small molecule inhibitors (SMIs) that downregulate components of the ERK pathway have shown improved clinical outcomes in BC patients, and several clinical trials have shown successful outcomes (NCT03971409, NCT03395899).[110] Current clinical measures rely on immunohistochemistry (IHC) analysis to guide initial treatments. But IHC is mostly qualitative, suffers from inter-user variability, and often lacks accuracy when presented with heterogeneous tumors.[111,112] Clinical decisions based on change in tumor size in response to therapy are inherently slow and low-throughput as a decrease in tumor burden can take several weeks. Therefore, an unmet clinical need exists for rapid, accurate, and cost-effective diagnostic tools that can guide the best treatment choices at the earliest time point and reduce mortality due to ineffective cancer therapies.

Metabolic reprograming is an emerging hallmark of cancer.[113] Cancer cells reprogram their metabolism to maintain viability and proliferate to metastatic disease.[114,115] Such metabolic rewiring goes beyond the well-known Warburg effect (glycolytic activity),[116] and includes a cumulative change in phospholipids, amino acids, lipids and fatty acids.[117,118] Emerging evidences now support that SMIs show an immediate inhibition of this altered metabolism in cancer cells

22

before a reduction in tumor size is observed, presenting a more sensitive endpoint to treatment response.[119,120] Metabolic response in clinical practice is traditionally measured with fluorodeoxyglucose-positron emission tomography (FDG-PET), which is both cost-prohibitive and has poor sensitivities to drug response.[121] Further, FDG-PET is limited in evaluating treatment response of patients undergoing therapy with mitogen-activated protein kinase (MEK) inhibitors targeting the ERK pathway. This limitation of FDG-PET is primarily due to its ability to only visualize changes in glycolytic activity, whereas inhibition of MEK has minimal impact on glycolytic effect.[122,123] It is also noteworthy that ^{18}F-FDG uptake is often enhanced by endothelial proteins such as vascular endothelial growth factor, which is overexpressed in BC, resulting in false diagnosis.[124]

In this work, we addressed the limitations of current clinical measures by demonstrating the utility of Raman spectroscopy (RS) combined with multivariate statistical analysis for tracking alterations in multiple metabolites in response to SMIs of the ERK pathway in BC cells. RS is an established optical spectroscopy that measures inelastic scattering of photons induced by the vibrational bonds in samples.[33,34,65,125] RS is a low-cost, rapid, label-free, and stain-free technique and has been utilized in breast cancer for diagnosis and surgical guidance.[126-128] RS is also nondestructive allowing sample archival and retesting for accurate measure of therapeutic response.[129-132] Here, we leveraged the advantages of Raman spectral mapping in its ability to first measure dynamic changes at the single-cell level with high sensitivity; second spatiotemporally resolve multiplexed metabolic changes; and third enable quantitative analysis. We treated triple-negative BC cell line MDA-MB-231 with Trametinib, a potent and specific MEK1/2 allosteric inhibitor,[133] that downregulates MEK signaling in the ERK pathway. MDA-MB-231 has basal-like properties and is known to have BRAF and KRAS mutations, which represent two major

oncogenic drivers in the ERK pathway (Figure 2.1). Treatment response to Trateminib was assessed with RS and resulting data were analyzed with principal component analysis (PCA). PCA allowed us to reduce the data dimensions of the multiple peaks in RS to a smaller number of principal components or loadings that carry all of the relevant spectral information necessary for classification.[134,135] We also treated MDA-MB-231 cells with phosphatidylinositol-3-kinase (PI3K) inhibitor (Alpelisib) and showed that these cells were resistant to this treatment. Finally, we studied an estrogen receptor (ER) positive BC cell line, MCF-7, which was resistant to Trametinib. Spectral trends from RS were then verified with mass spectrometry (MS), a gold standard in metabolomics. Note that MS by itself is not conducive to early and rapid drug screening since it is both time- and labor- intensive, and expensive. But RS trends validated with MS presented a complementary platform[125,136] for rapid, high-throughput, and single-cell level drug screening (with RS) combined with ensemble analysis of large volume of cells (with MS) to simultaneously confirm the changes in multiple metabolites post-treatment (Figure 2.1). By correlating the metabolic changes observed with RS and MS, we demonstrated that our approach can distinguish responders from nonresponders as a function of drug dosage, drug type targeting different signaling pathways, and cell type examining different BC lines. Our study goes beyond the traditional assays of cell viability and immunoblotting measurements and highlights early and improved drug response selectivity with tremendous translational potential.
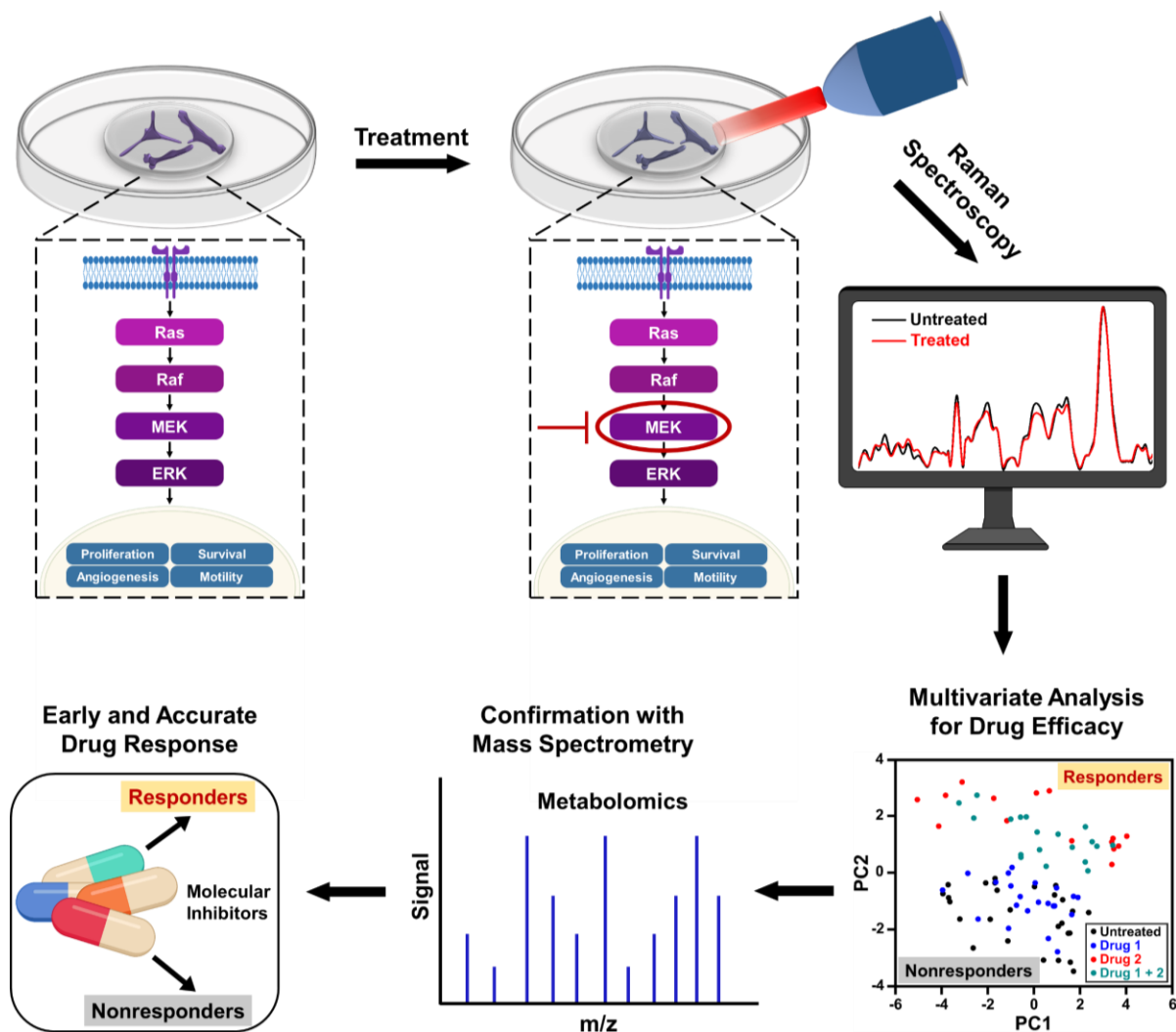
Figure 2.1 Schematic representation of metabolic changes probed in breast cancer cells with RS after treatment with small molecule inhibitors downregulating the ERK pathway. RS data combined with multivariate analysis and confirmed with mass spectrometry provide an early response to treatment distinguishing responders from nonresponders.

2.3 Materials and Methods

2.3.1 Cell Culture

MDA-MB-231 cells were purchased from the American Type Culture Collection (ATCC, HTB-26). The cells were cultured in Dulbecco's modified Eagle's medium (DMEM, Gibco) supplemented with 10% fetal bovine serum (FBS, Thomas Scientific). MCF-7 cells (ATCC, HTB-22) were cultured in Eagle's minimum essential medium (EMEM, ATCC) supplemented with 10%

FBS (ATCC), 1% penicillin/streptomycin (Gibco), and 0.01 mg/mL human recombinant insulin (Invitrogen). The cells were maintained at 37 °C and 5% CO_2. Afterwards, MDA-MB-231 or MCF-7 cells were seeded on 6 well plates at approximately 60% confluency. Once the cells have attached to the plates, different concentrations of MEKi (Trametinib, Selleck Chemical), PI3Ki (Alpelisib, Selleck Chemical), or a combination of two in complete media were added. After 72 h of incubation, old media were removed, and the cells were trypsinized. Detached cells were centrifuged at $125 \times g$ for 7 min to remove dead cells and then re-seeded on poly-L-lysine (Sigma) coated calcium fluoride windows (CaF_2, Crystran). Once the cells reattached on the CaF_2 disks, media were removed. Next, the cells on CaF_2 disks were washed three times with phosphate buffer saline (PBS), fixed by 4% formaldehyde (methanol-free) at room temperature for 10 min, washed with PBS three times again, and dried at room temperature prior to Raman mapping.

2.3.2 In Vitro Raman Mapping and Analysis

The cells on CaF_2 disks were visualized using a Renishaw inVia Raman microscope system. Brightfield images of the cells were captured with a 100× objective. A rectangular area capturing 3 – 4 cells was selected for Raman mapping at 2 µm by 2 µm resolution. Raman spectra for the entire map were obtained with a 785 nm laser (10 mW) with 1200 lines/mm grating with 10 s acquisition time. Afterwards, cosmic ray removal was performed with nearest neighbor method using the Renishaw WiRE 3.4 software. A custom MATLAB (R2019a) code was used to perform smoothing and background correction. The spectra were first smoothed by using the Savitzsky and Golay filter with fifth order and coefficient value of 47 (points). An automated and modified polyfit method was applied to remove fluorescent background by using a 11th order polynomial with a threshold of 0.0001. To eliminate non-cell pixels from the rectangular map, biological peak at 1440 cm^{-1} was selected to generate the cellular masks. The pixels were considered cell, or

"mask" when the intensities were higher than the set threshold. A Gaussian function was utilized to smooth the edges of the cell mask. The brightfield optical images were used to ensure the accuracy of the final cell masks. Clusters of pixels in the Raman map were then averaged, normalized using standard normal variate method and defined as one cell for PCA analysis. PCA was performed by using the MATLAB built-in "pca" function where the analyzed data were mean centered by default. Therefore, the variations of PC score shown in Figure 2.2d, 2.3b, 2.4a,b, 2.6b and A.8b represent the results of PCA. These variations were not contributed by any biases from the raw data. Two principal components were plotted to discriminate each treatment group.

2.3.3 Viability Assay

MDA-MB-231 or MCF-7 cells were passaged and seeded on 96 well plates. Once the cells were attached to the plates overnight, different concentrations of MEKi (Trametinib) or PI3Ki (Alpelisib) in complete media were added to the wells. After 72 h of treatment, old media in each well were removed and replaced with 100 µL of fresh media mixed with 10 µL of 12 mM 3-(4,5-dimethylthiazol-2-yl)-2,5-diphenyltetrazolium bromide (MTT, Thermo Fisher Scientific). After 3 h of incubation, 85 µL of the media solution in each well was removed and 50 µL of dimethyl sulfoxide (DMSO) was added to solubilize and dissolve the formazan. The plates were incubated at 37 °C for 10 min, and the absorbance of each well was read at 540 nm using a Biotek Synergy H1 plate reader.

2.3.4 Western Blot

MDA-MB-231 or MCF-7 cells were passaged, counted, and seeded on 6 well plates. The number of cells seeded on each well was counted by a scepter to ensure that each sample contained the same number of cells and proteins. Once the cells were attached to the plates overnight, different concentrations of MEKi (Trametinib) or PI3Ki (Alpelisib) in complete media were added

27

to the wells. After 6 h of treatment, lysis buffer was added to the cells and incubated at 4 °C for 30 min. Lysates were then centrifuged at 18,000 g at 4 °C for 15 min. Equal amounts of proteins were mixed with Laemmli buffer and boiled for 5 min. The samples were then loaded on 10% SDS-PAGE, and subsequently transferred onto nitrocellulose membranes through electrophoresis overnight at cold room. The membranes were blocked before adding primary antibodies. Primary and secondary antibodies were prepared in the blocking buffer. All antibodies were purchased from Cell Signaling Technology. Primary antibodies were against AKT (9272S), phosphor-AKT (9271S), ERK 1/2 (9102S) and phosphor-ERK 1/2 (9101S).

2.3.5 Mass Spectrometry

MDA-MB-231 cells were first seeded on 6 well plates and then treated with either MEKi (Trametinib) or PI3Ki (Alpelisib) for 72 h. After treatment, cells were washed with 1X PBS three times and detached by trypsin (Gibco). Trypsin was removed by centrifuge at $125 \times g$, and cells were resuspended in a small volume of 1X PBS. A lyophilizer (Labconco) was then utilized to remove any solvent. Dried cells were stored at -80 °C. The snap frozen cell pellets were weighed and reconstituted in a specified volume of methanol/water (3:1) to yield a cell density of 12.4 mg/mL. Cells were then flash frozen on dry ice and thawed at 5 °C three times to facilitate complete lysis. An aliquot of cell lysate (700 L) was combined with chloroform (500 L) in a clean glass vial, vortexed vigorously, and centrifuged at $3000 \times g$ for 5 min to achieve efficient phase separation. The aqueous (top) layer containing polar metabolites was transferred to a clean Eppendorf tube, evaporated to dryness under a gentle stream of nitrogen gas, and reconstituted in 200 L of acetonitrile/water (2:1) containing 250 M tyrosine (phenyl-3,5-d$_2$) internal standard. Forty-two amino acid analogues were measured in the aqueous fraction by a targeted HILIC-MS/MS method. The chloroform (bottom) layer containing nonpolar metabolites was transferred

28

to a clean glass vial, evaporated to dryness under a gentle stream of nitrogen gas, and reconstituted in 170 L of methanol containing 3 M carbamazepine and 30 L of a 10X solution of SPLASH LIPIDOMIX standard (Avanti Polar Lipids). The chloroform fraction was analyzed by reverse phase LC-high resolution MS for untargeted metabolomics.

For analysis of amino acid, LC-MS/MS analysis was performed using an Acquity UPLC system (Waters) interfaced with a TSQ Quantum Ultra^{TM} triple-stage quadrupole mass spectrometer (Thermo Fisher Scientific). The mass spectrometer was equipped with an IonMax source housing and a heated electrospray ionization (ESI) probe. Individual reference standards of all analytes were infused into the mass spectrometer for the optimization of ESI and selected reaction monitoring (SRM) parameters. Detection was based on SRM using the following optimized source parameters (positive ionization): spray voltage at 5 kV; capillary temperature at 300 °C; vaporizer temperature at 185 °C; tube lens of 52 V at *m/z* 184; N_2 sheath gas pressure 50 (arbitrary units); and N_2 auxiliary gas pressure 5 (arbitrary units). Data acquisition and quantitative spectral analysis were done using Thermo-Finnigan Xcalibur version 2.0.7 SP1 and Thermo-Finnigan LCQuan version 2.5.6, respectively. A Zic-cHILIC analytical column (3 μm, 2.1 × 150 mm, Merck SeQuant) was used for all chromatographic separations. Mobile phases were made up of 0.2% acetic acid and 15 mM ammonium acetate in (A) H_2O/CH_3CN (9:1) and in (B) $CH_3CN/CH_3OH/H_2O$ (90:5:5). Gradient conditions were as follows: 0 – 2 min, B = 85%; 2 – 5 min, B = 85 – 30%; 5 – 9 min, B = 30%; 9 – 11 min, B = 30 – 85%; and 11 – 20 min, B = 85%. The flow rate was maintained at 300 L/min, and the total chromatographic run time was 20 min. The sample injection volume was 10 L. The autosampler injection valve and the sample injection needle were flushed and washed sequentially with mobile phase A (1 mL) and mobile phase B (1 mL) between each injection.

For analysis of untargeted lipidomics, discovery metabolomics data were acquired using a *Vanquish* ultrahigh performance liquid chromatography (UHPLC) system interfaced to a *Q Exactive HF* quadrupole/orbitrap mass spectrometer (Thermo Fisher Scientific). Samples were injected a total of four times. Two injections were made in positive ESI mode followed by two injections in negative mode. Chromatographic separation was performed with a reverse-phase Acquity BEH C18 column (1.7 m, 2.1 × 150mm, Waters) at a flow rate of 300 L/min. Mobile phases were made up of 10 mM ammonium acetate in (A) H_2O/CH_3CN (1:1) and in (B) CH_3CN/iPrOH (1:1). Gradient conditions were as follows: 0 – 1 min, B = 20%; 1 – 8 min, B = 20 – 100%; 8-10 min, B = 100%; 10 – 10.5 min, B = 100 – 20%; and 10.5 – 15 min, B = 20%. The total chromatographic run time was 20 min, and the sample injection volume was 10 L. Mass spectra were acquired over a precursor ion scan range of *m/z* 100 to 1,200 at a resolving power of 30,000 using the following ESI source parameters: spray voltage at 5 kV (3 kV in negative mode); capillary temperature 300 °C; S-lens RF level at 60 V; N_2 sheath gas pressure 40 (arbitrary units); N_2 auxiliary gas pressure 10 (arbitrary units); and auxiliary gas temperature at 100 °C. MS/MS spectra were acquired for the top-five most abundant precursor ions with an MS/MS AGC target of 10^5, a maximum MS/MS injection time of 100 ms, and a normalized collision energy of 30 eV. Chromatographic alignment, peak picking, and statistical comparisons were performed using Compound Discoverer version 3.0 (Thermo Fisher Scientific). All differential features (samples *vs.* controls) having a *p* value of <0.05 and a fold change of >1.5 were processed for molecular matches in the Chemspider, mzCloud, HMDB, and KEGG databases based on precursor ion exact masses (+/- 5 ppm) and MS/MS fragmentation patterns. Metabolite matches were then filtered to exclude biologically irrelevant drugs and environmental contaminants. The finalized list of putative identifications was mapped to relevant biological pathways using the Metabolika software

module. Pooled QCs were injected to assess the performance of the LC and MS instruments at the beginning and at the end of each sequence. The results of mass spectroscopy were visualized using the heatmap generated by Python.

2.3.6 Statistical Analysis

All data were presented as mean ± standard deviation. Differences between two groups were assessed using GraphPad Prism 8 with unpaired two-sided Student's t-tests for the calculation of *p* values. Here, * indicates *p* <0.05, ** indicates *p* <0.01, *** indicates *p* <0.001 and **** indicates *p* <0.0001.

2.4 Results and Discussion

We recorded spatial Raman maps and measured the corresponding spectra of MDA-MB-231 cells in response to treatment with MEK inhibitor (MEKi) Trametinib. We measured ~20 – 25 individual cells per treatment group (Figure A.1) with a near-infrared 785 nm laser and 100× objective. Cells were seeded on poly-L-lysine coated calcium fluoride (CaF_2) disks to minimize substrate-induced background and fixed by 4% formaldehyde after 72 h of treatment. High resolution maps of a few cells were acquired in a single rectangular requisition at 2 µm by 2 µm resulting in 50 – 500 pixels per cell dictated by the size of the cell. Acquired spectra were then smoothed,[137-140] background subtracted following literature methods[141,142] and finally normalized for further analysis. The representative original Raman spectra acquired from each cell and step-by-step spectral processing are shown in Figure A.2. The mean normalized Raman spectra of the MDA-MB-231 cells treated with Trametinib at its working concentration (50 nM)[143,144] showed significant changes in multiple peaks relative to untreated cells (Figure 2.2a). To understand how the Raman footprint changed post-treatment, the difference spectrum was obtained by subtracting

31

the mean normalized Raman spectrum of treated cells from the untreated cells (Figure 2.2b). Here, positive differences indicate Raman peak intensities decreased after treatment, and negative differences indicate an increase in Raman peak intensities post-treatment. The key Raman peaks identified are shown with arrow, and the corresponding metabolites/proteins are listed in Table 2.1. These peak assignments were determined based on literature findings.[145]
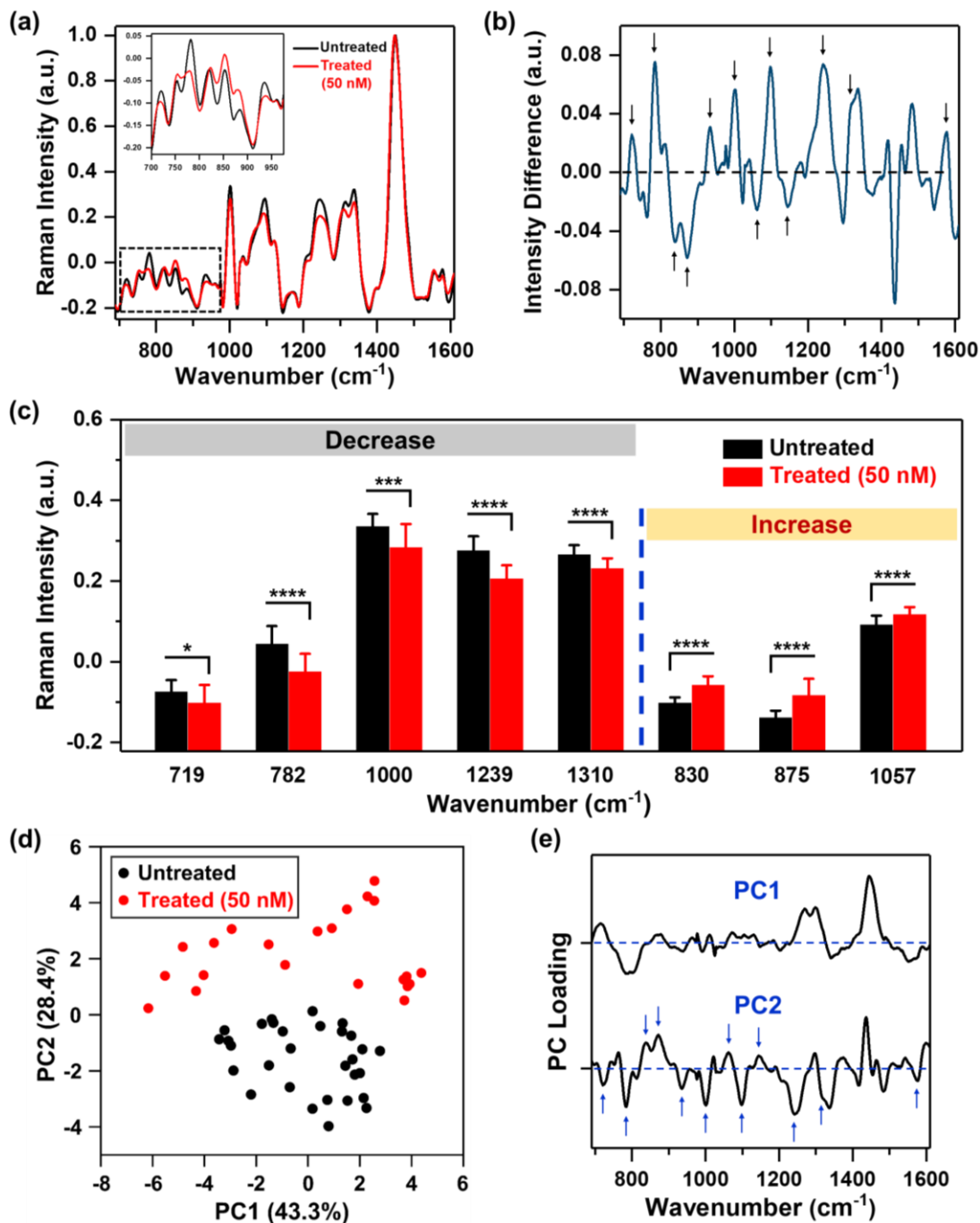
Figure 2.2 MDA-MB-231 cells treated with Trametinib and probed with RS. (a) Mean normalized Raman spectra of untreated cells (black) and cells treated with Trametinib at its working concentration 50 nM (red). Spectra were normalized to 1440 cm^{-1} biological peak. The inset showed a magnified view of the smaller wavenumber region. (b) Difference spectrum obtained from (a) by subtracting the mean normalized Raman spectrum of cells treated with Trametinib (50 nM) from the untreated cells to highlight changes in Raman footprint. Relevant peaks that either increased or decreased with treatment are shown with arrows. (c) Selective Raman peaks that decreased with treatment including phosphatidylcholine (719 cm^{-1}), DNA (782 cm^{-1}), phenylalanine (1000 cm^{-1}), Amide III (1239 cm^{-1}) and lipids & fatty acids (1310 cm^{-1}). Selective Raman peaks that increased after treatment including tyrosine (830 cm^{-1}), sphingomyelin (875 cm^{-1}), and lipids (1057 cm^{-1}). Here, * indicates $p < 0.05$, *** indicates $p < 0.001$, and **** indicates $p < 0.0001$ determined by student's t-test. (d) Principal component analysis showing clustering of untreated cells relative to those treated with Trametinib represented in a scatter plot. (e) Corresponding PC loading showing both PC1 and PC2. Relevant peaks in PC2 that distinguished the treated from untreated group are shown with arrows.

Table 2.1 Peak assignments for Raman spectral bands.[145]

Peak (cm^{-1})	Assignment
719	Phosphocholine and Phosphatidylcholine
782	DNA
787	Phosphatidylserine
830	Tyrosine
875	Sphingomyelin
935	Proteins and Amino Acids
1000	Phenylalanine
1057	Lipids
1094	DNA
1163	Tyrosine
1239	Amide III
1310	Lipids and Fatty Acids
1575	DNA
1582	Phenylalanine

We then quantified the changes in selective Raman peaks (Figure 2.2c and A.3) and correlated the observed trends to metabolic response to SMIs of the ERK pathway in breast cancer. A decrease in the Raman peak at 719 cm^{-1} was observed post-treatment corresponding to phosphocholine and phosphatidylcholine (PC). Cancer cells are known to upregulate PC which is the most abundant phospholipid in the cancer cell membrane. Aberrant PC metabolism may result

from enhanced choline kinase expression or activity.[146] Due to the relevance of PC in tumor progression, it is considered as a predictive biomarker for monitoring tumor response.[147,148] Emerging evidences suggest a strong correlation between choline metabolism and the ERK signaling cascade, where MEK inhibition decreases PC and its precursors,[123,149] and this trend is well supported by our RS results. The difference spectrum also showed a decrease in the Raman footprint of DNA (782, 1094 and 1575 cm^{-1}), indicating that the cytotoxic effect of Trametinib induced apoptosis and decrease in DNA replication.[150] A decrease in cell viability with treatment response also reduced the ability of cells to synthesize proteins, which corresponded well with a decrease in Raman peaks of amide III (1239 cm^{-1}), and phenylalanine (1000 and 1582 cm^{-1}) that is an essential amino acid necessary for protein synthesis. A decrease in Raman footprint of lipids/fatty acids (1310 cm^{-1}) was also observed, which is not surprising as cancer cells are known to rewire their metabolic circuit by dysregulating levels of lipids. Alterations in lipids often converge on the activation of the ERK pathway.[117] Lipids and fatty acids metabolism is also mediated by crosstalk between receptor tyrosine kinases (RTKs) and downstream signaling *via* ERK.[151] RTKs are overexpressed in most tumor types and activate cancer cells proliferation and survival. The epidermal growth factor receptor (EGFR) RTK is overexpressed in MDA-MB-231 cells,[152] and EGFR aberrations are known to stimulate the ERK pathway.[153] These correlations indicate that MEK inhibition with Trametinib is likely to reduce some lipids/fatty acids as observed with RS (and also validated with MS).

Our quantitative analysis also showed that several Raman peaks increased after treatment (Figure 2.2c and A.3), including tyrosine (830 and 1163 cm^{-1}), sphingomyelin (875 cm^{-1}), and a subset of lipids (1057 cm^{-1}). Tyrosine residues play a critical role in RTKs such as EGFR. EGFR overexpression results in phosphorylation of the protein tyrosine residues, which then activates

34

downstream signaling *via* ERK.[154] Therefore, we expect that MEK inhibition with Trametinib would result in dephosphorylation of tyrosine kinase. This dephosphorylation would manifest as an increase of tyrosine in Raman signal as the phosphorylated form of tyrosine decreased post-treatment as observed in our results. Sphingomyelin, a sphingosine-based phospholipid that exists in cell membranes, presents an anticancer role through ceramide release leading to apoptosis, and is known to augment the cytotoxicity of SMIs by activating sphingomyelinase enzyme activity.[155,156] Therefore, an increase in Raman intensity of sphingomyelin post-treatment is expected given its potent biological role in cancer cell metabolism. Finally, a subset of lipids (1057 cm^{-1}) increased post-treatment (confirmed with MS as discussed later), demonstrating that lipid metabolism in cancer is a highly complex phenomenon.

To identify major patterns in Raman spectra that distinguish the untreated cells from the treatment group (50 nM MEKi), we applied PCA to the data sets. The first and second principal component, PC1 and PC2, presented in a two-dimensional PC scatter plot (Figure 2.2d) showed clear clustering between the groups with a variance level of 43.3% for PC1 and 28.4% for PC2. Each dot in the plot represents one cell/spectrum with dimension reduction. In the corresponding PC loading (Figure 2.2e) spectral features in PC1 were likely due to the intrinsic variabilities between the cellular groups. Dominant peak positions in PC2 corresponded well to the peaks identified in the difference spectrum (Figure 2.2b) supporting the metabolic alterations we discussed above.

Next, we probed the ability of RS in distinguishing responders from nonresponders by examining cellular response to treatment as a function of Trametinib concentration (1, 50 and 300 nM) (Figure 2.3a). PCA scatter plot showed distinguishable clustering between the responsive and nonresponsive groups with a variance level of 45.4% and 19.6% for PC1 and PC2, respectively

(Figure 2.3b). Here, the cells treated with Trametinib at, and well above the working concentration (50 and 300 nM) were grouped on the negative side of PC2 and categorized as responders. The untreated cells and those treated with significantly low concentration of Trametinib (1 nM) were clustered together on the positive side of PC2 and categorized as nonresponders. The features in both PC1 and PC2 (Figure A.4) had good concordance to the trends observed in Figure 2.2e, and were also supported by ratiometric analysis of individual Raman peaks (Figure A.5) as a function of Trametinib concentration. Ratiometric analysis of the different metabolites is well aligned with our discussion above on metabolic changes in response to treatment with MEKi.
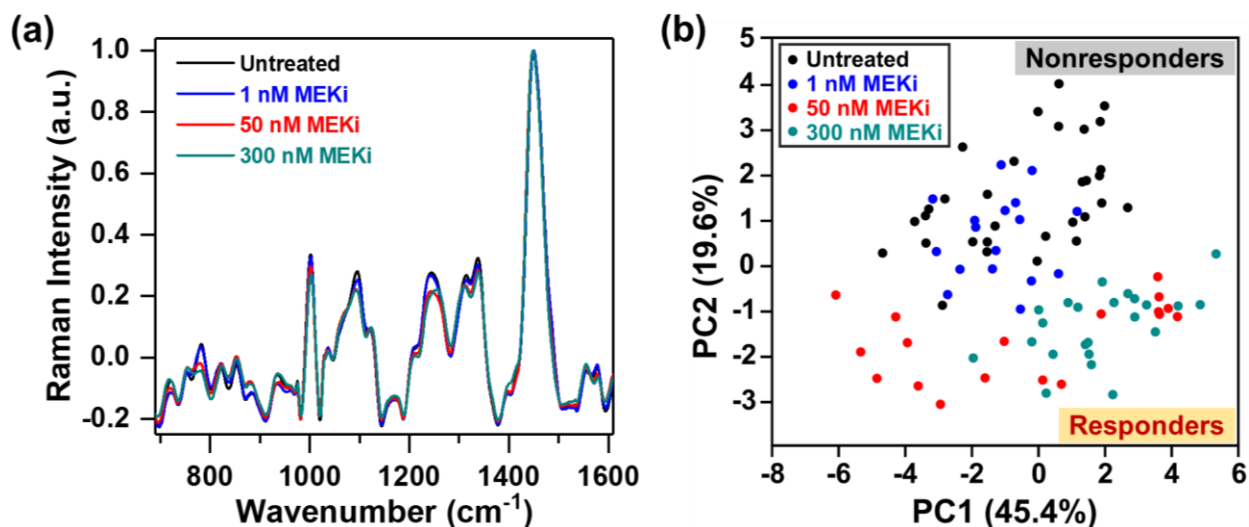
Figure 2.3 RS distinguishing responders from nonresponders as a function of Trametinib dosage. (a) Mean normalized Raman spectra of untreated MDA-MB-231 cells and those treated with various concentrations (1, 50 and 300 nM) of MEKi (Trametinib). Spectra were normalized to 1440 cm^{-1} biological peak. (b) PC scatter plot showing clustering of cells based on Trametinib concentrations differentiating responders from nonresponders.
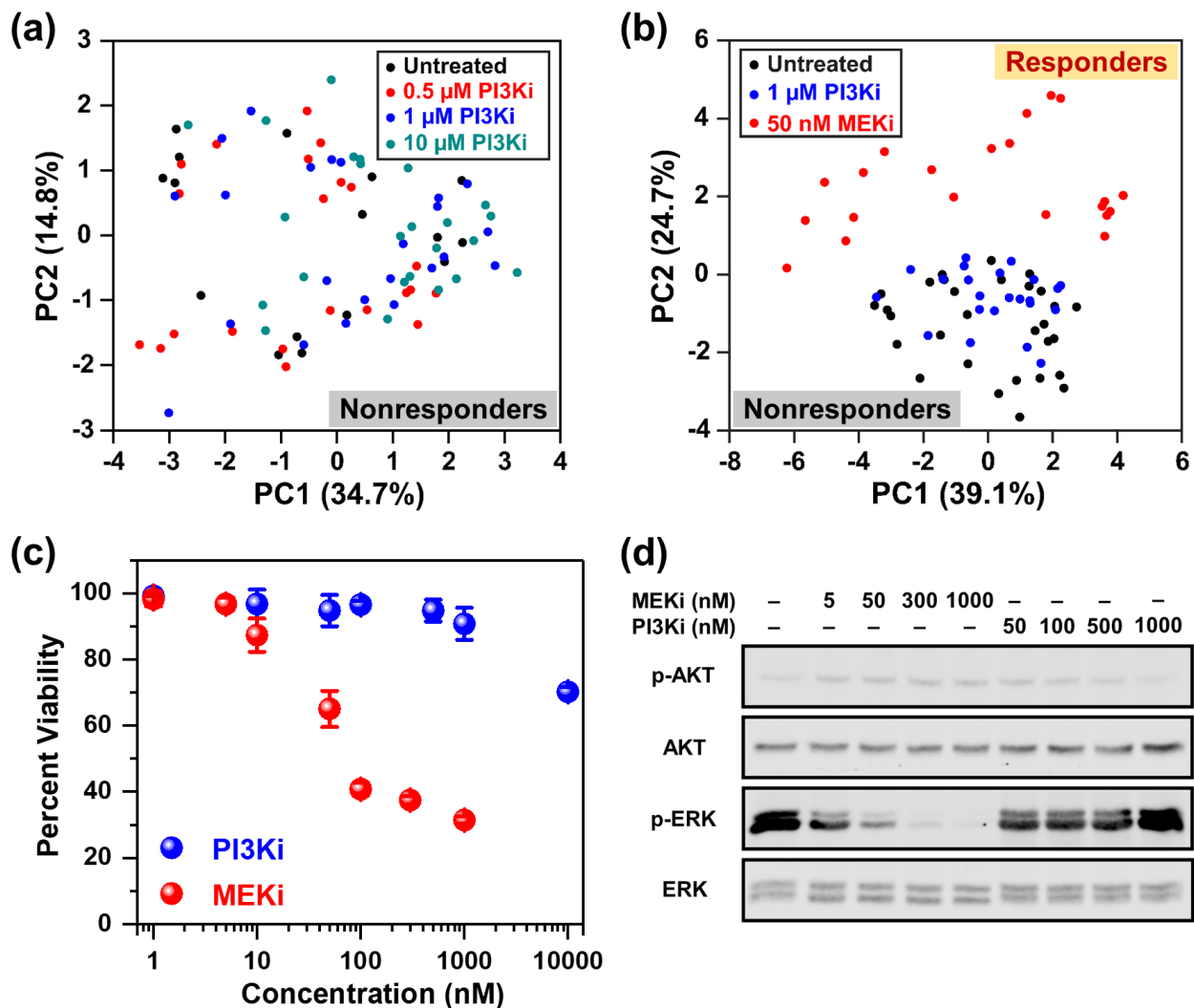
Figure 2.4 RS distinguishing responders from nonresponders as a function of drug type. (a) PCA scatter plot comparing MDA-MB-231 cells in response to different concentrations (0.5, 1 and 10 µM) of PI3Ki (Alpelisib) showing no distinct clustering among groups. (b) PCA scatter plot comparing untreated cells (black) to those treated with 1 µM of PI3Ki (Alpelisib, blue) and 50 nM of MEKi (Trametinib, red). Clear clustering of cells was observed for those responsive to treatment relative to nonresponders. (c) MTT viability assay of cells treated for 72 h with MEKi (Trametinib) or PI3Ki (Alpelisib) at 0 – 10 µM concentrations (n = 4 per concentration). Cell viability was measured at 540 nm. All data were presented as mean ± standard deviation. (d) Immunoblotting analysis of cells in response to treatment with MEKi (Trametinib) or PI3Ki (Alpelisib) at increasing concentrations showed reduced ERK1/2 phosphorylation for cells that responded to treatment.

In addition to the ERK pathway, the mammalian target of rapamycin (mTOR) pathway consisting of the PI3K/AKT/mTOR cascade is also upregulated in BC.[157] Whereas multiple SMIs,

such as PI3K inhibitor (Alpelisib), have shown favorable outcomes in clinical trials (NCT02155088, NCT02998476, NCT01241500, *etc*.), BCs that are estrogen receptor (ER), progesterone receptor (PR) and/or human epidermal growth factor receptor 2 (HER2) negative are poorly responsive to these treatments. MDA-MB-231 cells have ER, PR, and HER2 triple-negative status and are known to be resistant to Alpelisib and other SMIs of the mTOR pathway.[158,159] We performed RS and investigated the cellular response of MDA-MB-231 cells upon treatment with different concentrations of Alpelisib (0.5, 1 and 10 µM), where the working concentration of Alpelisib is ~1 µM. Besides a slight decrease in amino acids (935 and 1000 cm^{-1}) upon treatment with Alpelisib, overall minimal changes were observed in Raman peaks corresponding to DNA, phospholipids, lipids, and fatty acids (Figure A.6a) identified earlier. The PC scatter plot of PC1 *vs*. PC2 (Figure 2.4a) clearly showed that across all concentrations of PI3Ki, there was no clustering demonstrating that MDA-MB-231 cells were resistant to Alpelisib even beyond its working concentration. The corresponding PC loading is shown in Figure A.6b.

Next, we examined the ability of RS in distinguishing responders from nonresponders as a function of drug type. Here, cells were treated with 1 µM of PI3Ki or 50 nM of MEKi and compared to untreated cells. The mean normalized Raman spectra of the MDA-MB-231 cells treated with MEKi (50 nM) showed significant changes in multiple peaks compared to untreated cells or those treated with PI3Ki (1 µM) (Figure A.7a). The spectral differences between untreated cells and those treated with PI3Ki (1 µM) were minimal. The PC scatter plot further confirmed the results and clearly differentiated cells that responded and those that were resistant to treatment (Figure 2.4b). The untreated cells and those treated with PI3Ki (1 µM) were clustered together and defined as nonresponders, whereas the cells treated with MEKi (50 nM) were grouped and defined as responders. Additionally, PC1 and PC2 accounted for 39.1% and 24.7% of the total

variance, respectively. The corresponding PC loading (Figure A.7b) shared similar features as the PC loading shown in Figure 2.2e. These results suggested that the metabolites summarized in Table 2.1 also played a critical role in differentiating BC cells response to PI3Ki (Alpelisib). Trends observed in RS were further verified with cell viability (MTT) assay (Figure 2.4c). MDA-MB-231 cells were treated for up to 72 h and the percentage of viable cells was measured. MTT assay supported our findings with RS and showed that cells were not responsive to PI3Ki (Alpelisib) where 90% of the cells were viable at the working concentration of the drug (1 µM) and 75% were viable at 10X higher concentration. The cells were highly responsive to MEKi (Trametinib) in a dose-dependent manner with ~30% cells viable at the highest concentration of drug evaluated in our study (1 µM MEKi). We also performed immunoblotting assay (Figure 2.4d) to further confirm the trends observed in RS and MTT assay and to determine if the observed trends among responders (MEKi treated) resulted from inhibition of the ERK pathway. Activation of the ERK pathway produces an abundance of phosphorylated ERK (p-ERK) which then stimulates downstream signaling. Therefore, inhibition of the ERK pathway with Trametinib reduced p-ERK, but minimal changes were observed in p-ERK for PI3K inhibition in BC cells. Immunoblotting results supported RS results discussed in Figure 2.2c where upon treatment an increase in tyrosine was observed resulting from a decrease in phosphorylated tyrosine kinase. Western blot also showed neither inhibitor changed the levels of phosphorylated AKT, which is the downstream effector of PI3K in the mTOR cascade. We also examined the impact of combinatorial treatment of Trametinib (50 nM) + Alpelisib (1 µM) in MDA-MB-231 cells (Figure A.8). PCA showed cells treated with combination therapy clustered with those treated with Trametinib alone. Additional details are provided in the Appendix.

		Responders	Nonresponders
		Trametinib	Alpelisib
Amino Acid Metabolism	Pyroglutamic Acid	0.72	0.56
	L-Lysine	0.96	1.62
	L-Glutamine	0.70	0.56
	Creatinine	0.54	0.56
Membrane Phospholipid Metabolism	Phosphocholine	0.68	1.03
	Phosphatidylcholine	0.65	1.08
	Lysophosphatidylcholine	0.67	0.95
	Sphingomyelin	1.55	0.98
	Phosphoserine	0.83	0.91
Lipid and Fatty Acid Metabolism	Icosa-Tetraenoic Acid	0.09	0.91
	Pantothenic Acid	0.59	0.94
	all-cis-4,7,10,13,16-Docosapentaenoic Acid	0.20	0.75
	N-Acetyle-DL-Glutamic Acid	0.39	0.98
	Palmitoleic Acid	0.21	0.64
	E-Tokoferol	0.22	1.11
	Eicosatrienoic Acid	0.25	0.86
	5β-Cholanoic Acid	0.46	0.87
	D-Glucosyl-β-1,1-N-Palmitoyl-D-Erythro-Sphingosine	1.75	0.92
	2-Hydroxy-N-(1,3-Trihydroxy-2-Octadecanyl)Tricosanamide	1.67	1.31

Figure 2.5 Mass spectroscopic analysis of MDA-MB-231 cells treated with Trametinib (MEKi) or Alpelisib (PI3Ki) at their working concentrations (MEKi: 50 nM; PI3Ki: 1 µM). The numbers were a ratio of treated cells to untreated cell control where closer to 1 indicated minimal changes in metabolites. All differential features (samples *vs.* controls) had a *p* value of <0.05.

To further validate the metabolic changes observed in RS in response to molecular inhibitors, we performed LC-MS/MS on cell extracts (Figure 2.5). Mass spectrometry (MS) is a gold standard in metabolomics sampling a large volume of cells and identifying specific metabolites with both high selectivity and sensitivity. MDA-MB-231 cells were treated with MEK (Trametinib, 50 nM) or P13K (Alpelisib, 1 µM) inhibitor at their working concentration. After 72 h of treatment, cells were resuspended in PBS, dried, weighted and then analyzed with MS. The metabolites assessed with MS were represented *via* a heat map where numbers shown are the ratio

of integrated area of treated cells to those of untreated control cells. The ratio <1 indicates metabolites decreased with treatment, and ratio >1 indicates metabolites increased post-treatment. Representative metabolites were grouped into three main categories: amino acids (AAs), membrane phospholipids, and lipids and fatty acids. In response to treatment with Trametinib, the observed decrease in AAs was consistent with findings in the literature as cancer cells are known to have upregulated *de novo* synthesis of AAs and an increase in corresponding membrane transporters and metabolic enzymes.[160,161] AAs are the building blocks of proteins and intricately participate in protein synthesis. Therefore, a decrease in AAs in BC cells after treatment was likely contributed by an inhibition of these catabolic enzymes. Further, decrease in cell viability post-treatment with Trametinib also reduced AAs and subsequent protein synthesis, a trend that was supported by RS (Figure 2.2c, A.3 and A.5). Additionally, a decrease in phosphatidylcholine and other choline precursors also supported the trends observed in RS and was consistent with literature findings noted earlier that demonstrate a decrease in choline metabolism with MEK inhibition. However, not all membrane phospholipids decreased with MEK inhibition in BC cells. MS measurement supported RS trends of increase in sphingomyelin after treatment with Trametinib, explained in the Figure 2.2c discussion. We also observed a striking decrease in lipids and fatty acids metabolism with MEK inhibition also supported by our RS findings (Figure 2.2c and A.5). Note however, MS showed a subset of lipids increased post-treatment which was also observed in RS where the lipid peak at 1057 cm^{-1} (Figure 2.2c) increased in intensity. These findings suggested that a future lipidomics study will be necessary to unravel the crosstalk between lipids/fatty acids metabolism and pro-oncogenic downstream signaling pathways. For cells treated with Alpelisib, a decrease in amino acids was observed in MS which likely resulted from a decrease in protein synthesis, also observable as a decrease in the RS footprint at 935 and 1000

cm^{-1} (Figure A.6a). But overall, treatment with Alpelisib resulted in minimal changes in both

membrane phospholipids, and lipids and fatty acids in MS. These results collectively show that

MS validates the findings from RS, and these two techniques are complementary in providing

rapid drug screening and corresponding metabolic rewiring at the cellular level.
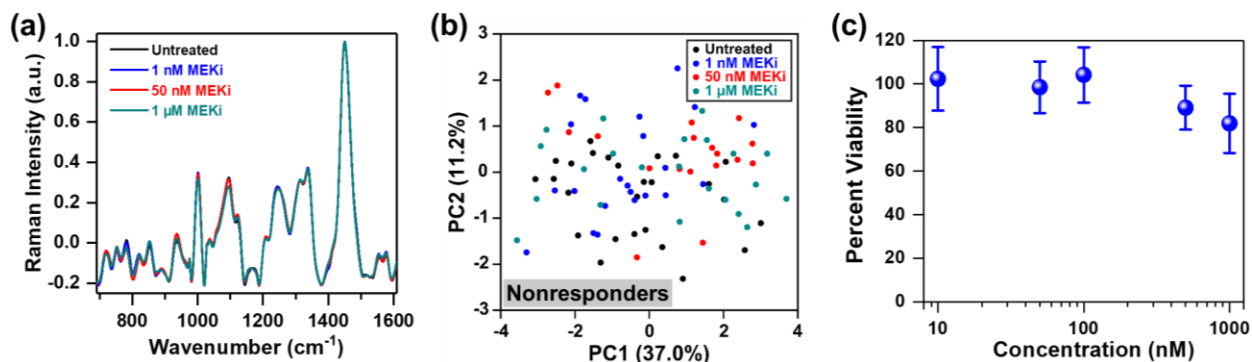
Figure 2.6 MCF-7 cells treated with Trametinib and interrogated with RS. (a) Mean normalized Raman spectra of untreated cells (black) relative to those treated with MEKi (Trametinib) at 1 nM (blue), 50 nM (red) and 1 µM (cyan). Spectra were normalized to 1440 cm^{-1} biological peak. Minimal changes in Raman footprint were observed. (b) PCA scatter plot comparing untreated cells with those treated with Trametinib showing no distinct clustering among groups. (c) MTT viability assay of cells treated for 72 h with Trametinib at various concentrations (n = 4 for each concentration). Cell viability was measured at 540 nm. All data were presented as mean ± standard deviation.

Thus far, our approach has focused on distinguishing responders from nonresponders

within the same cell line as a function of dosage and drug type. Next, we evaluated if RS can

determine treatment response in an ER-positive cell line, which represents a large subset of BC.

We chose MCF-7 as a model of ER-positive cell line[162] with no known KRAS mutations, and

resistance to selective MEK inhibitors. MCF-7 cells were treated with Trametinib at various

concentrations (1 nM, 50 nM and 1 µM), and cellular response was assessed with RS.

Representative original Raman spectra of MCF-7 cells, and Raman spectra after smoothing and

background subtraction were shown in Figure A.9. Minimal changes were observed in most of

the Raman peaks as a function of drug concentration (Figure 2.6a) and PCA scatter plot

corroborated that MCF-7 cells were resistant to Trametinib with no clear clustering of cells for any of the concentrations (Figure 2.6b). These findings were further confirmed with cell viability assay (Figure 2.6c) which showed MCF-7 cells were not responsive to MEK inhibition with Trametinib where 80% of the cells remained viable even at a significant high concentration of 1 µM. A comparison of the PC loading for MCF-7 cells treated with Trametinib (Figure A.10) with those of MDA-MB-231 cells (Figure 2.2e, A.4, A.7b and A.8c) showed significant differences in treatment response between the two BC cells supporting the cell viability results of treatment resistance. A few features in PC loading of MCF-7 (Figure A.10, indicated by arrows) arose from DNA (782 cm^{-1}), amino acids (856 cm^{-1}), proteins (935 and 1123 cm^{-1}), and lipids/fatty acids (1330 cm^{-1}) were likely due to decrease in cell viability at the highest concentration of Trametinib as observed in RS (Figure 2.6a) and viability assay (Figure 2.6c).

2.5 Conclusions

In summary, this work addressed a critical need in early and accurate drug screening which goes beyond the traditional approaches (*e.g.*, viability assay and immunoblotting) in distinguishing responders from nonresponders. Here, we performed RS to probe metabolic reprograming in breast cancer cells and evaluated treatment response to potent and clinically approved SMIs by examining alterations in metabolites. Our findings demonstrated that RS combined with multivariate analysis presented a powerful platform with tremendous clinical significance differentiating BC cells that were responsive to SMIs as a function of dosage, drug type, and cell type. Findings with RS were verified with MS, a workhorse in metabolomics, by examining various oncometabolites. Primarily we showed that triple-negative MDA-MB-231 BC cells were responsive to Trametinib, an inhibitor of the ERK pathway, and nonresponsive to Alpelisib, an

inhibitor of the mTOR pathway, supported by a collective change in DNA, membrane phospholipids, amino acids, lipids, and fatty acids. We also demonstrated that ER-positive MCF-7 BC cells were resistant to Trametinib with minimal changes in metabolites and no classification among treatment groups as seen in PCA. Our results suggested that these oncometabolites represented an important hallmark of cancer that can be targeted to both treat cancer and understand resistance mechanisms.[163] Whereas this work demonstrated our capability in 2D cultures, our future work will focus on the utility of organotypic cultures to understand metabolic rewiring in a system that recapitulates the human tumor microenvironment. As our understanding expands in how cancer cells become addicted to specific metabolic pathways,[164] we anticipate that RS validated with MS and combined with sophisticated machine learning algorithms[165,166] will enable us to identify novel anticancer drugs that target these metabolic vulnerabilities. Ultimately, we expect this platform will have significant impact on cancer patients identifying those resistant to drug combinations even before therapy begins and guiding clinical decisions to an optimal treatment plan.

Chapter 3

PRADA: PORTABLE REUSABLE ACCURATE DIAGNOSTICS WITH NANOSTAR ANTENNAS FOR MULTIPLEXED BIOMARKER SCREENING

3.1 Summary

Precise monitoring of specific biomarkers in biological fluids with accurate biodiagnostic sensors is critical for early diagnosis of diseases and subsequent treatment planning. In this work, we demonstrated an innovative biodiagnostic sensor, portable reusable accurate diagnostics with nanostar antennas (PRADA), for multiplexed biomarker detection in small volumes (~50 µL) enabled in a microfluidic platform. Here, PRADA simultaneously detected two biomarkers of myocardial infarction, cardiac troponin I (cTnI), which is well accepted for cardiac disorders, and neuropeptide Y (NPY), which controls cardiac sympathetic drive. In PRADA immunoassay, magnetic beads captured the biomarkers in human serum samples, and gold nanostars (AuNSs) "antennas" labeled with peptide biorecognition elements and Raman tags detected the biomarkers *via* surface-enhanced Raman spectroscopy (SERS). The peptide conjugated AuNS-SERS barcodes were leveraged to achieve high sensitivity, with a limit of detection (LOD) of 0.0055 ng/mL of cTnI, and a LOD of 0.12 ng/mL of NPY comparable to commercially available test kits. The innovation of PRADA was also in the regeneration and reuse of the same sensor chip for ~14 cycles. We validated PRADA by testing cTnI in 11 de-identified cardiac patient samples of various demographics within a 95% confidence interval and high precision profile. We envision

low-cost PRADA will have tremendous translational impact and amenable to resource-limited settings for accurate treatment planning in patients.

3.2 Introduction

Rapid and accurate detection of disease-specific biomarkers is imperative for monitoring human health, planning treatment, and responding post-treatment.[167,168] Enzyme-linked immunosorbent assays (ELISAs) and mass spectrometry are the current clinical standards for detecting and measuring biomarkers in clinical samples. Although these workhorses of clinical laboratories yield accurate diagnostics, long sample preparation times, high operational costs, large sample volumes, and low rates of analysis limit the utility of these techniques for early and rapid detection.[169] The limitations of current techniques have motivated the development of a broad array of biodiagnostic sensors based on colorimetry, electrochemistry, surface plasmon resonance (SPR), Raman, and fluorescence.[170-175] For clinical applications, biodiagnostic devices must rigorously meet the following functions: (a) multiplexed detection of biomarkers enabling accurate and quantitative bioanalysis at clinically relevant levels; (b) straightforward sample preparation and real-time readout times; (c) portability and low sample consumption for translation to resource-limited settings; (d) prolonged reagent shelf life and stability; and (e) reusable to lower diagnostic and analysis costs.[176,177]

In this work, we have designed a new paradigm in diagnostic sensor, PRADA, which synergistically integrates all of these functionalities to allow multiplexed detection of biomarkers in human serum at clinically relevant levels. Portable reusable accurate diagnostics with nanostar antennas (PRADA), is a sandwich immunoassay using polyclonal antibodies (pAbs) functionalized magnetic beads to capture the biomarkers (Figure 3.1). Near-infrared resonant gold

46

nanostars (AuNSs) "antennas" labeled with Raman tags and short peptide biorecognition elements (BREs) detect the biomarkers *via* surface enhanced Raman spectroscopy (SERS). The immunoassay is assembled in a microfluidic device to allow low sample volumes, minimize the assay time, facilitate multiplexed detection, and enable reusability of PRADA. The seamless integration of each of the components of PRADA into a single functional platform allowing a portable and affordable multiplexed biodiagnostic is unprecedented. SERS is a promising immunodetection technique due to its exceptional sensitivity, specificity, and multiplexing ability with minimal spectral overlap between various reporter molecules.[178-182] The antenna-like behavior of AuNSs is attributable to their unique geometry, where their core acts as an antenna and absorbs near-infrared light and their branches behave as emitters to localize the absorbed light at the tips to generate intense electric fields.[63,67,183] We have shown that the near-field electromagnetic radiation generated at the protrusions of AuNSs gives rise to a $>10^9$ enhancement in SERS signal, resulting in ultrasensitive detection *in vitro*, *in vivo*, and in biosensors.[33,64-66]

Here, we demonstrated multiplexed detection of two biomarkers of myocardial infarction including cardiac troponin I (cTnI) and neuropeptide Y (NPY) with PRADA with high sensitivity and specificity in patient sera. cTnI is a well-accepted serum biomarker of cardiac arrest, stress, and ischemic stroke.[184,185] cTnI is routinely assessed in patient samples in clinical laboratories to detect myocardial damage, with a clinical range for at-risk patients of >0.03 ng/mL.[186] NPY is a sympathetic co-transmitter and critical to cardiovascular homeostasis including cardiac remodeling and angiogenesis.[187,188] It has been correlated to stress, anxiety, and post-traumatic stress disorder[189,190] at a clinically relevant level of ≤1.5 ng/mL.[191] Our results showed that PRADA achieved highly sensitive detection of both biomarkers of acute myocardial infarction ideal for risk stratification. The high sensitivity and specificity of PRADA were leveraged by the

peptide biorecognition elements (BREs) conjugated to AuNS-SERS barcodes. Short peptides represent an attractive alternative to monoclonal antibodies (mAbs) due to their low cost, long shelf life, and stability, and their small size enables high sensitivity in PRADA.[192,193] We also demonstrated PRADA was reusable where the microfluidic device can be regenerated for multiple cycles. We envision that PRADA will be ultimately useful in resource-limited settings, where a low-cost, reusable, and user-friendly point-of-care is necessary for patient sample analysis given that affordable portable Raman spectrometers are now readily available.
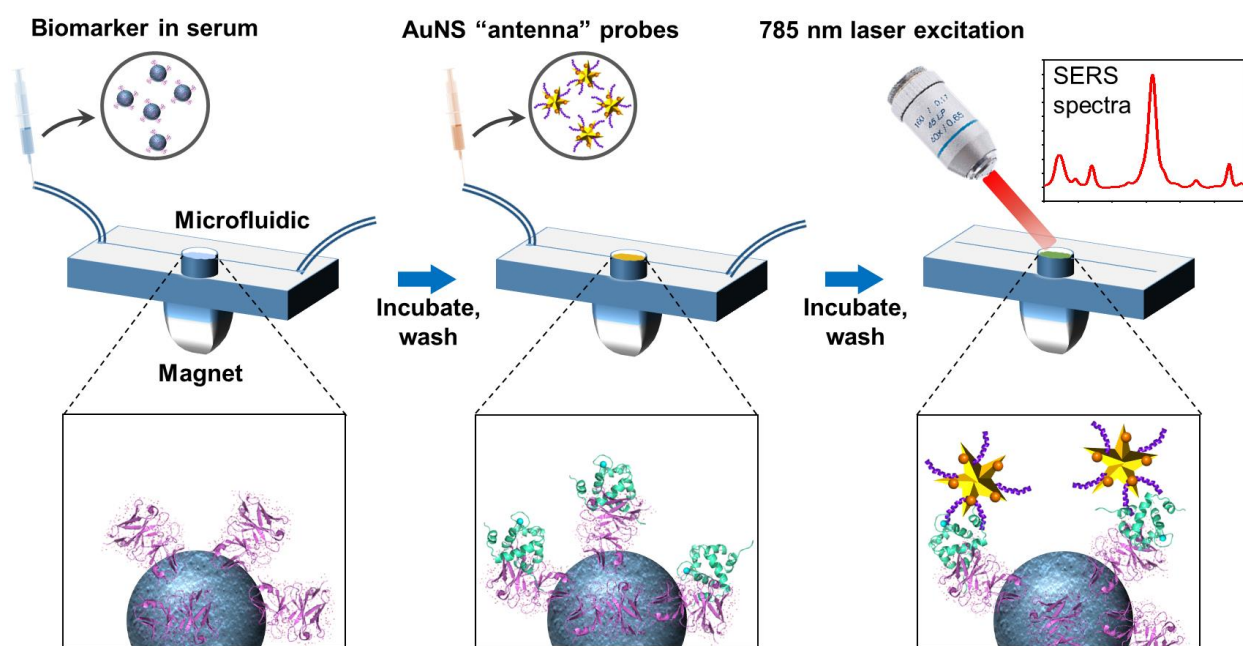
Figure 3.1 Schematic representation of PRADA. Antibody-conjugated magnetic beads are incubated with the antigens in the human serum to capture the biomarkers. Raman tags labeled AuNSs "antenna" detection probes with peptide BREs then form a sandwich immunocomplex, followed by excitation with 785 nm laser to enable SERS-based detection.

3.3 Materials and Methods

3.3.1 Materials

Carboxylated magnetic beads, 1-ethyl-3-(3-dimethylaminopropyl) carbodiimide (EDC), *N*-hydroxysulfosuccnimide (NHS), 2-(4-morpholino)ethane sulfonic acid (MES), tris(hydroxymethyl)aminomethane (Tris base), acetone and microscope glass slides were

purchased from ThermoFisher Scientific. Gold (III) chloride trihydrate (HAuCl$_4$), (4-(2-hydroxyethyl)-1-piperazineethanesulfonic acid) (HEPES), Sylgard 184, phosphate-buffered saline (PBS), ethanol, and trichloro(phenyl)silane (TCPS) were purchased from Sigma-Aldrich. The Milli-Q water (18 MΩ) was obtained from a Milli-Q Direct-Q 3UV system. Anti-cTnI (ab47003) and anti-NPY antibodies (ab30914) were purchased from Abcam. Raman tags, 5,5-dithio-bis-(2-nitrobenzoic acid) (DTNB) and para-mercaptobenzoic acid (pMBA), were purchased from TCI America. P2 (-WQIAYNEHQWQGGGC-) and NP3 (-FPNWSLRPMNQMGGGC-) peptides were purchased from Genscript. Methoxy poly(ethylene glycol)-silane (mPEG-silane, MW 5000) was purchased from Laysan Bio. Patient samples were purchased from Discovery Life Science.

3.3.2 Instrumentation

The plasmon resonance of bare and functionalized AuNSs was measured with a Varian Cary 5000 UV-Vis NIR spectrophotometer. The size and shape of AuNSs were visualized using an Osiris transmission electron microscope (TEM) at 200 keV. The morphology of complete immunocomplexes was visualized using a Zeiss Merlin scanning electron microscope (SEM). The Raman measurements were taken for 5 seconds exposure time using a Renishaw inVia Raman microscope system with a 785 nm laser that delivered ~30 mW of power. A 50× objective lens was used to focus a laser spot on the surface of microfluidic device. An oxygen plasma cleaner was used to bind the patterned PDMS layer onto a clean microscope glass slide.

3.3.3 Preparation of Antibody-Conjugated Magnetic Beads Capture Probes

To prepare the antibody-conjugated magnetic beads, 6.65 µL of carboxylated magnetic beads were separated by a magnet and washed twice with 100 µL of 25 mM MES (pH 5) for 10 min on an inverter (18 rpm). The surfaces of magnetic beads were active through the reaction with 50 µL of 50 mg/mL EDC (dissolved in cold 25 mM MES) and 50 µL of 50 mg/mL NHS (dissolved

in cold 25 mM MES) on an inverter (18 rpm) at room temperature for 30 min. Next, the magnetic

beads were separated by a magnet and washed twice with 10X PBS (pH 7.4). Then, the magnetic

beads were resuspended in 1 mL of 0.006 mg/mL anti-cTnI or 0.41 mL of 0.006 mg/mL anti-NPY

antibodies (in 1X PBS) with gentle mixing (4 rpm) at 4 °C. Nonspecifically bound antibodies

were washed three times with 1X PBS (pH 7.4). Unreacted carboxylic groups were deactivated

with 50 mM Tris (pH 7.4) with gentle mixing (4 rpm) at 4 °C. The final magnetic beads were then

washed three times with 1X PBS and stored in 1X PBS (pH 7.4) at 4 °C for future use.

3.3.4 Preparation of Functionalized Gold Nanostars Detection Probes

AuNSs were synthesized through the one-step and seedless method, as described in our

previously published procedures.[67] First, 18 mL of Milli-Q water at 18 MΩ was mixed with 12

mL of 200 mM HEPES (pH 7.4 ± 0.2) by gentle inversion. Next, 300 µL of 20 mM chloroauric

acid was added. The solution was mixed by gentle inversion and left undisturbed at room

temperature for 75 min. To conjugate Raman tags to the AuNS surfaces, 3 µL of 10 mM DTNB

or pMBA (in 100% ethanol) were added to 30 mL of AuNSs and reacted for 15 min with constant

stirring at 4 °C. The solution was then centrifuge at 6000 rpm for 20 min to remove excess Raman

tags. AuNS-DTNB or AuNS-pMBA were resuspended with Milli-Q water (18 MΩ) at a

concentration of 1.14 mg/mL. Afterwards, 25 µL of 1 mg/mL of P2 or 10 µL of 1 mg/mL NP3

peptide was added to AuNS-DTNB or AuNS-pMBA, respectively, and reacted for 1 hour with

gentle mixing (4 rpm) at 4 °C. Lastly, the fully functionalized AuNSs (AuNS-DTNB-P2 or AuNS-

pMBA-NP3) were centrifuged at 4000 rpm and resuspended in Milli-Q water (18 MΩ) at a

concentration of 5.72 mg/mL. The solution was stored at 4 °C for future use.

3.3.5 Singleplexed Biomarker Detection

The prepared antibody-conjugated magnetic beads (50 µL) were added to a well of the passivated microfluidic device through the inlet channel. Afterwards, 50 µL of cTnI or NPY at various concentrations spiked with human serum was added into the well and allowed to mix with magnetic beads for 1 h at 4 °C. The cTnI concentrations studied here were 0.004, 0.007, 0.02, 0.05, 0.1, 0.5, 1, 10, 50, 200, 600, 1000, 3000, 5000, 10000, 16000, and 28000 ng/mL. The NPY concentrations studied were 0.08, 0.12, 0.3, 0.5, 1, 10, 100, 200, 600, 800, 1500, 3000, 4000, 5000, and 9000 ng/mL. The well was washed three times with 1X PBS by flowing through the inlet channel and then collecting the waste with a syringe from the outlet channel. Then 50 µL of prepared AuNS-DTNB-P2 or AuNS-pMBA-NP3 was added to the well and allowed to mix for 1 h at 4 °C. The unbound AuNSs were suctioned out by a syringe as waste, and the well was washed three times with Milli-Q water (18 MΩ). The microfluidic device was dried for 10 min at room temperature and then imaged using a Renishaw inVia Raman microscope system. A blank sample was prepared in the absence of cTnI or NPY and was used as a control. Each sample was prepared with three replicates. At least 300 Raman spectra from different locations were obtained per replicate of sample.

3.3.6 Multiplexed Biomarker Detection

To assess the feasibility of multiplexed biomarker detection, 25 µL of anti-cTnI-conjugated magnetic beads and 25 µL of anti-NPY-conjugated magnetic beads were mixed and added to a well of the passivated microfluidic device through the inlet channel. cTnI (25 µL) and NPY (25 µL) at targeted concentrations spiked with human serum were added into the well and allowed to mix for 1 h at 4 °C. The combinations of biomarker concentration tested here were 3000 ng/mL cTnI + 1500 ng/mL NPY, 1000 ng/mL cTnI + 600 ng/mL NPY, 400 ng/mL cTnI + 200 ng/mL

NPY, 200 ng/mL cTnI + 100 ng/mL NPY, 5 ng/mL cTnI + 10 ng/mL NPY, 0.5 ng/mL cTnI + 1 ng/mL NPY, and 0.05 ng/mL cTnI + 0.3 ng/mL NPY. Note: these antigens were spike with human serum. The well was washed three times with 1X PBS by flowing through the inlet channel and then collecting the waste with a syringe from the outlet channel. Then 20 µL of AuNS-DTNB-P2 and 40 µL of AuNS-pMBA-NP3 were added into the well and allowed to mix for 1 h at 4 °C. The unbound AuNSs were suctioned out by a syringe as waste, and the well was washed three times with Milli-Q water (18 MΩ). The microfluidic device was dried for 10 min at room temperature and then imaged using a Renishaw inVia Raman microscope system. A blank sample was prepared in the absence of cTnI and NPY and was used as a control. Each sample was prepared with three replicates. At least 300 Raman spectra were obtained per replicate of sample.

3.3.7 Reusability

The reusability of PRADA was leveraged with the magnetic beads, as removal of the magnet allowed us to wash off the entire immunoassay *via* gentle rinsing of the device. Note: the magnetic beads were not covalently attached to the glass surface but held in place with the magnet. The device was then cleaned with acetone followed by Milli-Q water (18 MΩ). The Raman spectra for the cleaned device were then measured to ensure there were no residual signal from the previous sample. The devices were also viewed in the microscope to ensure all the magnetic beads were washed off. The entire assay was repeated, 14 times with the same microfluidic device to demonstrate reusability.

3.3.8 Microfluidic Device Fabrication and Passivation

All steps regarding the fabrication of microchannel patterns were performed using facilities within the cleanroom affiliated with the Vanderbilt Institute of Nanoscale Science and Engineering (VINSE). To make a microchannel mold, mr-DWL_40 resist was cast on a clean silicon wafer

and spin-coated at 1000 rpm for 1 minute, yielding a 60 μm-thick resist layer. Then designed patterns were directly written into the photoresist using a laser writer (Heidelberg, μPG 101). The wafer with patterned resist was coated with a thin layer of TCPS to facilitate subsequent removal. To make a microfluidic device, liquid polydimethylsiloxane (PDMS) (Sylgard 184) was mixed in a 1:10 ratio of curing agent and PDMS resin, degassed in a desiccator and carefully poured onto the resist mold placed in a petri dish. After curing in an oven for 3 h at 65 °C, the PDMS layer was cut and peeled off the resist mold. Holes were punched at the inlet and outlet of the microchannels using an 8.5 mm internal diameter punch. A clean microscope glass slide was bonded to the patterned PDMS layer by exposing to an oxygen plasma for 4 min. Each well of the microfluidic device was then passivated with 150 μL of 20 mM mPEG-silane (dissolved in 100% acetone) for 1 hour at room temperature to avoid non-specific binding. The microfluidic device was cleaned with Milli-Q water (18 MΩ) and dried with nitrogen. The passivated device was stored at -20 °C in glovebox for future use.

3.3.9 Statistical Analysis

The LOD for the assay was estimated as follows: $LOD = LOB + 1.645(SD_{lowest\ concentration\ sample})$, where LOB (limit of blank) was obtained by $LOB = mean_{blank} + 1.645(SD_{blank})$, in which the average signal of the blank (the immunocomplex without antigen) is added to 5% false-negative rate. All data are presented as mean ± standard deviation. The sensitivity curves of both cTnI and NPY were fitted with four-parameter logistic function using the GraphPad Prism8 program. Passing-Bablok regression analysis was performed on patient samples using the MedCalc program. A custom MATLAB code was used to perform smoothing and biological fluorescent background subtraction of Raman spectra. Smoothing of the data was done by following the Savitzsky and Golay method with 5th order and coefficient value of 33. Modified

polynomial fit method was performed to subtract the background fluorescence. A polynomial with 7th order was used to fit the Raman spectra with threshold of 0.0001.

3.4 Results and Discussion

The design of PRADA (Figure 3.1) includes pAbs functionalized magnetic beads that were assembled onto a passivated microfluidic device *via* a magnet to form a uniform layer. These capture probes were then incubated with human serum to capture the relevant biomarkers through the antibody-antigen interactions. Next, AuNSs labeled with Raman tags (AuNS-SERS barcodes) and small peptide BREs were introduced which bound to different sites on the biomarkers, completing the sandwich immunocomplex. This assay was followed by SERS measurements with a Raman setup equipped with a 785 nm continuous-wave laser and analyzed for quantification of the antigens present in serum. Here, we first showed the individual detection of cTnI and NPY followed by multiplexed detection of both biomarkers simultaneously.

The sensitivity and specificity of PRADA are governed by the controlled synthesis of the capture and detection probes (Figure 3.2a). Here, the capture probes were prepared by activating carboxylic acid-functionalized magnetic beads *via* 1-ethyl-3-(3-dimethylaminopropyl) carbodiimide (EDC) and *N*-hydroxysulfosuccnimide (NHS) coupling, and subsequent functionalization with anti-cTnI or anti-NPY pAbs. Functionalized capture probes were then incubated with human serum spiked with cTnI or NPY antigens where biomarkers were captured *via* antibody-antigen binding. The sandwich immunocomplex was completed with AuNS-SERS barcodes covalently conjugated with peptide BREs. The detection of cTnI was enabled with AuNSs labeled with 5,5-dithio-bis-(2-nitrobenzoic acid) (DTNB) Raman tags and P2 peptides (Figure 3.2b), and detection of NPY was facilitated with AuNSs labeled with para-

mercaptobenzoic acid (pMBA) Raman tags and NP3 peptides (Figure 3.2c). Here, AuNSs with 50 – 70 nm tip-to-tip dimension (Figure 3.3a) were synthesized with a biological buffer, 2-[4-(2-hydroxyethyl)piperazin-1-yl]ethanesulfonic acid (HEPES), as described in our previously published procedures.[33,67,183] Further, DTNB and pMBA are ideal Raman tags for this platform because they are covalently linked to the AuNS surfaces *via* a thiol group, enabling SERS signal amplification *via* both electromagnetic and chemical enhancements. The dominant Raman peaks at 1325 cm^{-1} (symmetric stretching mode of the nitro group of DTNB) and 1580 cm^{-1} (ring stretching mode of pMBA) also do not overlap enabling multiplexed detection of both biomarkers.
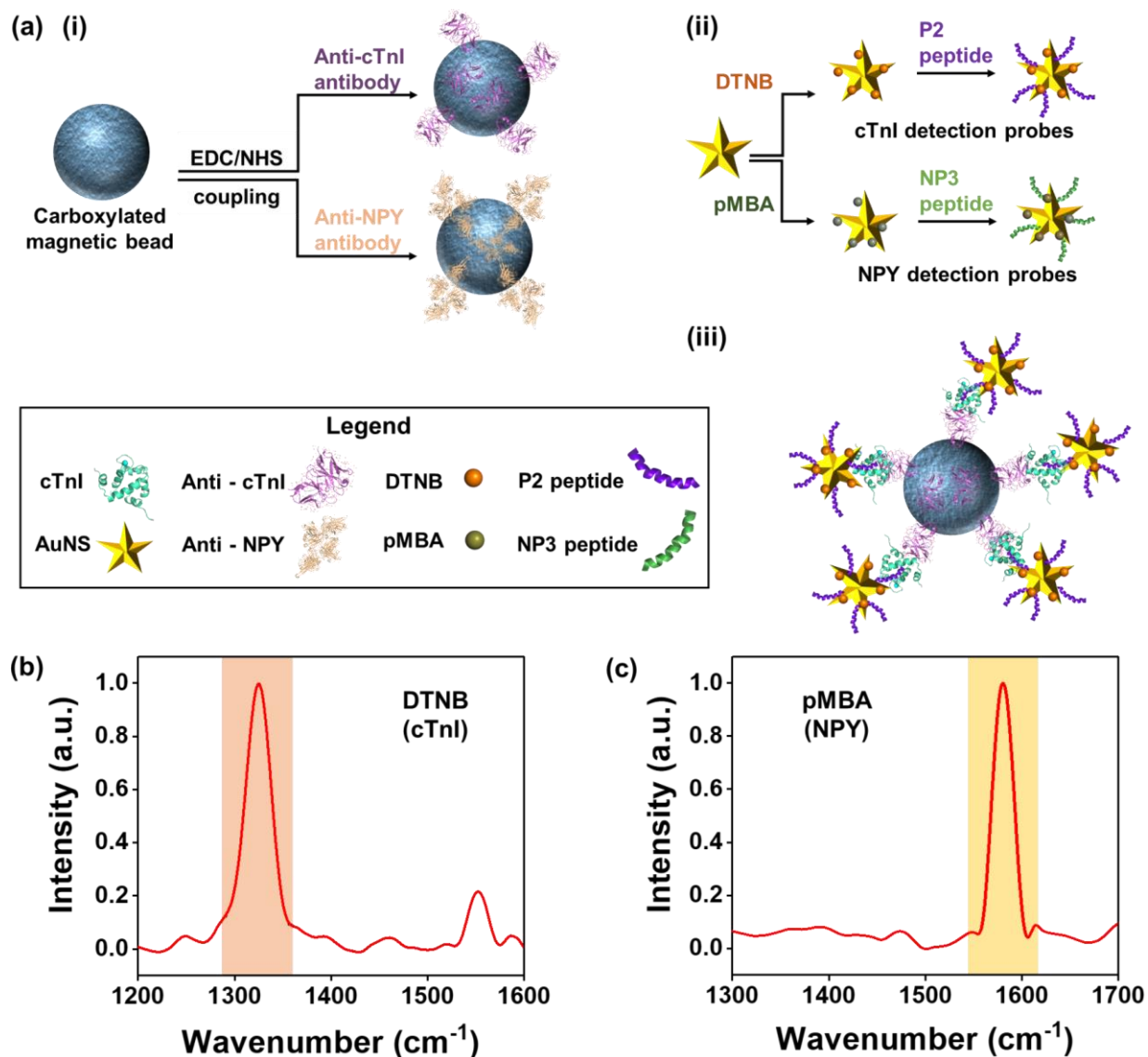
Figure 3.2 Fabrication of PRADA. (a) Schematic of the synthesis of capture and detection probes. (i) Magnetic beads functionalized with pAbs as capture probes. (ii) AuNSs conjugated with SERS barcodes and peptide BREs as detection probes. (iii) The representative complete immunocomplex formed by capture probes, target antigens, and detection probes. (b,c) Normalized Raman spectra of AuNSs functionalized with DTNB (1325 cm^{-1}) and pMBA (1580 cm^{-1}) reporter molecules for cTnI and NPY detection, respectively; the signature peaks are highlighted.

In our platform, the peptide BRE plays a critical role in the biomarker detection. The P2 peptides (-WQIAYNEHQWQGGGC-), computationally evolved from a phage display peptide, had nanomolar binding affinity to cTnI.[194] The bioconjugation of P2 peptides to AuNSs was achieved *via* Au-S linkage by introducing a cysteine residue at the C-terminus of the peptide. A tri-glycine spacer domain was inserted between the C-terminal cysteine and the P2 peptide to extend the binding domain away from the gold surface. The NPY binding peptide, NP3 (-FPNWSLRPMNQMGGGC-), was also identified from a phage display peptide library.[195] The short peptides bind to different regions of antigens without competing with the target sites of antibodies on the capture probes. These dodecapeptides have an average size of 2 – 3 nm obtained by molecular modelling calculations; this size is the molecular length of a linear, unconstrained, and extended dodecameric peptide.[196] The peptide functionalized and constrained on a nanoparticle surface is likely to have a smaller size. The peptide size is significantly smaller than mAbs (~10 nm) which facilitated high sensitivity of PRADA by enabling the nanostars to maintain their orientation with respect to the antigen receptor with minimal steric hindrance. Antibodies are typically attached to gold nanoparticle surfaces *via* long chain linkers which often compromise their orientation and consequently binding efficacy, lowering overall sensitivity.[193] Of note, we chose to use P2 peptide instead of anti-cTnI antibody as the peptide was evolved to bind residues 114 – 141 of troponin with high affinity whereas anti-cTnI antibody bound to the N-terminus region of full length troponin. The binding affinity of P2 peptide was confirmed in our previous

work by measuring the dissociation constants (K_D) of the P2 peptide or mAb in the presence of 114 – 141 troponin fragment or full length troponin.[194] The K_D of the peptide remained constant independent of troponin target (fragment or full length), while the K_D of the antibody was 100-fold lowered using the troponin fragment lacking the N-terminus binding region. These results confirmed that the peptide and antibody binding domains were non-overlapping. But the binding affinity of the peptide and antibody for full length troponin was very similar (0.27 *vs* 0.12 nM), as measured by SPR.[194,197]

After biofunctionalization of AuNSs with peptides and SERS barcodes, a ~18 nm red shift in the plasmon resonance (Figure 3.3b) was observed attributed to an increase in hydrodynamic size and change in refractive index of the medium. Scanning electron micrographs (SEM) confirmed the successful synthesis of the complete immunocomplex (Figure 3.3c-e and A.11) where AuNS-SERS barcodes retained their morphology after complexing with functionalized magnetic beads. Note: SERS measurements were only acquired from samples where the magnetic beads formed a uniform monolayer aided with a magnet (Figure A.12a,b). Samples with multilayers of the complete immunocomplex or aggregated AuNSs were avoided to minimize hot-spot formation and variability in the measurements (Figure A.12c-f).
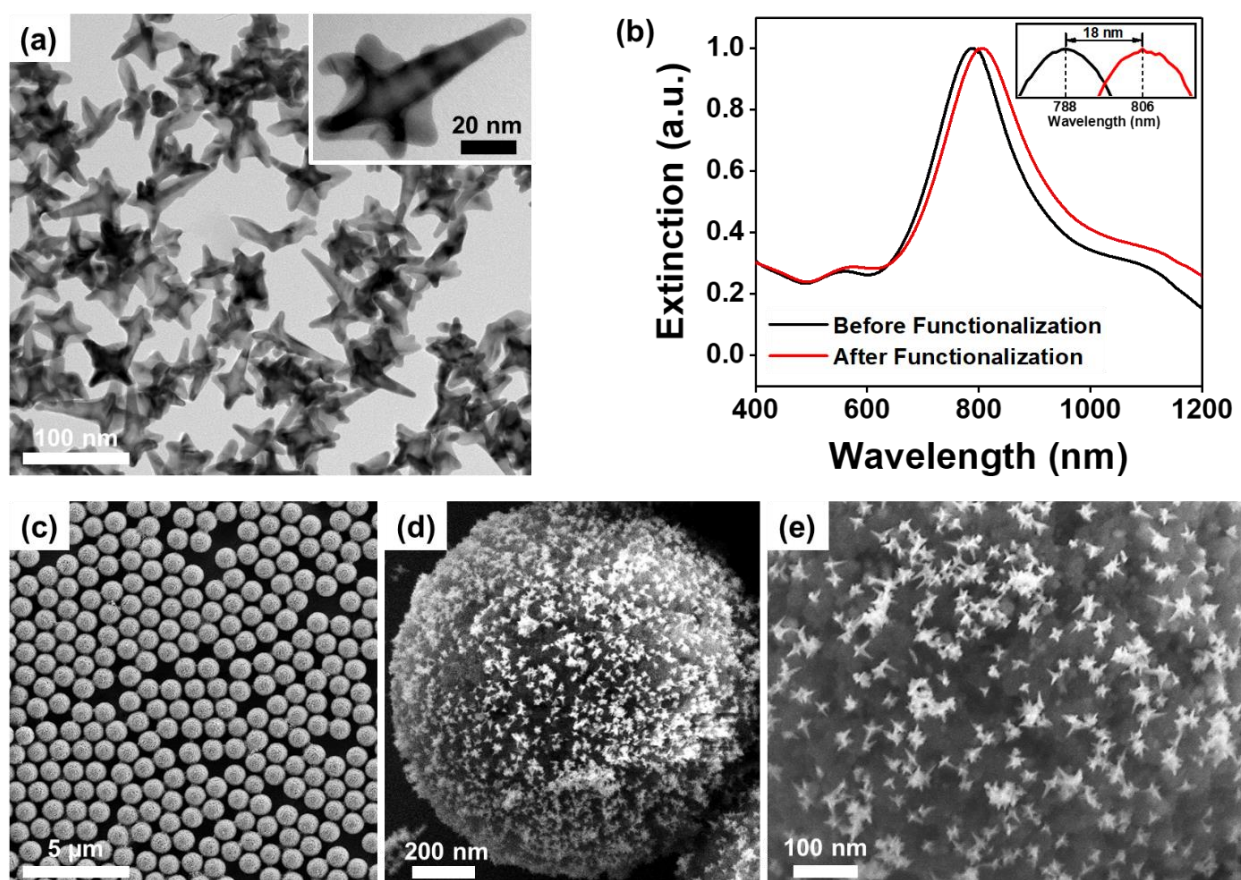
Figure 3.3 Characterization of PRADA. (a) Transmission electron micrograph of AuNSs showing their anisotropic morphology. (b) Extinction spectra of bare AuNSs and AuNSs functionalized with Raman reporter molecules and peptide BREs. (c-e) SEM images of complete immunocomplexes at various magnifications with magnetic beads capture probes and AuNS-SERS barcodes detection probes.

We first demonstrated the feasibility of PRADA in detection of single biomarkers in human serum in a microfluidic device. We chose a simple and low-cost microfluidic design with an inlet and outlet, and a sample chamber for incubation of samples, mixing, and evaluation of biomarkers (Figure 3.1). The magnetic bead capture probes, which are uniformly distributed in the entire sample chamber (Figure A.12a,b), also aid in mixing with the AuNS-SERS barcode detection probes by placing the microfluidic devices on a stir plate. Therefore, the design of microfluidic chips with multiple mixing channels is unnecessary here as such complex devices are both time

and labor intensive, and cost prohibitive.[198,199] We chose to measure the accuracy of PRADA in commercially available de-identified human patient serum (Discovery Life Sciences Inc.) to recapitulate clinical diagnostics where biomarkers of interest competes with other serum constituents to be captured by the magnetic beads. Human serum contains approximately 4000 metabolites,[200,201] which would compete to bind to the targeted sites. Here, different concentrations of cTnI or NPY were spiked into human serum and followed by monitoring the change in intensity of the signature peaks of the AuNS-SERS barcodes bound to cTnI or NPY antigen *via* the peptide BREs. The cTnI baseline of the purchased serum was 0.015 ng/mL, whereas the amount of NPY in the serum was not provided by Discovery Life Science. However, a blank Raman signal of the serum was obtained in the absence of antigens (with the capture and detection probes). Minimal interference effects were observed in the blank control which suggested minimal baseline NPY. Each sample was prepared with three replicates, and the sensitivity and specificity of PRADA were quantitatively evaluated. At least 300 spectra obtained from different locations per replicate of sample were used for quantitative analysis. Spectra were background subtracted, averaged, and smoothed using a Savitzky-Golay filter.[202] The representative Raman spectra of immunocomplexes for various concentrations of cTnI are shown in Figure 3.4a. The relative SERS intensity of DTNB at 1325 cm^{-1} was used for quantitative evaluation of cTnI concentrations. The corresponding sensitivity curve obtained from the SERS measurements was fitted using the four-parameter logistic (4PL) function (Table A.1) showing that the Raman intensity increased in a logarithmic manner with increasing concentrations of cTnI in the range of 0.02 to 5000 ng/mL (Figure 3.4b). This 4PL function has been shown previously to have a robust fit to plasmonic and SERS-based biosensors.[203] However, the SERS intensity at 1325 cm^{-1} was linear at low concentrations of cTnI in the quantification region (Figure 3.4c). The

LOD of cTnI was estimated to be 0.0055 ng/mL from this fit; all parameters for LOD calculation are provided in Table A.2. Our assay is also clinically relevant because patients diagnosed with myocardial infarction typically have a cTnI concentration of >0.03 ng/mL.[186] Of note, the low region indicated the concentrations below the LOD of PRADA and the saturated region represented where the sandwich immunocomplex was oversaturated and unable to distinguish differences in such high concentrations.[204]

We followed a similar approach in the utility of PRADA to detect NPY spiked in de-identified human serum. The signature Raman peak of pMBA at 1580 cm^{-1} was monitored (Figure 3.4d). The quantification region also showed a logarithmic increase with NPY concentrations ranging from 0.3 to 5000 ng/mL (Figure 3.4e), whereas a linear correlation was found in the range of 0.3 to 100 ng/mL (Figure 3.4f). The LOD of NPY was calculated to be 0.12 ng/mL (Table A.2). The clinical level of NPY of at-risk patients with high level of stress and anxiety is ≤1.5 ng/mL and lower concentrations are desired for risk prediction.[191] These results demonstrated that PRADA is a versatile platform for quantitative analysis of biomarkers in human biofluids with high sensitivity and specificity.
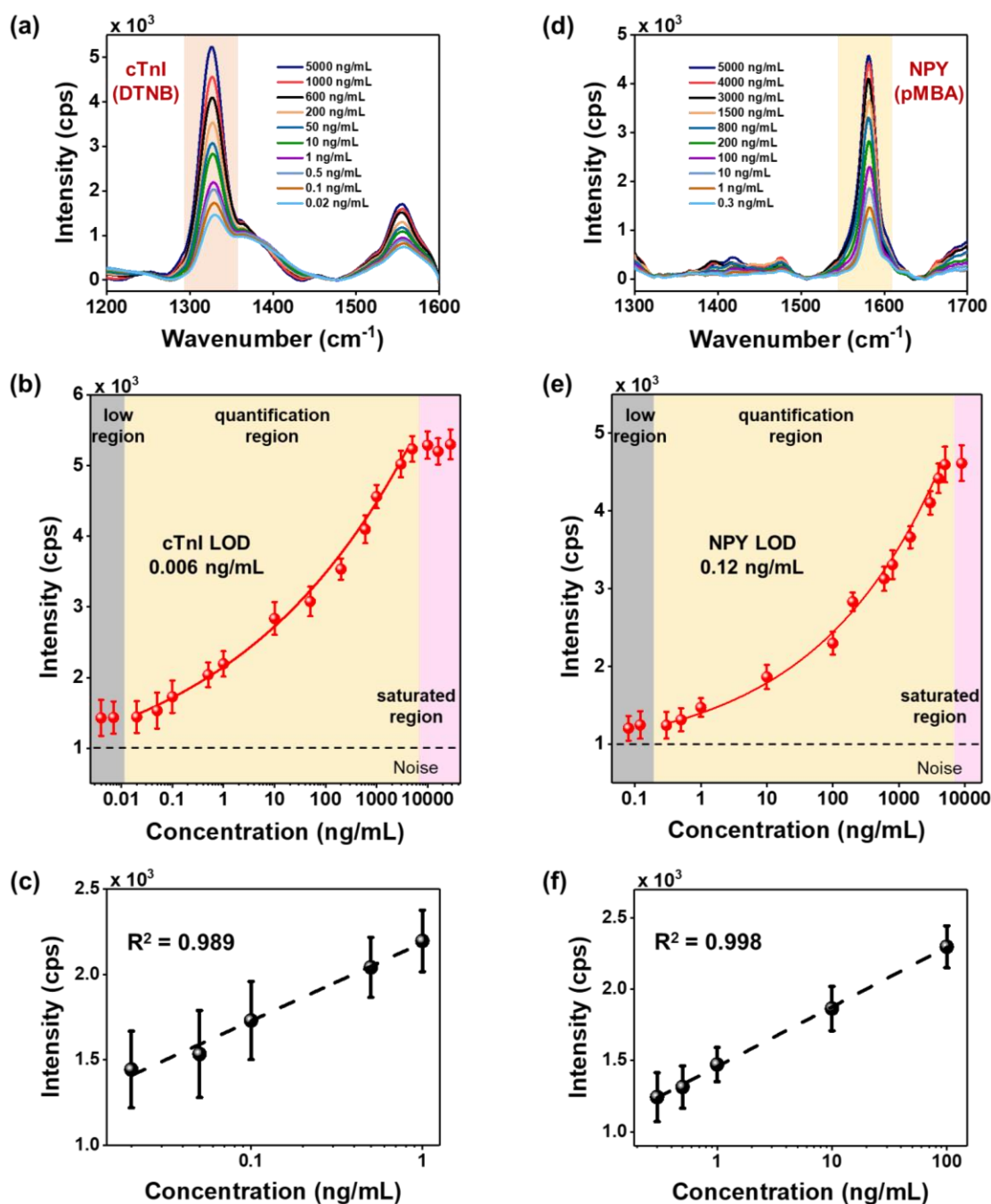
Figure 3.4 cTnI and NPY detection with PRADA. (a) Raman spectra of cTnI in human serum and (b) SERS intensity at the characteristic DTNB peak (1325 cm^{-1}) as a function of cTnI concentrations. The low region (gray box) is where the concentrations were below the detection limit; quantification region (yellow box) was used to determine LOD with a 4PL function fit; and saturated region (pink box) was where high density of analytes saturated PRADA. (c) Linear fit of the DTNB peak at low concentrations of cTnI in the range of 0.02 to 1 ng/mL. (d) Raman spectra of NPY in human serum by monitoring the pMBA peak at 1580 cm^{-1}. (e) SERS intensity at the characteristic pMBA peak as a function of NPY concentrations. (f) Linear fit of the pMBA peak at low concentrations of NPY ranging from 0.3 to 100 ng/mL. Error bars indicate the standard deviations from at least 5 measurements. A base 10 logarithmic scale was used for *x*-axis.

61

Next, we demonstrated that microfluidics-based PRADA enabled accurate multiplexed detection of biomarkers in serum. Multiplexed bioanalysis in a single sample is of significant interest to predict the complex phenotype of myocardial infarction, which often results in false prognosis.[205] Here, the narrow spectral features of SERS allowed multiplexed detection offering high sensitivity and minimum overlap between corresponding Raman tags. We simultaneously detected cTnI and NPY (Figure 3.5a) by using a 1:1 mixture of magnetic beads conjugated with either anti-cTnI pAbs or anti-NPY pAbs, which served as the capture probes in a multi-well microfluidic device (Figure 3.5b). A multi-well device is particularly relevant for field-use or in resource-limited settings where several patient samples can be analyzed at the same time to determine the status of multiple biomarkers. Afterwards, serum samples with no antigens (control), 1:1 mixture of cTnI and NPY at various concentrations (see Figure 3.5 caption) were incubated with the capture probes. After removing unbound antigens with a washing step, 1:1 mixture of detection probes targeting cTnI (AuNS-P2-DTNB) and NPY (AuNS-NP3-pMBA) were incubated. Multiplexed detection was achieved with PRADA where clear peaks of DTNB (1325 cm^{-1}) and pMBA (1580 cm^{-1}) were observable with minimal non-specific binding for the no antigen control. Additionally, the Raman signal of both biomarkers intensified with the increase in biomarkers' concentration.

We then demonstrated that PRADA can be reused over multiple cycles by simply washing and regenerating the microfluidic devices. We used the same microfluidic device to detect 0.1 ng/mL of cTnI for 14 cycles by repeated washing and reusing (Figure 3.5c). The reusability of PRADA was leveraged with the magnetic beads, as removal of the magnet allowed us to wash off the entire assay and regenerate the microfluidic sensor chip. Our regeneration approach has several merits. First, PRADA had minimal signal loss after multiple cycles, which outperformed chemical

regeneration approaches that have been reported to have ~40% signal loss during each cycle.[206] In chemical regeneration, low pH glycine buffer or detergent solutions are introduced to detach the antigens from antibodies, enabling reusability of the sensor chip with the same set of antibodies between samples.[207] However, chemical regeneration is ineffective when using patient biofluids due to the presence of proteases and bacteria that can degrade these antibodies.[208] Low signal loss after multiple cycles emphasized the strength of PRADA and our magnetic regeneration approach. Second, prior to regeneration, the microbead/antigen/nanostar immunocomplex representing each patient sample can be archived (by removing the magnet) for future analysis. Sample archival is possible due to the high stability of the AuNS-SERS barcodes as they do not photobleach and are amenable to long-term storage.[33] These results demonstrated that PRADA is a robust multiuse platform that allows diagnosis of multiple biomarkers of interest within minutes and has the potential to analyze patient samples in biofluids with high accuracy and specificity.
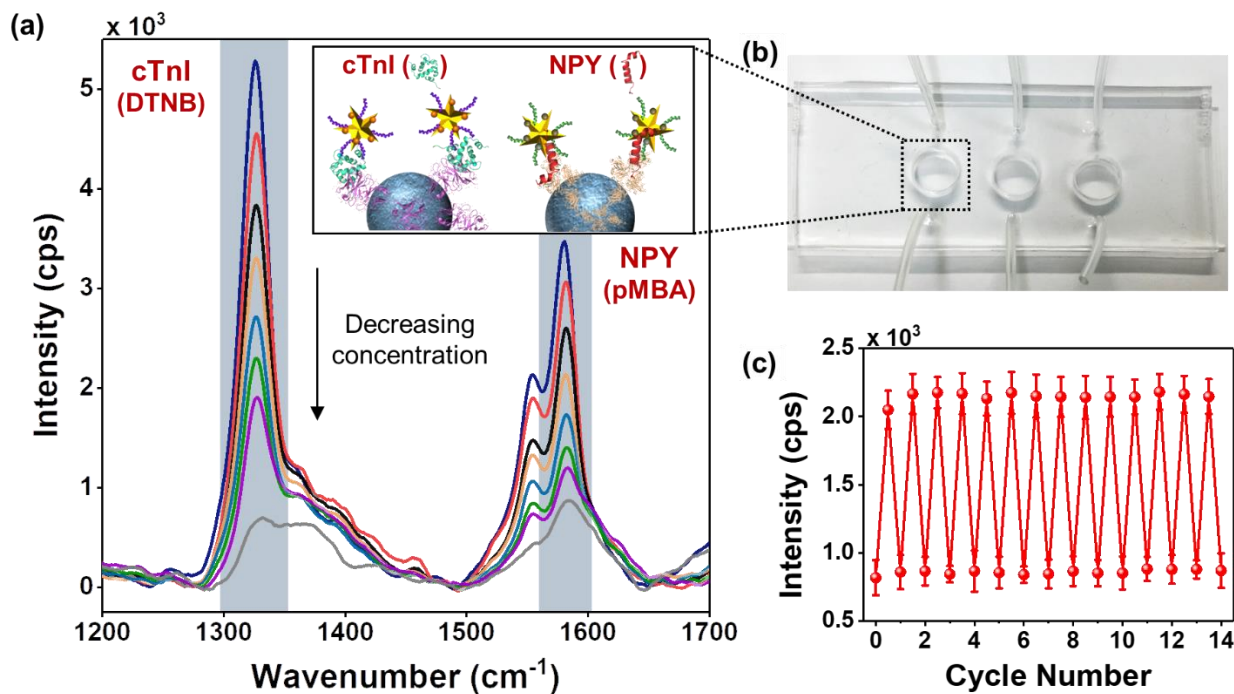
Figure 3.5 Multiplexing and reusability with PRADA. (a) Multiplexed detection of both cTnI and NPY in a three-well microfluidic device. The concentrations measured in ng/mL for cTnI/NPY are 3000/1500 (blue), 1000/600 (red), 400/200 (black), 200/100 (orange), 5/10 (light

blue), 0.5/1 (green), 0.05/0.3 (purple, control (gray). The inset is a schematic representation of multiplexed detection of both biomarkers. (b) Image of a microfluidic device utilized in the experiments. (c) Demonstration of reusability of PRADA where the same microfluidic chip was reused 14 times after washing and regenerating. Here, 0.1 ng/mL of cTnI was detected at the DTNB Raman peak with minimal signal loss. Error bars indicate the standard deviations from at least 5 measurements.
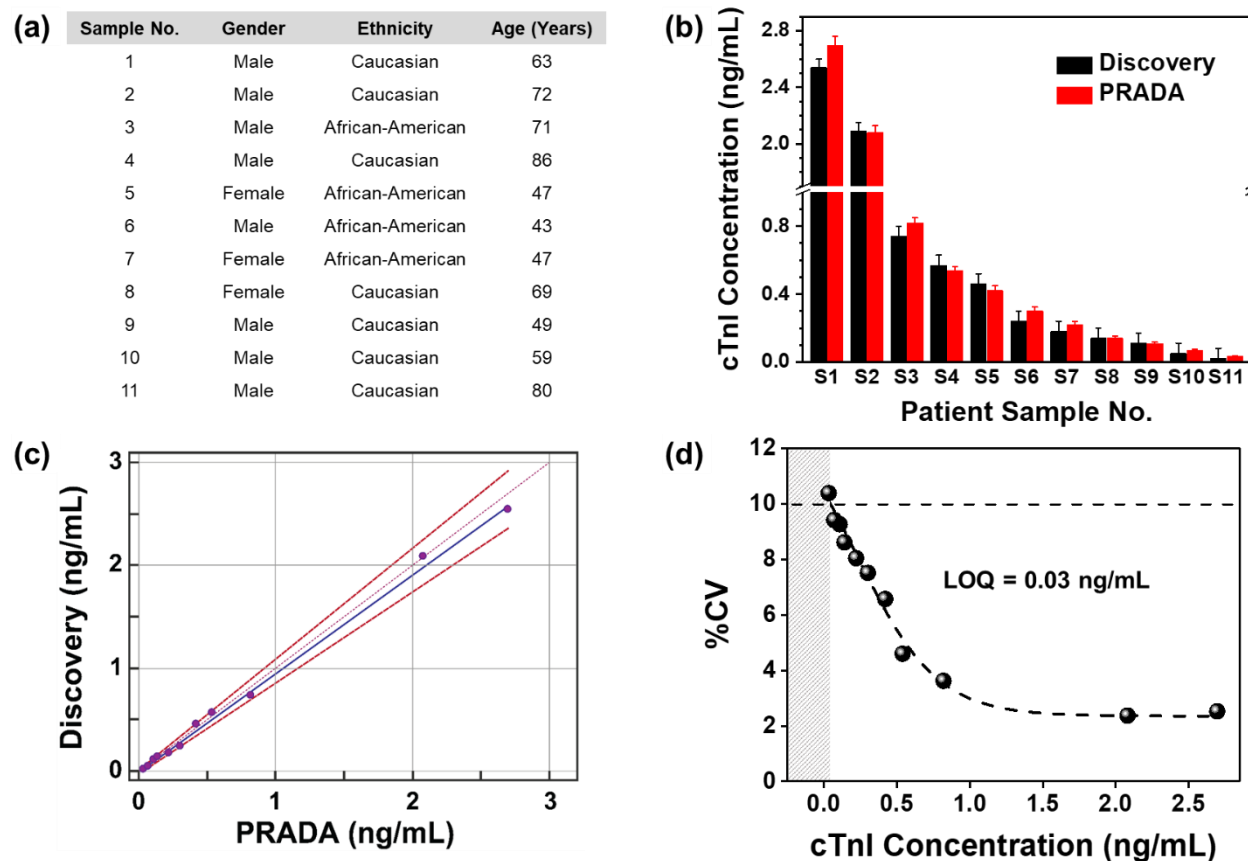
Figure 3.6 PRADA for cardiac patient sample analysis. (a) Demographics of 11 patient samples purchased from Discovery Life Sciences including their gender, race, and age, and the cTnI levels. (b) Comparison of cTnI determined with PRADA and those obtained from Discovery Life Sciences measured using the ABBOTT ARCHITECT chemiluminescence assay system. The standard error in Discovery data was <0.06 ng/mL. Error bars in SERS data indicate the standard deviations from at least 5 measurements. (c) Passing-Bablok regression analysis between PRADA and Discovery Life Sciences to determine accuracy of PRADA. (d) %CV corresponding to mean cTnI concentrations for the 11 patient samples using PRADA where the 10% CV level is indicated with a dotted line achieving an LOQ of ~0.03 ng/mL.

We then demonstrated the translational impact of PRADA by validating our approach in evaluating serum from 11 de-identified cardiac patients with varying levels of cTnI. These serums were purchased from the open biobank Discovery Life Sciences. The NPY values were not provided for these samples. A three-well microfluidic device was used to enable multiple patient sample analysis simultaneously. The PRADA assay was performed like described above where capture probes for cTnI were introduced in microfluidic wells followed by introducing the patient serum, and then followed by the AuNS-SERS barcodes. Multiple washing steps were executed to ensure high accuracy of PRADA. Relevant patient information including gender, race, and age is shown in Figure 3.6a. Our effort was to demonstrate that PRADA is applicable to a wide range of patient demographics including gender, ethnicity, and age. SERS spectra of the patient samples were measured in triplicates (Figure A.13) to determine the cTnI levels. PRADA levels were then compared to those provided by Discovery Life Sciences measured using the ABBOTT ARCHITECT chemiluminescence assay system (Figure 3.6b). The manufacturer provided standard error in their data to be <0.06 ng/mL where the level consistent with acute myocardial infarction was ≥0.5 ng/mL based on their samples. Our results showed regardless of the cTnI concentration and patient demographics, PRADA achieved high accuracy in serum analysis. Further, Passing-Bablok regression analysis was performed to estimate the variation and systematic bias between cTnI concentrations obtained with PRADA in patient samples and the values from Discovery Life Sciences (Figure 3.6c). Regression analysis indicated good conformity between the two assays as the scattered points (purple) and associated regressions (blue) of the data were within the 95% confidence intervals (CIs) which include the intercept and slope of 0 and 1, respectively (Table A.3). The results showed that all values obtained with PRADA were clinically valid, and within the acceptable range.

We calculated a precision profile which determined the limit of quantification (LOQ) of PRADA in analyzing patient samples and ensuring that these results matched with our sensitivity curve shown in Figure 3.4b,c. Here, the LOQ is defined as the lowest concentration of cTnI that can be reliably detected with a coefficient variation (CV) less than or equal to 10%.[209] By definition LOQ can be equal to or higher than the LOD but not lower, as LOD provides an estimate of bias and imprecision at very low analyte concentrations. We obtained the mean cTnI concentrations with PRADA for the 11 patient sera (measured in triplicates) and calculated the %CV for each sample (Figure 3.6d). A curve was fitted through the plot of %CV as a function of cTnI concentration, and the LOQ of PRADA was determined to be 0.03 ng/mL corresponding to the 10% CV level of the curve. The data suggests that PRADA will allow quantitative analysis of cTnI in patient sera at ≥0.03 ng/mL with high accuracy (right of the gray region). Our reported LOD and LOQ are lower than many troponin immunoassays published in the literature, and comparable to commercial assays (Table A.4). Of note, multiplexing is not offered by many of these commercial assays. But our LOQ was limited by the availability of patient samples from Discovery Life Sciences where lowest concentrations of cTnI that were available for purchase was >0.01 ng/mL. We were also limited by the small patient population we evaluated here (11); most commercially available assays examine >1000 patients to establish their quantification range[210] where patients with no risk of myocardial infarction have <<0.01 ng/mL. We expect the LOQ of PRADA will significantly improve in a future cohort study where patients will be recruited to exemplify the translational impact of this platform.

3.5 Conclusions

In summary, this study presented an innovative biodiagnostic platform, PRADA, demonstrating multiplexed detection of two biomarkers of myocardial infarction, cTnI and NPY, in a simple microfluidic device. We achieved an LOD of 0.0055 ng/mL for cTnI and an LOD of 0.12 ng/mL for NPY in patient serum. We showed that PRADA can be regenerated and reused where the same microfluidic chip can be recycled for multiple cycles with minimal signal loss between cycles. Reusability of PRADA also allowed to archive samples for future bioanalysis. Finally, we validated the clinical significance of PRADA by evaluating cTnI in cardiac patient serum of various demographics and achieved an LOQ of $\geq$ 0.03 ng/mL at 10% CV which was higher than many troponin immunoassays published in the literature, and comparable to commercial assays. Whereas in this proof-of-concept study, we demonstrated the multiplexing of two biomarkers in human serum, our future work focuses on the utility of PRADA to detect >10 biomarkers in patient samples enabled by the narrow spectral features of SERS. Further, PRADA can be translated to other biomarkers beyond those probed here, as identification of peptides that exhibit high binding affinities to various targets is already being pursued by many commercial sources that routinely generate a number of different peptides. Although this approach is limited by biomarker targets wherein the antigen structure is known and the location of a binding site on the target molecule can be predicted, we envision that PRADA will ultimately enable a precise scoring system to determine patient outcome. PRADA score can then be integrated with artificial intelligence interfaces as well as smart phones for cost-effective health monitoring.[211,212]

Chapter 4

SURFACE PROPERTIES AND ROUTE OF SYSTEMIC DELIVERY CONTROL THE IN
VIVO DISTRIBUTION, BREAKDOWN, AND EXOCYTOSIS OF RADIOLABELED GOLD
NANOSTARS

4.1 Summary

Successful clinical translation of the use of nanoparticles (NPs) requires long-term and comprehensive studies involving biocompatibility, uptake, biodistribution and excretion of NPs in biological systems. In this work, we demonstrated the use of multimodal gold nanostars (AuNSs) for toxicity and ultimate fate studies. We first synthesized AuNSs with 60 – 80 nm tip-to-tip dimensions, conjugated with a generic immunoglobulin G (IgG) antibody to explore untargeted biodistribution, and radiolabeled with ^{64}Cu to enable positron emission tomography (PET) imaging. The long-term (90 days) toxicity of this functionalized AuNSs (F-AuNSs) was probed by *in vitro* viability and cell cycle studies and *in vivo* inflammatory responses and histopathological changes. F-AuNSs were highly biocompatible both *in vitro* and *in vivo*. The route of systemic administration (intraperitoneal *vs.* intravenous injection) did not induce any significant differences in toxicity. The *in vivo* biodistribution studies combining (a) PET imaging, (b) gamma counts of ^{64}Cu radiolabeled F-AuNSs, (c) transmission electron micrograph (TEM) and (d) inductively coupled plasma mass spectrometry (ICP-MS) analysis of gold in tissues indicated that the delivery route had significant impact on F-AuNS accumulation in tissues within the first 24 h post injection and confirmed the long-term presence (90 days) of F-AuNSs in tissues. The TEM images showed the breakdown of F-AuNSs within tissues implying the importance to evaluate their uptake and localization mechanism, interaction with other molecules in biological systems, and exocytosis and clearance as a function of physicochemical properties of broken NPs. We found that uptake of F-AuNSs was dominated by clathrin-mediated endocytosis, but other pathways including

caveolae-mediated endocytosis, macropinocytosis and phagocytosis also contributed. Further, sodium dodecyl sulfate polyacrylamide gel electrophoresis (SDS-PAGE) and proteomic studies demonstrated that F-AuNSs dramatically minimized the protein corona effect, and the adsorbed proteins on F-AuNSs promoted their blood circulation and intracellular uptake. Finally, the interaction between gold NPs (AuNPs) and a lipid membrane simulated by the Martini coarse-grained method indicated that the excretion of AuNPs relied on their physicochemical properties and the lipid composition of membrane. This in-depth study assessed from *in vitro*, *in vivo*, and mechanistic simulation aspects revealed excellent biocompatibility of F-AuNSs and highlighted their tremendous translational potential.

4.2 Introduction

Engineered gold nanoparticles (NPs) have gained great momentum in nanomedicine due to their unique physical and chemical properties. Gold nanostars (AuNSs) have been of particular interest because of (a) special geometry giving rise to 9 – 10 orders of magnitude signal enhancement in molecule of interests when used as contrast agents for optical imaging, (b) ease of synthesis with a biological buffer to promote biocompatibility and (c) straightforward surface functionalization *via* a gold-thiol/amine bond with a wide variety of molecules for biomedical applications.[33,34,67,183] When using for diagnostics and therapeutics, *in vivo* fate and toxicity of AuNSs are crucial aspects that need to be evaluated. Several studies have investigated the short-term (up to 15 days)[33,213,214] toxicological profile of AuNSs *in vivo*, but the long-term evaluations remain unexplored and are important for their clinical translation. Further, the majority reports have focused on the *in vivo* toxicity of polyethylene glycol (PEG) coated NPs which do not

represent the plethora of surface ligands used for the functionalization.[215-217] Therefore, an unmet need exists for a systematic long-term evaluation of the toxicological profile of AuNSs.

Two dominant aspects that are generally evaluated in toxicity studies include (a) the assessment of the effect of NPs on biological systems (*e.g.*, viability and histopathological change)[218] and (b) determination of bio-behaviors of NPs in biological environment (*e.g.*, cellular uptake, biodistribution, excretion and interaction with other biomolecules).[219-221] Particularly, it is well-established that proteins in a biological milieu are readily adsorbed onto the surface of NPs, forming a layer known as protein corona (PC).[71] Emerging evidences support that physicochemical properties of NPs, such as shape, size, surface charge and functionalization, largely affect the composition of PC adsorbed.[222-224] In this regard, a detailed characterization of PC is needed to understand its role in modulating the bio-identity of NPs. Additionally, previous studies showed that heavy metal NPs (*e.g.*, quantum dots)[225] were likely to have long retention times within mononuclear phagocytic system (MPS) which potentially initiated inflammatory responses and induced chronic toxicity. Assessing the ultimate fate of NPs highly depends on their uptake pathway, intracellular localization, and exocytosis. Much progress has been made in elucidating pathways for the uptake of NPs including clathrin-mediated endocytosis, caveolae-mediated endocytosis, macropinocytosis and phagocytosis.[226-229] However, relatively little attention has been given to how these NPs leave tissues (*e.g.*, the mechanism behind systemic excretion).[219,230] This question has been complicated by the fact that NPs are readily degraded[231] in organelles (*e.g.*, endosomes and lysosomes) with an acidic environment rendering excretion based on the interactions between the breakdown NPs with varying physicochemical properties and lipid bilayer membranes of organelles.

70

In this work, we conducted an in-depth toxicological study of AuNSs functionalized with a generic immunoglobulin G (IgG) antibody to explore untargeted biodistribution and radiolabeled with ^{64}Cu to enable positron emission tomography (PET) imaging which provided depth-resolved whole-body images to allow the localization of NPs. We first examined the impact of functionalized AuNSs (F-AuNSs) on viability and cell cycle of murine macrophage cells *in vitro*. We then intraperitoneally or intravenously delivered F-AuNSs in mice to evaluate long-term (90 days) toxicity by measuring standard serum inflammatory markers and observing histopathological changes. Our results showed that F-AuNSs were highly biocompatible both *in vitro* and *in vivo*. The route of systemic administration did not induce any significant differences in toxicity. To understand the biodistribution of F-AuNSs *in vivo*, we performed a correlative study combining (a) PET imaging, (b) gamma counts of ^{64}Cu radiolabeled F-AuNSs, (c) transmission electron micrograph (TEM) and (d) inductively coupled plasma mass spectrometry (ICP-MS) analysis of gold in tissues as a function of delivery route and period of time. Our results indicated that the route of systemic delivery had significant impact on F-AuNS accumulation in tissues within the first 24 h post injection and confirmed the long-term presence (90 days) of F-AuNSs in tissues. Further, F-AuNSs underwent morphological changes from the star to spherical-like shape with fewer short branches. These *in vivo* biodistribution studies suggested that (a) *in vivo* uptake and localization of F-AuNSs was controlled by their cellular-level endocytosis and intracellular trafficking; (b) *in vivo* breakdown and reshaping was likely directed by F-AuNSs interaction with serum proteins and formation of protein corona; and (c) exocytosis and clearance of F-AuNSs was a function of the shape and surface properties of the "broken" NPs that resulted from the degradation of F-AuNSs. Based on these *in vivo* biodistribution results, we further evaluated the internalization mechanism by incubating macrophage cells with pathway inhibitors

71

and found that uptake of F-AuNSs was dominated by clathrin-mediated endocytosis, but other pathways also contributed, indicating the degradation of F-AuNSs were likely caused by the acidic environment in endosomes or lysosomes. Additionally, sodium dodecyl sulfate polyacrylamide gel electrophoresis (SDS-PAGE) and proteomic studies demonstrated that F-AuNSs dramatically minimized protein adsorption. The small amounts of adsorbed proteins on F-AuNSs were able to extend their blood circulation and promote intracellular uptake, implying the role of physicochemical properties of NPs on the protein corona effect. Finally, we assessed the exocytosis of F-AuNSs by simulating the interaction between gold NPs (AuNPs) and a lipid membrane using the Martini coarse-grained (CG) method. Our simulations indicated that the excretion of AuNPs relied on their physicochemical properties and the lipid composition of membrane. This comprehensive study covering *in vitro*, *in vivo*, and mechanistic simulation work revealed great biocompatibility of F-AuNSs and emphasized their tremendous translational potential.

4.3 Materials and Methods

4.3.1 Materials

Gold (III) chloride trihydrate ($HAuCl_4 \cdot 3H_2O$), (4-(2-hydroxyethyl)-1-piperazine-ethanesulfonic acid) (HEPES), fetal bovine serum (FBS), dimethyl sulfoxide (DMSO), cytochalasin B, genistein, rottlerin and monodansyl cadaverine, dithiothreitol (DTT) and β-mercaptoethanol were purchased from Sigma-Aldrich. The Milli-Q water (18 MΩ) was obtained from a Milli-Q Direct-Q 3UV system. OPSS-PEG-SVA-2000 and NH_2-PEG-SH-5000 were purchased from Laysan Bio. IgG2a antibodies (BE0089, Clone 2A3) were purchased from Bio X cell. Sodium bicarbonate ($NaHCO_3$), hydrochloric acid (HCl), nitric acid (HNO_3), phosphate-

buffered saline (PBS), 3-(4,5-dimethylthiazol-2-yl)-2,5-diphenyltetrazolium bromide (MTT), Alexa Fluor 488 NHS ester, formaldehyde, normal goat serum, Triton X-100, antifade mountant with DAPI, and Novex tris-glycine SDS running buffer were purchased from Thermo Fisher Scientific. 2-S-(4-aminobenzyl)-1,4,7-triazacyclononane-1,4,7-triacetic acid) (p-NH$_2$-Bn-NOTA) was purchased from Macrocyclics. Dulbecco's modified Eagle's medium (DMEM) and penicillin/streptomycin were purchased from Gibco. Laemmli sample buffer, protein standards and mini-protein gel were purchased from Bio-Rad.

4.3.2 Synthesis of AuNSs

Bare AuNSs were synthesized by the one-step and seedless-mediated method.[67] Briefly, 18 mL of Milli-Q water at 18 MΩ was mixed with 12 mL of 200 mM HEPES at pH 7.4 ± 0.2. Next, 300 μL of 20 mM HAuCl$_4$·3H$_2$O was added. The solution was mixed by gentle inversion and reacted at room temperature for 75 min.

4.3.3 Functionalization of AuNSs

To functionalize AuNSs with antibodies, bifunctional linkers OPSS-PEG-SVA-2000 were first reacted with IgG2a antibodies. Briefly, 72 μL of 1 mg/mL IgG2a antibody reconstituted in 100 mM NaHCO$_3$ buffer (pH 8.4 ± 0.2) was mixed with 8 μL of 80 mg/mL OPSS-PEG-SVA-2000 solution and allowed to react on an inverter (4 rpm) at 4 °C for 24 h. Afterwards, 80 μL of OPSS-PEG-anti-IgG2a was added to 6 mL of AuNSs at 1.14 mg/mL. The solution was then mixed on an inverter at 4 °C for another 24 h. Post AuNSs-anti-IgG2a reaction, the chelator, NOTA, was conjugated to the gold. Briefly, OPSS-PEG-SVA-2000 linkers were reacted with NOTA at 1:1 molar ratio at 4 °C for 10 h. OPSS-PEG-NOTA was then reacted with AuNSs-anti-IgG2a at 4 °C for 12 h. Then the functionalized AuNSs (AuNSs-anti-IgG2a-NOTA) were centrifuged at 4000 rpm for 10 min and resuspended with Milli-Q water at a concentration of 5 mg/mL. Lastly,

AuNSs-anti-IgG2a-NOTA nanoparticles were radiolabeled with ^{64}Cu followed by 75 min incubation at room temperature with gentle shaking every 15 min. PD-10 desalting columns were used to remove nonchelated copper.

4.3.4 Characterization of Nanoparticles

The plasmon resonance of bare and functionalized AuNSs was measured with a Varian Cary 5000 UV-Vis NIR spectrophotometer. The hydrodynamic size and zeta potential of nanoparticles were measured with a Malvern Nano ZS dynamic light scattering apparatus. The size and shape of AuNSs were visualized with an Osiris TEM at 200 keV.

4.3.5 Cell Viability

RAW 264.7 or J774A.1 cells were cultured in DMEM supplemented with 10% FBS and 1% penicillin/streptomycin. Cell cultures were maintained at 37 °C in a humidified 5% CO_2 atmosphere. Cells were seeded at 1×10^4 cells/well in a 96-well plate and treated with different concentrations of F-AuNSs for 24 h. Following incubation, old media in each well were removed, and 100 µL of fresh media mixed with 10 µL of 12 mM MTT was added to each well. After 2 h of incubation, 85 µL of media solution was removed and 50 µL of DMSO was added to solubilize the precipitated formazan crystals. The plates were incubated at 37 °C for 10 min, and the absorbance was measured at 540 nm using a BIO-TEK Synergy H1 plate reader.

4.3.6 Cell Cycle Analysis

RAW 264.7 or J774A.1 cells were seeded at 3×10^5 cells/well in a 6-well plate and then treated with F-AuNSs (100 µg/mL) for 24 h. After incubation, cells were harvested and centrifuged at 1200 rpm for 10 min, and the supernatant was discarded. The cell pellets were fixed with 66% ethanol and stored at -20 °C until analysis. The fixed cell suspensions were washed

three times with PBS by centrifugation at 1500 rpm for 10 min. The cells were resuspended in 0.1% Triton X-100. The cell pellets were further treated with the mixture of propidium iodide (50 µg/mL) and RNase A (550 U/mL) at 37 °C in the dark for 30 min. Samples were then subjected to a flow cytometer (BD FACSCanto), and data were analyzed using BD FACSDiva (version 8.0.1).

4.3.7 In Vivo Toxicity Study of AuNSs

Female 10-week-old mouse (C57BL/6J, Jackson laboratory) was injected intraperitoneally or intravenously with 0.8 mg of F-AuNSs. Mice were sacrificed at 1-, 7-, 30-, 45- or 90-days post injection. Cardiac blood (~600 µL/mouse) was collected for both complete blood count and serum liver/kidney metabolite studies. Complete blood counts were performed using the forcyte veterinary hematology analyzer (Oxford Science), and blood chemistries were measured by the Vet Axcel chemistry analyzer (Alfa Wassermann). Additionally, liver, spleen, kidney, heart, and lung of each mouse were retrieved and fixed in 6% formalin for H&E staining. H&E images were captured using Leica DMi8.

4.3.8 PET Imaging and Biodistribution

Mice were injected intraperitoneally or intravenously with 0.8 mg of F-AuNSs with 800 µCi of ^{64}Cu activity. Afterwards, mice were placed in a small animal imaging PET/CT machine (Siemens Inveon) and imaged at 2 and 24 h post injection. The mice were anesthetized with 2% isoflurane during imaging. All PET data sets were reconstructed using the MAP algorithm into $128 \times 128 \times 95$ slices with a voxel size of $0.095 \times 0.095 \times 0.08$ cm^3 at a beta value of 0.01. The PET images were normalized to the injected dose. After imaging (24 h post injection), mice were euthanized by cervical dislocation under deep isoflurane anesthesia. Tissues were then harvested,

weighted and placed in scintillation vials for gamma counting using Hidex AMG automatic gamma counter.

4.3.9 Inductively Coupled Plasma-Mass Spectrometry

Mice were injected intraperitoneally or intravenously with 0.8 mg of F-AuNSs. For each mouse, the liver, spleen, kidney, heart, lung, stomach, brain, muscle, bone, pancreas, and intestine were retrieved at 1-, 7-, 30-, 45- or 90-days post injection. Tissues were first snap frozen in liquid nitrogen. Tissues were then dried with a lyophilizer (Labconco), weighted and then placed in 80% trace-metal grade aqua regia for 72 h. Afterwards, aqua regia was boiled off and the tissue samples were reconstituted with 10 mL of 2% nitric acid. Filters with 0.45 µm diameter were used to remove any impurities in the samples prior to ICP-MS measurements. The ICP-MS instrument (Perkin Elmer NexION 2000) was operated at 1.5 kW radio frequency power, 15 L/min argon plasma flow, 0.9 L/min nebulizer flow, and 1 s integration time for 3 replicates. A six-point calibration curve in the range of 0.5 and 1000 µg/L was performed for gold isotope 197. Analytical blanks and standards (10 µg/L) were measured for every $3 - 5$ samples to ensure the readings were within 15% of the specified value.

4.3.10 Transmission Electron Microscope Imaging of Tissues

Mice were injected intraperitoneally or intravenously with 0.8 mg of F-AuNSs. The mice were sacrificed at 7-, 45- or 90-days post injection. Liver, spleen, and kidney were then retrieved. All tissues were dissected into 1 mm by 1 mm pieces with razor blades and immediately immersed in 2.5% glutaraldehyde in 0.1 M cacodylate buffer (pH 7.4 ± 0.1) for 24 h at 4 °C. The specimens were further fixed with 1% osmium tetroxide for 1 h and enblock stained with 1% uranyl acetate for 30 min. The samples were dehydrated with a graded ethanol series and then infiltrated with Epon 812 resin (Electron Microscopy Sciences) using propylene oxide as a transition solvent. The

Epon 812 was polymerized at 60 °C for 48 h, sectioned at 70 nm using a Leica EM UC7 Ultramicrotome and collected on 300 mesh nickel grids. The sections were stained with 2% uranyl acetate and lead citrate. TEM imaging was performed on a Tecnai T12 at 100 kV using an AMT CCD camera.

4.3.11 Nanoparticle Uptake Study

To investigate the mechanism of nanoparticle uptake, the synthesis of particles was slightly modified. Post AuNSs-anti-IgG2a reaction, particles were fluorescent labeled instead of conjugation with NOTA. For fluorescent labeling, 25 mg/mL of NH_2-PEG-SH-5000 was first mixed with 1 mg/mL of Alexa Fluor 488 NHS ester at room temperature for 2 h on an inverter. The mixture was then reacted with AuNSs-anti-IgG2a at 4 °C for 3 h. The functionalized AuNSs (AuNSs-anti-IgG2a-488) was centrifuged at 4000 rpm for 10 min to remove excess free dyes and resuspended with Milli-Q water at a concentration of 5 mg/mL.

For the uptake studies, RAW 264.7 or J774A.1 cells were seeded at 3×10^5 cells/well in a 6-well plate overnight. Prior to the exposure to nanoparticles, cells were first pretreated at 37 °C with different pathway inhibitors: cytochalasin B (10 µg/mL, 2 h), genistein (200 µM, 1 h), rottlerin (2 µM, 30 min) and monodansyl cadaverine (200 µM, 10 min), respectively. To investigate the energy-dependence of uptake mechanism, cells were pre-incubated at 4 °C for 1 h. Afterwards, F-AuNSs (100 µg/mL) were added and incubated for 6 h. Negative controls (*i.e.*, cells without the presence of inhibitors and nanoparticles) were also included. The mechanism of nanoparticle uptake was determined by flow cytometry.

4.3.12 Confocal Imaging

RAW 264.7 or J774A.1 cells (5000 cells/well) were seeded in 8-well chamber slides (Lab-Tek) and incubated overnight. Cells were then exposed to F-AuNSs (100 µg/mL) at different time

points (2, 4, 6, 8, 12, 18 and 24 h), fixed with 4% formaldehyde solution for 10 min, permeabilized with 0.1% Triton X-100 for 1 h, and blocked with 10% normal goat serum solution at room temperature for 1 h. Cells were incubated overnight at 4 °C with anti-EEA1 antibody (Abcam, ab109110, 1/250) for early endosome staining or anti-RAB7 antibody (Abcam, ab126712, 1/50) for late endosome staining, and washed three times followed by staining with Alexa Fluor 594-conjugated anti-rabbit IgG (Abcam, ab150080, 1/500). For lysosome imaging, cells were stained with BioTracker NIR 633 (Sigma, 1/500) according to the manufacturer's instructions. Slides were mounted with DAPI nuclear dye and visualized under a Leica SP5 X MP confocal microscope. Images were captured utilizing a 63× objective.

4.3.13 Proteins Immobilized on Nanoparticles

To study the protein corona on bare and functionalized AuNSs, the nanoparticle dispersion was incubated with 60% FBS at 37 °C for 1, 24 and 48 h under constant agitation. Particles were separated from the supernatant by centrifugation at 6000 rpm and 4 °C for 20 min. The pellets were resuspended in PBS and washed three times by centrifugation at 4000 rpm and 4 °C for 10 min to remove unbound proteins.

4.3.14 SDS-PAGE Electrophoresis

Proteins immobilized on particles (5 mg/mL) was mixed with Laemmli sample buffer (2×) containing freshly added 5% β-mercaptoethanol at a ratio of 1:1 and boiled at 95 °C for 10 min. Treated samples were then loaded in a 4-20% mini-protein gel. The gels were run for 30 min at 200 V in Novex tris-glycine SDS running buffer (1×). Silver staining of gels was performed according to the manufacturer-provided procedures (Fujifilm Wako, 291-50301). Gels were visualized by UMAX PowerLook 1100 scanner. Proteins adsorbed onto particles were quantified using ImageJ.

4.3.15 Proteomic Study of Surface Protein Corona

Crude protein extracts were reduced with DTT. The cysteines were modified with iodoacetamide and then digested overnight with trypsin/Lys-C at an enzyme to protein ratio of 1:25. Formic acid was added to stop digestion. Samples were then desalted using a C18 MicroSpin columns (Nest Group) before drying in a speedvac concentrator. The peptides were then separated using an EASY-nLC 1200 UHPLC system coupled to Nanospray Flex ion source (Thermo Fisher Scientific). The Q Exactive Hybrid Quadrupole-Orbitrap mass spectrometer with an HCD fragmentation cell (Thermo Fisher Scientific) was used for mass spectrometric analysis. Raw files were analyzed using Proteome Discoverer (Thermo Fisher Scientific, version 2.4). MS/MS spectra were searched with Mascot against Sprot-all.

4.3.16 Martini Coarse-Grained Simulation

All simulations were performed using the Martini coarse-grained force field (version 2.2)[232] description implemented in the GROMACS 5.1.4 package.[233] Both van der Waals and electrostatic interactions had a cutoff of 1.1 nm. The isotropic Parrinello-Rahman pressure coupling scheme was coupled to control the pressures at 1 bar and the compressibility at 3×10^{-4} bar^{-1}.[234] The system temperature was maintained at 310 K by v-rescale coupling scheme with a time constant of $\tau = 1$ ps.[235] Periodic boundary conditions were imposed in all three *x*-, *y*- and *z*-directions. The AuNP was placed approximately at the center of the vesicle. Initially, the AuNP was fixed to perform a 100 ns balance simulation. To gain the insights into the complete exocytosis process of AuNP from the membrane, pull simulations were applied in the *z* direction by using a constant force 1000 kJ/mol/nm^2 to the center of mass of the AuNP. All systems were simulated for 300 ns with a time step of 20 fs. Data visualization was performed with Visual Molecular Dynamics (VMD).[236] Four different shapes of AuNPs were examined including sphere, cylinder,

cone and tetrahedron. Two different sizes of AuNPs were studied including 4.5 and 35 nm^3. The nanocrystalline structure of AuNPs was characterized by the face-centered cubic (FCC) structure with a lattice constant of 0.408 nm. For the membrane vesicles, the initial structure was constructed online by CHARMM-GUI Martini make.[237] To evaluate the effect of membrane composition on the AuNP translocation, two different types of vesicles with an initial diameter of 17 nm were constructed: purely composed of dipalmitoylphosphatidylcholine (DPPC) or dioleoylphosphatidylcholine (DOPC). The DPPC vesicle with fully saturated chains contained a total of 2550 lipid molecules. The DOPC vesicle was unsaturated with one double bond in each tail containing a total of 2394 lipid molecules. The initial size of the simulation box was $26 \times 26 \times 80$ nm^3. Water molecules and counterions (Na^+ and Cl^-) were added in the simulation box to neutralize the system.

4.3.17 Statistical Analysis

All data were presented as mean ± standard deviation. The sample sizes were estimated based on our previously published work.[33] Statistical significance was determined by GraphPad Prism 8 with unpaired two-sided Student's t-tests for the calculation of p values. Here, * indicates $p < 0.05$, ** indicates $p < 0.01$, *** indicates $p < 0.001$, and **** indicates $p < 0.0001$.

4.4 Results and Discussion

Bare gold nanostars (B-AuNSs) were synthesized through a one-step seedless method with a biological buffer, 4-(2-hydroxyethyl)-1-piperazine-ethanesulfonic acid (HEPES) as described in our previously published work.[33,34,67] The low binding affinity of HEPES on gold surface facilitated straightforward surface modification enabling us to design the functionalized AuNSs (F-AuNSs). F-AuNSs were designed by conjugating antibodies and chelators to AuNS surfaces

via a bifunctional orthopyridyl disulfide-poly(ethylene glycol)-succinimidyl valerate (OPSS-PEG-SVA) linker. The thiols on the OPSS group were covalently bound to AuNSs and SVA esters reacted with amines on antibodies or chelators to form a stable amide bond (Figure 4.1a). We chose a generic immunoglobulin G (IgG) antibody for the synthesis to explore untargeted biodistribution of F-AuNSs, as antibody-nanoparticle conjugates have prolonged blood circulation, enhanced nanoparticle-cellular interactions, and longer residence time in the tissues.[238] The PEG ligands on the linker hindered protein adsorption and subsequent clearance by the mononuclear phagocyte system (MPS).[239] The diagnostic capability of F-AuNSs to provide anatomical information *in vivo* was enabled by the utility of ^{64}Cu radiolabel chelated to 2-S-(4-aminobenzyl)-1,4,7-triazacyclononane-1,4,7-triacetic acid) (p-NH$_2$-Bn-NOTA) and conjugated to AuNSs *via* the same linker. We chose ^{64}Cu-NOTA complex for F-AuNSs enabled positron emission tomography and computed tomography (PET/CT) imaging due to its excellent stability, high labeling yield,[240-242] and clinical significance (clinical trial #NCT04167969).[243] AuNSs were anisotropic with overall dimensions of 60 – 80 nm (Figure 4.1b), a size regime amenable to rapid extravasation through fenestrations in vasculature enabling longitudinal imaging and time-course study.[239] The functionalization of AuNSs with antibodies and ^{64}Cu-NOTA resulted in a ~40 nm shift in the plasmon resonance (Figure 4.1c) indicating an increase in particle size and change in refractive index of the medium. Consistent with UV-Vis results, the size of B-AuNSs and F-AuNSs measured using dynamic light scattering showed similar trends (Figure 4.1d). F-AuNSs also showed a near-neutral surface charge (Figure 4.1e), attributable to the PEG chains in the linker, which was desirable to reduce the adsorption of serum proteins and promote longer circulation half-life. We also confirmed metal chelation with inductively coupled plasma mass spectrometry (ICP-MS) using "cold" non-radioactive Cu to NOTA conjugated AuNSs. The results

demonstrated 1.02 ± 0.044 µg Cu/mg Au for F-AuNSs relative to 0.084 ± 0.0010 µg Cu/mg Au

for B-AuNSs control indicating successful radiolabeling (Figure 4.1f). The F-AuNSs were highly

stable in aqueous media, buffers (PBS), and cell culture media (supplemented with and without

serum) for up to 90 days (Figure A.14). Minimal changes were observed in the intensity and full

width at half maximum (FWHM) of the extinction spectra during this time span indicating long

shelf-life of F-AuNSs.
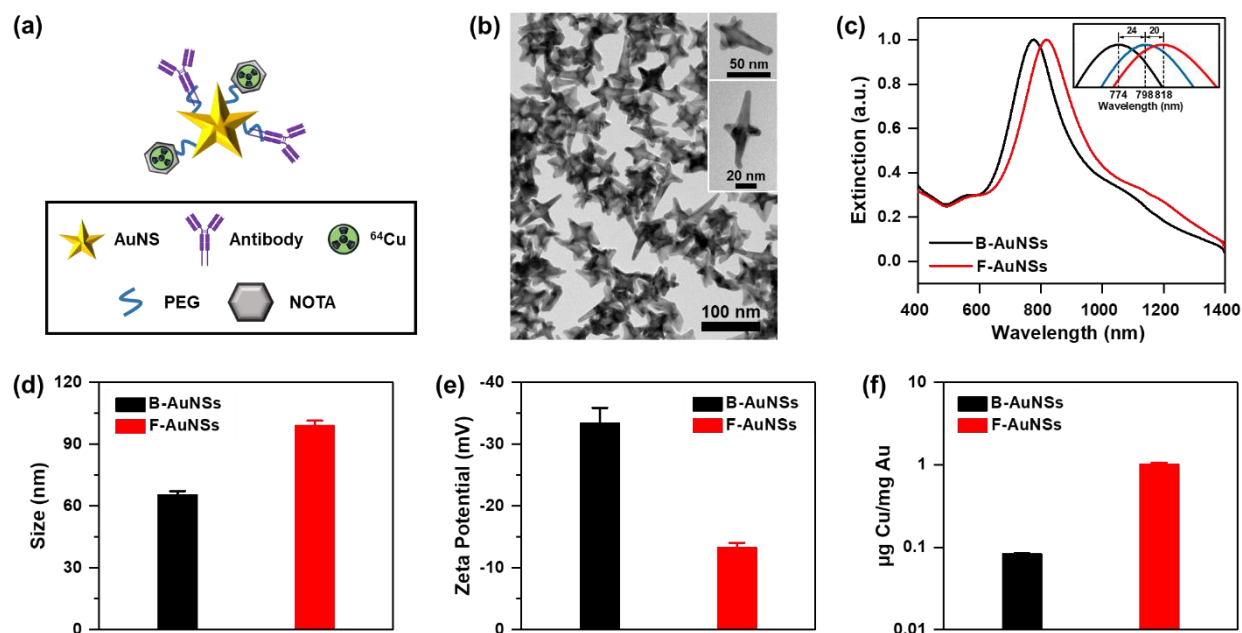
Figure 4.1 Design and characterization of bare (B-AuNSs) and functionalized gold nanostars (F-AuNSs). (a) Schematic illustration showing F-AuNSs were conjugated with IgG2a antibodies and NOTA *via* a bifunctional linker followed by chelation with ^{64}Cu radioisotopes. (b) Transmission electron micrograph of AuNSs showing their anisotropic structure. (c) Extinction spectra of B-AuNSs and F-AuNSs. The inset showed peak shifts when B-AuNSs (black) were bound with antibodies (blue) and further ^{64}Cu-NOTA complex to form F-AuNSs (red). (d) Hydrodynamic size and (e) zeta potential of B-AuNSs and F-AuNSs from dynamic light scattering. (f) Quantification of cold Cu chelation to F-AuNSs with ICP-MS. Data were presented as mean ± standard deviation (n = 3).

Whereas the short-term (up to 15 days) toxicity profile of AuNSs has been evaluated *in vivo*,[213,214] the long-term impact of AuNSs *in vivo* remains unexplored and is critical to the clinical translation of nanoparticles. The current understanding of the toxicological effects of gold

nanoparticles (NPs) is limited to PEG coated NPs, which do not accurately represent the plethora of NPs that have been investigated with diagnostic and therapeutic modalities.[215-217] Such nanoparticles have several functional ligands on their surface which control their physicochemical properties and *in vivo* efficacy. Therefore, we performed systematic long-term (up to 90 days) evaluation of the toxicological profile of F-AuNSs to ultimately correlate to their degradation *in vivo* and exocytosis from tissues. We first studied the cell viability of F-AuNSs *in vitro* in murine macrophage cell lines RAW 264.7 and J774A.1 and observed minimal changes in the viability of both cell lines indicating F-AuNSs had high *in vitro* biocompatibility (Figure A.15a). We chose macrophage cells to accurately represent *in vivo* settings since NPs were taken up by spleen- and liver-resident macrophages.[244-246] Furthermore, previous studies have demonstrated that the non-toxic nanoparticles tested using classical toxicity assays may lead to severe cell cycle disruption and cause DNA damage.[247] Therefore, we studied the impact of F-AuNSs on cell cycle, which is a series of stages for cell division and replication. Cell cycle includes four phases (G_1, S, G_2 and M) where the activation of each phase is driven by the progression and completion of the previous phase.[248,249] A cell cycle starts with the G_1 phase where cells increase their size followed by DNA synthesis during the S phase and protein synthesis needed for cell division in the G_2 phase. In the final M phase, cells divide forming two daughter cells. Here, we evaluated the effect of F-AuNSs on cell cycle through flow cytometry measurements which showed minimal alterations in cell cycle stages for both macrophage cell lines (Figure A.15b). Literature evidence has suggested that the grafting density of polymers and other moieties on nanoparticle surface is directly correlated to alterations in cell cycle.[250] Our results implied that optimal grafting density of functional groups was achieved in F-AuNS synthesis.
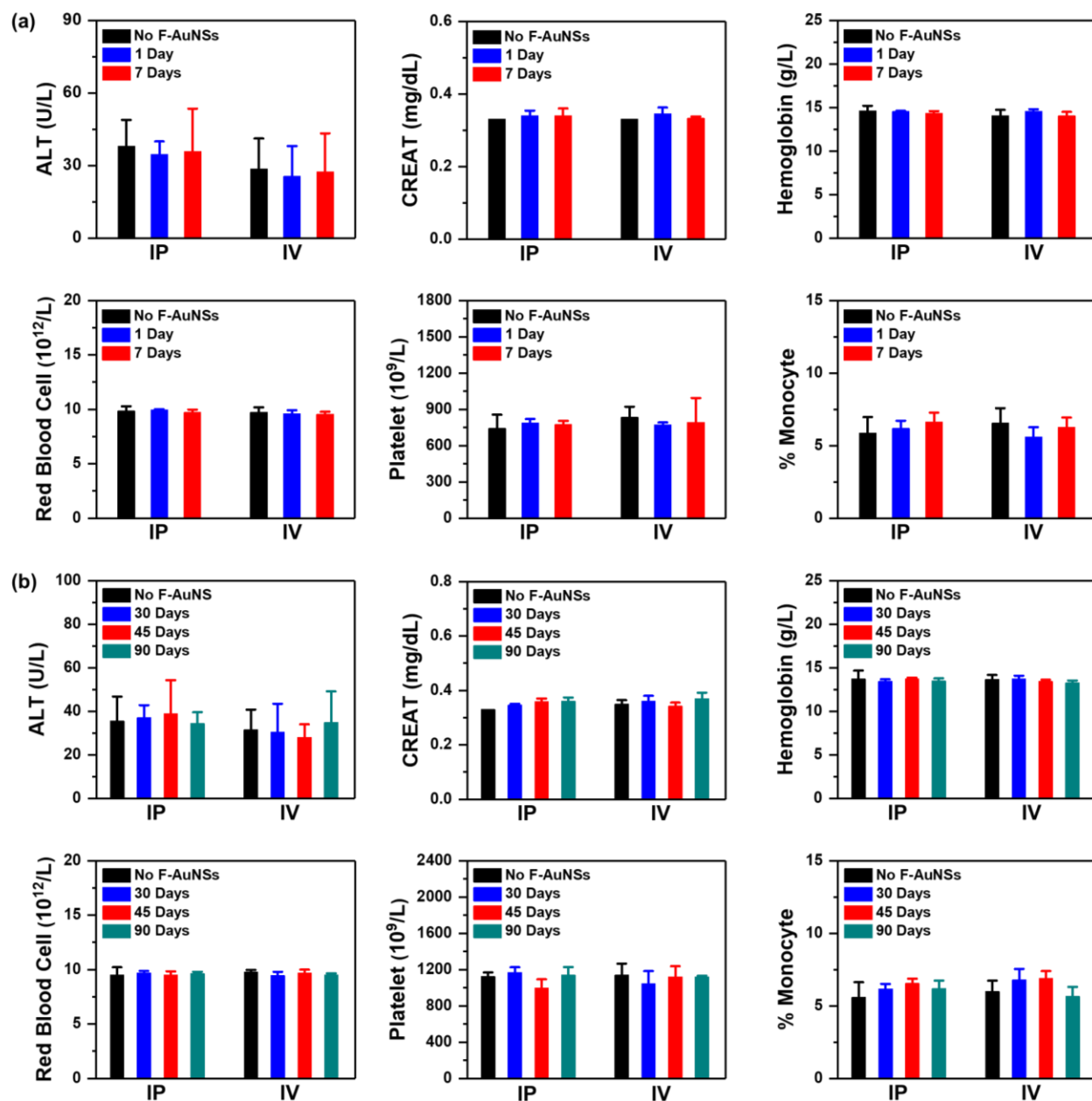
Figure 4.2 Toxicity evaluation of F-AuNSs *in vivo*. Serum inflammatory markers and complete blood count of mice received F-AuNSs intraperitoneally (IP) and intravenously (IV) were compared to control mice which received PBS at both short- and long-terms. (a) Short-term measurements include 1- and 7-days post-delivery results. (b) Long-term is defined as 30-, 45- and 90-days post-injection results. Irrespective of injection routes, no significant abnormalities in hepatic, renal and hematological functions were observed, indicating good biocompatibility of F-AuNSs. Data were presented as mean ± standard deviation (n = 4).

We further examined the toxicity of F-AuNSs *in vivo* in 10-week-old healthy C57BL/6 mice by measuring standard serum inflammatory markers. Mice received F-AuNSs at a dose of 0.04 mg/g mouse weight intraperitoneally (IP) or intravenously (IV), and sera were collected from a parallel cohort of mice at 1-, 7-, 30-, 45- and 90-days post F-AuNS delivery to evaluate both short- and long-term inflammatory response. This dosage of F-AuNSs is comparable or lower than other studies utilizing gold nanostars.[33,251] Alanine aminotransferase (ALT), aspartate aminotransferase (AST) and total bilirubin (TBIL) are measures of hepatic toxicity; high levels of these proteins are indicative of liver damage.[252,253] Creatinine (CREAT) and blood urea nitrogen (BUN) are markers of kidney function, where CREAT results from muscle metabolism and its concentration in sera correlates to nanoparticle glomerular filtration rate.[254] BUN is a primary metabolite derived from proteins and amino acid catabolism and filtered out of blood by glomeruli. We also measured complete blood count in mouse serum, including hemoglobin, red blood cells, white blood cells, platelet concentration, monocyte counts, and lymphocyte counts. Our results showed mice that received F-AuNSs had comparable serum marker levels to control mice that received PBS (Figure 4.2 and A.16) both in the short-term (1 and 7 days) and long-term (30, 45 and 90 days) indicative of minimal toxicity induced by F-AuNSs. The route of systemic administration also did not induce any significant differences in these serum markers. We further confirmed these observations with hematoxylin and eosin (H&E) staining of major organs, including spleen, liver, kidney, lung, and heart (Figure A.17 and A.18) and observed no noticeable histopathological changes irrespective of injection routes.
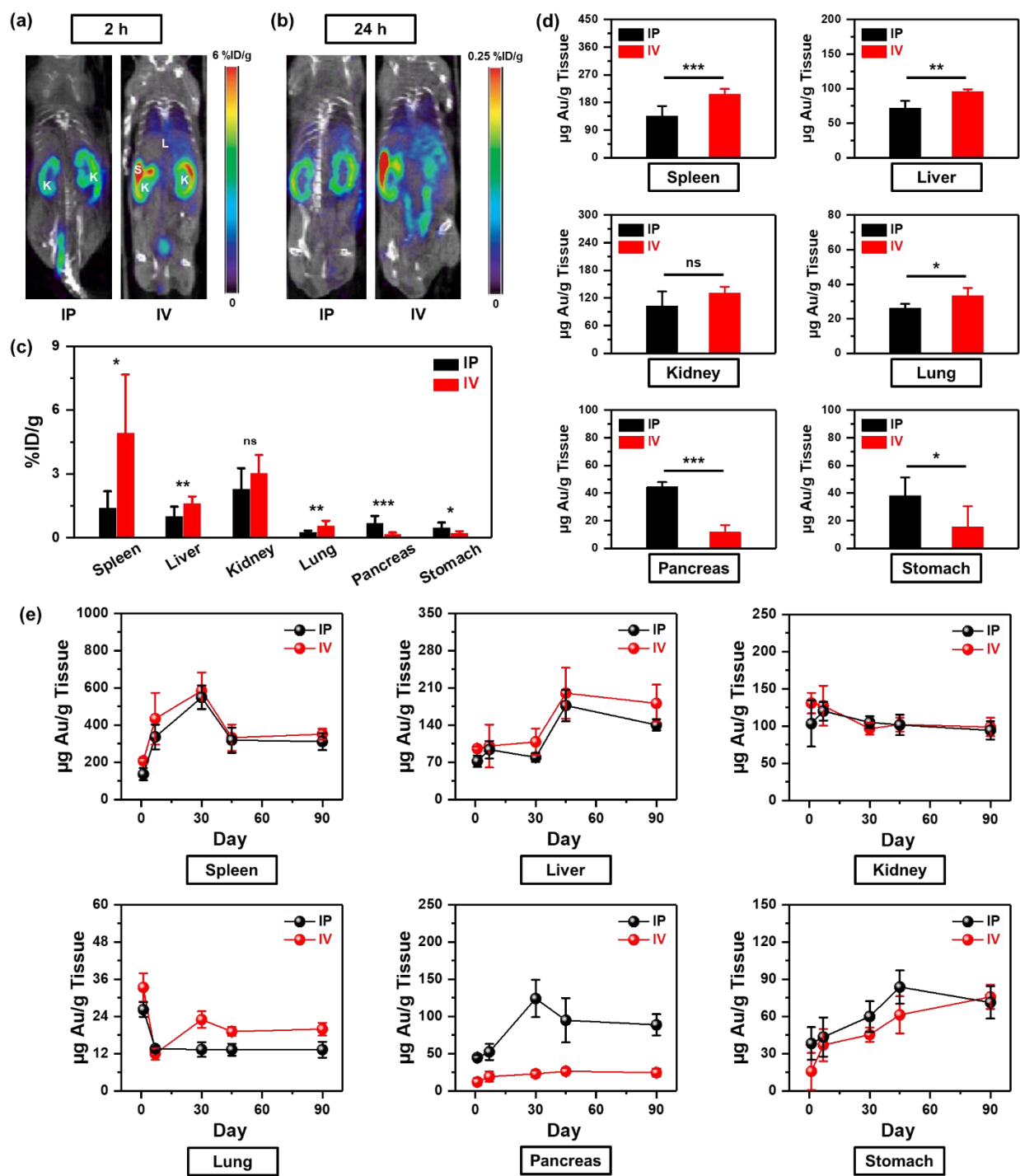
Figure 4.3 Biodistribution of F-AuNSs *in vivo*. Whole-body PET/CT images of mouse at (a) 2 and (b) 24 h post F-AuNSs delivery *via* IP or IV injection. *K* represents kidney, *S* represents spleen, and *L* represents liver. (c) Biodistribution of F-AuNSs from harvested organs *via* gamma counter after IP or IV injection at 24 h post injection (n = 5). (d) Quantitative ICP-MS analysis of biodistribution of F-AuNSs in mice 24 h post particle delivery (n = 4). (e) Biodistribution and clearance of F-AuNSs of major organs at 1-, 7-, 30-, 45- and 90-days post-delivery (n = 4). Here, data were presented as mean ± standard deviation. * indicates $p < 0.05$, ** indicates $p < 0.01$, *** indicates $p < 0.001$, and ns indicates not significant.

While some prior studies have demonstrated that the route of administration *in vivo* controls the biodistribution of nanoparticles,[95,255] these studies have not shown a longitudinal time-course study of the short-term and long-term impact of route of delivery of nanoparticles on various tissues. Here, we have performed a correlative study combining PET imaging, biodistribution analysis *via* gamma counts of ^{64}Cu radiolabeled F-AuNSs, and ICP-MS analysis of gold in tissues to assess the biodistribution of F-AuNSs up to 90 days post-delivery. PET is a useful clinical technique that provides depth-resolved whole-body images of the localization of diagnostic and therapeutic agents and enables us to visualize the distribution of F-AuNSs in mice within the first 24 h post-delivery as a function of route of administration. Here, healthy C57BL/6 mice were injected *via* either IP or IV with F-AuNSs at a dose of 0.04 mg/g mouse weight with ~800 µCi of ^{64}Cu radioactivity. PET images acquired at 2 and 24 h post-injection showed that F-AuNSs when delivered *via* IP were retained within the peritoneal cavity and transport out of the peritoneal cavity was slow at 2 h post-delivery, and showed a preferential accumulation in the kidney at both time-point (Figure 4.3a,b). In contrast, mice that received F-AuNSs *via* IV displayed immediate accumulation of nanoparticles in spleen, kidney, and liver at 2 h post-injection followed by the continuous localization in these tissues over 24 h. Gamma counts of harvested tissues at 24 h post injection quantified a significantly higher uptake of F-AuNSs within the spleen, liver, and lungs when delivered *via* IV (Figure 4.3c). IV delivery of F-AuNSs also showed higher uptake in heart, brain, bone, and muscle (Figure A.19) demonstrating that this route of administration was preferred for nanoparticle delivery to most organs. However, F-AuNSs delivered *via* IP had higher uptake in the pancreas and stomach likely due to the proximity of these organs to peritoneal cavity. Interestingly, there were no significant differences in the accumulation of F-AuNSs in the kidney and intestine (Figure 4.3c and A.19) as a function of the route of

administration. We further confirmed that the activity detected from gamma counts accurately represented ^{64}Cu bound to F-AuNSs (not free ^{64}Cu) by comparing with quantitative ICP-MS analysis of gold content in these organs retrieved 24 h post IP and IV delivery of F-AuNSs (Figure 4.3d and A.20a). The results were consistent with findings from gamma count biodistribution suggesting that ^{64}Cu was appropriately chelated to F-AuNSs and supporting our hypothesis that the route of systemic delivery had significant impact on tissue accumulation within the first 24 h post injection.

Next, we assessed the long-term accumulation of F-AuNSs by determining the gold content in various organs with ICP-MS retrieved at 1, 7, 30, 45 and 90 days after a single IP or IV injection (Figure 4.3e and A.20b). Our results showed the maximum accumulation time-point of F-AuNSs varied in different organs and both IP and IV delivery showed similar trends (except in the pancreas) indicating the route of administration of F-AuNSs had minimal impact in the long-term distribution. We observed in the spleen maximum accumulation of F-AuNSs occurred at 30 days followed by rapid splenic clearance at 45 days and retention in spleen up to 90 days. In the liver, however, maximum F-AuNSs was found at 45 days post-delivery followed by slow clearance up to 90 days. Our results showed that (i) the conjugation of various ligands including PEG resulted in prolonged circulation of F-AuNSs and ultimate accumulation in the MPS organs, and (ii) F-AuNSs were cleared through the MPS *via* hepatobiliary excretion and not through recirculation into blood, consistent with previous observations in the literature.[256,257] Surprisingly, we found significant accumulation of F-AuNSs in the kidney comparable to that in the liver despite the accepted belief that NPs >10 nm are not taken up by kidneys. We hypothesized that F-AuNSs distribution in the kidney was likely attributable to multiple factors. First, the densely packed PEG chains and well functionalized surface of F-AuNSs reduced *in vivo* agglomeration improving stability and blood

circulation that enabled entry and accumulation in the kidneys. Second, the ~95 nm size of F-AuNSs resulted in the glomerular endothelial fenestrae filtration and promoted kidney accumulation. This finding was consistent with literature findings that supported NPs undergoing renal filtration must pass through: (1) glomerulus endothelium containing pores (fenestra) of 80 – 100 nm; (2) the negatively charged glomerular basement membrane with pores of 5 – 8 nm; and (3) a slit diaphragm of podocytes with pores of around 15 nm.[79,80] We noted that F-AuNSs did break down into smaller gold NPs in major organs (discussed in Figure 4.4 and 4.5) but elimination through the glomeruli remained slow and thus kidney accumulation was observed even at 90 days.

Biodistribution of F-AuNSs in lung and heart showed higher accumulation when delivered IV consistent with literature findings[258] and had similar overall trends showing high gold content within 24 h post-delivery when F-AuNSs were in active circulation followed by gradual decrease in concentration. These findings supported our toxicity analysis (Figure 4.2 and A.16-A.18) indicating F-AuNSs should have minimal lung toxicity and cause no adverse cardiovascular effects critical to translation of these NPs. We also had a surprising observation that IP delivery of F-AuNSs resulted in a statistically significant high accumulation in the pancreas relative to IV delivery, which peaked at 30 day post-delivery and then slowly cleared. High distribution of NPs in pancreas *via* IP administration likely arose from intraperitoneal circulation and uptake by tissue-resident and peritoneal macrophages which honed to the pancreas. F-AuNSs also showed uptake in the stomach, slightly higher *via* IP delivery, indicating they penetrated *via* the mucus layer and were absorbed by gastrointestinal epithelial cells and stable enough to be retained against rapid gastric emptying. High stomach content of gold may also be contributed by mice engaging in coprophagia of excreted F-AuNSs. Additionally, brain, bone and muscles had minimal gold content which decreased over time although at different rates (Figure A.20b). These results were

expected as NPs >10 nm cannot pass through the blood brain barrier and had limited transvacular transport through the small fenestrations in bone and muscle. Uptake of F-AuNSs in the intestines could be through enterocytes in the upper small intestine or possibly through passive uptake during cell turnover.[259,260] Our in-depth biodistribution analysis has several implications that will guide researchers in understanding the role of delivery route, NP shape, and surface characteristics in directing tissue-specific entry.
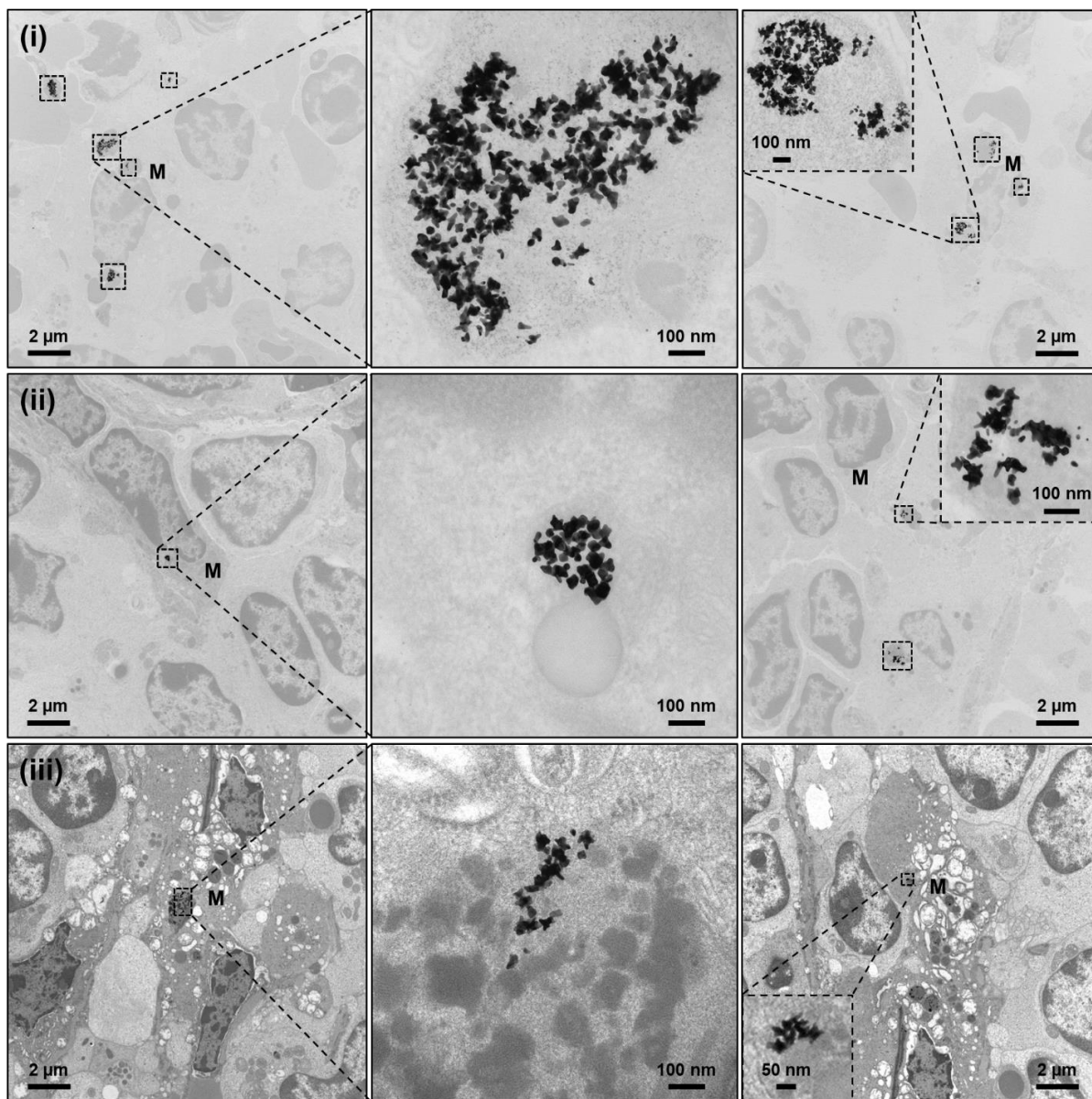
Figure 4.4 Representative TEM micrographs of spleen of mice taken (i) 7, (ii) 45 and (iii) 90 days after the intraperitoneal injection of F-AuNSs. Here, *M* represents macrophage.
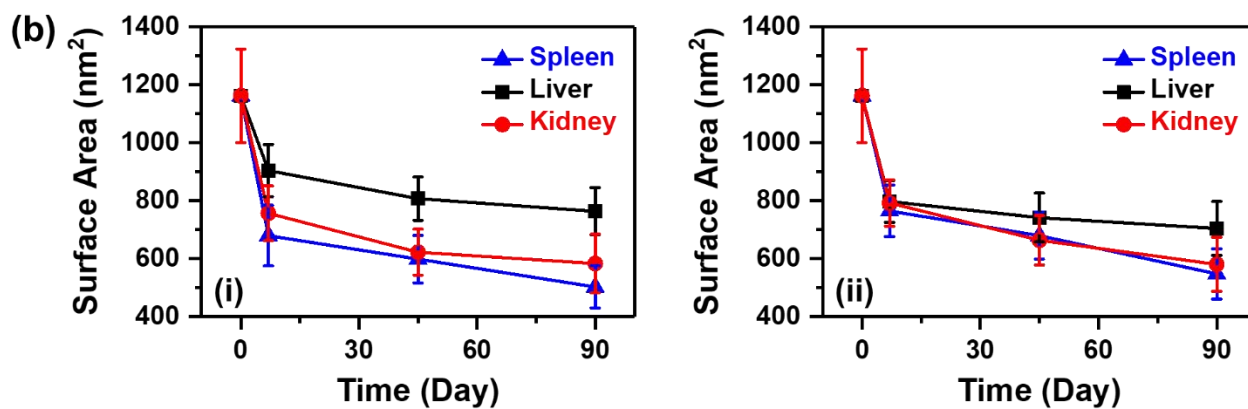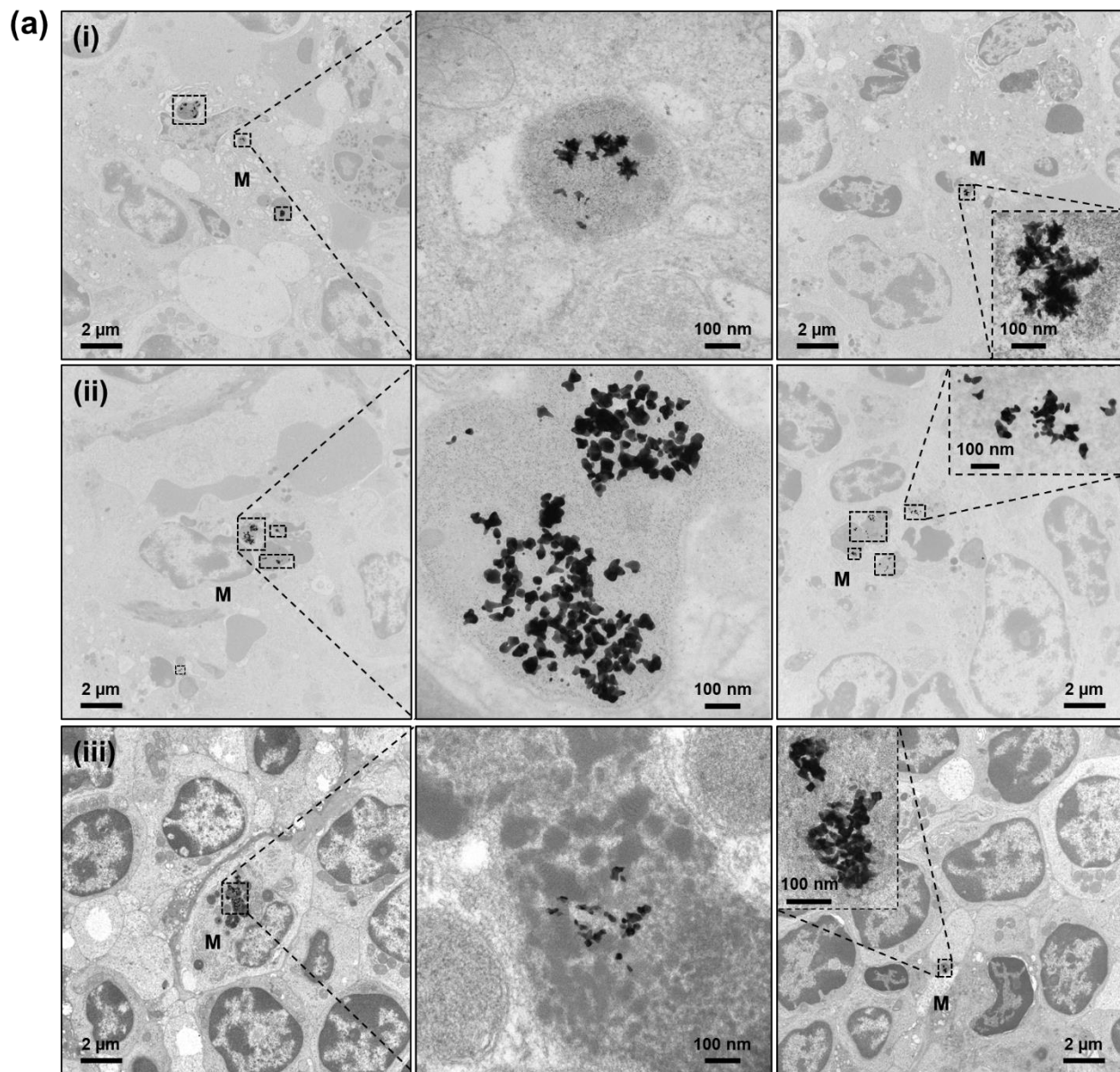
Figure 4.5 (a) Representative TEM micrographs of spleen of mice taken (i) 7, (ii) 45 and (iii) 90 days after the intravenous injection of F-AuNSs. Here, *M* represents macrophage. (b)

Quantification of surface area of F-AuNSs from TEM images. Here, day zero represents as-synthesized F-AuNSs before they were delivered in mice. The TEM images used for surface area calculation include that of spleen, liver and kidneys harvested 7, 45 and 90 days after (i) IP and (ii) IV delivery of F-AuNSs. The error bars were calculated by counting surface area of >100 particles per group from TEM images taken at the same magnification.

In addition to quantitatively measure of gold content in tissues, we examined the morphology of F-AuNSs from 7 – 90 days in tissues to understand their long-term fate which controlled their cellular exocytosis and clearance. Transmission electron micrographs (TEM) of spleen of mice that received F-AuNSs (0.04 mg/g mouse weight) *via* IP (Figure 4.4 and A.21) and IV (Figure 4.5a and A.22) showed for the first time the surprising breakdown of F-AuNSs *in vivo* as early as 7 days post systemic delivery. The breakdown of F-AuNSs after IP delivery began with breaking off of the nanostar protrusions which ultimately transformed into smaller spherical-like nanostructures with fewer short branches (Figure 4.4 and A.21). The reshaping of F-AuNSs from the star to spherical shape was expected given the higher thermodynamic stability of spherical morphology, which suggested for a given size anisotropic non-spherical NPs will have a rapid breakdown *in vivo* enabling faster clearance. F-AuNSs were primarily found in splenic macrophages located in the endosome/lysosome indicating that F-AuNSs were endocytosed consistent with literature findings for gold NPs.[33,65,261] The morphological transformation of F-AuNSs was likely catalyzed by the acidic and enzymatic degradation in endosomes or lysosomes. F-AuNSs delivered *via* IV demonstrated similar shape deformation in splenic macrophages. However, the degradation process started sometime after the 7-day time point (Figure 4.5a and A.22) suggesting that F-AuNSs stayed in circulation longer when delivered *via* IV and had a slower uptake by the spleen. We also investigated the morphological changes of F-AuNSs in the excised liver and kidneys of mice. In the liver, independent of the route of delivery, F-AuNSs primarily accumulated in Kupffer cells, the liver-resident macrophages, consistent with our previous

findings[65] of AuNSs (Figure A.23 and A.24). The number of Kupffer cells and their corresponding function vary in different zones of the hepatic lobules where Kupffer cells found in the periportal zones have a higher phagocytic activity.[262,263] Whereas prior studies have indicated spherical gold NPs are cleared *via* endothelial cells and hepatocytes of liver,[257] we did not observe F-AuNSs in either of these cell types suggesting both shape and surface properties determined their *in vivo* fate and ultimate exocytosis. Surprisingly, the breakdown of F-AuNSs in the liver was much slower than the spleen suggesting Kupffer cells had a slower turnover than splenic macrophages. Similar to liver, in the kidneys F-AuNSs showed slow breakdown independent of the route of administration and gradually reshaped into sphere-like shapes between 7 – 45 days post-delivery (Figure A.25 and A.26). F-AuNSs were primarily located in the glomeruli or interstitial cells around the proximal convoluted tubules indicating intact F-AuNSs (~95 nm) permeated through the 80 – 100 nm pores of the fenestrated glomerular endothelia but did not pass through pores of glomerular basement membrane (5 – 8 nm) and slit diaphragm (~15 nm). A few non-clustered F-AuNSs did transiently enter the mesangium at earlier time-points but retention over longer time-scales was not observed due to lack of phagocytosis by mesangial cells. However, post-breakdown smaller and broken F-AuNSs were found in interstitial cells (90 days time point, Figure A.25 and A.26). These findings supported our ICP-MS results which clarified the long-term presence of F-AuNSs in kidneys. To quantify the breakdown of F-AuNSs as a function of the route of administration in the major organs, we measured the surface area of >100 particles in TEM images at each time point (with ImageJ) and compared that to as-prepared F-AuNSs before injection (Figure 4.5b). Our results showed a dramatic decrease in surface area of F-AuNSs in spleen, liver, and kidney independent of the route of delivery but the rate of F-AuNSs breakdown varied in each tissue.

Collectively, the biodistribution studies, morphological analysis, and quantitative measure of surface area suggested that: (I) *in vivo* uptake and localization of F-AuNSs were controlled by their cellular-level endocytosis and intracellular trafficking; (II) *in vivo* stability, breakdown, and ultimate reshaping were likely directed by F-AuNSs interaction with serum proteins and formation of protein corona; and (III) exocytosis and clearance of F-AuNSs were a function of the shape and surface properties of the "broken" NPs that resulted from the degradation of F-AuNSs. To understand the role of each of these critical parameters in the ultimate fate of F-AuNSs, we have performed thorough *in vitro* mechanistic studies and Martini coarse-grained simulation that are discussed further.
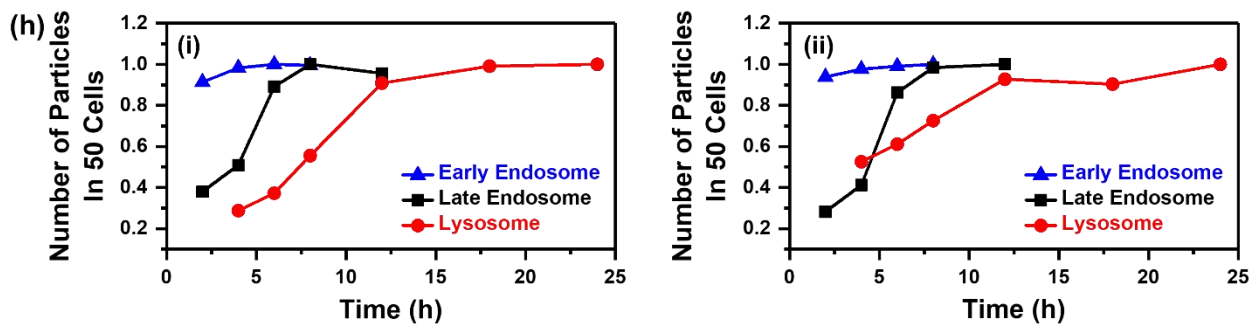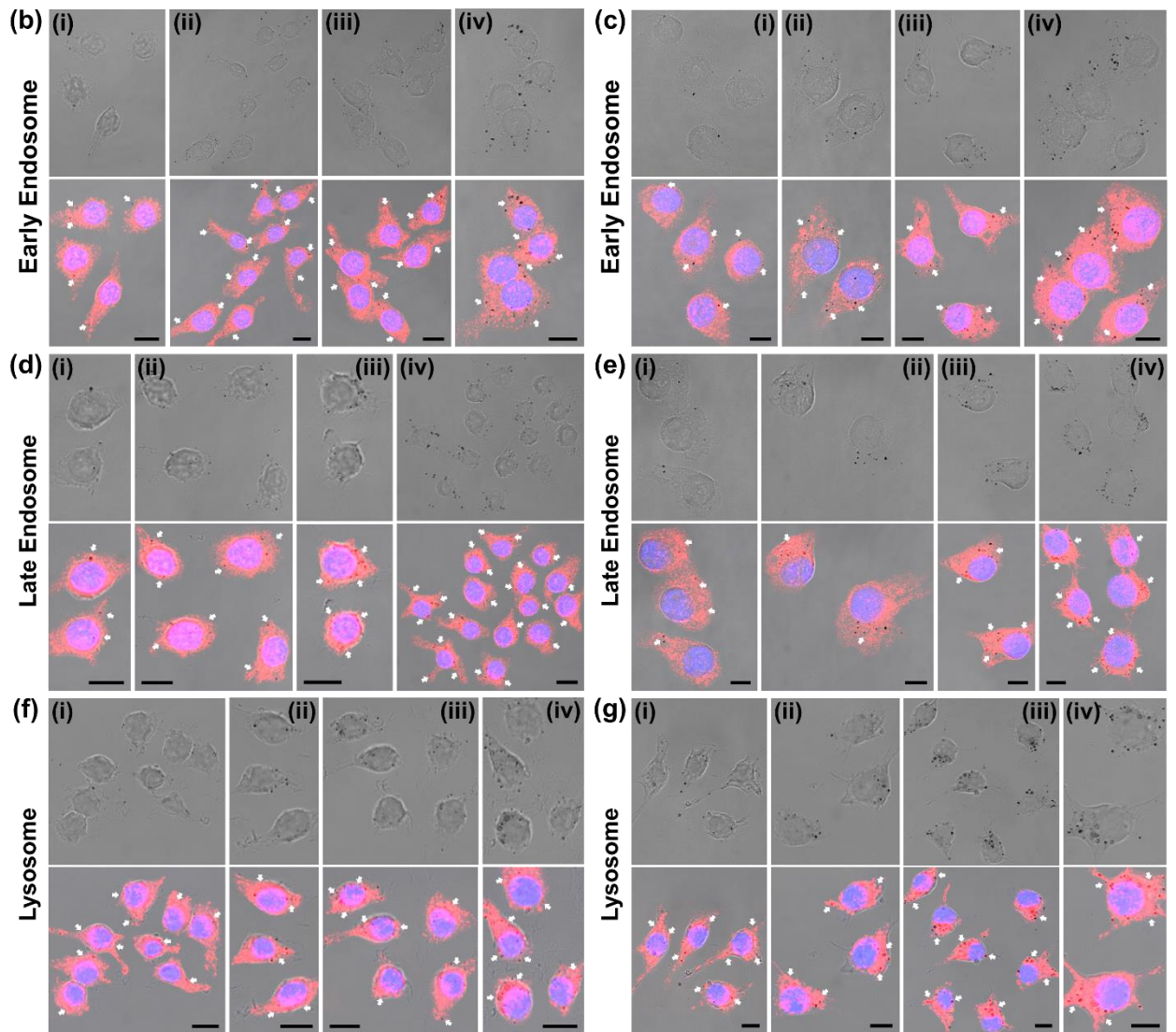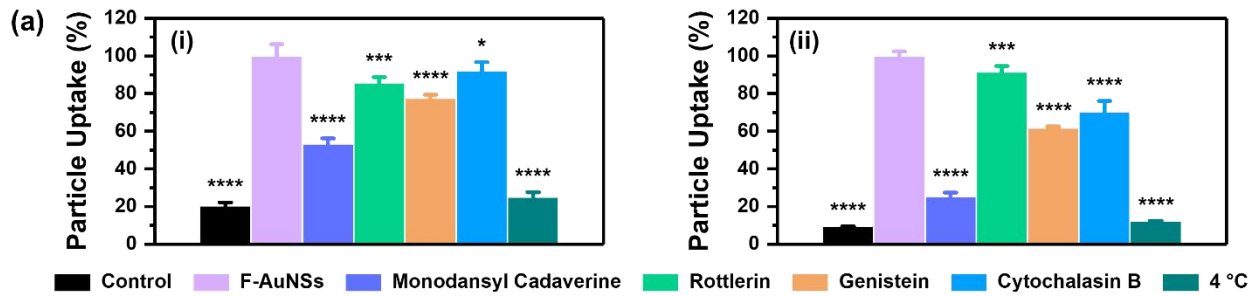
Figure 4.6 Intracellular trafficking of F-AuNSs *in vitro*. (a) Internalization of F-AuNSs in (i) RAW 264.7 and (ii) J774A.1 incubated with different inhibitors including monodansyl cadaverine (200 µM, 10 min) for clathrin-mediated endocytosis, rottlerin (2 µM, 30 min) for macropinocytosis, genistein (200 µM, 1 h) for caveolae-mediated endocytosis, cytochalasin B (10 µg/mL, 2 h) for phagocytosis and 4 °C (1 h) for all energy-dependent uptake pathways, respectively. Cells without F-AuNSs and without inhibitor are denoted as 'Control' (negative control) and incubated with only F-AuNSs but without any inhibitors at 37 °C are marked as 'F-AuNSs' (positive control). Here, data were presented as mean ± standard deviation (n = 4 per group and N = 2 independent experiments). * indicates $p < 0.05$, *** indicates $p < 0.001$, **** indicates $p < 0.0001$ *vs.* 'F-AuNSs' (positive control). Colocalization of F-AuNSs with (b, c) early endosome shown as red fluorescence for (i) 2, (ii) 4, (iii) 6 and (iv) 8 h, (d, e) late endosome shown as red fluorescence for (i) 2, (ii) 4, (iii) 6 and (iv) 8 h, and (f, g) lysosome shown as pseudo-colored red for (i) 4, (ii) 8, (iii) 18 and (iv) 24 h in RAW 264.7 and J774A.1, respectively. The nucleus in each cell was stained with DAPI (blue). Scale bar is 10 µm. White arrows point to particles. (h) Total number of F-AuNSs in 50 cells colocalized with early endosome, late endosome, and lysosome in (i) RAW 264.7 and (ii) J774A.1, respectively.

In vivo fate of NPs is ultimately controlled by their cellular-level endocytosis pathway, which is broadly described into clathrin-mediated endocytosis, macropinocytosis, caveolae-mediated endocytosis, and phagocytosis.[264-267] Briefly, (i) clathrin-mediated endocytosis dominates most receptor-ligand binding and traffics NPs from endosomes to lysosomes through clathrin-coated pits; (ii) macropinocytosis is a non-specific pathway and transports NPs to macropinosomes; (iii) caveolae-mediated endocytosis translocates NPs to Golgi apparatus or endoplasmic reticulum; and (iv) phagocytosis, the primary mechanism of engulfment by macrophages and other phagocytes, is initiated after protein corona formation and opsonization of NPs. Here, we assessed the uptake mechanism of F-AuNSs in two macrophage cell lines (RAW 264.7 and J774A.1) where cells were pre-incubated with different uptake inhibitors prior to incubating with F-AuNSs. Monodansyl cadaverine blocked transglutaminase 2, an enzyme required for receptor crosslinking in the region of clathrin-coated pits, and was used as an inhibitor for clathrin-mediated endocytosis.[268] Macropinocytosis was inhibited by rottlerin through filamentous actin modification or blocking of ruffle formation.[269] Genistein blocked caveolae-

mediated endocytosis by inhibiting a tyrosine kinase,[270] and cytochalasin B was used to inhibit

phagocytosis by disrupting actin polymerization.[271] Cells were also exposed to 4 °C but without

inhibitors to determine whether F-AuNSs uptake followed an energy-dependent process. MTT

cell viability assay indicated that inhibitors did not have toxic effect on cells at the concentrations

and incubation time used (Figure A.27). The uptake of F-AuNSs in the cells was then

quantitatively analyzed using flow cytometry after co-incubation with or without inhibitors.

Consistent with literature findings where gold NPs are primarily taken up by clathrin-mediated

pathway,[272] uptake of F-AuNSs was dominated by clathrin-mediated endocytosis in both cell lines

as well as followed energy-dependent internalization (Figure 4.6a). However, we found that other

pathways also contributed to F-AuNSs uptake in cells suggesting that unlike PEG coated NPs, the

characteristics of the surface ligands functionalized on F-AuNSs likely promoted their high *in vitro*

uptake *via* multiple intracellular pathways. We further investigated the longitudinal intracellular

trafficking of F-AuNSs in different cellular organelles including early endosomes, late-endosomes,

and lysosomes. Cells were incubated with F-AuNSs for 24 h followed by labeling with anti-EEA1

antibody and anti-RAB7 antibody for early and late endosome staining, respectively. F-AuNSs

co-localized with early endosome near the cellular membrane (Figure 4.6b,c) while with late

endosome F-AuNSs surrounded the nuclei (Figure 4.6d,e). Cells were also stained with a selective

lysosomal dye, BioTracker NIR 633, which revealed that colocalization of F-AuNSs with

lysosome primarily occurred around the perinuclear region suggesting that F-AuNSs were

eventually transported to lysosomes (Figure 4.6f,g). We also quantified the number of F-AuNSs

in 50 cells that were co-localized with each of these organelles in both macrophage cells lines as a

function of time (Figure 4.6h). Our longitudinal study revealed that F-AuNSs colocalized with

early endosomes within the first 4 h of incubation, then transported to late endosome occurred in

the 6 – 12 h regime followed by migration to lysosomes which peaked at ~12 h post incubation and remained steady till end of the study at 24 h. These compelling *in vitro* results supported our *in vivo* findings where F-AuNSs were observed in endosomal/lysosomal compartments in splenic macrophages and Kupffer cells in the liver.
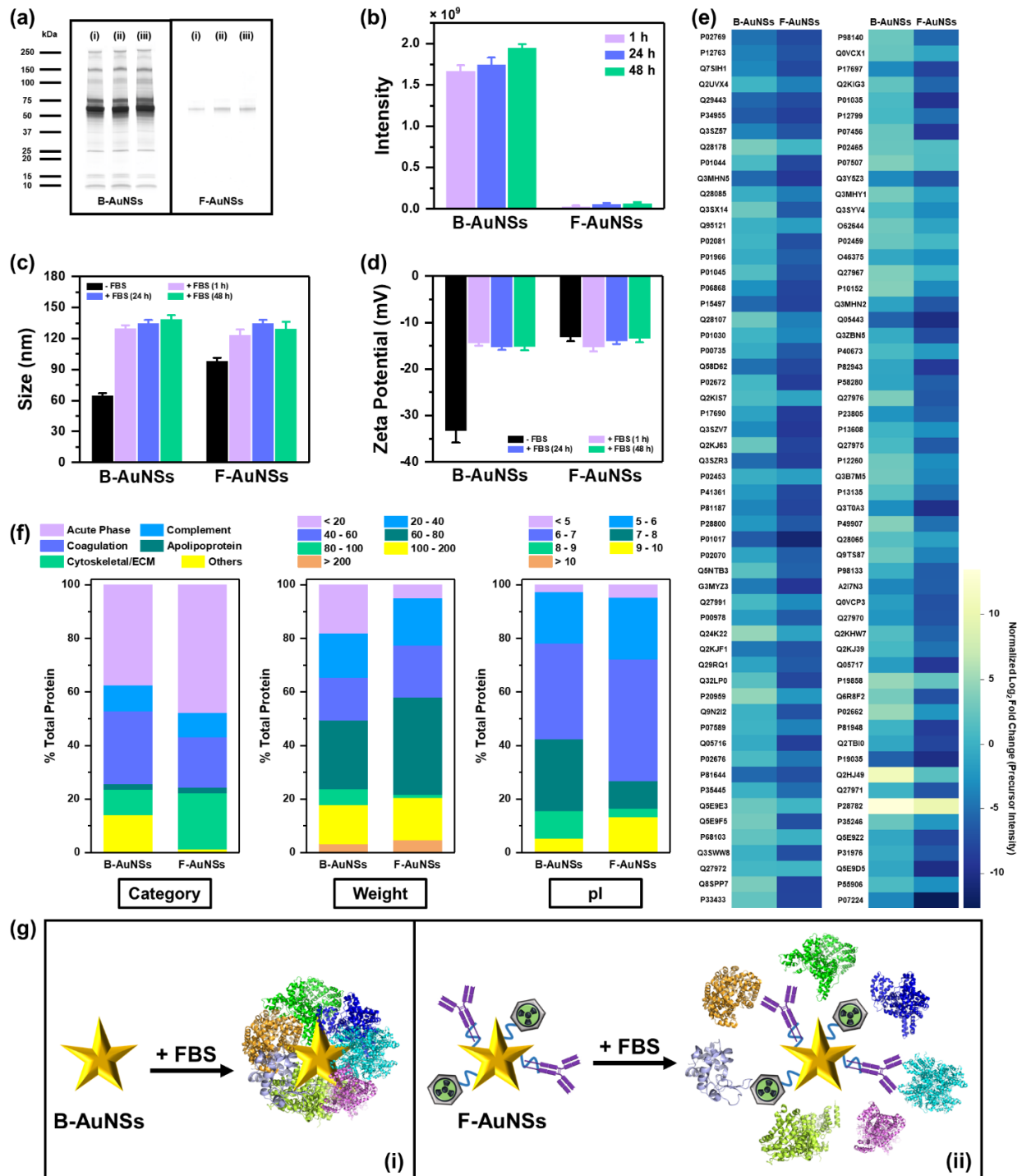
Figure 4.7 Proteomic study of surface protein corona. (a) B-AuNSs and F-AuNSs were treated with 60% FBS for (i) 1, (ii) 24 and (iii) 48 h and the amount of FBS immobilized on the surface of particles was determined by SDS-PAGE. (b) Quantification of band intensity. (c) Size and (d) surface charge analysis of B-AuNSs and F-AuNSs after treatment with 60% FBS for 1, 24 and 48 h. (e) Classification of protein corona components identified by quantitative LC-MS/MS. A total of 213 proteins were identified and the 112 most abundant proteins were used to make the heat map. (f) Proteins attached to each particle were classified by category, molecular weight (kDa) and pI. (g) Schematic representation of (i) B-AuNSs and (ii) F-AuNSs with FBS. Here, data were presented as mean ± standard deviation (n = 4).

It is well-established that proteins and other biomolecules in a biological milieu are readily adsorbed on the particle surfaces, forming a coating layer that is known as protein corona (PC). PC is currently recognized as the major factor in modulating particles' physicochemical properties and compromising their transport, targeting and cell uptake capabilities.[273,274] Previous studies have shown that the formation of PC on the particle surface can be regulated by modifying surface functionalization, which can enhance the colloidal stability and prolong the circulation time in blood by escaping from MPS clearance.[222,223,275] To confirm if the functionalization of AuNSs in our present study can reduce serum protein absorption, we first incubated B-AuNSs and F-AuNSs with 60% fetal bovine serum (FBS) for 1, 24 and 48 h at 37 °C followed by several centrifugation and washing steps to completely remove unbound proteins. We used sodium dodecyl sulfate polyacrylamide gel electrophoresis (SDS-PAGE) visualized by silver staining to confirm that no free proteins were detected in the supernatant at the last washing step (Figure A.28a-c). Proteins adsorbed on particles were then loaded into SDS-PAGE (Figure 4.7a) and negatively-charged B-AuNSs were found to adsorb a larger amount of protein than near neutrally-charged F-AuNSs, which was reinforced by the quantification of band intensities (Figure 4.7b). These results indicated that functionalization of AuNSs could reduce the interactions with serum proteins. Additionally, significant amounts of proteins were attached to particle surfaces even at 1 h suggesting that PC can be quickly formed. To further confirm the particle-protein interactions, the

physical characterizations were investigated by measuring hydrodynamic size and zeta potential. The treatment with FBS on B-AuNSs and F-AuNSs increased its size by ~105% and 30%, respectively (Figure 4.7c and A.28d,e). An increase in particle size after treatment demonstrated the large surface area adsorption of proteins on the particle surface. Zeta potential measurements revealed that anionic B-AuNSs changed surface charge from ~ -35 to -15 upon incubation with FBS, while F-AuNSs showed no significant differences after treatment confirming the decreased particle-protein interactions after functionalization (Figure 4.7d). We then investigated the composition of serum proteins adsorbed on each particle by using liquid chromatography tandem mass spectrometry (LC-MS/MS). A total of 213 proteins were identified and the 112 most abundant proteins were selected, plotted based on their normalized relative abundances on each particle and then represented *via* a heat map (Figure 4.7e). The LC-MS/MS results also demonstrated that F-AuNSs exhibited the lower tendency to be adsorbed by proteins. The identified proteins were further classified according to the protein classification, molecular weight, and isoelectric point (Figure 4.7f). It is noteworthy that F-AuNSs adsorbed significantly higher acute phase proteins and lower coagulation proteins than those on B-AuNSs. These results suggested that F-AuNSs can increase their blood circulation by decreasing the uptake from MPS and further confirmed our previous biodistribution results that the concentration of gold in the spleen and liver tended to rise over time to a maximum around 30 – 45 days. Additionally, significantly amounts of cytoskeletal and extracellular matrix (ECM) proteins were adsorbed onto F-AuNSs with respect to B-AuNSs. ECM proteins include fibrous proteins such as collagen and elastin, and glycoproteins such as fibronectin and laminins. Collagen and fibronectin are major components of ECM that regulate cell adhesion, proliferation, and migration. Previous literatures have demonstrated that nanoparticles pre-adsorbed with ECM proteins can enhance cell adhesion

and migration.[276] We therefore hypothesized that F-AuNSs would have more efficient intracellular uptake and delivery compared to that of B-AuNSs. We further classified surface-bound proteins according to their molecular weight (Figure 4.7f, middle panel). B-AuNSs with size of ~65 nm presented a strong affinity of proteins with MW < 20 kDa. Our result was in agreement with previous study on 40 nm AuNSs which showed a tendency toward interactions with low MW proteins.[71] We also observed a trend that F-AuNSs with a larger size (~95 nm) adsorbed a greater fraction of proteins with higher molecular weight consistent with many other results in the literature.[224] However, proteins with MW < 80 kDa contributed to 75 – 80% of the adsorbed proteins for both B-AuNSs and F-AuNSs. Lastly, classification of proteins based on isoelectric point (pI) showed that 58% and 74% of surface-bound proteins on B-AuNSs and F-AuNSs, respectively, had a negative charge where pI is <7 (Figure 4.7f, right panel). Both types of particles adsorbed mainly proteins with a pI between 6 and 7 (36% for B-AuNSs and 45% for F-AuNSs). However, B-AuNSs adsorbed ~three-fold proteins with a pI between 7 and 9 compared to F-AuNSs (37% *vs.* 13%), whereas F-AuNSs adsorbed ~three-fold proteins with a pI between 9 and 10 relative to B-AuNSs (13% *vs.* 5%). These results demonstrated that anionic B-AuNSs preferentially bound positively charged proteins, whereas near-neutral charged F-AuNSs were mainly adsorbed by negatively charged proteins. We hypothesized that protein absorption on particles was most likely driven by electrostatic interactions. All of the above results indicated that B-AuNSs had a greater tendency to be adsorbed by proteins relative to F-AuNSs (Figure 4.7g). Even though the overall protein adsorption was hindered by the functionalization of particles, PC cannot be fully suppressed, and a certain amount of serum proteins did adsorb on the surface of F-AuNSs. However, these adsorbed proteins on F-AuNSs extended particles' blood circulation and promoted intracellular uptake, consistent with our above long-term biodistribution results.
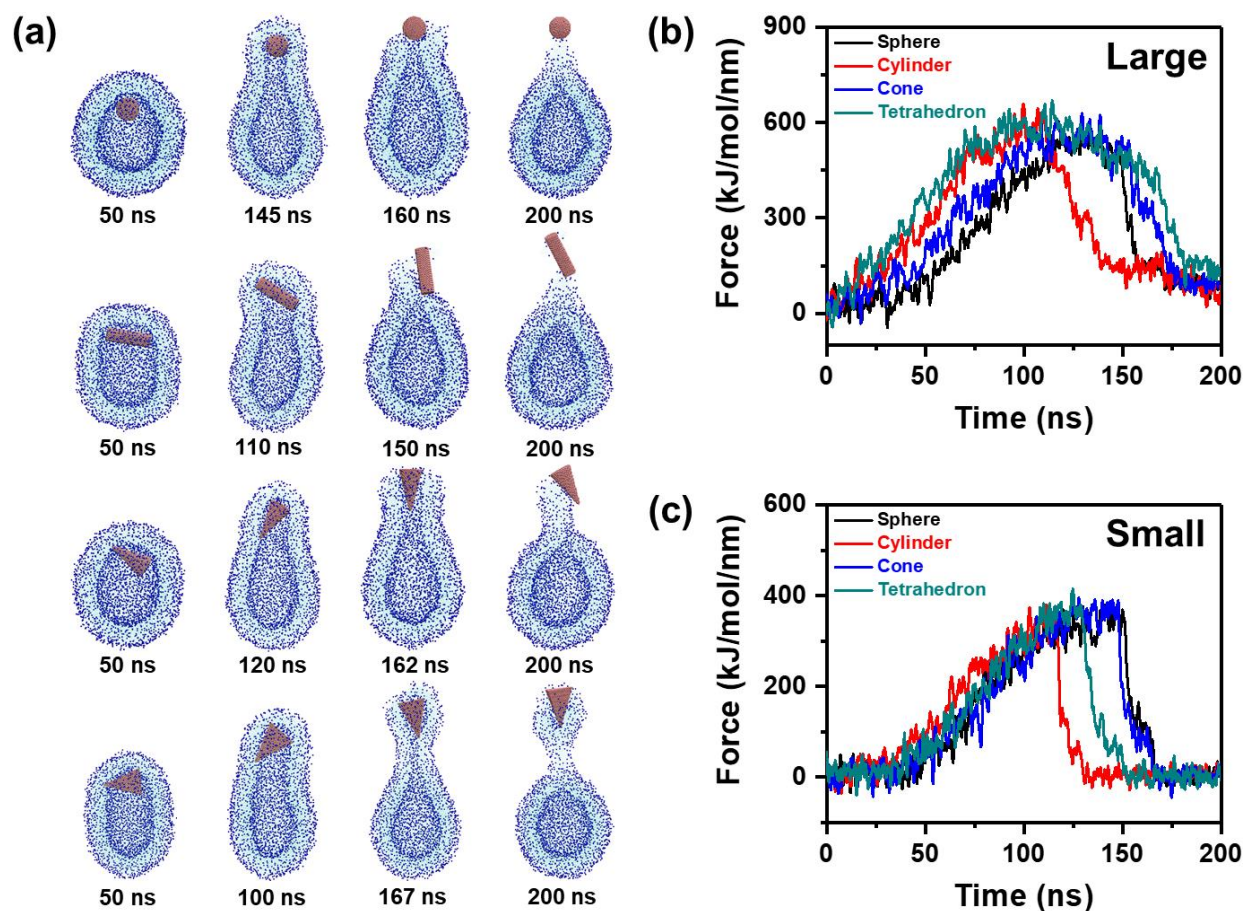
Figure 4.8 Effect of nanoparticle shape and size on exocytosis. (a) Snapshots of translocation of AuNPs (volume ≈ 35 nm^3) with varying shapes across the model DPPC lipid membranes for cellular exocytosis. The interaction force between (b) large- (volume ≈ 35 nm^3) or (c) small-sized (volume ≈ 4.5 nm^3) AuNPs with different shapes and membranes composed of DPPC lipid as a function of time.

Our previous studies have shown that F-AuNSs were degraded within cells before exocytosis (Figure 4.4, 4.5a and A.21-A.26). *In vivo* clearance of F-AuNSs was ultimately controlled by the physicochemical properties of the broken gold NPs (AuNPs), such as shape, size, and surface charge. To understand the translocation process of AuNPs, we have simulated the interaction between the AuNP and a lipid bilayer using the Martini coarse-grained (CG) method. Martini CG is one of the most common CG methods for studying membrane systems due to its easy-to-use building block principle. The Martini model is based on a four-to-one mapping

indicating that on average four heavy atoms and associated hydrogens are represented by one CG bead.[232] Nonbonded interactions between neutral beads of Martini are solely described by Lennard-Jones potentials, while charged beads also include Coulombic interactions.[277] The interaction strength of the Lennard-Jones potential allows for discrimination between different levels of polarity of the CG beads. This model features four main types of CG bead: polar (P), intermediately polar (N), nonpolar (C) and charged (Q).[277] By decreasing the degree of freedom of the system through atom grouping, the Martini CG model can be used to explore the interaction between AuNPs and the membrane at a longer simulation period in line with physiological phenomena.[278] We first evaluated the effect of shape on the translocation behavior of AuNPs. Four different shapes with equivalent volume (~ 35 nm^3) were included in the simulation, namely sphere, cylinder, cone and tetrahedron (Figure A.29, top row), as similar shapes were found in our previous TEM images (Figure 4.4, 4.5a and A.21-A.26). The model lipid membrane was composed of zwitterionic dipalmitoylphosphatidylcholine (DPPC), which represented the phospholipids in living cell membranes and had been employed in previous simulation studies.[279-281] To observe the exit patterns of NPs, an external force was applied to the center of mass of particle in the *z* direction. The representative snapshots of each shape are shown in Figure 4.8a. After contacting with AuNPs, the lipid bilayer protruded outward to accommodate the penetration and subsequently bended around the AuNPs. It is noteworthy that isotropic AuNPs (*e.g.*, sphere) showed no orientational dependence, while anisotropic AuNPs (*e.g.*, cylinder, cone and tetrahedral) reoriented with a flat side toward the membrane upon increased wrapping until the long axis was perpendicular to the membrane (Figure 4.8a and A.30). This reorientation was expected as less membrane deformation was induced and thus thermodynamically favorable, and has been reported previously.[282,283] The interaction force between the AuNP and membrane indicated that cylindrical

AuNPs were cleared faster compared to spherical ones followed by cones and tetrahedrons (Figure 4.8b). This result was expected as the locally flat part of cylindrical AuNPs rendered them to adhere to the membrane with small adhesion strengths in contrast to spheres.[282] The anisotropic structures examined all have flat faces but different surface areas. The surface area of each flat face in cylinder, cone and tetrahedron is 4.5, 12.5 and 13.0 nm^2, respectively. The increased translocation time of cone and tetrahedron compared to cylinder was likely due to the increased adhesion, bending and tension of membrane upon interaction with a larger flat face, consistent with previous observations in the literature.[284,285] Next, we studied the effect of size on the translocation behavior of AuNPs (Figure 4.8c). By comparing the maximum force between large- and small-sized AuNPs (600 *vs.* 400 kJ/mol/nm), we noticed that decreasing size generally decreased the physical difficulties for the AuNPs to translocate across the lipid membrane. This finding was not surprising as small-sized (~4.5 nm^3) AuNPs were able to roam freely through a pore and did not interact much with membrane, consistent with many other studies in the literature.[286,287] Further, before small-sized AuNPs penetrated the inner membrane, the curves of four different shapes were similar to each other, indicating that effect of shape was not significant during this period of time. Once small-sized AuNPs entered the lipid bilayer, the shape affected the reorientation of AuNPs and membrane deformation, which ultimately led to different translocation behaviors. In our simulation, cylindrical AuNPs exited membrane faster than tetrahedrons followed by spheres and cones.
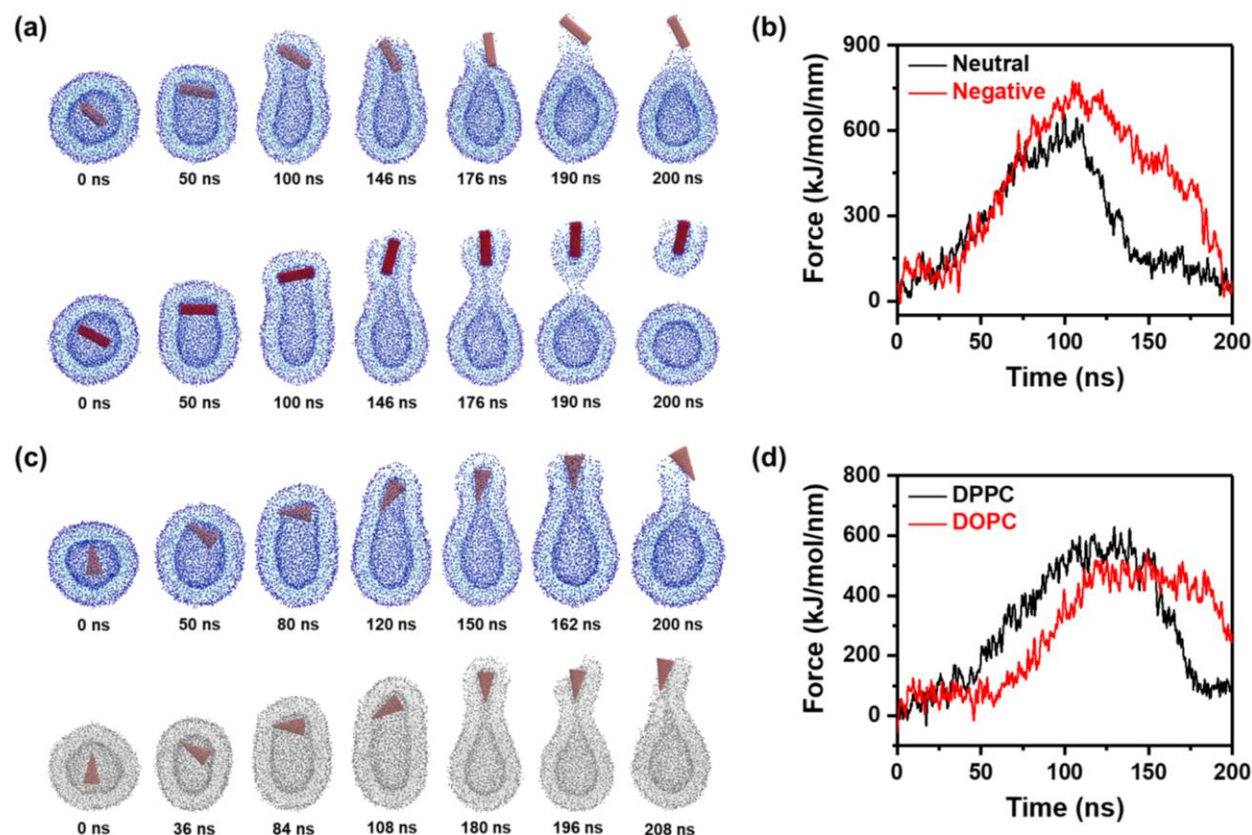
Figure 4.9 Effect of nanoparticle surface charge and lipid composition on exocytosis. (a) Snapshots of translocation of neutral (top row) or negatively-charged (bottom row) AuNPs across the model cell membranes composed of DPPC lipids for cellular exocytosis. (b) The interaction force between the neutral or negatively-charged AuNPs and DPPC membranes as a function of time. (c) Snapshots of translocation of neutral-charged AuNPs across the cell membranes composed of DPPC (top row) or DOPC (bottom row) lipids. (d) The interaction force between the neutral-charged AuNPs and membranes composed of DPPC or DOPC as a function of time.

The breakdown of intact and functionalized F-AuNSs not only generated particles with varying shape and size, but also affected their surface properties, especially the surface charge of AuNPs. In our previous results, F-AuNSs showed a near-neutral surface charge, while bare AuNSs were negatively charged (Figure 4.1e). To evaluate the effect of AuNP surface charge, we performed simulations of 35 nm^3 cylindrical AuNPs featuring neutral and anionic surface charges. The negatively-charged AuNPs were constructed by an inert gold core and an anionic gold shell. The snapshots showed that both neutral and anionic AuNPs proceeded through a laying-down-

then-standing-up sequence (Figure 4.9a). But a small neck was created when the long axis of anionic NP was perpendicular to the membrane (t = 176 ns). Subsequently, a defect in the neck was created (t = 190 ns) resulting in the separation of the bent membrane covered around the anionic AuNPs from the main vesicle. Shortly afterwards, the membrane rupture was healed, and two membranes started to separate (t = 200 ns). In contrast to the anionic AuNPs, neutral AuNPs bypassed the bilayer directly without forming a membrane-bound vesicle. Further, the anionic AuNPs showed higher interaction force with the membrane (*e.g.*, 750 *vs.* 600 kJ/mol/nm for the anionic and neutral AuNPs, respectively) and slower translocation compared to the neutral AuNPs (Figure 4.9b), consistent with previous literature findings.[286,287] This result was expected as the anionic AuNPs had low membrane adhesion and thus was energetically less favorable. In addition to surface charge evaluation, we further examined the effect of lipid type in the simulation. This study is important as it is well-known that different tissues exhibit specific lipid compositions,[288] which could potentially explain our previous results that the breakdown and clearance of AuNPs in the liver was much slower than the spleen. Here, we compared the translocation of neutral-charged cone-shaped AuNPs (35 nm^3) across the membrane composed of either DPPC or dioleoylphosphatidylcholine (DOPC). The zwitterionic DOPC lipid has slightly higher molecular weight compared to DPPC and contains two double bonds on the fatty acid lipid tails (Figure A.31). The snapshots and interaction force (Figure 4.9c,d) both demonstrated that the AuNPs translocated the DOPC membrane slower than that of DPPC. We hypothesized that the soft DOPC rendered longer time for the long axis of AuNPs to orientate from the parallel to perpendicular direction. Further, the maximum interaction force between the AuNPs and DOPC was lower compared to that of DPPC (*e.g.*, 500 *vs.* 600 kJ/mol/nm). These results indicated that the stiffness of membrane had a significant impact on the AuNP translocation. Collectively, our simulations demonstrated

106

that the exocytosis of AuNPs depended on the physicochemical properties of AuNPs and the lipid composition of membrane.

4.5 Conclusions

In summary, this work addresses a critical need in evaluating toxicity and ultimate fate of F-AuNSs. Here, we performed the long-term (90 days) toxicity studies by evaluating *in vitro* viability and cell cycle studies and *in vivo* inflammatory responses and histopathological changes. Our findings demonstrated high biocompatibility of F-AuNSs both *in vitro* and *in vivo*. We also evaluated the untargeted biodistribution of F-AuNSs through (a) PET imaging, (b) gamma counts of ^{64}Cu radiolabeled F-AuNSs, (c) TEM and (d) ICP-MS analysis of gold in tissues as a function of delivery route and period of time. Primarily we showed that the delivery route greatly affected the F-AuNS accumulation in tissues within the first 24 h post injection and confirmed the long-term presence (90 days) of F-AuNSs in tissues. Further, we assessed the impact of cellular uptake and protein corona effect on the breakdown of F-AuNSs within tissues. We found that clathrin-mediated endocytosis was a major pathway for F-AuNSs uptake, but other pathways also contributed, indicating that the degradation of F-AuNSs was likely due to acidic environments in endosomes or lysosomes. Additionally, F-AuNSs were able to significantly reduce protein adsorption compared to bare AuNSs, implying the importance of physicochemical properties on minimizing the protein corona effect. Finally, the breakdown of F-AuNSs indicated that exocytosis of F-AuNSs was a function of the shape, size, and surface properties of the broken AuNPs. Our Martini coarse-grained simulations suggested that both physicochemical properties of AuNPs and the lipid composition of membrane affected the clearance. Whereas this work demonstrated the *in vivo* studies in mice, our future work focuses on the utility of large animals to

107

understand the toxicity and ultimate fate of NPs. We envision that this study will provide a great guidance for researchers to determine aspects needed to be considered when evaluating the biocompatibility of NPs.

Chapter 5

CONCLUSIONS AND FUTURE OUTLOOKS

5.1 Conclusions

With the emergence of advanced molecular profiling approaches, the heterogeneous landscape of various diseases can now be accurately measured revealing that the "one-size fits all" approach to treatment is ineffective in understanding the complex pathophysiology of diseases. Personalized medicine driven by each patient's unique molecular, physiological, and behavioral characteristics has led to a paradigm shift. Yet, the biggest bottleneck to personalized medicine is the accurate and rapid detection of targeted biomarkers that represent each disease model. Biomarker screening can accelerate clinical decisions and improve therapeutic outcomes by *a priori* predicting patients who will respond to treatment and those who will require alternative therapies. This dissertation describes the development of novel biomarker detection platforms, which were designed to revolutionize the accessibility of personalized medicine.

In chapter 2, we performed label-free RS to probe metabolic reprograming in breast cancer cells and evaluated treatment response to potent and clinically approved SMIs by examining alterations in metabolites. Our findings demonstrated that RS combined with multivariate analysis presented a powerful platform with tremendous clinical significance differentiating BC cells that were responsive to SMIs as a function of dosage, drug type, and cell type. Findings with RS were verified with MS, a workhorse in metabolomics, by examining various oncometabolites. Primarily we showed that triple-negative MDA-MB-231 BC cells were responsive to Trametinib, an inhibitor of the ERK pathway, and nonresponsive to Alpelisib, an inhibitor of the mTOR pathway, supported by a collective change in DNA, membrane phospholipids, amino acids, lipids, and fatty acids. We also demonstrated that ER-positive MCF-7 BC cells were resistant to Trametinib with

minimal changes in metabolites and no classification among treatment groups as seen in PCA. Our results suggested that these oncometabolites represented an important hallmark of cancer that can be targeted to both treat cancer and understand resistance mechanisms.

In chapter 3, we presented an innovative biodiagnostic platform, PRADA, demonstrating multiplexed detection of two biomarkers of myocardial infarction, cTnI and NPY, in a simple microfluidic device. We achieved an LOD of 0.0055 and 0.12 ng/mL for cTnI and NPY in patient serum, respectively. We showed that PRADA can be regenerated and reused where the same microfluidic chip can be recycled for ~14 cycles with minimal signal loss between cycles. Reusability of PRADA also allowed to archive samples for future bioanalysis. Finally, we validated the clinical significance of PRADA by evaluating cTnI in cardiac patient serum of various demographics and achieved an LOQ of ≥ 0.03 ng/mL at 10% CV which was higher than many troponin immunoassays published in the literature, and comparable to commercial assays. We envision low-cost PRADA will have tremendous translational impact and amenable to resource-limited settings for accurate treatment planning in patients.

In chapter 4, we evaluated the long-term (90 days) toxicity and ultimate fate of F-AuNSs. By examining *in vitro* viability and cell cycle studies and *in vivo* inflammatory responses and histopathological changes, we demonstrated high biocompatibility of F-AuNSs both *in vitro* and *in vivo*. We also performed the untargeted biodistribution of F-AuNSs through (a) PET imaging, (b) gamma counts of ^{64}Cu radiolabeled F-AuNSs, (c) TEM and (d) ICP-MS analysis of gold in tissues as a function of delivery route and period of time. Primarily we showed that the delivery route greatly affected the F-AuNS accumulation in tissues within the first 24 h post injection and confirmed the long-term presence (90 days) of F-AuNSs in tissues. Further, we assessed the impact of cellular uptake and protein corona effect on the breakdown of F-AuNSs within tissues.

We found that clathrin-mediated endocytosis was a major pathway for F-AuNSs uptake, but other pathways also contributed, indicating that the degradation of F-AuNSs was likely due to acidic environments in endosomes or lysosomes. Additionally, F-AuNSs were able to significantly reduce protein adsorption compared to bare AuNSs, implying the importance of physicochemical properties on minimizing the protein corona effect. Finally, the breakdown of F-AuNSs indicated that exocytosis was a function of the shape, size, and surface properties of the broken AuNPs. Our Martini coarse-grained simulations suggested that both physicochemical properties of AuNPs and the lipid composition of membrane affected the clearance. This in-depth study highlights the tremendous translational potential of F-AuNSs and provides a great guidance for researchers to determine aspects needed to be considered when evaluating the biocompatibility of NPs.

5.2 Future Outlooks

Significant future work is motivated and promised by the results presented in this dissertation. In chapter 2, we demonstrated the utility of RS to explore metabolic alterations in two-dimensional (2D) tumor cells. Two-dimensional culture plays a vital role in the biomedical research but has many limitations. The main limitation is that 2D cultures grown as a monolayer on flat and rigid surfaces do not adequately take into account the actual microenvironments harbored within a tumor including interactions between cells and extracellular matrix (ECM).[289] Three-dimensional (3D) cultures have gained tremendous attention due to their evident advantages in providing more accurate depiction of physiological conditions and more predictive data for *in vivo* studies.[290] The additional dimensionality of 3D cultures induces physical constraints to cells and affects the spatial interactions with surrounding cells. Through affecting the signal transduction from the outside to inside of cells, genetic expression and cellular behaviors are

ultimately changed in 3D cultures. Further, PCA was applied to differentiate different treatment groups in this work. PCA is a well-established method for dimensionality reduction of datasets but minimizes information loss.[291] Despite attractive features associated with PCA, the covariance matrix is difficult to be evaluated in an accurate manner with large datasets.[291] Computing the covariance of large datasets is also expensive, which requires $O(nd^2)$ operations when diagonalizing the covariance matrix of n vectors in a space of d dimensions where n and d could be several thousands. Deep learning algorithms which extract complicated data features at high levels of confidence through a hierarchical learning process are promising alternatives.[292] Extensive studies have shown that deep learning algorithms are superior when dealing with learning from large unsupervised datasets in a greedy layer-wise fashion[293] and thus have great potentials to be utilized in recognizing cellular drug responses upon treatment. Finally, we employed RS to identify metabolic changes. However, Raman signals are intrinsically weak that may result in low signal to noise ratios and increase difficulties in data analysis.[44] SERS that exploits the metallic NPs to enhance Raman signals at least $9 - 10$ orders of magnitude is a powerful tool providing sensitive, selective and non-destructive information.[45] Therefore, looking into the future, the potential of RS in cancer research can be further exploited. The Raman fingerprints nondestructively revealing metabolic profiles in 3D organoids or *in vivo* models can uncover the molecular basis of the disease and enable rapid drug screening ensuring the most effective treatment is provided at the earliest time point. Specifically, we envision that in the near future, hyperspectral Raman images will be decomposed into several images showing the spatial distribution and abundance of biomolecules in cells and tissues, which will play vital roles in medicine, ranging from 3D mapping of small molecules in cells to studying diseases in tissues (computational histology). Advances in deep learning algorithms can decompose the overall

spectrum within each pixel into the signatures of different molecules and accelerate spectral processing and data interpretation, especially in a large and high-dimensional clinical dataset. Further, significant improvements in fiber optics, detectors and handheld spectrometer would also help RS accessible for clinical translation. Therefore, we anticipate that RS will continue to receive attention in future as a promising tool to assess metabolomics.

In chapter 3, we demonstrated the use of PRADA for simultaneous detection of two biomarkers through SERS in a simple microfluidic platform. The future work will focus on the detection of >10 biomarkers in biofluids. To achieve this goal, a quantitative method for selecting Raman tags that have minimal prominent peak overlapping needs to be developed. Evaluating the overlap of Raman tags using a correlation matrix calculated from SERS spectra is a great way to first screen and select potential candidates. Deep learning algorithms are then applied to determine the optimal ratio of each Raman tag that can achieve minimal signal overlapping. Further, detecting multiple biomarkers requires a more sophisticated microfluidic design incorporating an efficient mixing system, as poor mixing results in the formation and inhomogeneity of the hot spot distribution on the magnetic beads and then leads to site-dependent results. Lastly, we validated PRADA with limited patient samples. However, most commercially available assays examine >1000 patients to establish their quantification.[210] The LOQ of PRADA will significantly improve in a future cohort study where more patient samples will be collected to exemplify the translational impact of this platform. Even though there is still much work to be done before PRADA can be commercialized and implemented in practice, this platform holds a high potential for on-field and cost-effective applications. The footprint and the costs of PRADA can be substantially reduced thanks to the continuous development of miniaturized and fiber-based Raman apparatus. Further, moving from small-scale and clean-room based fabrication towards large-scale or *in situ* synthesis

of reliable substrates will promote a wide range of applications of this platform. Bulky syringe pumps could also be replaced with small units or by self-acting capillary forces. Additionally, the combination of SERS with microfluidic devices yields more reproducible results for the quantitative measurement of analytes at the low concentrations, which is a crucial breakthrough for SERS because it overcomes the difficulties related to the experimental conditions, such as the degree of aggregation, the different sizes of metal colloids, and inhomogeneous distributions of molecules on the metal surface. With extensive and on-going efforts, more techniques will promote the development of this area. We believe that the interests in applying SERS combining lab-on-a-chip technique in diagnosis will be constantly growing in the near future.

The unique characteristics of AuNPs have rendered them to be used in a variety of applications. However, these unique features are postulated to be the major contributors for NP-induced toxicity which arises from the complicated interplay between particle characteristics (*e.g.*, shape, size, charge and surface property), the route of administration and biological environment. In chapter 4, we examined the toxicity, untargeted biodistribution and ultimate fate of functionalized AuNSs in mice. The mouse model has long served as the preferred species for biomedical applications due to their small size, ease of maintenance, relatively short life span and well-characterized genotypes.[294] Although mouse studies provide invaluable information about the biodistribution and toxicity of nanoparticles, results obtained in mice may have limited translatability to human physiology. Large animals serve as a good alternative because of their better anatomical, physiological and genetic similarity to humans and allowance of repeated sampling from the same animal.[295] To meet the regulatory requirements, currently the wealth of toxicity studies of NPs have been conducted in the field. However, we must treat and compare toxicity results from different studies with caution because of the inherent discrepancies found

114

amongst toxicity study with respect to different NP formulations. Therefore, a unifying protocol for the toxicological profiling of NPs is inevitably needed in order to achieve reliable outcomes that have realistic implications for the human usage of NPs.
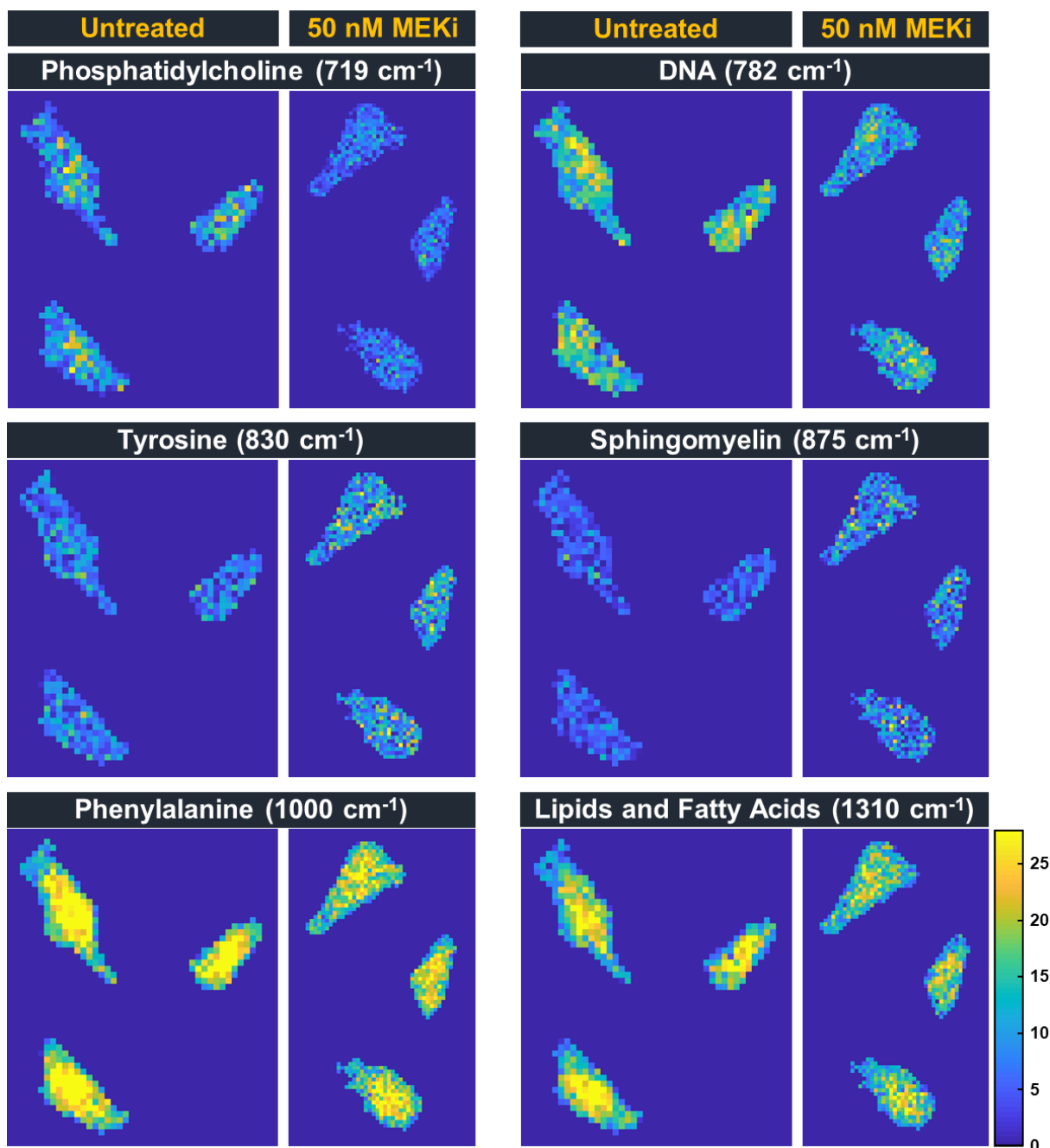
Figure A.1 Representative Raman spatial maps of untreated MDA-MB-231 cells and those treated with MEKi (Trametinib, 50 nM) shown at 719 cm^{-1} (phosphatidylcholine), 782 cm^{-1} (DNA), 830 cm^{-1} (tyrosine), 875 cm^{-1} (sphingomyelin), 1000 cm^{-1} (phenylalanine) and 1310 cm^{-1} (lipids and fatty acids). The corresponding spectra and quantification of these peaks before and after treatment were shown in Figure 2.2a,c in the main text. Raman intensity decreased post-treatment at 719, 782, 1000, and 1310 cm^{-1}, but increased post-treatment at 830, and 875 cm^{-1}.
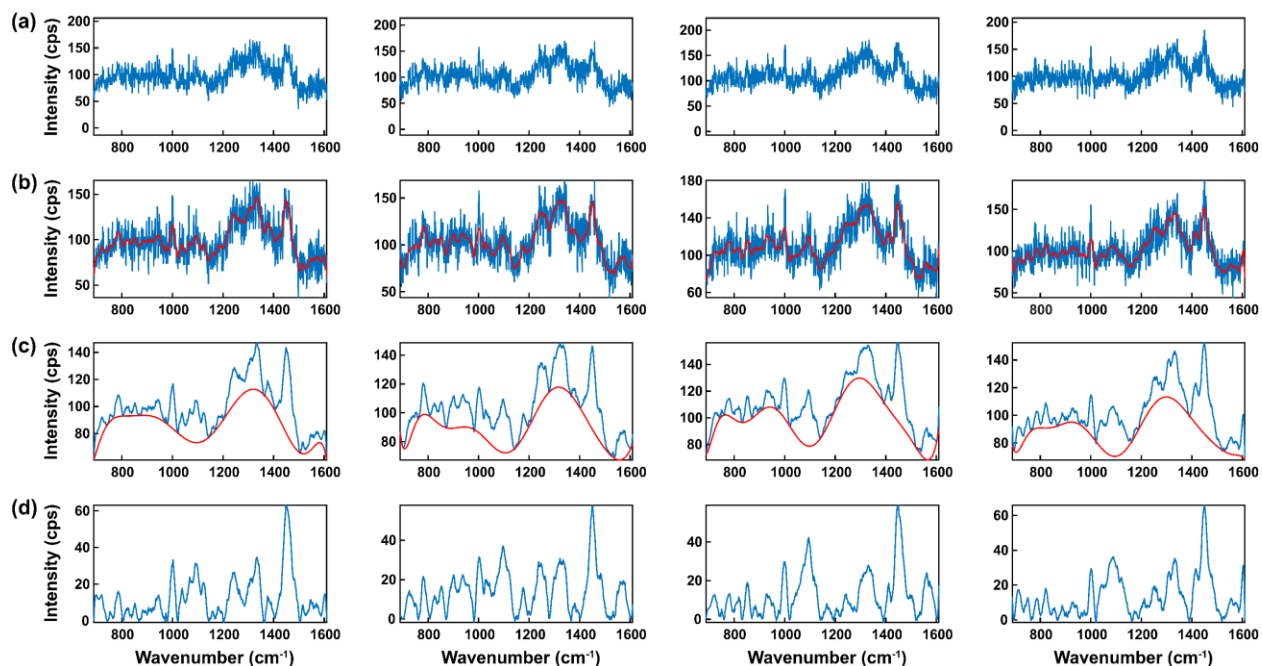
Figure A.2 Examples of individual spectrum for the Raman map acquired from each MDA-MB-231 cell. (a) Representative raw Raman spectra. (b) The raw spectra were smoothed (Savitzsky-Golay, fifth-order polynomial, 47 points). (c) The spectra were then baseline corrected (11th-order polynomial, 0.0001 threshold). (d) The spectra after smoothing and baseline correction.
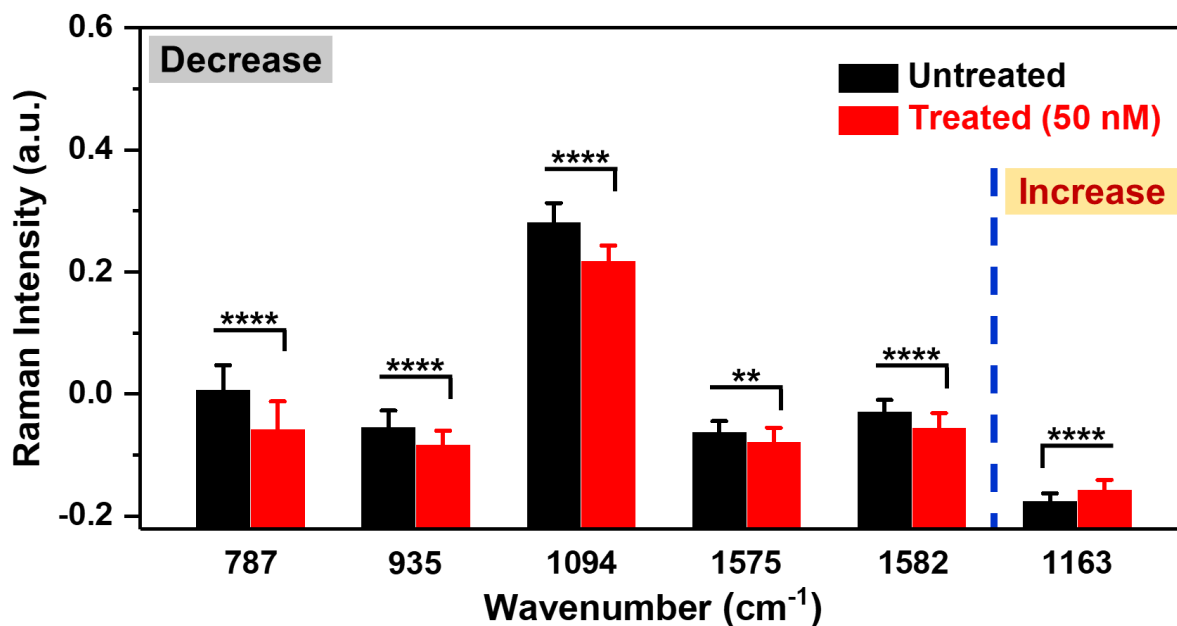
Figure A.3 MDA-MB-231 cells treated with Trametinib and probed with RS. Selective Raman peaks that decreased with treatment including phosphatidylserine (787 cm^{-1}), proteins and amino acids (935 cm^{-1}), DNA (1094 and 1575 cm^{-1}) and phenylalanine (1582 cm^{-1}). Selective Raman peak that increased after treatment including tyrosine (1163 cm^{-1}). Here, ** indicates $p < 0.01$ and **** indicates $p < 0.0001$ determined by student's t-test.
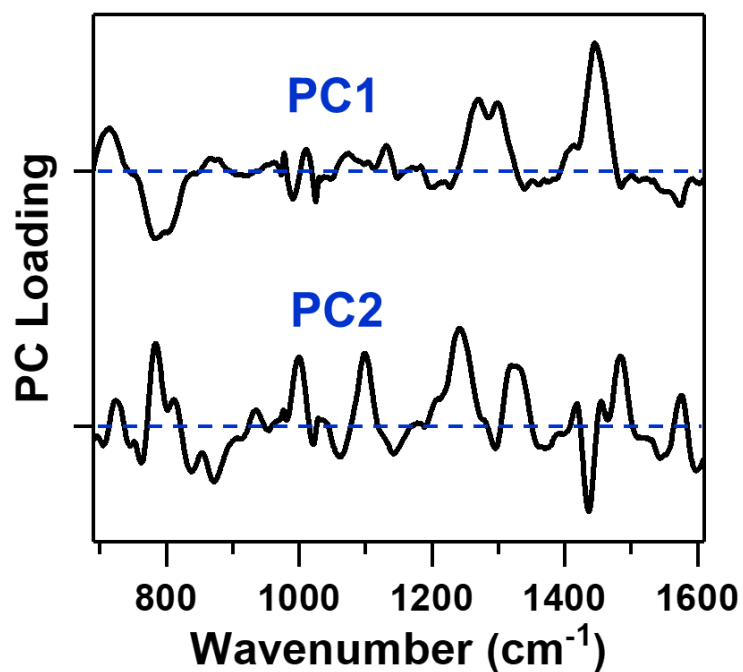
Figure A.4 PC loading of MDA-MB-231 cells treated with various concentrations of Trametinib (1, 50 and 300 nM) relative to untreated cells. The corresponding PC scatter plot is shown in Figure 2.3b. The features in both PC1 and PC2 generally correlated well to the PC loading shown in Figure 2.2e that is the simplest case only comparing untreated cells to those treated with Trametinib at its working concentration (50 nM).
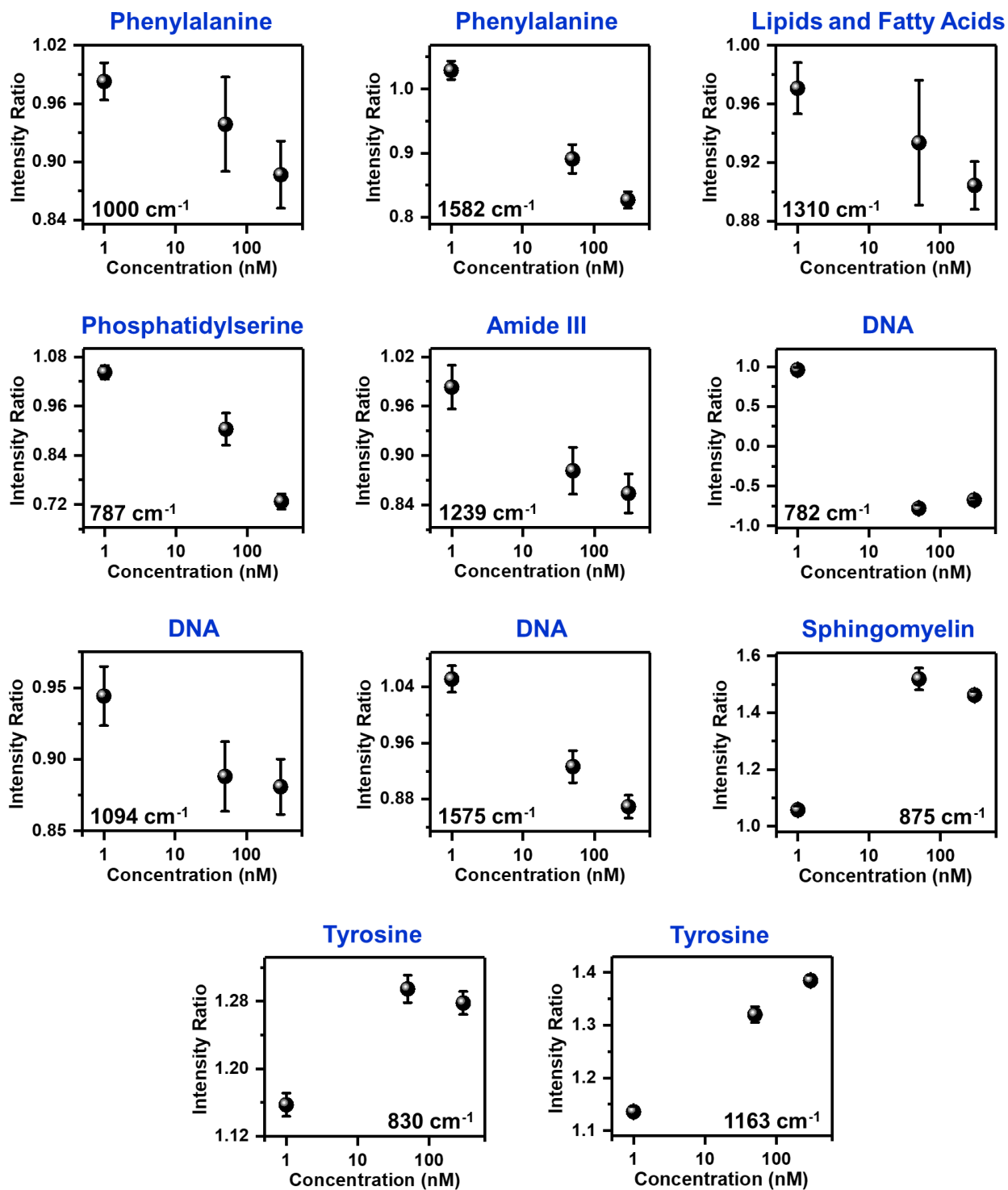
Figure A.5 Ratiometric analysis of metabolites by examining changes in Raman footprint when MDA-MB-231 cells were treated with various concentrations of Trametinib (1, 50 and 300 nM) compared with untreated cells. Several metabolites decreased and some increased post-treatment.
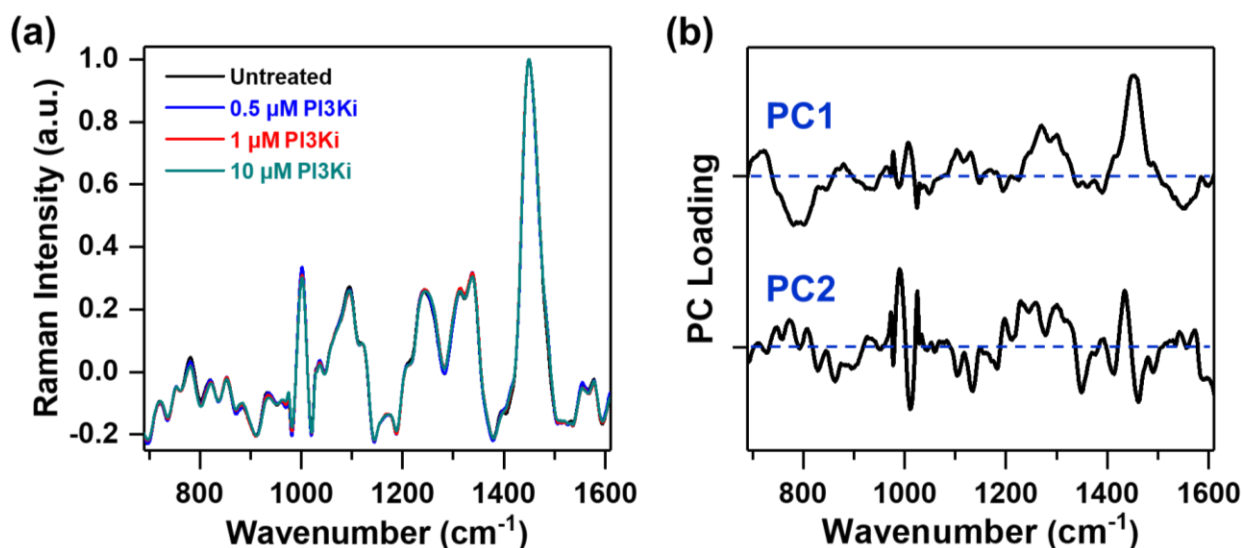
Figure A.6 MDA-MB-231 cells treated with Alpelisib and interrogated with RS. (a) Mean normalized Raman spectra of untreated MDA-MB-231 cells and those treated with various concentrations (0.5, 1 and 10 μM) of PI3Ki (Alpelisib). Spectra were normalized to 1440 cm^{-1} biological peak. (b) PC loading of MDA-MB-231 cells treated with various concentrations of Alpelisib relative to untreated cells. The corresponding PC scatter plot is shown in Figure 2.4a.
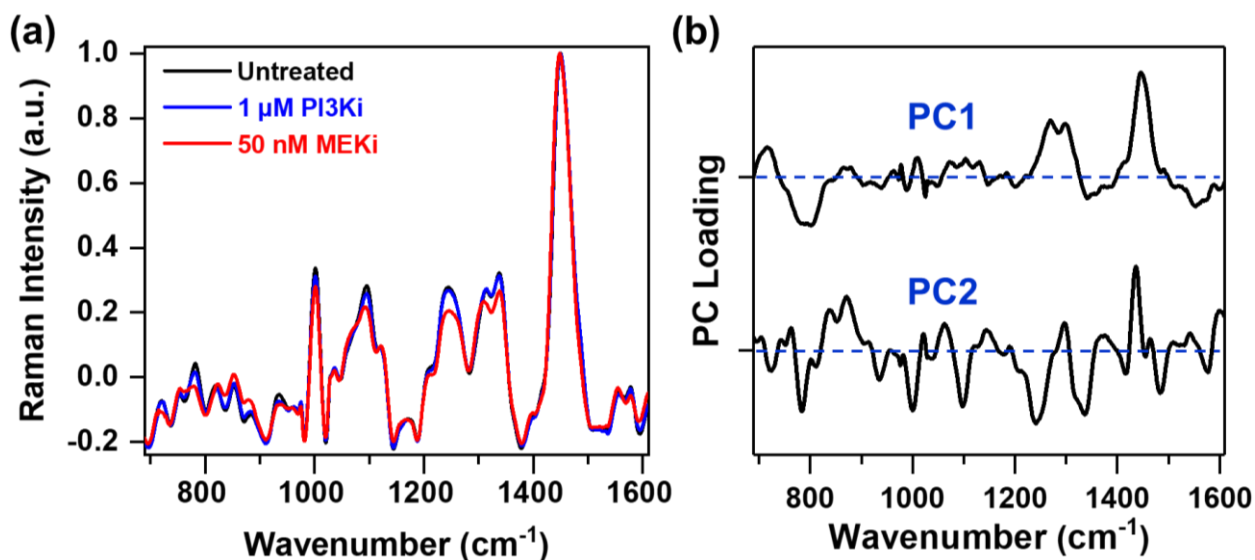
Figure A.7 RS distinguishing responders from nonresponders as a function of drug type. (a) Mean normalized Raman spectra of untreated MDA-MB-231 cells and those treated with MEKi (Trametinib) or PI3Ki (Alpelisib). Spectra were normalized to 1440 cm^{-1} biological peak. (b) PC loading of MDA-MB-231 cells treated with MEKi (Trametinib) or PI3Ki (Alpelisib) relative to untreated cells. The corresponding PC scatter plot is shown in Figure 2.4b.
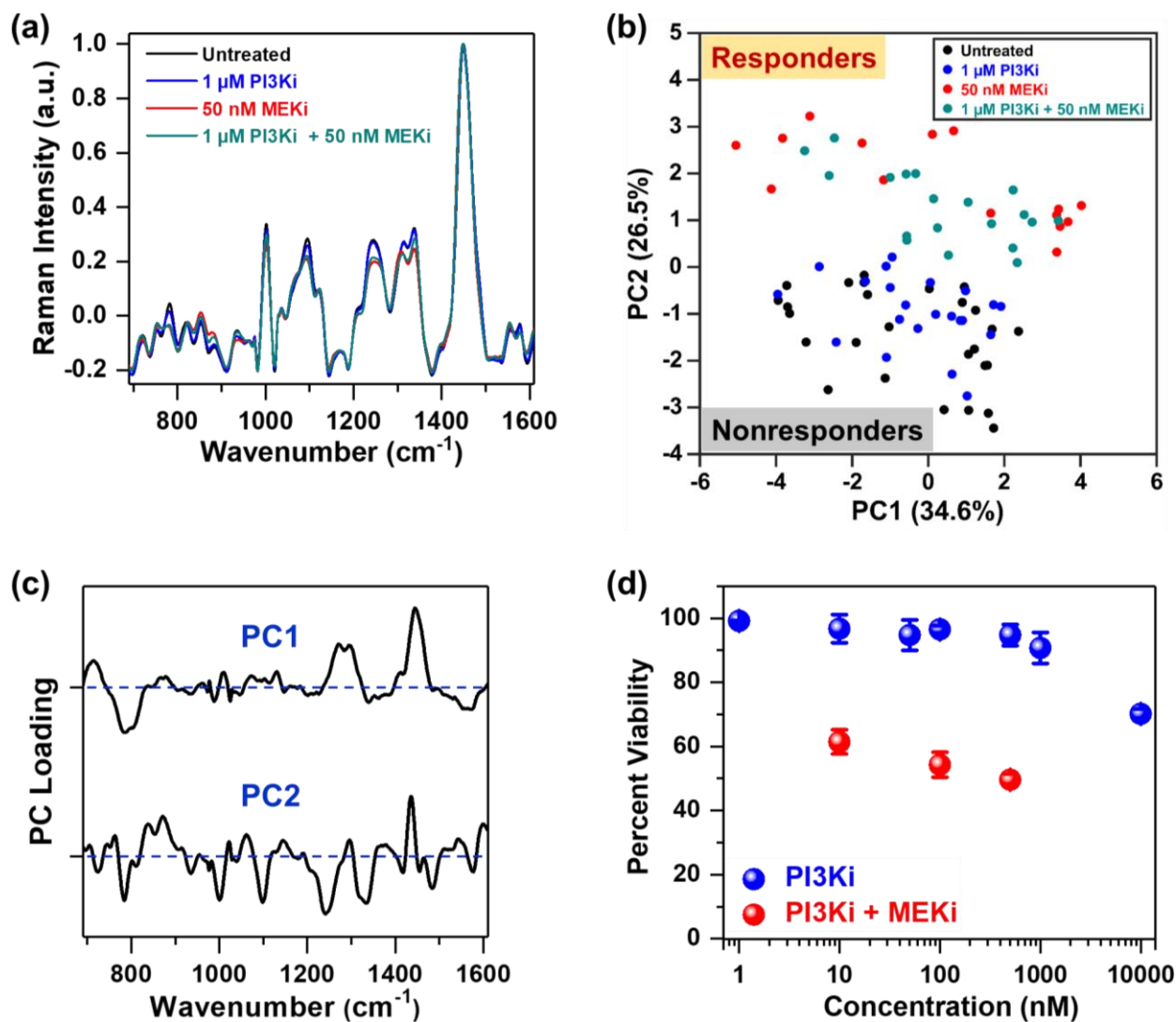
Figure A.8 Comparison of MDA-MB-231 cells treated with mono- or combination therapy. (a) Mean normalized Raman spectra of untreated cells (black) and cells treated with PI3Ki (Alpelisib, 1 μM, blue), MEKi (Trametinib, 50 nM, red), and combination treatment (1 μM PI3Ki + 50 nM MEKi, cyan). Spectra were normalized to 1440 cm^{-1} biological peak. (b) Corresponding PCA scatter plot. Clear clustering of cells was observed for cells that were responsive to treatment *vs.* nonresponsive. (c) PC loading of (b). (d) Cell viability assay comparing cells treated with PI3Ki (Alpelisib) at various concentrations, relative to combination treatment where the concentration of Trametinib was kept constant at 50 nM and that of Alpelisib was varied (10, 100 and 500 nM, n = 4 for each concentration). Cell viability was measured by a plate reader at 540 nm. All data were presented as mean ± standard deviation.

We investigated the impact of combinatorial treatment combining MEKi (Trametinib) and PI3Ki (Alpelisib) due to the strong evidence of convergence and crosstalk between the

PI3K/AKT/mTOR and Ras/Raf/MEK/ERK pathways that control oncogenic signaling.[296,297] Numerous clinical trials (NCT01347866, NCT01337765, NCT01390818, *etc.*) are currently underway to investigate the feasibility and efficacy of MEK and PI3K dual inhibition. We observed that the responders were differentiated from nonresponders in PCA where the cells treated with combination treatment clustered with those treated with Trametinib alone. The cells in the combination treatment groups did not differentiate from the monotherapy group. These observations implied that further experiments would be necessary with RS and MS to explore the complex changes in metabolic pathways after combination treatment. Further, PCA may not be sufficient in assessing results from combination treatments, and more advanced machine learning algorithms may be necessary.[166]
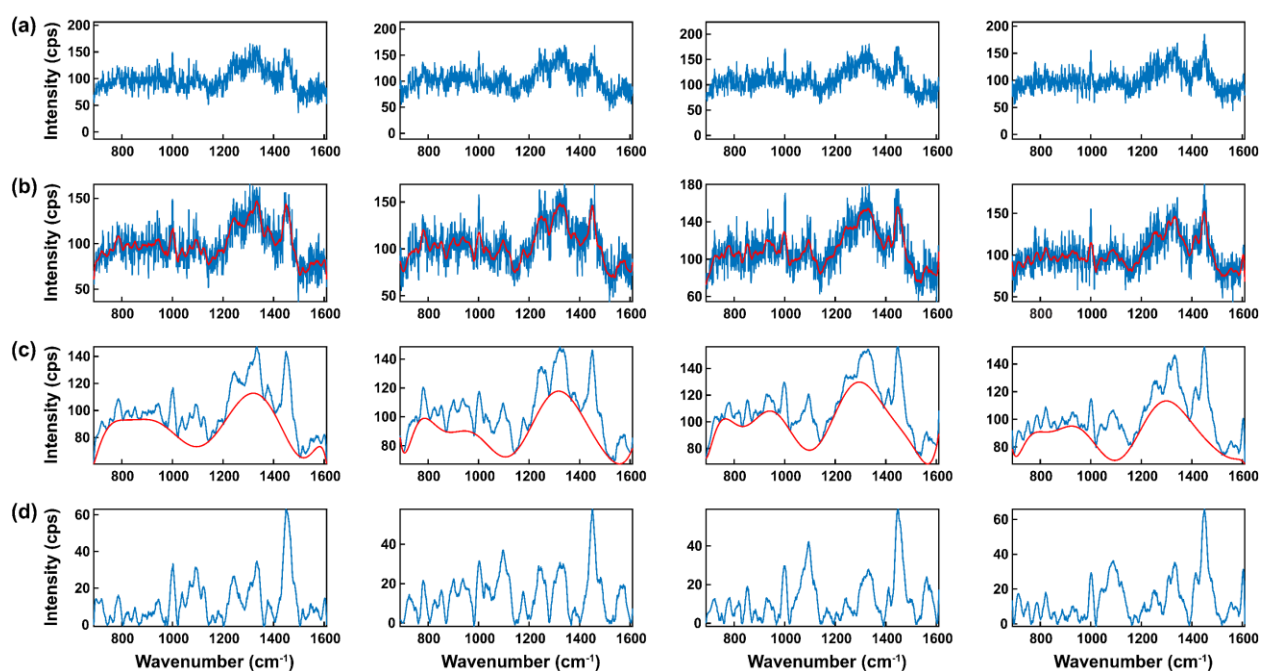
Figure A.9 Examples of individual spectrum for the Raman map acquired from each MCF-7 cell. (a) Representative raw Raman spectra. (b) The raw spectra were smoothed (Savitzsky-Golay, fifth-order polynomial, 47 points). (c) The spectra were then baseline corrected (11th-order polynomial, 0.0001 threshold). (d) The spectra after smoothing and baseline correction.
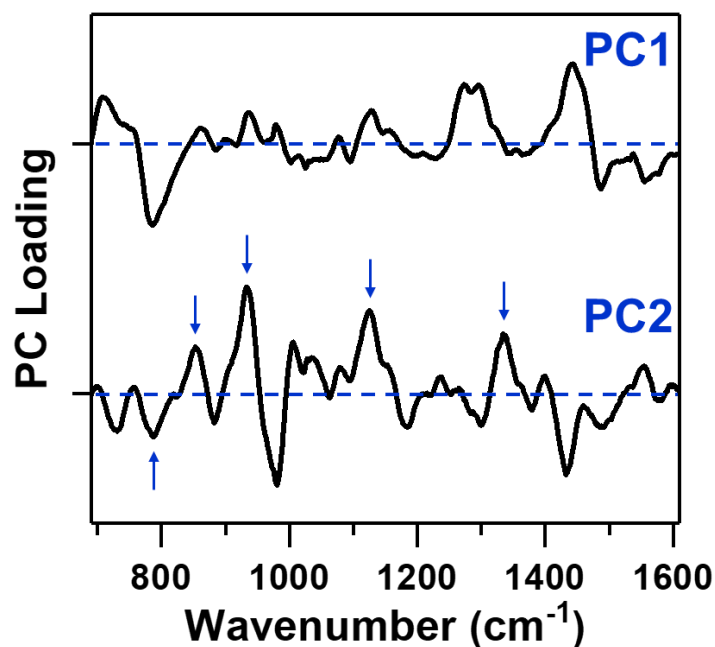
Figure A.10 PC loading of MCF-7 cells treated with various concentrations of MEKi (Trametinib) relative to untreated cells. The corresponding PC scatter plot is shown in Figure 2.6b.
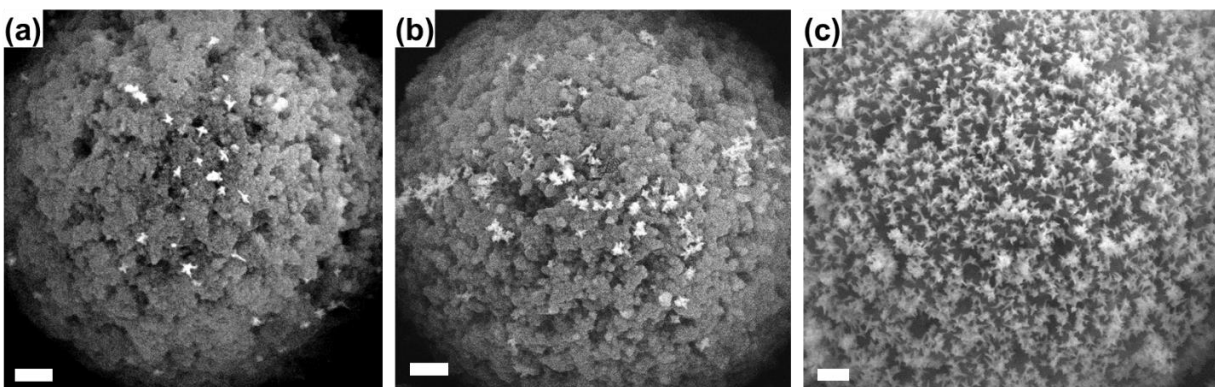
Figure A.11 Concentration-dependent SEM micrographs showing the complete immunocomplexes with magnetic bead capture probes + antigens + peptide coated AuNS-SERS barcode detection probes. Images are shown at (a) low (1 ng/mL), (b) medium (50 ng/mL), and (c) high (3000 ng/mL) concentration of cTnI. Scale bar is 200 nm in a – c.
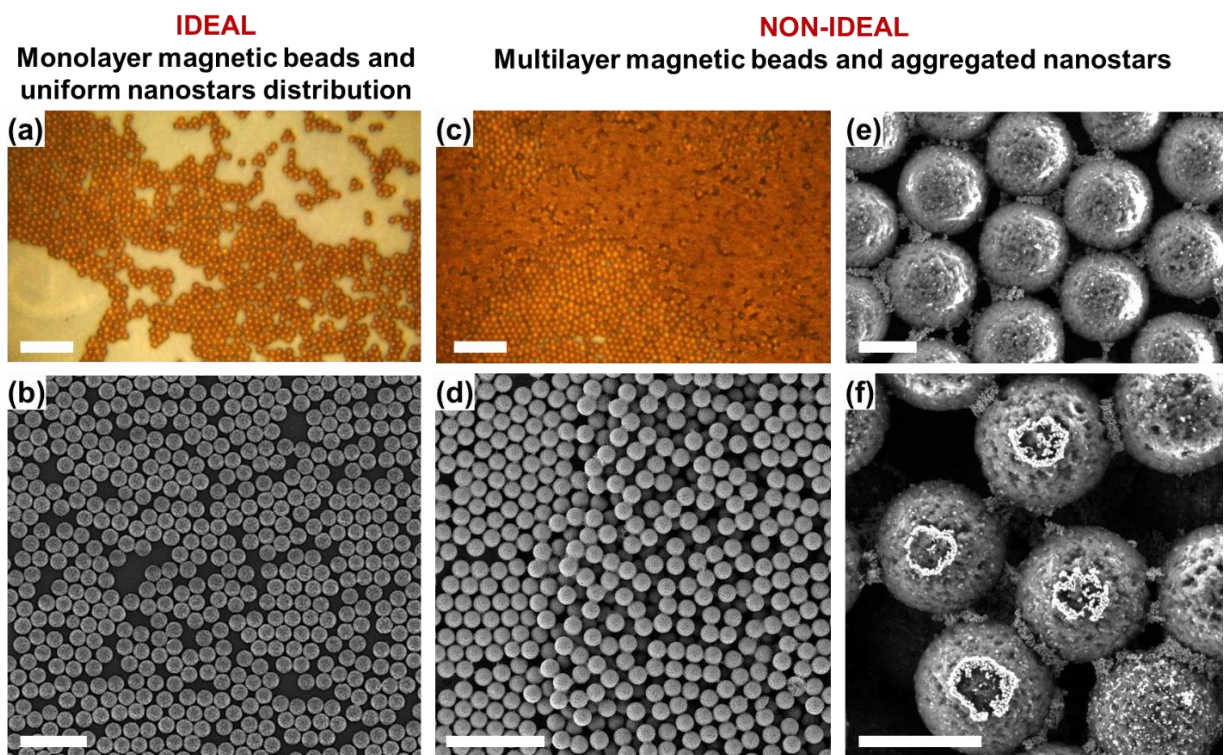
Figure A.12 Raman images, and SEM micrographs to showcase the (a,b) ideal conditions and (c-f) non-ideal conditions to perform PRADA. (a,b) PRADA was optimized to consistently generate ideal conditions with monolayers of magnetic beads and uniform distribution of nanostars resulting in highly reproducible results (also see Figure 3.3c-e). SERS measurements were not performed if prepared samples were non-ideal to minimize hot-spots and irreproducible results. Non-ideal conditions include (c,d) multilayers of magnetic beads and (e,f) non-uniform aggregated nanostars on beads. Scale bar is 20 µm in (a) and (c), 10 µm in (b) and (d), and 1 µm in (e) and (f).

Table A.1 Fitting parameters for the sensitivity curve of cTnI and NPY.

	cTnI	**NPY**
x_0	5.495×10^{24}	2.884×10^{16}
y_0	402.7	861.5
a	1.766×10^6	2.483×10^6
b	0.122	0.222
R^2	0.995	0.996

The sensitivity curve of cTnI and NPY in the quantification region was fitted using the 4PL function given below.

$$y = y_0 + \frac{a}{1 + \left(\frac{x_0}{x}\right)^b}$$

Table A.2 Calculations for limit of detection (LOD) of cTnI and NPY.

	cTnI	NPY
Mean$_{blank}$	796.82	766.29
SD$_{blank}$	95.77	97.72
LOB = Mean$_{blank}$ + 1.645 (SD$_{blank}$)	954.37	927.05
SD$_{lowest\ concentration\ sample}$	224.04	171.42
LOD (Intensity, cps) = LOB + 1.645 (SD$_{lowest\ concentration\ sample}$)	1322.92	1209.02
LOD (Concentration, ng/mL)	0.0055	0.12
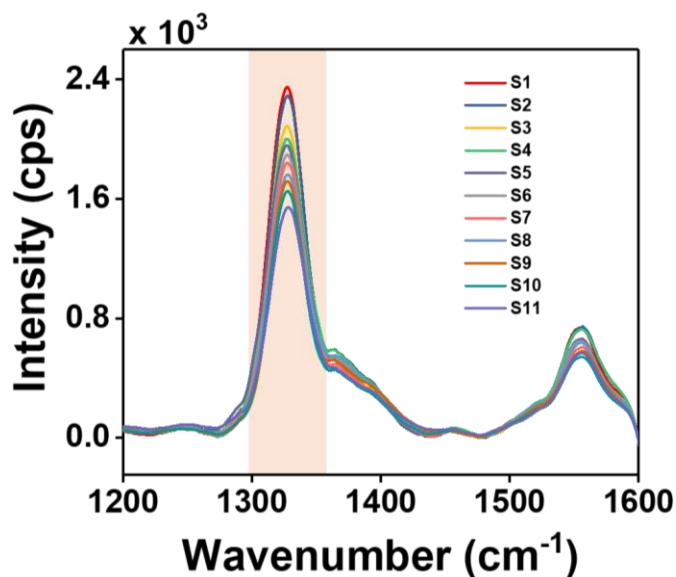
Figure A.13 SERS spectra of cTnI detection for 11 different patient samples using PRADA. All other patient information is shown in Figure 3.6a.

Table A.3 Passing-Bablok regression analysis of cTnI detection for the 11 patient samples.

Regression equation	y = -0.01134 + 0.9601 × x
Systematic differences	
Intercept A	-0.01134
95% CI	-0.02534 to 0.01475
Proportional differences	
Slope B	0.9601
95% CI	0.8850 to 1.0777
Linear model validity	No significant deviation from linearity (P = 1.00)

Table A.4 Comparison of analytical sensitivity parameters at 10% coefficient variation of PRADA and other cardiac troponin immunoassays recently published in the literature, and commercially available. *SPR*, Surface Plasmon Resonance; *LSPR*, Localized Surface Plasmon Resonance; *SERS*, Surface Enhanced Raman Spectroscopy; *CV*, Cyclic voltammetry; *EIS*, electrochemical impedance spectroscopy; *ELISA*, Enzyme-linked Immunosorbent Assay.

Platform	LOD (ng/mL)	LOQ (ng/mL)	Multiplexing	Ref./Manufacturer
SPR	0.50	N/A	No	Ref.[298]
LSPR	0.035	N/A	No	Ref.[193]
SERS	0.034	N/A	No	Ref.[299]
CV/EIS	0.024	N/A	No	Ref.[300]
CV	0.024	N/A	No	Ref.[97]
PRADA	**0.0055**	**0.032**	**Yes**	**This work**
ELISA	0.1	N/A	No	ThermoFisher[301]
Luminex	0.069	N/A	Yes	MilliporeSigma[302]
ARCHITECT STAT	0.010	0.050	No	Abbott[210]
ELECSYS	0.0050	0.012	No	Roche[303]
ADVIA Centaur	0.0022	0.0027	No	Siemens[304]
AIA	0.0021	0.031	No	Tosoh Bioscience[305]
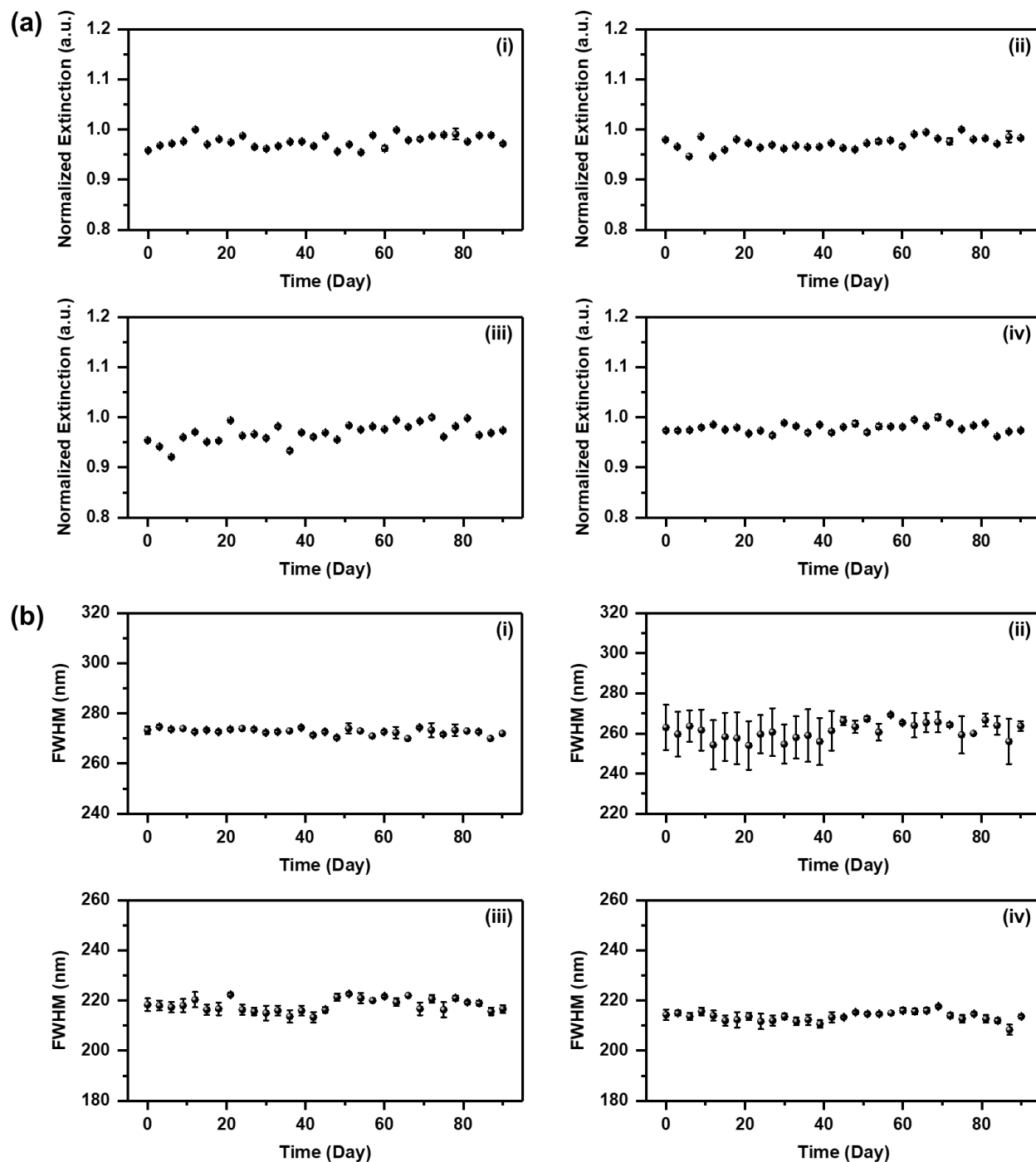
Figure A.14 Stability and shelf-life of F-AuNSs. Aliquots of concentrated F-AuNSs were dispersed in (i) water, (ii) PBS, (iii) media and (iv) media supplemented with serum. (a) Normalized extinction and (b) FWHM were measured every three days over 90 days. F-AuNSs were stored at 4 °C between measurements. All data were presented as mean ± standard deviation (n = 3). As observed, the successful functionalization with stable ligands resulted in high stability of F-AuNSs for three months.
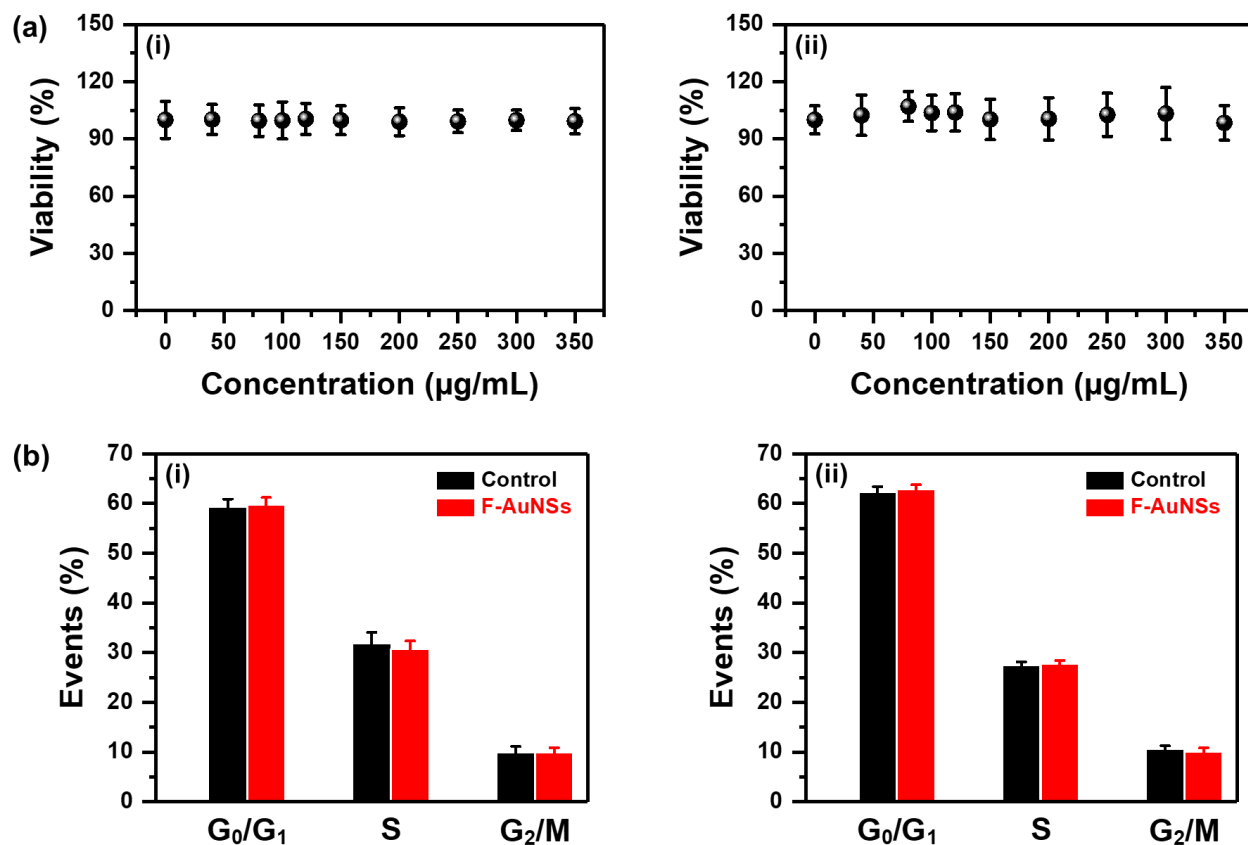
Figure A.15 Toxicity evaluation of F-AuNSs *in vitro*. (a) MTT cell viability assay of (i) RAW 264.7 and (ii) J774A.1 cells incubated for 24 h with F-AuNSs at 0 – 350 µg/mL concentrations (n = 5 per concentration and N = 3 independent experiments). Cell viability was measured at 540 nm. All data were presented as mean ± standard deviation. (b) Cell cycle analysis of (i) RAW 264.7 and (ii) J774A.1 cells upon incubation with F-AuNSs (100 µg/mL) for 24 h. No significant changes were observed in the different cell cycle phases compared to control cells that did not receive F-AuNSs in both macrophage cell lines. All data were presented as mean ± standard deviation (n = 6 per group and N = 3 independent experiments).
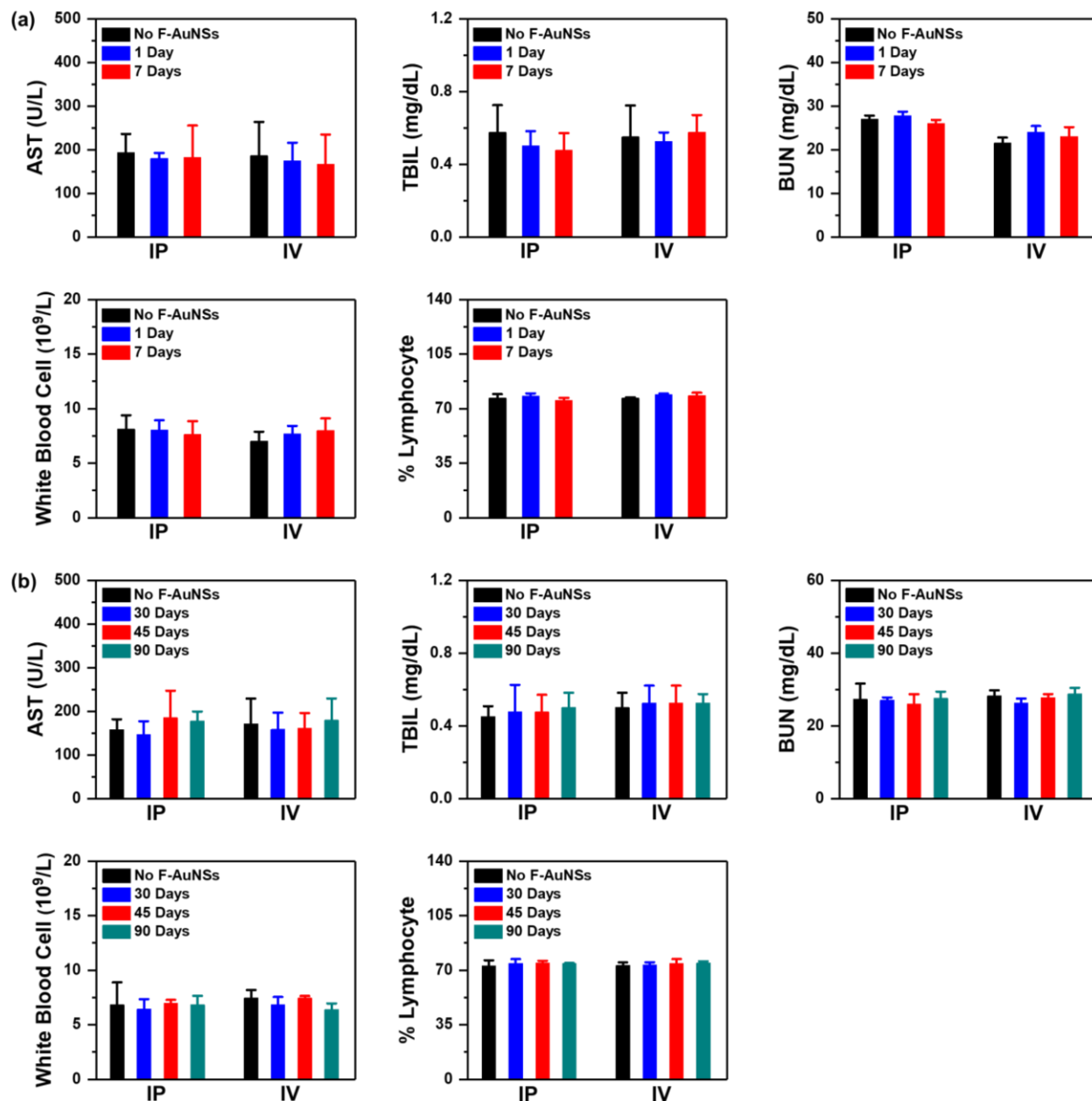
Figure A.16 Toxicity evaluation of F-AuNSs *in vivo*. Serum inflammatory markers and complete blood count of mice that received F-AuNSs intraperitoneally (IP) and intravenously (IV) were compared to control mice which received PBS. (a) Short-term measurements include 1- and 7-days post-delivery. (b) Long-term measurements include 30-, 45- and 90-days post-injection. Independent of the route of delivery, no significant abnormalities in hepatic, renal and hematological functions were observed, indicating F-AuNSs had high biocompatibility and minimal toxicity. Data were presented as mean ± standard deviation (n = 4).
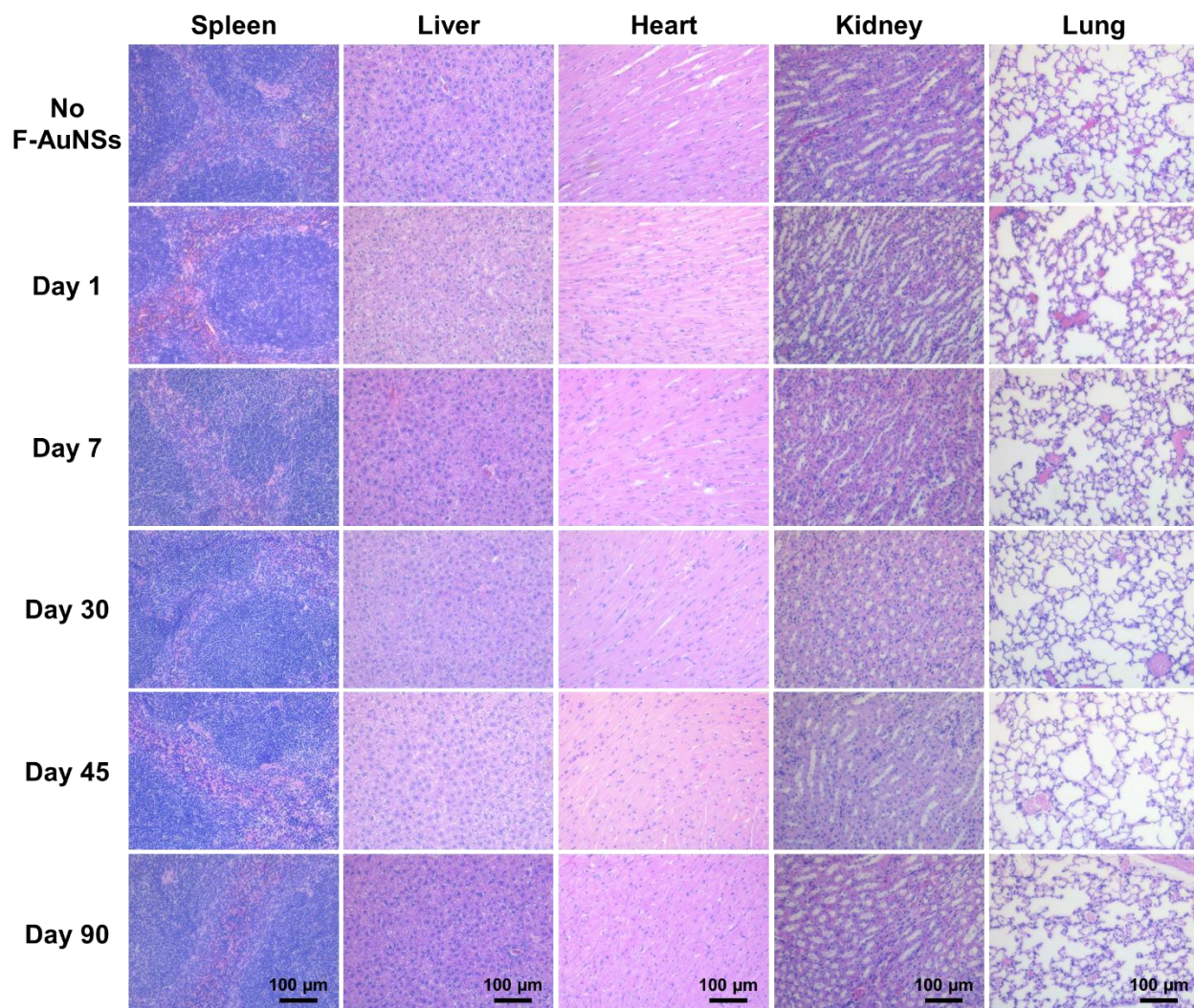
Figure A.17 H&E stain of major organs post IP delivery of F-AuNSs in healthy C57BL/6 mice. Spleen, liver, heart, kidney, and lung of mice were retrieved to evaluate toxicity of F-AuNSs. Histological evaluation of tissues showed minimal toxicity by F-AuNSs up to 90 days post IP administration. Here, "No F-AuNSs" control group represents organs of mice that received PBS only. Histology was performed on n = 3 mice.
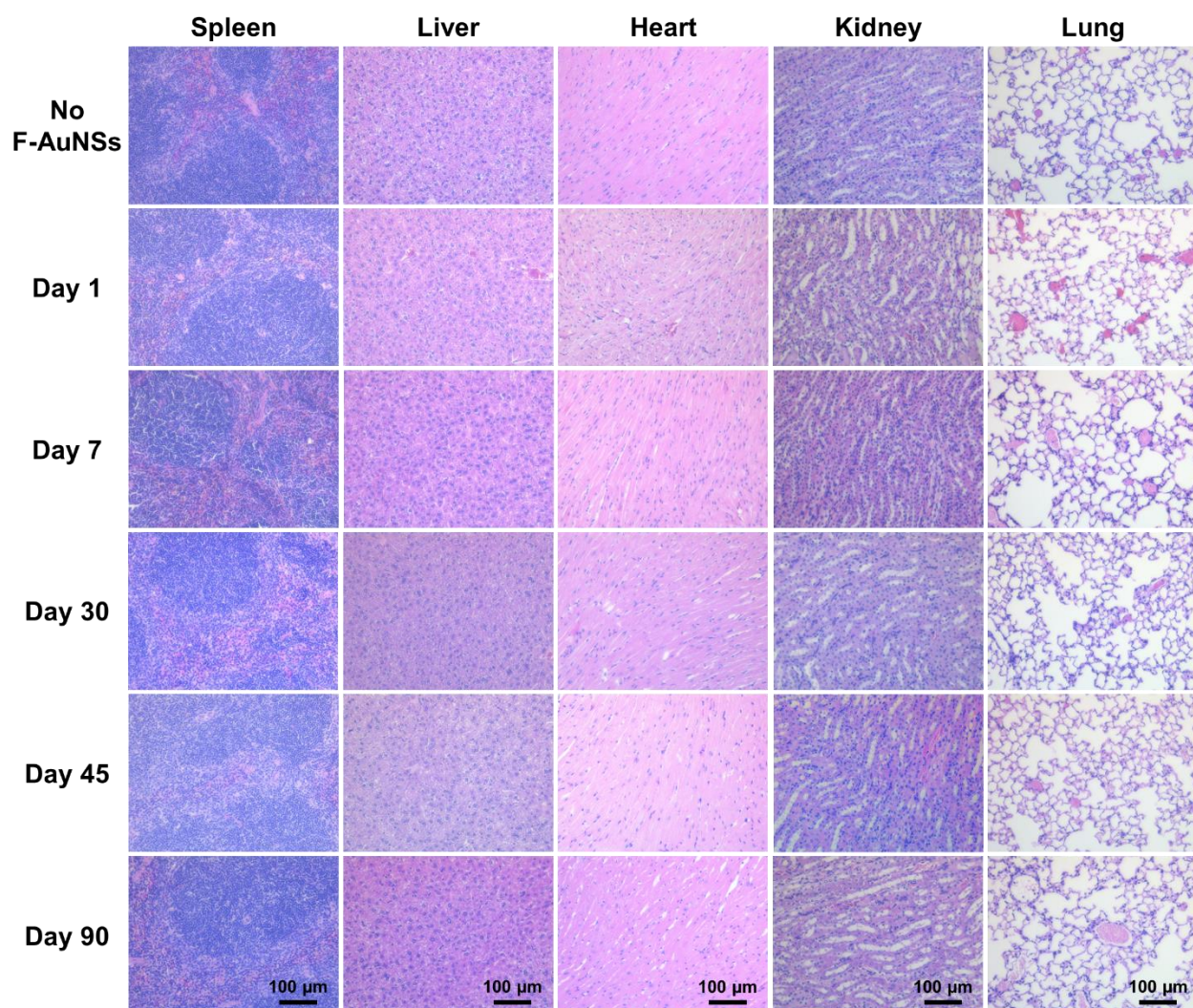
Figure A.18 H&E stain of major organs post IV delivery of F-AuNSs in healthy C57BL/6 mice. Spleen, liver, heart, kidney, and lung of mice were retrieved to evaluate toxicity of F-AuNSs. Histological evaluation of tissues showed minimal toxicity by F-AuNSs up to 90 days post IV administration. Here, "No F-AuNSs" control group represents organs of mice that received PBS only. Histology was performed on n = 3 mice.
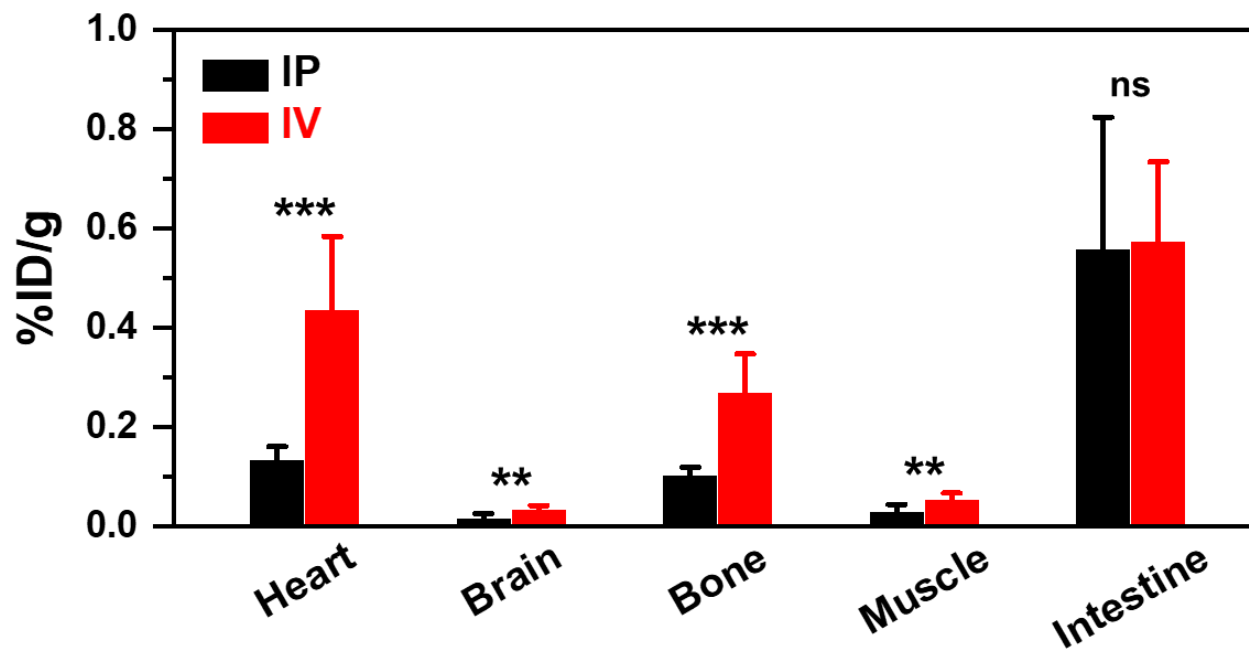
Figure A.19 of F-AuNSs obtained with ^{64}Cu gamma counts of organs harvested 24 h after either IP or IV delivery of F-AuNSs (n = 5). Here, ** indicates $p < 0.01$, *** indicates $p < 0.001$, and ns indicates not significant.
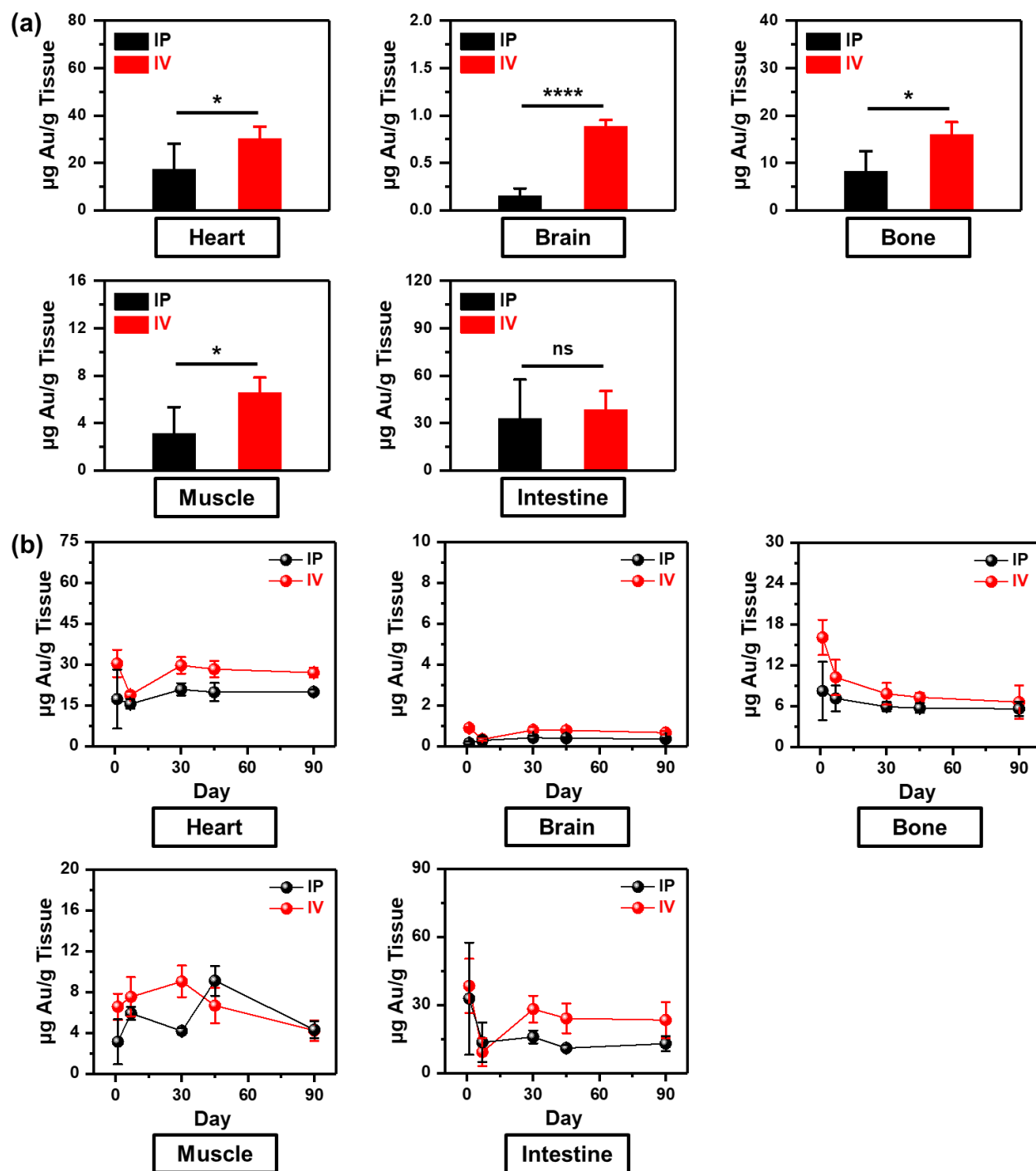
Figure A.20 (a) Quantitative ICP-MS analysis of biodistribution of F-AuNSs in mice 24 h post particle delivery (n = 4) showing Au content in mice tissues. (b) Biodistribution and clearance of F-AuNSs of major organs at 1-, 7-, 30-, 45- and 90-days post-delivery (n = 4). Here, data were presented as mean ± standard deviation. * indicates $p < 0.05$, **** indicates $p < 0.0001$, and ns indicates not significant.
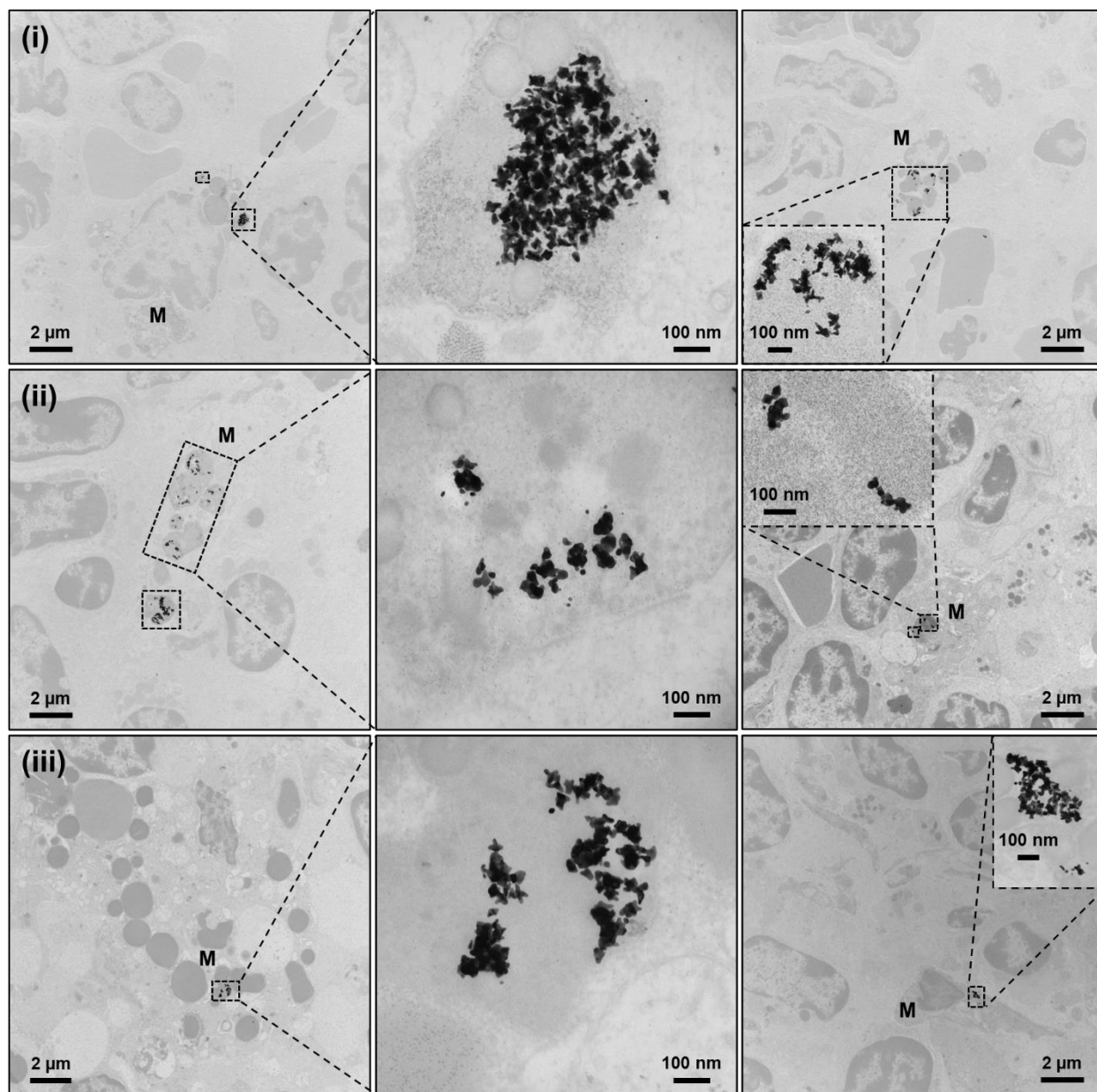
Figure A.21 Representative TEM micrographs of spleen harvested from mice (i) 7, (ii) 45 and (iii) 90 days after IP delivery of F-AuNSs. Here, *M* represents splenic macrophages.
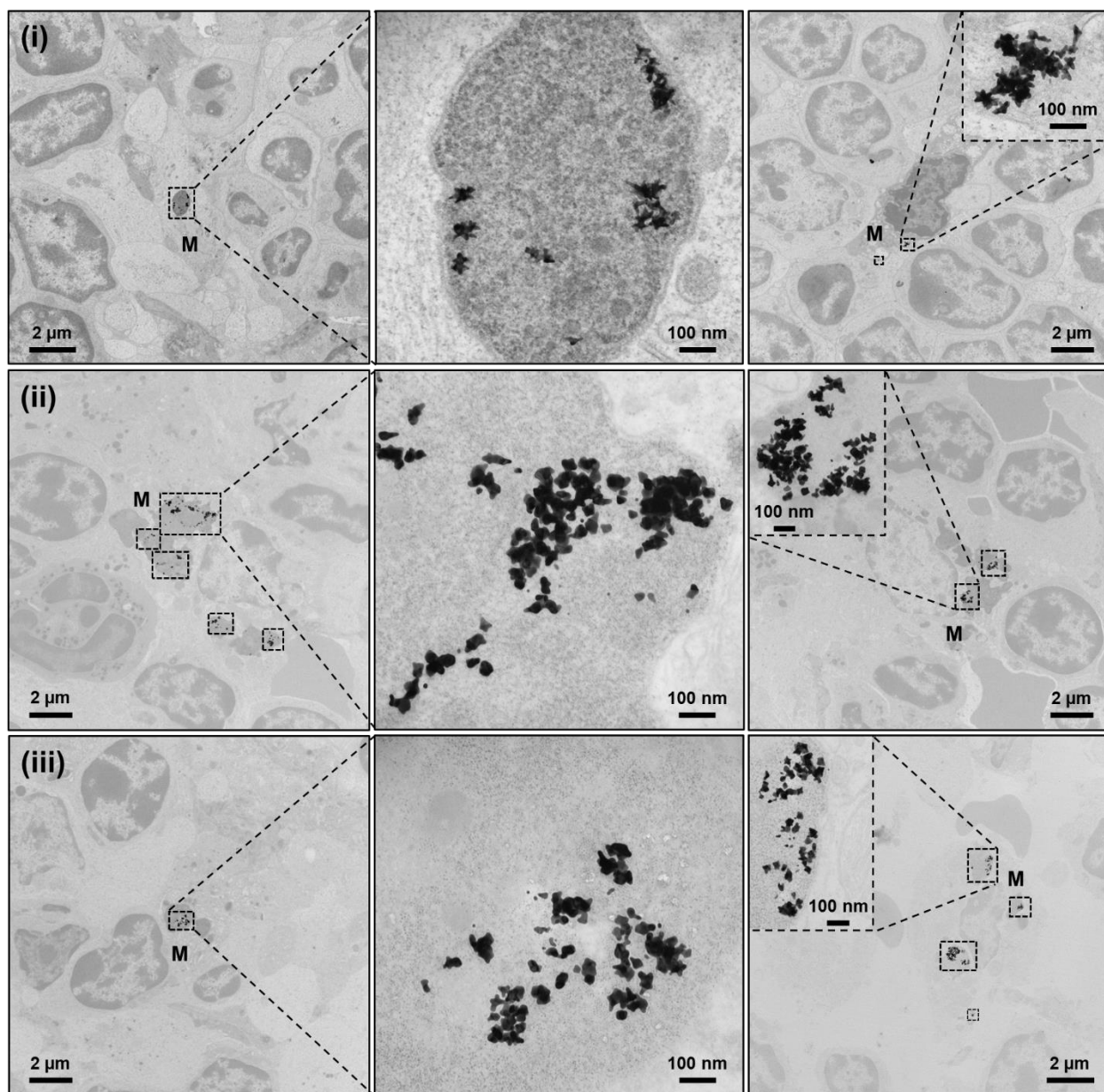
Figure A.22 Representative TEM micrographs of spleen harvested from mice (i) 7, (ii) 45 and (iii) 90 days after IV delivery of F-AuNSs. Here, *M* represents splenic macrophages.
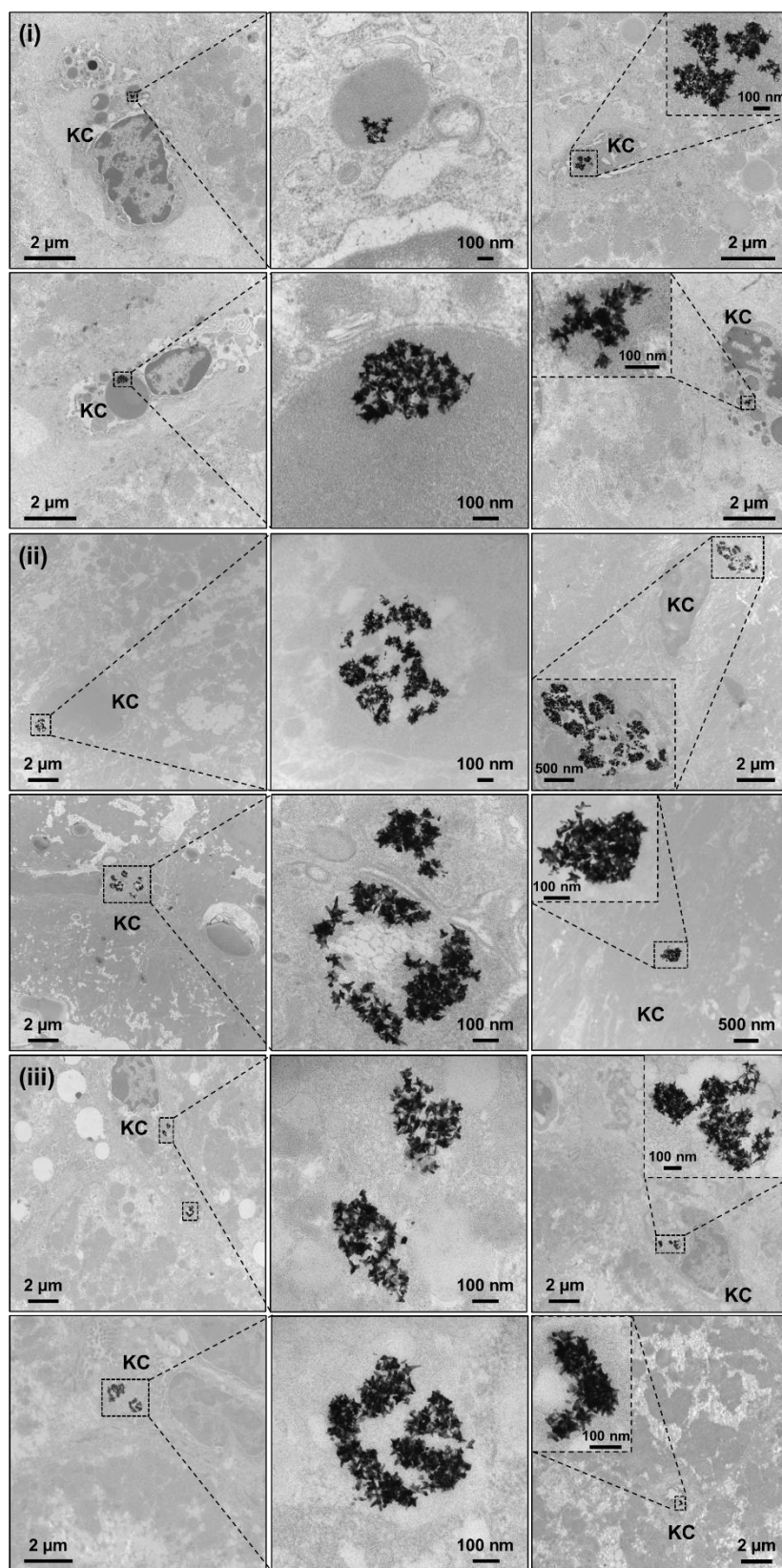
Figure A.23 Representative TEM micrographs of liver harvested from mice (i) 7, (ii) 45 and (iii) 90 days after IP delivery of F-AuNSs. *KC* represents Kupffer cells.

136
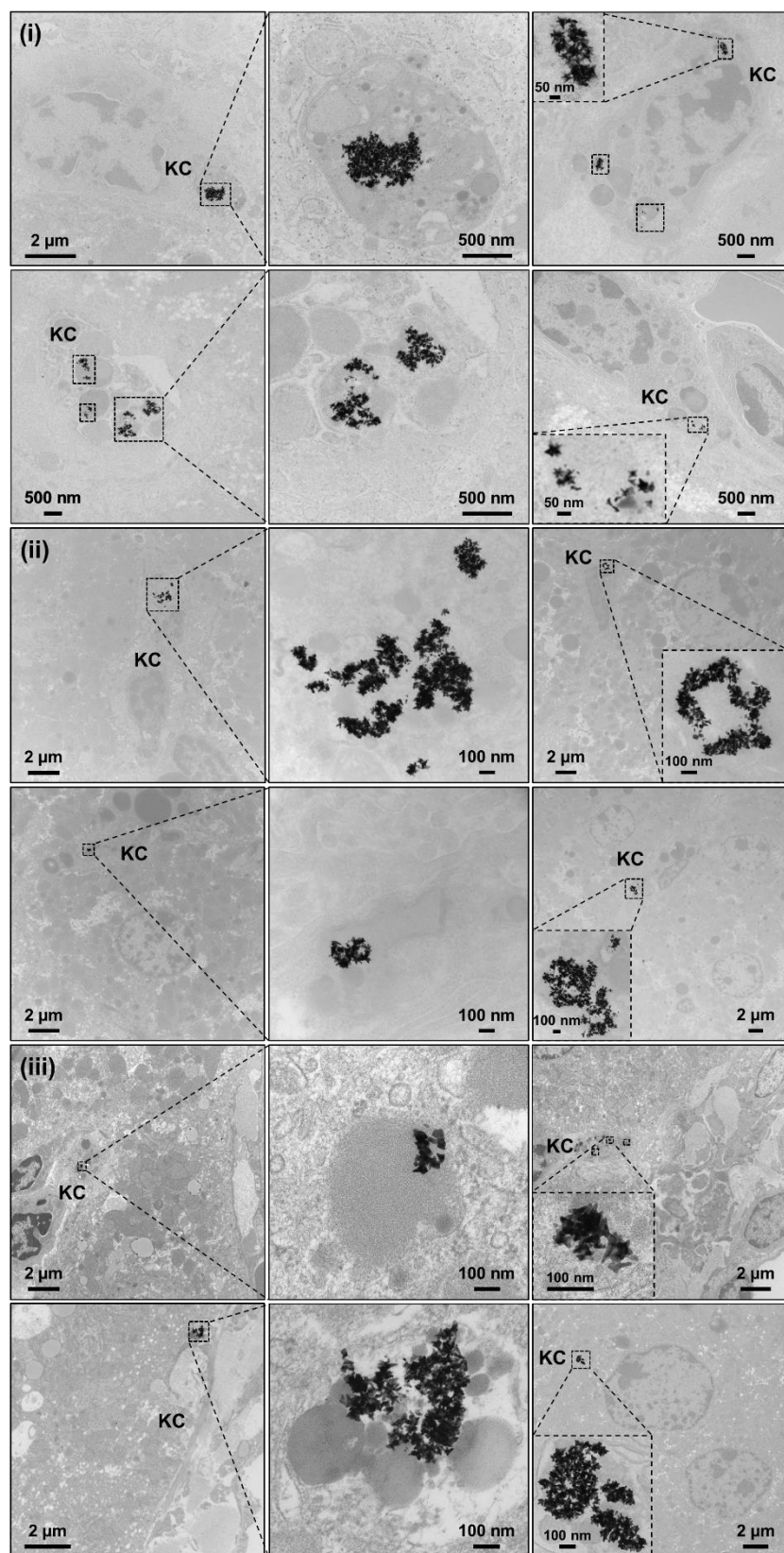
Figure A.24 Representative TEM micrographs of liver harvested from mice (i) 7, (ii) 45 and (iii) 90 days after IV delivery of F-AuNSs. *KC* represents Kupffer cells.
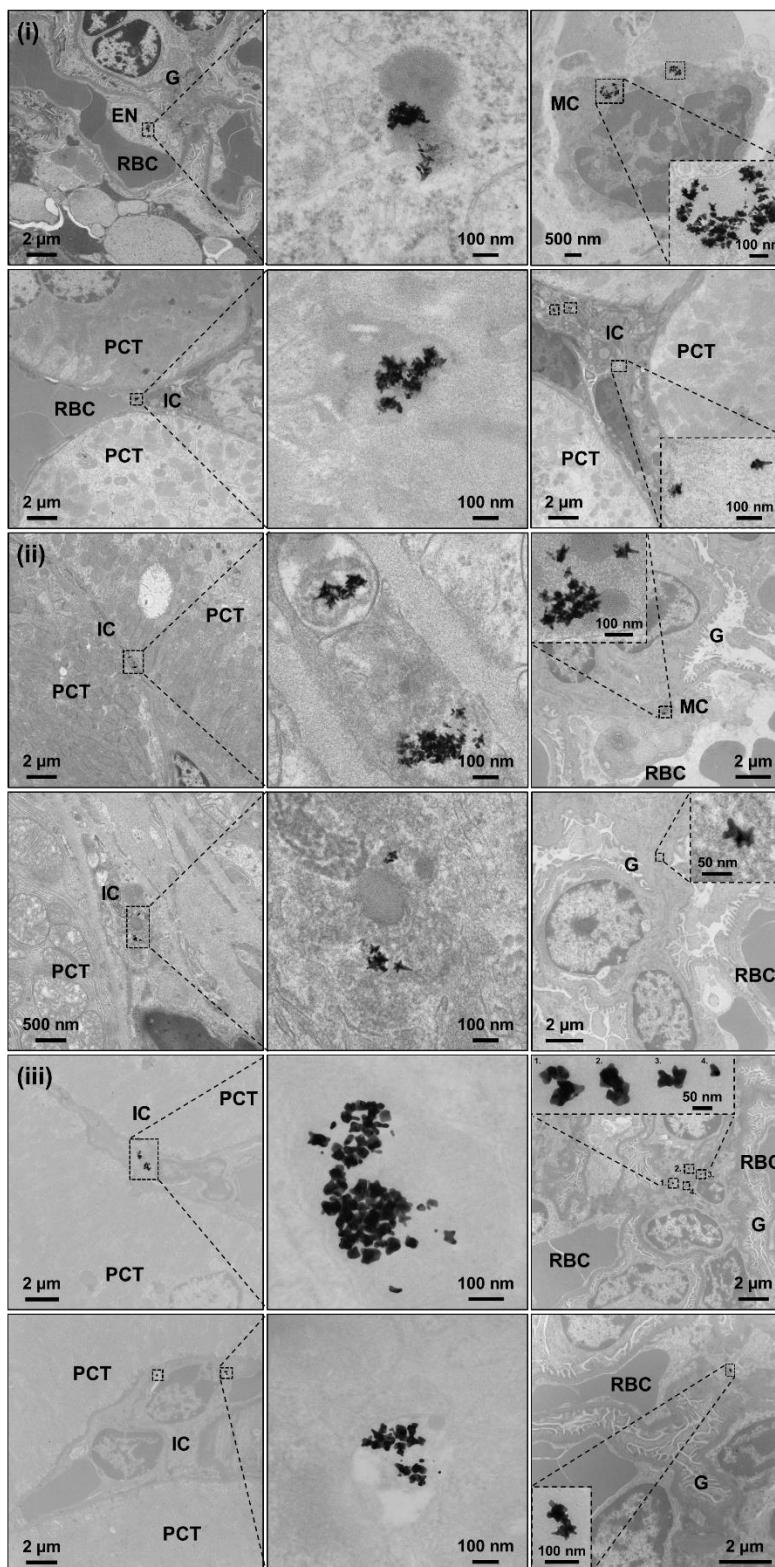
Figure A.25 Representative TEM micrographs of kidney harvested from mice (i) 7, (ii) 45 and (iii) 90 days after IP delivery of F-AuNSs. *G* represents glomeruli; *EN* represents endothelial cell; *IC* represents interstitial cell; *MC* represents mesangial cell; *PCT* represents proximal convoluted tubule; and *RBC* represents red blood cell.
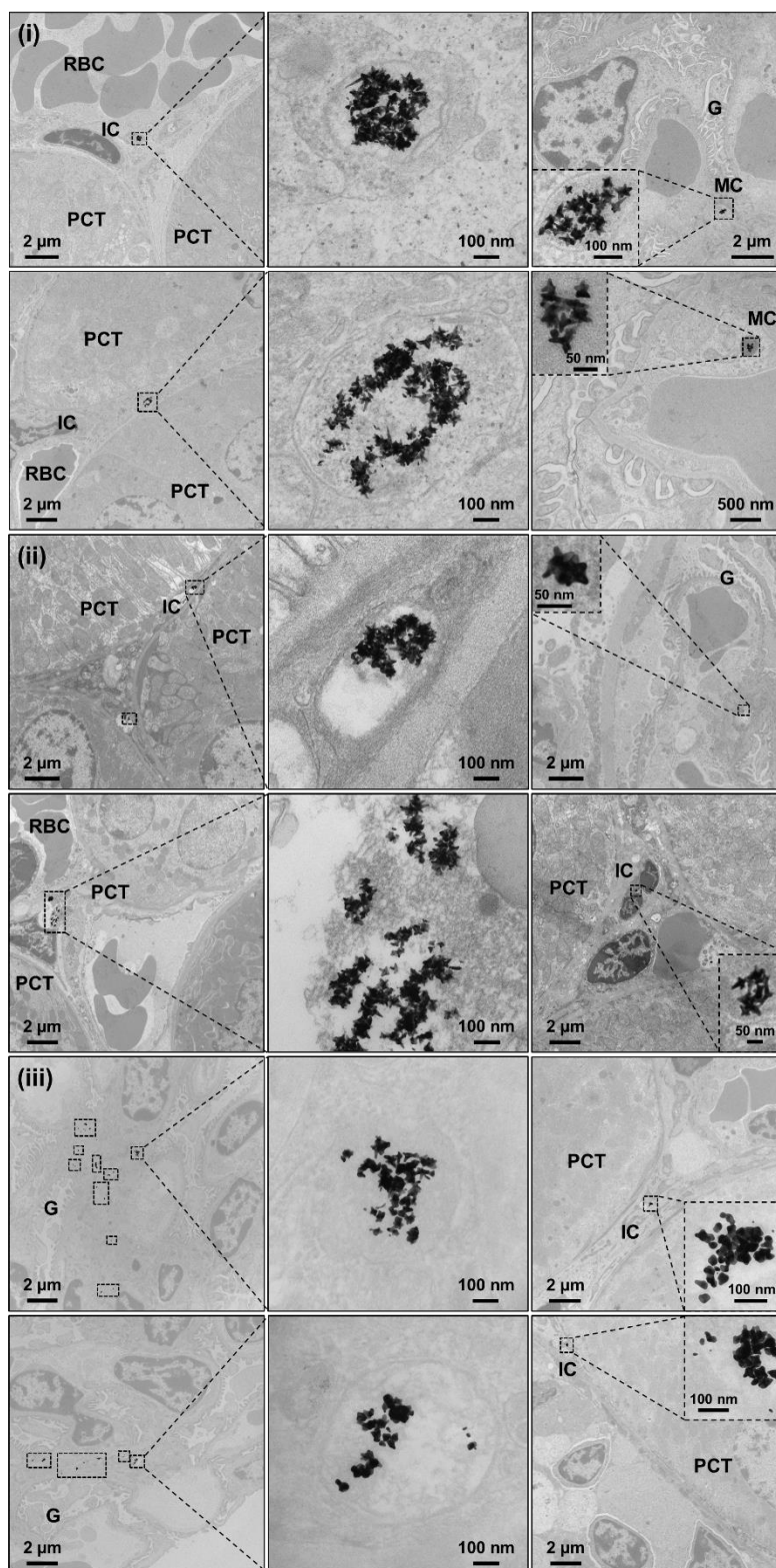
Figure A.26 Representative TEM micrographs of kidney harvested from mice (i) 7, (ii) 45 and (iii) 90 days after IV delivery of F-AuNSs. *G* represents glomeruli; *EN* represents endothelial cell; *IC* represents interstitial cell; *MC* represents mesangial cell; *PCT* represents proximal convoluted tubule; and *RBC* represents red blood cell.
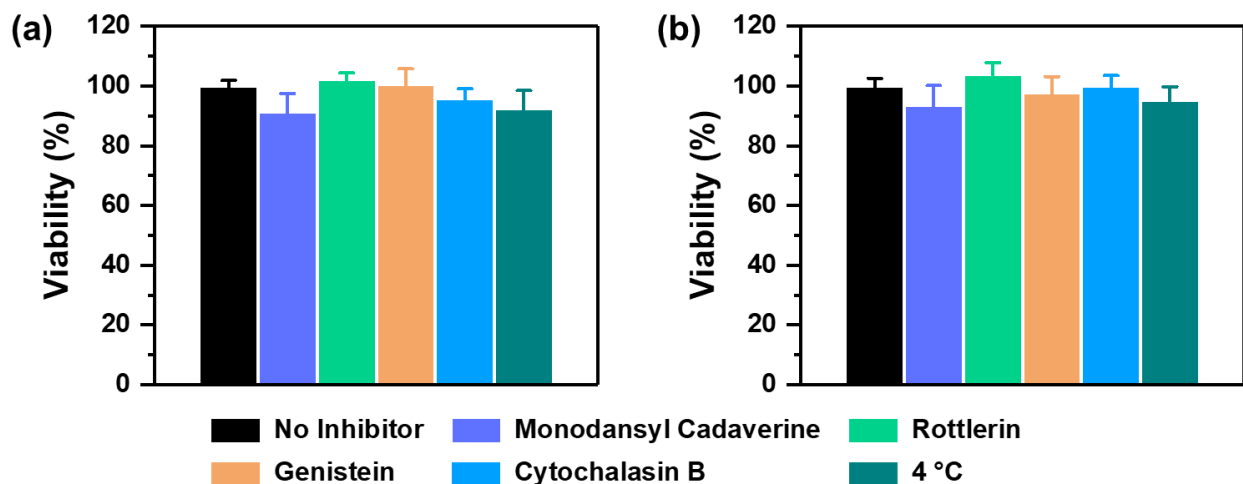
Figure A.27 MTT cell viability assay of (a) RAW 264.7 and (b) J774A.1 cells incubated for 8 h with inhibitors of the different endocytosis pathways including monodansyl cadaverine (200 µM), rottlerin (2 µM), genistein (200 µM), cytochalasin B (10 µg/mL) and cells incubated at 4 °C. These cells did not receive any F-AuNSs. Black bar represents control cells that did not receive any inhibitors. Cell viability was measured at 540 nm. All data were presented as mean ± standard deviation (n = 5 per concentration and N = 2 independent experiments).
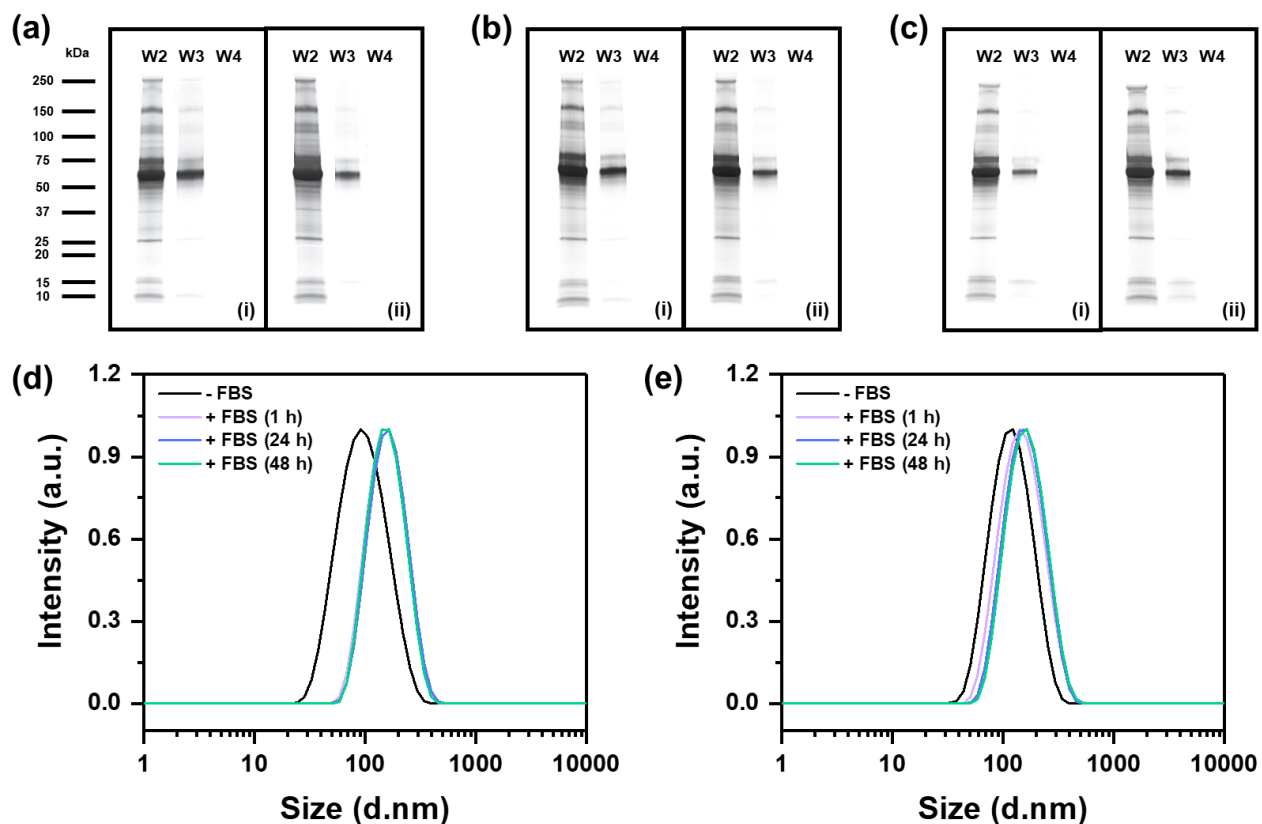
Figure A.28 Proteomic study of surface protein corona formation on F-AuNSs. Silver-stained SDS-PAGE showed that large unbound and loosely bound proteins were effectively removed by repeated centrifugation and washing and no free proteins were detected in the last washing step for (i) B-AuNSs and (ii) F-AuNSs incubated with 60% FBS for (a) 1, (b) 24 and (c) 48 h. *W2*, *W3* and *W4* represent washing step 2, 3 and 4. Hydrodynamic size of (d) B-AuNSs and (e) F-AuNSs after incubation with 60% FBS for 1, 24 and 48 h.
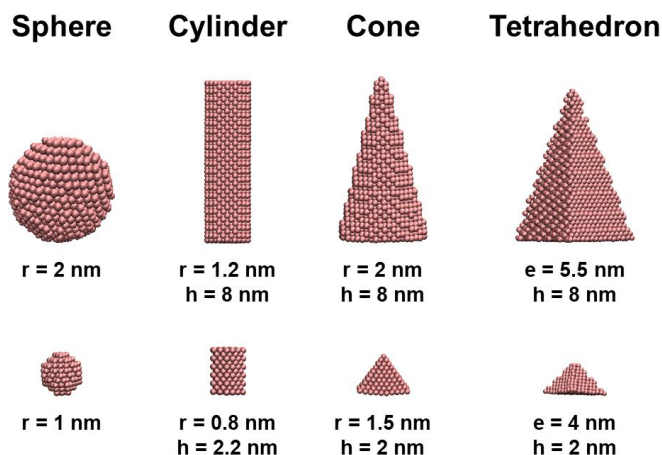
Figure A.29 Snapshots of four different shapes of nanoparticles. The top and bottom rows contain side-view of the nanoparticles with a volume ~35 and 4.5 nm^3, respectively. Here, *r*, *h* and *e* represent radius, height and edge, respectively.
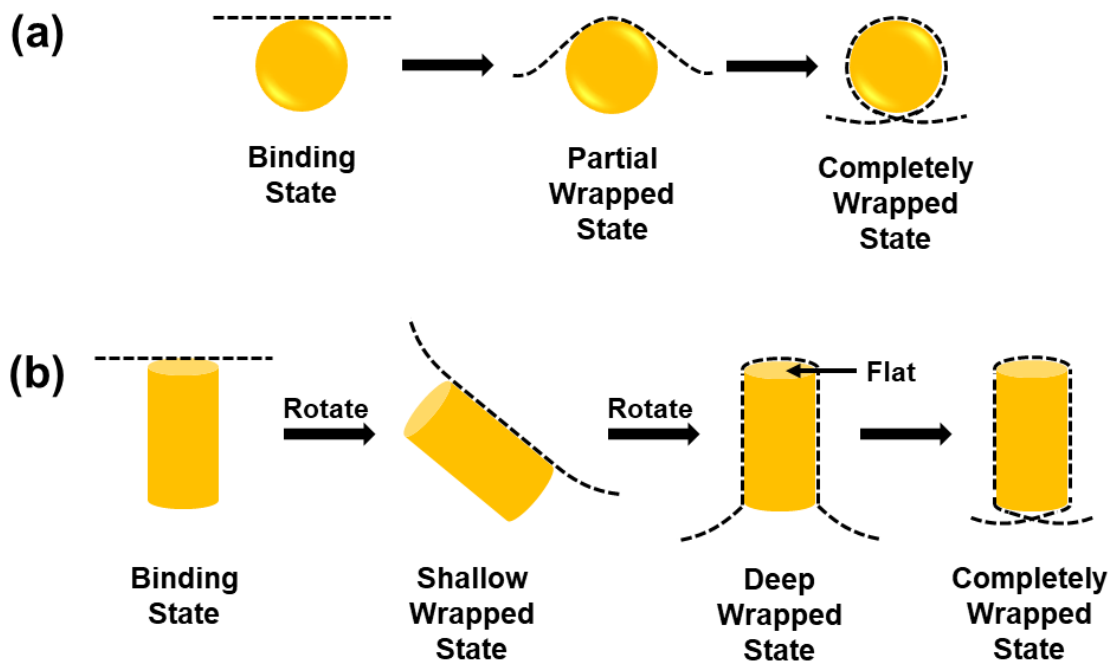
Figure A.30 Modes of nanoparticle exit by membrane wrapping. Compared to (a) the isotropic structures (*e.g.*, sphere), (b) anisotropic structures (*e.g.*, cylinder, cone and tetrahedron) first orient with a flat side toward the membrane, as this side requires less membrane deformation.
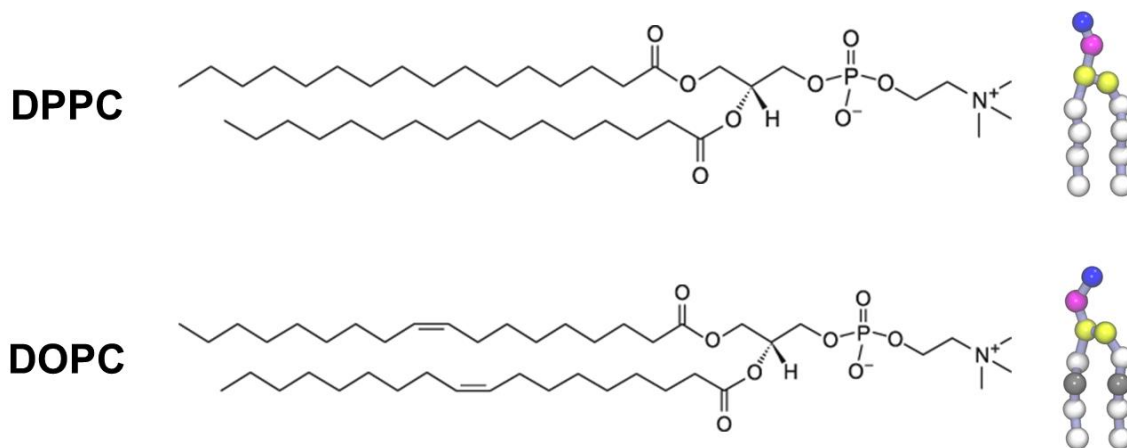
Figure A.31 Structures of DPPC and DOPC lipids. The molecular weights of DPPC and DOPC are 734 and 786 g/mol, respectively. DOPC has double bonds on the fatty acid lipid tails making it softer compared to DPPC.

REFERENCES

(1)   McClellan, J.; King, M.-C., Genetic heterogeneity in human disease. *Cell* **2010,** *141* (2), 210-217.

(2)   DeCordova, S.; Shastri, A.; Tsolaki, A. G.; Yasmin, H.; Klein, L.; Singh, S. K.; Kishore, U., Molecular heterogeneity and immunosuppressive microenvironment in glioblastoma. *Front. Immunol.* **2020,** *11* (1402).

(3)   Turashvili, G.; Brogi, E., Tumor heterogeneity in breast cancer. *Front. Med.* **2017,** *4* (227).

(4)   Ramón y Cajal, S.; Sesé, M.; Capdevila, C.; Aasen, T.; De Mattos-Arruda, L.; Diaz-Cano, S. J.; Hernández-Losa, J.; Castellví, J., Clinical implications of intratumor heterogeneity: challenges and opportunities. *J. Mol. Med.* **2020,** *98* (2), 161-177.

(5)   Chan, I. S.; Ginsburg, G. S., Personalized medicine: progress and promise. *Annu. Rev. Genomics Hum. Genet.* **2011,** *12*, 217-244.

(6)   Chouchane, L.; Mamtani, R.; Dallol, A.; Sheikh, J. I., Personalized medicine: a patient - centered paradigm. *J. Transl. Med.* **2011,** *9* (1), 206.

(7)   Sagner, M.; McNeil, A.; Puska, P.; Auffray, C.; Price, N. D.; Hood, L.; Lavie, C. J.; Han, Z.-G.; Chen, Z.; Brahmachari, S. K.; McEwen, B. S.; Soares, M. B.; Balling, R.; Epel, E.; Arena, R., The P4 health spectrum – a predictive, preventive, personalized and participatory continuum for promoting healthspan. *Prog. Cardiovasc. Dis.* **2017,** *59* (5), 506-521.

(8)   Hood, L.; Friend, S. H., Predictive, personalized, preventive, participatory (P4) cancer medicine. *Nat. Rev. Clin. Oncol.* **2011,** *8* (3), 184-187.

(9)   Strimbu, K.; Tavel, J. A., What are biomarkers? *Curr. Opin. HIV AIDS* **2010,** *5* (6), 463-466.

(10)   Anderson, L., Candidate-based proteomics in the search for biomarkers of cardiovascular disease. *J. Physiol.* **2005,** *563* (Pt 1), 23-60.

(11)   Boja, E. S.; Jortani, S. A.; Ritchie, J.; Hoofnagle, A. N.; Težak, Ž.; Mansfield, E.; Keller, P.; Rivers, R. C.; Rahbar, A.; Anderson, N. L.; Srinivas, P.; Rodriguez, H., The journey to regulation of protein-based multiplex quantitative assays. *Clin. Chem.* **2011,** *57* (4), 560-567.

(12)   Anderson, N. L., The clinical plasma proteome: a survey of clinical assays for proteins in plasma and serum. *Clin. Chem.* **2010,** *56* (2), 177-185.

(13)   Rifai, N.; Gillette, M. A.; Carr, S. A., Protein biomarker discovery and validation: the long and uncertain path to clinical utility. *Nat. Biotechnol.* **2006,** *24* (8), 971-983.

(14)   Qian, W.-J.; Jacobs, J. M.; Liu, T.; Camp, D. G., 2nd; Smith, R. D., Advances and challenges in liquid chromatography-mass spectrometry-based proteomics profiling for clinical applications. *Mol. Cell Proteomics* **2006,** *5* (10), 1727-1744.

(15) Angel, T. E.; Aryal, U. K.; Hengel, S. M.; Baker, E. S.; Kelly, R. T.; Robinson, E. W.; Smith, R. D., Mass spectrometry-based proteomics: existing capabilities and future directions. *Chem. Soc. Rev.* **2012,** *41* (10), 3912-3928.

(16) Whiteaker, J. R.; Zhao, L.; Anderson, L.; Paulovich, A. G., An automated and multiplexed method for high throughput peptide immunoaffinity enrichment and multiple reaction monitoring mass spectrometry-based quantification of protein biomarkers. *Mol. Cell Proteomics* **2010,** *9* (1), 184-196.

(17) Shi, T.; Su, D.; Liu, T.; Tang, K.; Camp, D. G., 2nd; Qian, W. J.; Smith, R. D., Advancing the sensitivity of selected reaction monitoring-based targeted quantitative proteomics. *Proteomics* **2012,** *12* (8), 1074-1092.

(18) Sturgeon, C.; Hill, R.; Hortin, G. L.; Thompson, D., Taking a new biomarker into routine use – a perspective from the routine clinical biochemistry laboratory. *Proteomics Clin. Appl.* **2010,** *4* (12), 892-903.

(19) Wu, C.; Liu, T.; Baker, E. S.; Rodland, K. D.; Smith, R. D., Mass spectrometry for biomarker development. In *General methods in biomarker research and their applications*, Preedy, V. R.; Patel, V. B., Eds. Springer: Dordrecht, 2015; pp 17-48.

(20) McDermott, J. E.; Wang, J.; Mitchell, H.; Webb-Robertson, B.-J.; Hafen, R.; Ramey, J.; Rodland, K. D., Challenges in biomarker discovery: combining expert insights with statistical analysis of complex omics data. *Expert Opin. Med. Diagn.* **2013,** *7* (1), 37-51.

(21) Schaffer, L. V.; Millikin, R. J.; Shortreed, M. R.; Scalf, M.; Smith, L. M., Improving proteoform identifications in complex systems through integration of bottom-up and top-down data. *J. Proteome Res.* **2020,** *19* (8), 3510-3517.

(22) Bogdanov, B.; Smith, R. D., Proteomics by FTICR mass spectrometry: top down and bottom up. *Mass Spectrom. Rev.* **2005,** *24* (2), 168-200.

(23) Reiter, L.; Claassen, M.; Schrimpf, S. P.; Jovanovic, M.; Schmidt, A.; Buhmann, J. M.; Hengartner, M. O.; Aebersold, R., Protein identification false discovery rates for very large proteomics data sets generated by tandem mass spectrometry. *Mol. Cell Proteomics* **2009,** *8* (11), 2405-2417.

(24) Gerszten, R. E.; Asnani, A.; Carr, S. A., Status and prospects for discovery and verification of new biomarkers of cardiovascular disease by proteomics. *Circ. Res.* **2011,** *109* (4), 463-474.

(25) Boja, E.; Rivers, R.; Kinsinger, C.; Mesri, M.; Hiltke, T.; Rahbar, A.; Rodriguez, H., Restructuring proteomics through verification. *Biomark. Med.* **2010,** *4* (6), 799-803.

(26) Picotti, P.; Aebersold, R., Selected reaction monitoring–based proteomics: workflows, potential, pitfalls and future directions. *Nat. Methods* **2012,** *9* (6), 555-566.

(27) Pitt, J. J., Principles and applications of liquid chromatography-mass spectrometry in clinical biochemistry. *Clin. Biochem. Rev.* **2009,** *30* (1), 19-34.

(28) Parker, C. E.; Borchers, C. H., Mass spectrometry based biomarker discovery, verification, and validation – quality assurance and control of protein biomarker assays. *Mol. Oncol.* **2014,** *8* (4), 840-858.

(29)   Anderson, N. L.; Anderson, N. G.; Haines, L. R.; Hardie, D. B.; Olafson, R. W.; Pearson, T. W., Mass spectrometric quantitation of peptides and proteins using stable isotope standards and capture by anti-peptide antibodies (SISCAPA). *J. Proteome. Res.* **2004,** *3* (2), 235-244.

(30)   Rauniyar, N., Parallel reaction monitoring: a targeted experiment performed using high resolution and high mass accuracy mass spectrometry. *Int. J. Mol. Sci.* **2015,** *16* (12), 28566-28581.

(31)   Hoofnagle, A. N.; Wener, M. H., The fundamental flaws of immunoassays and potential solutions using tandem mass spectrometry. *J. Immunol. Methods* **2009,** *347* (1-2), 3-11.

(32)   Auner, G. W.; Koya, S. K.; Huang, C.; Broadbent, B.; Trexler, M.; Auner, Z.; Elias, A.; Mehne, K. C.; Brusatori, M. A., Applications of Raman spectroscopy in cancer diagnosis. *Cancer Metastasis Rev.* **2018,** *37* (4), 691-717.

(33)   Ou, Y.-C.; Wen, X.; Johnson, C. A.; Shae, D.; Ayala, O. D.; Webb, J. A.; Lin, E. C.; DeLapp, R. C.; Boyd, K. L.; Richmond, A.; Mahadevan-Jansen, A.; Rafat, M.; Wilson, J. T.; Balko, J. M.; Tantawy, M. N.; Vilgelm, A. E.; Bardhan, R., Multimodal Multiplexed Immunoimaging with Nanostars to Detect Multiple Immunomarkers and Monitor Response to Immunotherapies. *ACS Nano* **2020,** *14* (1), 651-663.

(34)   Wen, X.; Ou, Y.-C.; Zarick, H. F.; Zhang, X.; Hmelo, A. B.; Victor, Q. J.; Paul, E. P.; Slocik, J. M.; Naik, R. R.; Bellan, L. M.; Lin, E. C.; Bardhan, R., PRADA: Portable Reusable Accurate Diagnostics with Nanostar Antennas for Multiplexed Biomarker Screening. *Bioeng. Transl. Med.* **2020,** *5* (3), e10165.

(35)   Wen, X.; Ou, Y.-C.; Bogatcheva, G.; Thomas, G.; Mahadevan-Jansen, A.; Singh, B.; Lin, E. C.; Bardhan, R., Probing metabolic alterations in breast cancer in response to molecular inhibitors with Raman spectroscopy and validated with mass spectrometry. *Chem. Sci.* **2020,** *11* (36), 9863-9874.

(36)   Hashimoto, K.; Badarla, V. R.; Kawai, A.; Ideguchi, T., Complementary vibrational spectroscopy. *Nat. Commun.* **2019,** *10* (1), 4411.

(37)   Friedrich, D. M., Two-photon molecular spectroscopy. *J. Chem. Educ.* **1982,** *59* (6), 472.

(38)   Shipp, D. W.; Sinjab, F.; Notingher, I., Raman spectroscopy: techniques and applications in the life sciences. *Adv. Opt. Photonics* **2017,** *9* (2), 315-428.

(39)   Tipping, W. J.; Lee, M.; Serrels, A.; Brunton, V. G.; Hulme, A. N., Stimulated Raman scattering microscopy: an emerging tool for drug discovery. *Chem. Soc. Rev.* **2016,** *45* (8), 2075-2089.

(40)   Moura, C. C.; Tare, R. S.; Oreffo, R. O. C.; Mahajan, S., Raman spectroscopy and coherent anti-Stokes Raman scattering imaging: prospective tools for monitoring skeletal cells and skeletal regeneration. *J. R. Soc. Interface* **2016,** *13* (118), 20160182.

(41)   Krafft, C.; Schie, I. W.; Meyer, T.; Schmitt, M.; Popp, J., Developments in spontaneous and coherent Raman scattering microscopic imaging for biomedical applications. *Chem. Soc. Rev.* **2016,** *45* (7), 1819-1849.

(42)   Krafft, C.; Schmitt, M.; Schie, I. W.; Cialla-May, D.; Matthäus, C.; Bocklitz, T.; Popp, J., Label-free molecular imaging of biological cells and tissues by linear and nonlinear Raman spectroscopic approaches. *Angew. Chem. Int. Ed.* **2017,** *56* (16), 4392-4430.

(43)   Ghita, A.; Matousek, P.; Stone, N., Exploring the effect of laser excitation wavelength on signal recovery with deep tissue transmission Raman spectroscopy. *Analyst* **2016,** *141* (20), 5738-5746.

(44)   Jones, R. R.; Hooper, D. C.; Zhang, L.; Wolverson, D.; Valev, V. K., Raman techniques: fundamentals and frontiers. *Nanoscale Res. Lett.* **2019,** *14* (1), 231.

(45)   Langer, J.; Jimenez de Aberasturi, D.; Aizpurua, J.; Alvarez-Puebla, R. A.; Auguié, B.; Baumberg, J. J.; Bazan, G. C.; Bell, S. E. J.; Boisen, A.; Brolo, A. G.; Choo, J.; Cialla-May, D.; Deckert, V.; Fabris, L.; Faulds, K.; García de Abajo, F. J.; Goodacre, R.; Graham, D.; Haes, A. J.; Haynes, C. L.; Huck, C.; Itoh, T.; Käll, M.; Kneipp, J.; Kotov, N. A.; Kuang, H.; Le Ru, E. C.; Lee, H. K.; Li, J.-F.; Ling, X. Y.; Maier, S. A.; Mayerhöfer, T.; Moskovits, M.; Murakoshi, K.; Nam, J.-M.; Nie, S.; Ozaki, Y.; Pastoriza-Santos, I.; Perez-Juste, J.; Popp, J.; Pucci, A.; Reich, S.; Ren, B.; Schatz, G. C.; Shegai, T.; Schlücker, S.; Tay, L.-L.; Thomas, K. G.; Tian, Z.-Q.; Van Duyne, R. P.; Vo-Dinh, T.; Wang, Y.; Willets, K. A.; Xu, C.; Xu, H.; Xu, Y.; Yamamoto, Y. S.; Zhao, B.; Liz-Marzán, L. M., Present and future of surface-enhanced Raman scattering. *ACS Nano* **2020,** *14* (1), 28-117.

(46)   Zong, C.; Xu, M.; Xu, L.-J.; Wei, T.; Ma, X.; Zheng, X.-S.; Hu, R.; Ren, B., Surface-enhanced Raman spectroscopy for bioanalysis: reliability and challenges. *Chem. Rev.* **2018,** *118* (10), 4946-4980.

(47)   Pérez-Jiménez, A. I.; Lyu, D.; Lu, Z.; Liu, G.; Ren, B., Surface-enhanced Raman spectroscopy: benefits, trade-offs and future developments. *Chem. Sci.* **2020,** *11* (18), 4563-4577.

(48)   Le Ru, E. C.; Etchegoin, P. G., Quantifying SERS enhancements. *MRS Bull.* **2013,** *38* (8), 631-640.

(49)   Pilot, R.; Signorini, R.; Durante, C.; Orian, L.; Bhamidipati, M.; Fabris, L., A review on surface-enhanced Raman scattering. *Biosensors* **2019,** *9* (2).

(50)   Dinish, U. S.; Olivo, M., SERS for sensitive biosensing and imaging. In *Handbook of photonics for biomedical engineering*, Ho, A. H.-P.; Kim, D.; Somekh, M. G., Eds. Springer: Dordrecht, 2017; pp 29-60.

(51)   Fong, K. E.; Yung, L.-Y. L., Localized surface plasmon resonance: a unique property of plasmonic nanoparticles for nucleic acid detection. *Nanoscale* **2013,** *5* (24), 12043-12071.

(52)   Masango, S. S.; Hackler, R. A.; Large, N.; Henry, A.-I.; McAnally, M. O.; Schatz, G. C.; Stair, P. C.; Van Duyne, R. P., High-resolution distance dependence study of surface-enhanced Raman scattering enabled by atomic layer deposition. *Nano Lett.* **2016,** *16* (7), 4251-4259.

(53)   Wang, Y.; Yan, B.; Chen, L., SERS tags: novel optical nanoprobes for bioanalysis. *Chem. Rev.* **2013,** *113* (3), 1391-1428.

(54)   Rodriguez-Lorenzo, L.; Fabris, L.; Alvarez-Puebla, R. A., Multiplex optical sensing with surface-enhanced Raman scattering: a critical review. *Anal. Chim. Acta* **2012,** *745*, 10-23.

(55)   Schuller, J. A.; Barnard, E. S.; Cai, W.; Jun, Y. C.; White, J. S.; Brongersma, M. L., Plasmonics for extreme light concentration and manipulation. *Nat. Mater.* **2010,** *9* (3), 193-204.

(56)   Dykman, L.; Khlebtsov, N., Gold nanoparticles in biomedical applications: recent advances and perspectives. *Chem. Soc. Rev.* **2012,** *41* (6), 2256-2282.

(57)   Jain, P. K.; Lee, K. S.; El-Sayed, I. H.; El-Sayed, M. A., Calculated absorption and scattering properties of gold nanoparticles of different size, shape, and composition: applications in biological imaging and biomedicine. *J. Phys. Chem. B* **2006,** *110* (14), 7238-7248.

(58)   Ringe, E.; Langille, M. R.; Sohn, K.; Zhang, J.; Huang, J.; Mirkin, C. A.; Van Duyne, R. P.; Marks, L. D., Plasmon length: a universal parameter to describe size effects in gold nanoparticles. *J. Phys. Chem. Lett.* **2012,** *3* (11), 1479-1483.

(59)   Trigari, S.; Rindi, A.; Margheri, G.; Sottini, S.; Dellepiane, G.; Giorgetti, E., Synthesis and modelling of gold nanostars with tunable morphology and extinction spectrum. *J. Mater. Chem.* **2011,** *21* (18), 6531-6540.

(60)   Kelly, K. L.; Coronado, E.; Zhao, L. L.; Schatz, G. C., The optical properties of metal nanoparticles: the influence of size, shape, and dielectric environment. *J. Phys. Chem. B* **2003,** *107* (3), 668-677.

(61)   Lim, B.; Xia, Y., Metal nanocrystals with highly branched morphologies. *Angew. Chem. Int. Ed.* **2011,** *50* (1), 76-85.

(62)   Burda, C.; Chen, X.; Narayanan, R.; El-Sayed, M. A., Chemistry and properties of nanocrystals of different shapes. *Chem. Rev.* **2005,** *105* (4), 1025-1102.

(63)   Webb, J. A.; Bardhan, R., Emerging advances in nanomedicine with engineered gold nanostructures. *Nanoscale* **2014,** *6* (5), 2502-2530.

(64)   Ou, Y.-C.; Wen, X.; Bardhan, R., Cancer immunoimaging with smart nanoparticles. *Trends Biotechnol.* **2020,** *38* (4), 388-403.

(65)   Ou, Y.-C.; Webb, J. A.; O'Brien, C. M.; Pence, I. J.; Lin, E. C.; Paul, E. P.; Cole, D.; Ou, S.-H.; Lapierre-Landry, M.; DeLapp, R. C.; Lippmann, E. S.; Mahadevan-Jansen, A.; Bardhan, R., Diagnosis of Immunomarkers In Vivo via Multiplexed Surface Enhanced Raman Spectroscopy With Gold Nanostars. *Nanoscale* **2018,** *10* (27), 13092-13105.

(66)   Webb, J. A.; Aufrecht, J.; Hungerford, C.; Bardhan, R., Ultrasensitive analyte detection with plasmonic paper dipsticks and swabs integrated with branched nanoantennas. *J. Mater. Chem. C* **2014,** *2* (48), 10446-10454.

(67)   Webb, J. A.; Erwin, W. R.; Zarick, H. F.; Aufrecht, J.; Manning, H. W.; Lang, M. J.; Pint, C. L.; Bardhan, R., Geometry-Dependent Plasmonic Tunability and Photothermal Characteristics of Multibranched Gold Nanoantennas. *J. Phys. Chem. C* **2014,** *118* (7), 3696-3707.

(68)   Xie, J.; Lee, J. Y.; Wang, D. I. C., Seedless, surfactantless, high-yield synthesis of branched gold nanocrystals in HEPES buffer solution. *Chem. Mater.* **2007,** *19* (11), 2823-2830.

(69) Elghanian, R.; Storhoff, J. J.; Mucic, R. C.; Letsinger, R. L.; Mirkin, C. A., Selective colorimetric detection of polynucleotides based on the distance-dependent optical properties of gold nanoparticles. *Science* **1997,** *277* (5329), 1078-1081.

(70) Tian, Y.; Luo, S.; Yan, H.; Teng, Z.; Pan, Y.; Zeng, L.; Wu, J.; Li, Y.; Liu, Y.; Wang, S.; Lu, G., Gold nanostars functionalized with amine-terminated PEG for X-ray/CT imaging and photothermal therapy. *J. Mater. Chem. B* **2015,** *3* (21), 4330-4337.

(71) García-Álvarez, R.; Hadjidemetriou, M.; Sánchez-Iglesias, A.; Liz-Marzán, L. M.; Kostarelos, K., In Vivo Formation of Protein Corona on Gold Nanoparticles. The Effect of Their Size and Shape. *Nanoscale* **2018,** *10* (3), 1256-1264.

(72) Li, Y.; Wang, X.; Gao, L.; Hu, P.; Jiang, L.; Ren, T.; Fu, R.; Yang, D.; Jiang, X., Aptamer-conjugated gold nanostars for targeted cancer photothermal therapy. *J. Mater. Sci.* **2018,** *53* (20), 14138-14148.

(73) Liu, Y.; Yuan, H.; Fales, A.; Register, J.; Vo-Dinh, T., Multifunctional gold nanostars for molecular imaging and cancer therapy. *Front. Chem.* **2015,** *3* (51).

(74) Alkilany, A. M.; Lohse, S. E.; Murphy, C. J., The gold standard: gold nanoparticle libraries to understand the nano-bio interface. *Acc. Chem. Res.* **2013,** *46* (3), 650-661.

(75) Ferrari, M., Cancer nanotechnology: opportunities and challenges. *Nat. Rev. Cancer* **2005,** *5* (3), 161-171.

(76) Peer, D.; Karp, J. M.; Hong, S.; Farokhzad, O. C.; Margalit, R.; Langer, R., Nanocarriers as an emerging platform for cancer therapy. *Nat. Nanotechnol.* **2007,** *2* (12), 751-760.

(77) Geissmann, F.; Manz, M. G.; Jung, S.; Sieweke, M. H.; Merad, M.; Ley, K., Development of monocytes, macrophages, and dendritic cells. *Science* **2010,** *327* (5966), 656-661.

(78) Murray, P. J.; Wynn, T. A., Protective and pathogenic functions of macrophage subsets. *Nat. Rev. Immunol.* **2011,** *11* (11), 723-737.

(79) Kamaly, N.; He, J. C.; Ausiello, D. A.; Farokhzad, O. C., Nanomedicines for Renal Disease: Current Status and Future Applications. *Nat. Rev. Nephrol.* **2016,** *12* (12), 738-753.

(80) Du, B.; Jiang, X.; Das, A.; Zhou, Q.; Yu, M.; Jin, R.; Zheng, J., Glomerular Barrier Behaves As an Atomically Precise Bandpass Filter in a Sub-Nanometre Regime. *Nat. Nanotechnol.* **2017,** *12* (11), 1096-1102.

(81) Arami, H.; Khandhar, A.; Liggitt, D.; Krishnan, K. M., In vivo delivery, pharmacokinetics, biodistribution and toxicity of iron oxide nanoparticles. *Chem. Soc. Rev.* **2015,** *44* (23), 8576-8607.

(82) Chin, C. D.; Linder, V.; Sia, S. K., Lab-on-a-chip devices for global health: past studies and future opportunities. *Lab Chip* **2007,** *7* (1), 41-57.

(83) Yager, P.; Edwards, T.; Fu, E.; Helton, K.; Nelson, K.; Tam, M. R.; Weigl, B. H., Microfluidic diagnostic technologies for global public health. *Nature* **2006,** *442* (7101), 412-418.

(84) Tasoglu, S.; Gurkan, U. A.; Wang, S.; Demirci, U., Manipulating biological agents and cells in micro-scale volumes for applications in medicine. *Chem. Soc. Rev.* **2013,** *42* (13), 5788-5808.

(85)   Land, K. J.; Boeras, D. I.; Chen, X.-S.; Ramsay, A. R.; Peeling, R. W., REASSURED diagnostics to inform disease control strategies, strengthen health systems and improve patient outcomes. *Nat. Microbiol.* **2019,** *4* (1), 46-54.

(86)   Quesada-González, D.; Merkoçi, A., Nanomaterial-based devices for point-of-care diagnostic applications. *Chem. Soc. Rev.* **2018,** *47* (13), 4697-4709.

(87)   Primiceri, E.; Chiriacò, M. S.; Notarangelo, F. M.; Crocamo, A.; Ardissino, D.; Cereda, M.; Bramanti, A. P.; Bianchessi, M. A.; Giannelli, G.; Maruccio, G., Key enabling technologies for point-of-care diagnostics. *Sensors* **2018,** *18* (11).

(88)   Tokel, O.; Inci, F.; Demirci, U., Advances in plasmonic technologies for point of care applications. *Chem. Rev.* **2014,** *114* (11), 5728-5752.

(89)   Grossier, R.; Hammadi, Z.; Morin, R.; Magnaldo, A.; Veesler, S., Generating nanoliter to femtoliter microdroplets with ease. *Appl. Phys. Lett.* **2011,** *98* (9), 091916.

(90)   Gubala, V.; Harris, L. F.; Ricco, A. J.; Tan, M. X.; Williams, D. E., Point of care diagnostics: status and future. *Anal. Chem.* **2012,** *84* (2), 487-515.

(91)   Alyassin, M. A.; Moon, S.; Keles, H. O.; Manzur, F.; Lin, R. L.; Hæggstrom, E.; Kuritzkes, D. R.; Demirci, U., Rapid automated cell quantification on HIV microfluidic devices. *Lab Chip* **2009,** *9* (23), 3364-3369.

(92)   Sönnichsen, C.; Reinhard, B. M.; Liphardt, J.; Alivisatos, A. P., A molecular ruler based on plasmon coupling of single gold and silver nanoparticles. *Nat. Biotechnol.* **2005,** *23* (6), 741-745.

(93)   Schultz, S.; Smith, D. R.; Mock, J. J.; Schultz, D. A., Single-target molecule detection with nonbleaching multicolor optical immunolabels. *Proc. Natl. Acad. Sci.* **2000,** *97* (3), 996.

(94)   Sau, T. K.; Rogach, A. L.; Jäckel, F.; Klar, T. A.; Feldmann, J., Properties and applications of colloidal nonspherical noble metal nanoparticles. *Adv. Mater.* **2010,** *22* (16), 1805-1825.

(95)   Arvizo, R. R.; Bhattacharyya, S.; Kudgus, R. A.; Giri, K.; Bhattacharya, R.; Mukherjee, P., Intrinsic Therapeutic Applications of Noble Metal Nanoparticles: Past, Present and Future. *Chem. Soc. Rev.* **2012,** *41* (7), 2943-2970.

(96)   Jain, P. K.; Huang, X.; El-Sayed, I. H.; El-Sayed, M. A., Noble metals on the nanoscale: optical and photothermal properties and some applications in imaging, sensing, biology, and medicine. *Acc. Chem. Res.* **2008,** *41* (12), 1578-1586.

(97)   Gu, Z. Z.; Horie, R.; Kubo, S.; Yamada, Y.; Fujishima, A.; Sato, O., Fabrication of a metal-coated three-dimensionally ordered macroporous film and its application as a refractive index sensor. *Angew. Chem. Int. Ed. Engl.* **2002,** *41* (7), 1154-1156.

(98)   Lodewijks, K.; Van Roy, W.; Borghs, G.; Lagae, L.; Van Dorpe, P., Boosting the figure-of-merit of LSPR-based refractive index sensing by phase-sensitive measurements. *Nano Lett.* **2012,** *12* (3), 1655-1659.

(99)   Stewart, M. E.; Anderton, C. R.; Thompson, L. B.; Maria, J.; Gray, S. K.; Rogers, J. A.; Nuzzo, R. G., Nanostructured plasmonic sensors. *Chem. Rev.* **2008,** *108* (2), 494-521.

(100)   Hendry, E.; Carpy, T.; Johnston, J.; Popland, M.; Mikhaylovskiy, R. V.; Lapthorn, A. J.; Kelly, S. M.; Barron, L. D.; Gadegaard, N.; Kadodwala, M., Ultrasensitive detection and

characterization of biomolecules using superchiral fields. *Nat. Nanotechnol.* **2010,** *5* (11), 783-787.

(101) Estevez, M. C.; Otte, M. A.; Sepulveda, B.; Lechuga, L. M., Trends and challenges of refractometric nanoplasmonic biosensors: a review. *Anal. Chim. Acta* **2014,** *806*, 55-73.

(102) Su, K. H.; Wei, Q. H.; Zhang, X.; Mock, J. J.; Smith, D. R.; Schultz, S., Interparticle coupling effects on plasmon resonances of nanogold particles. *Nano Lett.* **2003,** *3* (8), 1087-1090.

(103) Jain, P. K.; El-Sayed, M. A., Plasmonic coupling in noble metal nanostructures. *Chem. Phys. Lett.* **2010,** *487* (4), 153-164.

(104) Schlather, A. E.; Large, N.; Urban, A. S.; Nordlander, P.; Halas, N. J., Near-field mediated plexcitonic coupling and giant rabi splitting in individual metallic dimers. *Nano Lett.* **2013,** *13* (7), 3281-3286.

(105) Schnell, M.; García-Etxarri, A.; Huber, A. J.; Crozier, K.; Aizpurua, J.; Hillenbrand, R., Controlling the near-field oscillations of loaded plasmonic nanoantennas. *Nat. Photon* **2009,** *3* (5), 287-291.

(106) Guo, L.; Jackman, J. A.; Yang, H.-H.; Chen, P.; Cho, N.-J.; Kim, D.-H., Strategies for enhancing the sensitivity of plasmonic nanosensors. *Nano Today* **2015,** *10* (2), 213-239.

(107) Haagenson, K. K.; Wu, G. S., The role of MAP kinases and MAP kinase phosphatase-1 in resistance to breast cancer treatment. *Cancer Metastasis Rev.* **2010,** *29* (1), 143-149.

(108) Bartholomeusz, C.; Gonzalez-Angulo, A. M.; Liu, P.; Hayashi, N.; Lluch, A.; Ferrer-Lozano, J.; Hortobágyi, G. N., High ERK protein expression levels correlate with shorter survival in triple-negative breast cancer patients. *Oncologist* **2012,** *17* (6), 766-774.

(109) Salaroglio, I. C.; Mungo, E.; Gazzano, E.; Kopecka, J.; Riganti, C., ERK is a pivotal player of chemo-immune-resistance in cancer. *Int. J. Mol. Sci.* **2019,** *20* (10), 2505.

(110) Schafer, J. M.; Lehmann, B. D.; Gonzalez-Ericsson, P. I.; Marshall, C. B.; Beeler, J. S.; Redman, L. N.; Jin, H.; Sanchez, V.; Stubbs, M. C.; Scherle, P.; Johnson, K. N.; Sheng, Q.; Roland, J. T.; Bauer, J. A.; Shyr, Y.; Chakravarthy, B.; Mobley, B. C.; Hiebert, S. W.; Balko, J. M.; Sanders, M. E.; Liu, P. C. C.; Pietenpol, J. A., Targeting MYCN-expressing triple-negative breast cancer with BET and MEK inhibitors. *Sci. Transl. Med.* **2020,** *12* (534), eaaw8275.

(111) Potts, S. J.; Krueger, J. S.; Landis, N. D.; Eberhard, D. A.; David Young, G.; Schmechel, S. C.; Lange, H., Evaluating tumor heterogeneity in immunohistochemistry-stained breast cancer tissue. *Lab. Invest.* **2012,** *92* (9), 1342-1357.

(112) Sompuram, S. R.; Vani, K.; Schaedle, A. K.; Balasubramanian, A.; Bogen, S. A., Quantitative assessment of immunohistochemistry laboratory performance by measuring analytic response curves and limits of detection. *Arch. Pathol. Lab. Med.* **2018,** *142* (7), 851-862.

(113) DeBerardinis, R. J.; Chandel, N. S., Fundamentals of cancer metabolism. *Sci. Adv.* **2016,** *2* (5), e1600200.

(114) Kroemer, G.; Pouyssegur, J., Tumor cell metabolism: cancer's achilles' heel. *Cancer Cell* **2008,** *13* (6), 472-482.

(115) Ward, Patrick S.; Thompson, Craig B., Metabolic reprogramming: a cancer hallmark even Warburg did not anticipate. *Cancer Cell* **2012,** *21* (3), 297-308.

(116) Liberti, M. V.; Locasale, J. W., The Warburg effect: how does it benefit cancer cells? *Trends Biochem. Sci.* **2016,** *41* (3), 211-218.

(117) Beloribi-Djefaflia, S.; Vasseur, S.; Guillaumond, F., Lipid metabolic reprogramming in cancer cells. *Oncogenesis* **2016,** *5* (1), e189.

(118) Munir, R.; Lisec, J.; Swinnen, J. V.; Zaidi, N., Lipid metabolism in cancer cells under metabolic stress. *Br. J. Cancer* **2019,** *120* (12), 1090-1098.

(119) Serkova, N. J.; Eckhardt, S. G., Metabolic imaging to assess treatment response to cytotoxic and cytostatic agents. *Front. Oncol.* **2016,** *6*, 152.

(120) Folger, O.; Jerby, L.; Frezza, C.; Gottlieb, E.; Ruppin, E.; Shlomi, T., Predicting selective drug targets in cancer through metabolic networks. *Mol. Syst. Biol.* **2011,** *7* (1), 501.

(121) Caldarella, C.; Treglia, G.; Giordano, A., Diagnostic performance of dedicated positron emission mammography using fluorine-18-fluorodeoxyglucose in women with suspicious breast lesions: a meta-analysis. *Clin. Breast Cancer* **2014,** *14* (4), 241-248.

(122) Lodi, A.; Woods, S. M.; Ronen, S. M., MR-detectable metabolic consequences of mitogen-activated protein kinase kinase (MEK) inhibition. *NMR Biomed.* **2014,** *27* (6), 700-708.

(123) Morelli, M. P.; Tentler, J. J.; Kulikowski, G. N.; Tan, A.-C.; Bradshaw-Pierce, E. L.; Pitts, T. M.; Brown, A. M.; Nallapareddy, S.; Arcaroli, J. J.; Serkova, N. J.; Hidalgo, M.; Ciardiello, F.; Eckhardt, S. G., Preclinical activity of the rational combination of selumetinib (AZD6244) in combination with vorinostat in KRAS-mutant colorectal cancer models. *Clin. Cancer Res.* **2012,** *18* (4), 1051-1062.

(124) Abouzied, M. M.; Crawford, E. S.; Nabi, H. A., 18F-FDG imaging: pitfalls and artifacts. *J. Nucl. Med. Technol.* **2005,** *33* (3), 145-155.

(125) Xiao, L.; Wang, C.; Dai, C.; Littlepage, L. E.; Li, J.; Schultz, Z. D., Untargeted tumor metabolomics with liquid chromatography-surface-enhanced Raman spectroscopy. *Angew. Chem., Int. Ed.* **2020,** *59* (9), 3439-3443.

(126) Thomas, G.; Nguyen, T. Q.; Pence, I. J.; Caldwell, B.; O'Connor, M. E.; Giltnane, J.; Sanders, M. E.; Grau, A.; Meszoely, I.; Hooks, M.; Kelley, M. C.; Mahadevan-Jansen, A., Evaluating feasibility of an automated 3-dimensional scanner using Raman spectroscopy for intraoperative breast margin assessment. *Sci. Rep.* **2017,** *7* (1), 13548.

(127) Paidi, S. K.; Rizwan, A.; Zheng, C.; Cheng, M.; Glunde, K.; Barman, I., Label-free Raman spectroscopy detects stromal adaptations in premetastatic lungs primed by breast cancer. *Cancer Res.* **2017,** *77* (2), 247.

(128) Hubbard, T. J. E.; Shore, A.; Stone, N., Raman spectroscopy for rapid intra-operative margin analysis of surgically excised tumour specimens. *Analyst* **2019,** *144* (22), 6479-6496.

(129) Qiu, S.; Li, M.; Liu, J.; Chen, X.; Lin, T.; Xu, Y.; Chen, Y.; Weng, Y.; Pan, Y.; Feng, S.; Lin, X.; Zhang, L.; Lin, D., Study on the chemodrug-induced effect in nasopharyngeal carcinoma cells using laser tweezer Raman spectroscopy. *Biomed. Opt. Express* **2020,** *11* (4), 1819-1833.

(130) Draux, F.; Gobinet, C.; Sulé-Suso, J.; Manfait, M.; Jeannesson, P.; Sockalingum, G. D., Raman imaging of single living cells: probing effects of non-cytotoxic doses of an anti-cancer drug. *Analyst* **2011,** *136* (13), 2718-2725.

(131) Farhane, Z.; Bonnier, F.; Howe, O.; Casey, A.; Byrne, H. J., Doxorubicin kinetics and effects on lung cancer cell lines using in vitro Raman micro-spectroscopy: binding signatures, drug resistance and DNA repair. *J. Biophotonics* **2018,** *11* (1), e201700060.

(132) Mondol, A. S.; Töpfer, N.; Rüger, J.; Neugebauer, U.; Popp, J.; Schie, I. W., New perspectives for viability studies with high-content analysis Raman spectroscopy (HCA-RS). *Sci. Rep.* **2019,** *9* (1), 12653.

(133) Patra, S.; Young, V.; Llewellyn, L.; Senapati, J. N.; Mathew, J., BRAF, KRAS and PIK3CA mutation and sensitivity to trastuzumab in breast cancer cell line model. *Asian Pac. J. Cancer Prev.* **2017,** *18* (8), 2209-2213.

(134) Bonnier, F.; Byrne, H. J., Understanding the molecular information contained in principal component analysis of vibrational spectra of biological systems. *Analyst* **2012,** *137* (2), 322-332.

(135) Pence, I.; Mahadevan-Jansen, A., Clinical instrumentation and applications of Raman spectroscopy. *Chem. Soc. Rev.* **2016,** *45* (7), 1958-1979.

(136) Meher, A. K.; Chen, Y.-C., Combination of Raman spectroscopy and mass spectrometry for online chemical analysis. *Anal. Chem.* **2016,** *88* (18), 9151-9157.

(137) Audier, X.; Heuke, S.; Volz, P.; Rimke, I.; Rigneault, H., Noise in stimulated Raman scattering measurement: from basics to practice. *APL Photonics* **2020,** *5* (1), 011101.

(138) Hernández, Y.; Lagos, L. K.; Galarreta, B. C., Development of a label-free-SERS gold nanoaptasensor for the accessible determination of ochratoxin A. *Sens. Biosensing Res.* **2020,** *28*, 100331.

(139) Niebling, S.; Kuchelmeister, H. Y.; Schmuck, C.; Schlücker, S., Quantitative label-free monitoring of peptide recognition by artificial receptors: a comparative FT-IR and UV resonance Raman spectroscopic study. *Chem. Sci.* **2012,** *3* (12), 3371-3377.

(140) Bovenkamp, D.; Micko, A.; Püls, J.; Placzek, F.; Höftberger, R.; Vila, G.; Leitgeb, R.; Drexler, W.; Andreana, M.; Wolfsberger, S.; Unterhuber, A., Line scan Raman microspectroscopy for label-free diagnosis of human pituitary biopsies. *Molecules* **2019,** *24* (19), 3577.

(141) Sinjab, F.; Sicilia, G.; Shipp, D. W.; Marlow, M.; Notingher, I., Label-free Raman hyperspectral imaging of single cells cultured on polymer substrates. *Appl. Spectrosc.* **2017,** *71* (12), 2595-2607.

(142) Fore, S.; Chan, J.; Taylor, D.; Huser, T., Raman spectroscopy of individual monocytes reveals that single-beam optical trapping of mononuclear cells occurs by their nucleus. *J. Opt.* **2011,** *13* (4), 044021.

(143)   Dai, X.; Xia, H.; Zhou, S.; Tang, Q.; Bi, F., Zoledronic acid enhances the efficacy of the MEK inhibitor trametinib in KRAS mutant cancers. *Cancer Lett.* **2019,** *442*, 202-212.

(144)   Leung, E. Y.; Kim, J. E.; Askarian-Amiri, M.; Rewcastle, G. W.; Finlay, G. J.; Baguley, B. C., Relationships between signaling pathway usage and sensitivity to a pathway inhibitor: examination of trametinib responses in cultured breast cancer lines. *PLoS One* **2014,** *9* (8), e105792.

(145)   Movasaghi, Z.; Rehman, S.; Rehman, I. U., Raman spectroscopy of biological tissues. *Appl. Spectrosc. Rev.* **2007,** *42* (5), 493-541.

(146)   Dobrzyńska, I.; Szachowicz-Petelska, B.; Darewicz, B.; Figaszewski, Z. A., Characterization of human bladder cell membrane during cancer transformation. *J. Membr. Biol.* **2015,** *248* (2), 301-307.

(147)   Glunde, K.; Serkova, N. J., Therapeutic targets and biomarkers identified in cancer choline phospholipid metabolism. *Pharmacogenomics* **2006,** *7* (7), 1109-1123.

(148)   Al-Saffar, N. M. S.; Troy, H.; de Molina, A. R.; Jackson, L. E.; Madhu, B.; Griffiths, J. R.; Leach, M. O.; Workman, P.; Lacal, J. C.; Judson, I. R.; Chung, Y.-L., Noninvasive magnetic resonance spectroscopic pharmacodynamic markers of the choline kinase inhibitor MN58b in human carcinoma models. *Cancer Res.* **2006,** *66* (1), 427.

(149)   Acciardo, S.; Mignion, L.; Joudiou, N.; Bouzin, C.; Baurain, J.-F.; Gallez, B.; Jordan, B. F., Imaging markers of response to combined BRAF and MEK inhibition in BRAF mutated vemurafenib-sensitive and resistant melanomas. *Oncotarget* **2018,** *9* (24), 16832-16846.

(150)   Klotz, B.; Kneitz, S.; Lu, Y.; Boswell, W.; Postlethwait, J.; Warren, W.; Walter, R. B.; Schartl, M., Expression signatures of cisplatin- and trametinib-treated early-stage medaka melanomas. *G3: Genes, Genomes, Genet.* **2019,** *9* (7), 2267-2276.

(151)   Muñoz-Pinedo, C.; El Mjiyad, N.; Ricci, J. E., Cancer metabolism: current perspectives and future directions. *Cell Death Discov.* **2012,** *3* (1), e248.

(152)   Subik, K.; Lee, J. F.; Baxter, L.; Strzepek, T.; Costello, D.; Crowley, P.; Xing, L.; Hung, M. C.; Bonfiglio, T.; Hicks, D. G.; Tang, P., The expression patterns of ER, PR, HER2, CK5/6, EGFR, Ki-67 and AR by immunohistochemical analysis in breast cancer cell lines. *Breast Cancer* **2010,** *4*, 35-41.

(153)   Wee, P.; Wang, Z., Epidermal growth factor receptor cell proliferation signaling pathways. *Cancers* **2017,** *9* (5), 52.

(154)   Maennling, A. E.; Tur, M. K.; Niebert, M.; Klockenbring, T.; Zeppernick, F.; Gattenlöhner, S.; Meinhold-Heerlein, I.; Hussain, A. F., Molecular targeting therapy against EGFR family in breast cancer: progress and future potentials. *Cancers* **2019,** *11* (12), 1826.

(155)   Ogretmen, B., Sphingolipid metabolism in cancer signalling and therapy. *Nat. Rev. Cancer* **2018,** *18* (1), 33-50.

(156)   Cheng, M.; Bhujwalla, Z. M.; Glunde, K., Targeting phospholipid metabolism in cancer. *Front. Oncol.* **2016,** *6*, 266.

(157) Saini, K. S.; Loi, S.; de Azambuja, E.; Metzger-Filho, O.; Saini, M. L.; Ignatiadis, M.; Dancey, J. E.; Piccart-Gebhart, M. J., Targeting the PI3K/AKT/mTOR and Raf/MEK/ERK pathways in the treatment of breast cancer. *Cancer Treat. Rev.* **2013,** *39* (8), 935-946.

(158) Cheng, S.-H.; Tseng, Y.-M.; Wu, S.-H.; Tsai, S.-M.; Tsai, L.-Y., Whey protein concentrate renders MDA-MB-231 cells sensitive to rapamycin by altering cellular redox state and activating GSK3β/mTOR signaling. *Sci. Rep.* **2017,** *7* (1), 15976.

(159) Elkabets, M.; Vora, S.; Juric, D.; Morse, N.; Mino-Kenudson, M.; Muranen, T.; Tao, J.; Campos, A. B.; Rodon, J.; Ibrahim, Y. H.; Serra, V.; Rodrik-Outmezguine, V.; Hazra, S.; Singh, S.; Kim, P.; Quadt, C.; Liu, M.; Huang, A.; Rosen, N.; Engelman, J. A.; Scaltriti, M.; Baselga, J., mTORC1 inhibition is required for sensitivity to PI3K p110a inhibitors in *PIK3CA*-mutant breast cancer. *Sci. Transl. Med.* **2013,** *5* (196), 196ra99.

(160) Vettore, L.; Westbrook, R. L.; Tennant, D. A., New aspects of amino acid metabolism in cancer. *Br. J. Cancer* **2020,** *122* (2), 150-156.

(161) Choi, B.-H.; Coloff, J. L., The diverse functions of non-essential amino acids in cancer. *Cancers* **2019,** *11* (5), 675.

(162) Metsiou, D. N.; Siatis, K. E.; Giannopoulou, E.; Papachristou, D. J.; Kalofonos, H. P.; Koutras, A.; Athanassiou, G., The impact of anti-tumor agents on ER-positive MCF-7 and HER2-positive SKBR-3 breast cancer cells biomechanics. *Ann. Biomed. Eng.* **2019,** *47* (8), 1711-1724.

(163) Yang, M.; Soga, T.; Pollard, P. J., Oncometabolites: linking altered metabolism with cancer. *J. Clin. Invest.* **2013,** *123* (9), 3652-3658.

(164) Vernieri, C.; Casola, S.; Foiani, M.; Pietrantonio, F.; de Braud, F.; Longo, V., Targeting cancer metabolism: dietary and pharmacologic interventions. *Cancer Discov.* **2016,** *6* (12), 1315.

(165) Ho, C.-S.; Jean, N.; Hogan, C. A.; Blackmon, L.; Jeffrey, S. S.; Holodniy, M.; Banaei, N.; Saleh, A. A. E.; Ermon, S.; Dionne, J., Rapid identification of pathogenic bacteria using Raman spectroscopy and deep learning. *Nat. Commun.* **2019,** *10* (1), 4927.

(166) Goldenberg, S. L.; Nir, G.; Salcudean, S. E., A new era: artificial intelligence and machine learning in prostate cancer. *Nat. Rev. Urol.* **2019,** *16* (7), 391-403.

(167) Romeo, A.; Leung, T. S.; Sánchez, S., Smart biosensors for multiplexed and fully integrated point-of-care diagnostics. *Lab Chip* **2016,** *16* (11), 1957-1961.

(168) Dincer, C.; Bruch, R.; Kling, A.; Dittrich, P. S.; Urban, G. A., Multiplexed point-of-care testing – xPOCT. *Trends Biotechnol.* **2017,** *35* (8), 728-742.

(169) Masson, J.-F., Surface plasmon resonance clinical biosensors for medical diagnostics. *ACS Sens.* **2017,** *2* (1), 16-30.

(170) Chen, P.; Chung, M. T.; McHugh, W.; Nidetz, R.; Li, Y.; Fu, J.; Cornell, T. T.; Shanley, T. P.; Kurabayashi, K., Multiplex serum cytokine immunoassay using nanoplasmonic biosensor microarrays. *ACS Nano* **2015,** *9* (4), 4173-4181.

(171) Wang, R.; Chon, H.; Lee, S.; Cheng, Z.; Hong, S. H.; Yoon, Y. H.; Choo, J., Highly sensitive detection of hormone estradiol E2 using surface-enhanced Raman scattering

based immunoassays for the clinical diagnosis of precocious puberty. *ACS Appl. Mater. Interfaces* **2016,** *8* (17), 10665-10672.

(172)   Luan, J.; Morrissey, J. J.; Wang, Z.; Derami, H. G.; Liu, K.-K.; Cao, S.; Jiang, Q.; Wang, C.; Kharasch, E. D.; Naik, R. R.; Singamaneni, S., Add-on plasmonic patch as a universal fluorescence enhancer. *Light Sci. Appl.* **2018,** *7* (1), 29.

(173)   Polavarapu, L.; Liz-Marzán, L. M., Towards low-cost flexible substrates for nanoplasmonic sensing. *Phys. Chem. Chem. Phys.* **2013,** *15* (15), 5288-5300.

(174)   Shen, L.; Hagen, J. A.; Papautsky, I., Point-of-care colorimetric detection with a smartphone. *Lab Chip* **2012,** *12* (21), 4240-4243.

(175)   Wan, Y.; Su, Y.; Zhu, X.; Liu, G.; Fan, C., Development of electrochemical immunosensors towards point of care diagnostics. *Biosens. Bioelectron.* **2013,** *47*, 1-11.

(176)   Rogers, M. L.; Boutelle, M. G., Real-time clinical monitoring of biomolecules. *Annu. Rev. Anal. Chem.* **2013,** *6*, 427-453.

(177)   Perkel, J. M., Pocket laboratories. *Nature* **2017,** *545* (7652), 119-121.

(178)   Cheng, Z.; Choi, N.; Wang, R.; Lee, S.; Moon, K. C.; Yoon, S. Y.; Chen, L.; Choo, J., Simultaneous detection of dual prostate specific antigens using surface-enhanced Raman scattering-based immunoassay for accurate diagnosis of prostate cancer. *ACS Nano* **2017,** *11* (5), 4926-4933.

(179)   Kang, H.; Jeong, S.; Koh, Y.; Geun Cha, M.; Yang, J.-K.; Kyeong, S.; Kim, J.; Kwak, S.-Y.; Chang, H.-J.; Lee, H.; Jeong, C.; Kim, J.-H.; Jun, B.-H.; Kim, Y.-K.; Hong Jeong, D.; Lee, Y.-S., Direct identification of on-bead peptides using surface-enhanced Raman spectroscopic barcoding system for high-throughput bioanalysis. *Sci. Rep.* **2015,** *5* (1), 10144.

(180)   Polavarapu, L.; Porta, A. L.; Novikov, S. M.; Coronado-Puchau, M.; Liz-Marzán, L. M., Pen-on-paper approach toward the design of universal surface enhanced Raman scattering substrates. *Small* **2014,** *10* (15), 3065-3071.

(181)   Wang, Z.; Zong, S.; Wu, L.; Zhu, D.; Cui, Y., SERS-activated platforms for immunoassay: probes, encoding methods, and applications. *Chem. Rev.* **2017,** *117* (12), 7910-7963.

(182)   Wang, Y.; Polavarapu, L.; Liz-Marzán, L. M., Reduced graphene oxide-supported gold nanostars for improved SERS sensing and drug delivery. *ACS Appl. Mater. Interfaces* **2014,** *6* (24), 21798-21805.

(183)   Ou, Y. C.; Webb, J. A.; Faley, S.; Shae, D.; Talbert, E. M.; Lin, S.; Cutright, C. C.; Wilson, J. T.; Bellan, L. M.; Bardhan, R., Gold nanoantenna-mediated photothermal drug delivery from thermosensitive liposomes in breast cancer. *ACS Omega* **2016,** *1* (2), 234-243.

(184)   Korley, F. K.; Jaffe, A. S., Preparing the United States for high-sensitivity cardiac troponin assays. *J. Am. Coll. Cardiol.* **2013,** *61* (17), 1753-1758.

(185)   Vasile, V. C.; Jaffe, A. S., High-sensitivity cardiac troponin for the diagnosis of patients with acute coronary syndromes. *Curr. Cardiol. Rep.* **2017,** *19* (10), 92.

(186)   Keller, T.; Zeller, T.; Ojeda, F.; Tzikas, S.; Lillpopp, L.; Sinning, C.; Wild, P.; Genth-Zotz, S.; Warnholtz, A.; Giannitsis, E.; Möckel, M.; Bickel, C.; Peetz, D.; Lackner, K.; Baldus,

S.; Münzel, T.; Blankenberg, S., Serial changes in highly sensitive troponin I assay and early diagnosis of myocardial infarction. *JAMA* **2011,** *306* (24), 2684-2693.

(187) Tan, C. M. J.; Green, P.; Tapoulal, N.; Lewandowski, A. J.; Leeson, P.; Herring, N., The role of neuropeptide Y in cardiovascular health and disease. *Front. Physiol.* **2018,** *9*, 1281.

(188) Herring, N.; Tapoulal, N.; Kalla, M.; Ye, X.; Borysova, L.; Lee, R.; Dall'Armellina, E.; Stanley, C.; Ascione, R.; Lu, C. J.; Banning, A. P.; Choudhury, R. P.; Neubauer, S.; Dora, K.; Kharbanda, R. K.; Channon, K. M., Neuropeptide-Y causes coronary microvascular constriction and is associated with reduced ejection fraction following ST-elevation myocardial infarction. *Eur. Heart J.* **2019,** *40* (24), 1920-1929.

(189) Sah, R.; Geracioti, T. D., Neuropeptide Y and posttraumatic stress disorder. *Mol. Psychiatry* **2013,** *18* (6), 646-655.

(190) Enman, N. M.; Sabban, E. L.; McGonigle, P.; Van Bockstaele, E. J., Targeting the neuropeptide Y system in stress-related psychiatric disorders. *Neurobiol. Stress* **2015,** *1*, 33-43.

(191) Morgan, C. A., 3rd; Wang, S.; Southwick, S. M.; Rasmusson, A.; Hazlett, G.; Hauger, R. L.; Charney, D. S., Plasma neuropeptide-Y concentrations in humans exposed to military survival training. *Biol. Psychiatry* **2000,** *47* (10), 902-909.

(192) Kuang, Z.; Kim, S. N.; Crookes-Goodson, W. J.; Farmer, B. L.; Naik, R. R., Biomimetic chemosensor: designing peptide recognition elements for surface functionalization of carbon nanotube field effect transistors. *ACS Nano* **2010,** *4* (1), 452-458.

(193) Tadepalli, S.; Kuang, Z.; Jiang, Q.; Liu, K.-K.; Fisher, M. A.; Morrissey, J. J.; Kharasch, E. D.; Slocik, J. M.; Naik, R. R.; Singamaneni, S., Peptide functionalized gold nanorods for the sensitive detection of a cardiac biomarker using plasmonic paper devices. *Sci. Rep.* **2015,** *5* (1), 16206.

(194) Xiao, X.; Kuang, Z.; Slocik, J. M.; Tadepalli, S.; Brothers, M.; Kim, S.; Mirau, P. A.; Butkus, C.; Farmer, B. L.; Singamaneni, S.; Hall, C. K.; Naik, R. R., Advancing peptide-based biorecognition elements for biosensors using in-silico evolution. *ACS Sens.* **2018,** *3* (5), 1024-1031.

(195) Kim, S.; Xing, L.; Islam, A. E.; Hsiao, M. S.; Ngo, Y.; Pavlyuk, O. M.; Martineau, R. L.; Hampton, C. M.; Crasto, C.; Slocik, J.; Kadakia, M. P.; Hagen, J. A.; Kelley-Loughnane, N.; Naik, R. R.; Drummy, L. F., In operando observation of neuropeptide capture and release on graphene field-effect transistor biosensors with picomolar sensitivity. *ACS Appl. Mater. Interfaces* **2019,** *11* (15), 13927-13934.

(196) Heinz, H.; Farmer, B. L.; Pandey, R. B.; Slocik, J. M.; Patnaik, S. S.; Pachter, R.; Naik, R. R., Nature of molecular interactions of peptides with gold, palladium, and Pd−Au bimetal surfaces in aqueous solution. *J. Am. Chem. Soc.* **2009,** *131* (28), 9704-9714.

(197) Park, J. P.; Cropek, D. M.; Banta, S., High affinity peptides for the recognition of the heart disease biomarker troponin I identified using phage display. *Biotechnol. Bioeng.* **2010,** *105* (4), 678-686.

(198) Chiu, D. T.; deMello, A. J.; Di Carlo, D.; Doyle, P. S.; Hansen, C.; Maceiczyk, R. M.; Wootton, R. C. R., Small but perfectly formed? Successes, challenges, and opportunities for microfluidics in the chemical and biological sciences. *Chem.* **2017,** *2* (2), 201-223.

(199) Liu, Z.; Han, X.; Qin, L., Recent progress of microfluidics in translational applications. *Adv. Healthc. Mater.* **2016,** *5* (8), 871-888.

(200) Psychogios, N.; Hau, D. D.; Peng, J.; Guo, A. C.; Mandal, R.; Bouatra, S.; Sinelnikov, I.; Krishnamurthy, R.; Eisner, R.; Gautam, B.; Young, N.; Xia, J.; Knox, C.; Dong, E.; Huang, P.; Hollander, Z.; Pedersen, T. L.; Smith, S. R.; Bamforth, F.; Greiner, R.; McManus, B.; Newman, J. W.; Goodfriend, T.; Wishart, D. S., The human serum metabolome. *PLoS One* **2011,** *6* (2), e16957.

(201) Bonifacio, A.; Cervo, S.; Sergo, V., Label-free surface-enhanced Raman spectroscopy of biofluids: fundamental aspects and diagnostic applications. *Anal. Bioanal. Chem.* **2015,** *407* (27), 8265-8277.

(202) Lieber, C. A.; Majumder, S. K.; Ellis, D. L.; Billheimer, D. D.; Mahadevan-Jansen, A., In vivo nonmelanoma skin cancer diagnosis using Raman microspectroscopy. *Lasers Surg. Med.* **2008,** *40* (7), 461-467.

(203) Zhang, D.; Huang, L.; Liu, B.; Ge, Q.; Dong, J.; Zhao, X., Rapid and ultrasensitive quantification of multiplex respiratory tract infection pathogen via lateral flow microarray based on SERS nanotags. *Theranostics* **2019,** *9* (17), 4849-4859.

(204) Yang, S.; Dai, X.; Stogin, B. B.; Wong, T.-S., Ultrasensitive surface-enhanced Raman scattering detection in common fluids. *Proc. Natl. Acad. Sci.* **2016,** *113* (2), 268.

(205) Giannitsis, E.; Katus, H. A., Cardiac troponin level elevations not related to acute coronary syndromes. *Nat. Rev. Cardiol.* **2013,** *10* (11), 623-634.

(206) Goode, J. A.; Rushworth, J. V.; Millner, P. A., Biosensor regeneration: a review of common techniques and outcomes. *Langmuir* **2015,** *31* (23), 6267-6276.

(207) Drake, A. W.; Klakamp, S. L., A strategic and systematic approach for the determination of biosensor regeneration conditions. *J. Immunol. Methods* **2011,** *371* (1-2), 165-169.

(208) Wikström, M. B.; Dahlén, G.; Kaijser, B.; Nygren, H., Degradation of human immunoglobulins by proteases from Streptococcus pneumoniae obtained from various human sources. *Infect. Immun.* **1984,** *44* (1), 33-37.

(209) Armbruster, D. A.; Pry, T., Limit of blank, limit of detection and limit of quantitation. *Clin. Biochem. Rev.* **2008,** *29 Suppl 1* (Suppl 1), S49-S52.

(210) Shah, A. S. V.; Griffiths, M.; Lee, K. K.; McAllister, D. A.; Hunter, A. L.; Ferry, A. V.; Cruikshank, A.; Reid, A.; Stoddart, M.; Strachan, F.; Walker, S.; Collinson, P. O.; Apple, F. S.; Gray, A. J.; Fox, K. A. A.; Newby, D. E.; Mills, N. L., High sensitivity cardiac troponin and the under-diagnosis of myocardial infarction in women: prospective cohort study. *BMJ* **2015,** *350*, g7873.

(211) Ayas, S.; Cupallari, A.; Ekiz, O. O.; Kaya, Y.; Dana, A., Counting molecules with a mobile phone camera using plasmonic enhancement. *ACS Photonics* **2014,** *1* (1), 17-26.

(212) Temiz, Y.; Delamarche, E., Sub-nanoliter, real-time flow monitoring in microfluidic chips using a portable device and smartphone. *Sci. Rep.* **2018,** *8* (1), 10603.

(213) Dam, D. H.; Culver, K. S.; Kandela, I.; Lee, R. C.; Chandra, K.; Lee, H.; Mantis, C.; Ugolkov, A.; Mazar, A. P.; Odom, T. W., Biodistribution and in vivo toxicity of aptamer-loaded gold nanostars. *Nanomedicine* **2015,** *11* (3), 671-679.

(214) Yang, L.; Kuang, H.; Zhang, W.; Aguilar, Z. P.; Wei, H.; Xu, H., Comparisons of the Biodistribution and Toxicological Examinations after Repeated Intravenous Administration of Silver and Gold Nanoparticles in Mice. *Sci. Rep.* **2017,** *7* (1), 3303.

(215) Du, Y.; Jiang, Q.; Beziere, N.; Song, L.; Zhang, Q.; Peng, D.; Chi, C.; Yang, X.; Guo, H.; Diot, G.; Ntziachristos, V.; Ding, B.; Tian, J., DNA-Nanostructure–Gold-Nanorod Hybrids for Enhanced In Vivo Optoacoustic Imaging and Photothermal Therapy. *Adv. Mater.* **2016,** *28* (45), 10000-10007.

(216) Liu, X.; Zhang, Q.; Knoll, W.; Liedberg, B.; Wang, Y., Rational Design of Functional Peptide–Gold Hybrid Nanomaterials for Molecular Interactions. *Adv. Mater.* **2020,** *32* (37), 2000866.

(217) Liu, Z.; Li, Y.; Li, W.; Xiao, C.; Liu, D.; Dong, C.; Zhang, M.; Mäkilä, E.; Kemell, M.; Salonen, J.; Hirvonen, J. T.; Zhang, H.; Zhou, D.; Deng, X.; Santos, H. A., Multifunctional Nanohybrid Based on Porous Silicon Nanoparticles, Gold Nanoparticles, and Acetalated Dextran for Liver Regeneration and Acute Liver Failure Theranostics. *Adv. Mater.* **2018,** *30* (24), 1703393.

(218) Rauch, J.; Kolch, W.; Laurent, S.; Mahmoudi, M., Big signals from small particles: regulation of cell signaling pathways by nanoparticles. *Chem. Rev.* **2013,** *113* (5), 3391-3406.

(219) Dykman, L. A.; Khlebtsov, N. G., Uptake of engineered gold nanoparticles into mammalian cells. *Chem. Rev.* **2014,** *114* (2), 1258-1288.

(220) Qiu, Y.; Rojas, E.; Murray, R. A.; Irigoyen, J.; Gregurec, D.; Castro-Hartmann, P.; Fledderman, J.; Estrela-Lopis, I.; Donath, E.; Moya, S. E., Cell uptake, intracellular distribution, fate and reactive oxygen species generation of polymer brush engineered CeO2−x NPs. *Nanoscale* **2015,** *7* (15), 6588-6598.

(221) He, B.; Yuan, L.; Dai, W.; Gao, W.; Zhang, H.; Wang, X.; Fang, W.; Zhang, Q., Dynamic bio-adhesion of polymer nanoparticles on MDCK epithelial cells and its impact on bio-membranes, endocytosis and paracytosis. *Nanoscale* **2016,** *8* (11), 6129-6145.

(222) Dai, Q.; Walkey, C.; Chan, W. C., Polyethylene Glycol Backfilling Mitigates the Negative Impact of the Protein Corona on Nanoparticle Cell Targeting. *Angew. Chem. Int. Ed.* **2014,** *53* (20), 5093-6.

(223) Wan, S.; Kelly, P. M.; Mahon, E.; Stöckmann, H.; Rudd, P. M.; Caruso, F.; Dawson, K. A.; Yan, Y.; Monopoli, M. P., The "sweet" side of the protein corona: effects of glycosylation on nanoparticle–cell interactions. *ACS Nano* **2015,** *9* (2), 2157-2166.

(224) Clemments, A. M.; Botella, P.; Landry, C. C., Protein adsorption from biofluids on silica nanoparticles: corona analysis as a function of particle diameter and porosity. *ACS Appl. Mater. Interfaces* **2015,** *7* (39), 21682-21689.

(225) Ye, L.; Yong, K.-T.; Liu, L.; Roy, I.; Hu, R.; Zhu, J.; Cai, H.; Law, W.-C.; Liu, J.; Wang, K.; Liu, J.; Liu, Y.; Hu, Y.; Zhang, X.; Swihart, M. T.; Prasad, P. N., A pilot study in non-human primates shows no adverse response to intravenous injection of quantum dots. *Nat. Nanotechnol.* **2012,** *7* (7), 453-458.

(226) Yu, S. S.; Lau, C. M.; Thomas, S. N.; Jerome, W. G.; Maron, D. J.; Dickerson, J. H.; Hubbell, J. A.; Giorgio, T. D., Size- and charge-dependent non-specific uptake of PEGylated nanoparticles by macrophages. *Int. J. Nanomedicine* **2012,** *7*, 799-813.

(227) Walkey, C. D.; Olsen, J. B.; Guo, H.; Emili, A.; Chan, W. C. W., Nanoparticle size and surface chemistry determine serum protein adsorption and macrophage uptake. *J. Am. Chem. Soc.* **2012,** *134* (4), 2139-2147.

(228) Arnida; Janát-Amsbury, M. M.; Ray, A.; Peterson, C. M.; Ghandehari, H., Geometry and surface characteristics of gold nanoparticles influence their biodistribution and uptake by macrophages. *Eur. J. Pharm. Biopharm.* **2011,** *77* (3), 417-423.

(229) Lunov, O.; Syrovets, T.; Loos, C.; Beil, J.; Delacher, M.; Tron, K.; Nienhaus, G. U.; Musyanovych, A.; Mailänder, V.; Landfester, K.; Simmet, T., Differential uptake of functionalized polystyrene nanoparticles by human macrophages and a monocytic cell line. *ACS Nano* **2011,** *5* (3), 1657-1669.

(230) Dobrovolskaia, M. A.; McNeil, S. E., Immunological properties of engineered nanomaterials. *Nat. Nanotechnol.* **2007,** *2* (8), 469-478.

(231) Balfourier, A.; Luciani, N.; Wang, G.; Lelong, G.; Ersen, O.; Khelfa, A.; Alloyeau, D.; Gazeau, F.; Carn, F., Unexpected intracellular biodegradation and recrystallization of gold nanoparticles. *Proc. Natl. Acad. Sci.* **2020,** *117* (1), 103.

(232) Marrink, S. J.; Risselada, H. J.; Yefimov, S.; Tieleman, D. P.; de Vries, A. H., The MARTINI force field: coarse grained model for biomolecular simulations. *J. Phys. Chem. B* **2007,** *111* (27), 7812-7824.

(233) Abraham, M. J.; Murtola, T.; Schulz, R.; Páll, S.; Smith, J. C.; Hess, B.; Lindahl, E., GROMACS: High performance molecular simulations through multi-level parallelism from laptops to supercomputers. *SoftwareX* **2015,** *1-2*, 19-25.

(234) Parrinello, M.; Rahman, A., Polymorphic transitions in single crystals: A new molecular dynamics method. *J. Appl. Phys.* **1981,** *52* (12), 7182-7190.

(235) Bussi, G.; Donadio, D.; Parrinello, M., Canonical sampling through velocity rescaling. *J. Chem. Phys.* **2007,** *126* (1), 014101.

(236) Humphrey, W.; Dalke, A.; Schulten, K., VMD: visual molecular dynamics. *J. Mol. Graph.* **1996,** *14* (1), 33-38.

(237) Jo, S.; Lim, J. B.; Klauda, J. B.; Im, W., CHARMM-GUI membrane builder for mixed bilayers and its application to yeast membranes. *Biophys. J.* **2009,** *97* (1), 50-58.

(238) Lin, X.; O'Reilly Beringhs, A.; Lu, X., Applications of Nanoparticle-Antibody Conjugates in Immunoassays and Tumor Imaging. *AAPS J.* **2021,** *23* (2), 43.

(239) Blanco, E.; Shen, H.; Ferrari, M., Principles of Nanoparticle Design for Overcoming Biological Barriers to Drug Delivery. *Nat. Biotechnol.* **2015,** *33* (9), 941-951.

(240) Wu, N.; Kang, C. S.; Sin, I.; Ren, S.; Liu, D.; Ruthengael, V. C.; Lewis, M. R.; Chong, H. S., Promising bifunctional chelators for copper 64-PET imaging: practical (64)Cu radiolabeling and high in vitro and in vivo complex stability. *J. Biol. Inorg. Chem.* **2016,** *21* (2), 177-184.

(241) Cooper, M. S.; Ma, M. T.; Sunassee, K.; Shaw, K. P.; Williams, J. D.; Paul, R. L.; Donnelly, P. S.; Blower, P. J., Comparison of (64)Cu-complexing bifunctional chelators for radioimmunoconjugation: labeling efficiency, specific activity, and in vitro/in vivo stability. *Bioconjug. Chem.* **2012,** *23* (5), 1029-1039.

(242) Woo, S. K.; Jang, S. J.; Seo, M. J.; Park, J. H.; Kim, B. S.; Kim, E. J.; Lee, Y. J.; Lee, T. S.; An, G. I.; Song, I. H.; Seo, Y.; Kim, K. I.; Kang, J. H., Development of (64)Cu-NOTA-trastuzumab for HER2 targeting: a radiopharmaceutical with improved pharmacokinetics for human studies. *J. Nucl. Med.* **2019,** *60* (1), 26-33.

(243) Lee, I.; Lim, I.; Byun, B. H.; Kim, B. I.; Choi, C. W.; Woo, S.-K.; Kim, K. I.; Lee, K. C.; Kang, J. H.; Seong, M.-K.; Kim, H.-A.; Noh, W. C.; Lim, S. M., A Preliminary Clinical Trial to Evaluate ^{64}Cu-NOTA-Trastuzumab as a Positron Emission Tomography Imaging Agent in Patients with Breast Cancer. *EJNMMI Res.* **2021,** *11* (1), 8.

(244) Gustafson, H. H.; Holt-Casper, D.; Grainger, D. W.; Ghandehari, H., Nanoparticle uptake: the phagocyte problem. *Nano Today* **2015,** *10* (4), 487-510.

(245) MacParland, S. A.; Tsoi, K. M.; Ouyang, B.; Ma, X. Z.; Manuel, J.; Fawaz, A.; Ostrowski, M. A.; Alman, B. A.; Zilman, A.; Chan, W. C.; McGilvray, I. D., Phenotype determines nanoparticle uptake by human macrophages from liver and blood. *ACS Nano* **2017,** *11* (3), 2428-2443.

(246) Mitchell, M. J.; Billingsley, M. M.; Haley, R. M.; Wechsler, M. E.; Peppas, N. A.; Langer, R., Engineering Precision Nanoparticles for Drug Delivery. *Nat. Rev. Drug Discov.* **2021,** *20* (2), 101-124.

(247) Wan, R.; Mo, Y.; Feng, L.; Chien, S.; Tollerud, D. J.; Zhang, Q., DNA Damage Caused by Metal Nanoparticles: Involvement of Oxidative Stress and Activation of ATM. *Chem. Res. Toxicol.* **2012,** *25* (7), 1402-1411.

(248) Hartwell, L. H.; Weinert, T. A., Checkpoints: Controls that Ensure the Order of Cell Cycle Events. *Science* **1989,** *246* (4930), 629.

(249) Kim, J. A.; Åberg, C.; Salvati, A.; Dawson, K. A., Role of Cell Cycle on The Cellular Uptake and Dilution of Nanoparticles in a Cell Population. *Nat. Nanotechnol.* **2012,** *7* (1), 62-68.

(250) Uz, M.; Bulmus, V.; Alsoy Altinkaya, S., Effect of PEG Grafting Density and Hydrodynamic Volume on Gold Nanoparticle–Cell Interactions: an Investigation on Cell Cycle, Apoptosis, and DNA Damage. *Langmuir* **2016,** *32* (23), 5997-6009.

(251) Liu, Y.; Ashton, J. R.; Moding, E. J.; Yuan, H.; Register, J. K.; Fales, A. M.; Choi, J.; Whitley, M. J.; Zhao, X.; Qi, Y.; Ma, Y.; Vaidyanathan, G.; Zalutsky, M. R.; Kirsch, D. G.; Badea, C. T.; Vo-Dinh, T., A Plasmonic Gold Nanostar Theranostic Probe for *In Vivo* Tumor Imaging and Photothermal Therapy. *Theranostics* **2015,** *5* (9), 946-960.

(252) Zhang, X. D.; Wu, D.; Shen, X.; Liu, P. X.; Yang, N.; Zhao, B.; Zhang, H.; Sun, Y. M.; Zhang, L. A.; Fan, F. Y., Size-dependent in vivo toxicity of PEG-coated gold nanoparticles. *Int. J. Nanomedicine* **2011,** *6*, 2071-2081.

(253) Chen, Y.; Wu, L.; Wang, Q.; Wu, M.; Xu, B.; Liu, X.; Liu, J., Toxicological evaluation of Prussian blue nanoparticles after short exposure of mice. *Hum. Exp. Toxicol.* **2016,** *35* (10), 1123-1132.

(254) Gowda, S.; Desai, P. B.; Kulkarni, S. S.; Hull, V. V.; Math, A. A. K.; Vernekar, S. N., Markers of Renal Function Tests. *N. Am. J. Med. Sci.* **2010,** *2* (4), 170-173.

(255) Li, Y. F.; Chen, C., Fate and toxicity of metallic and metal-containing nanoparticles for biomedical applications. *Small* **2011,** *7* (21), 2965-2980.

(256) Kumar, R.; Roy, I.; Ohulchanskky, T. Y.; Vathy, L. A.; Bergey, E. J.; Sajjad, M.; Prasad, P. N., In Vivo Biodistribution and Clearance Studies Using Multimodal Organically Modified Silica Nanoparticles. *ACS Nano* **2010,** *4* (2), 699-708.

(257) Hirn, S.; Semmler-Behnke, M.; Schleh, C.; Wenk, A.; Lipka, J.; Schäffler, M.; Takenaka, S.; Möller, W.; Schmid, G.; Simon, U.; Kreyling, W. G., Particle size-dependent and surface charge-dependent biodistribution of gold nanoparticles after intravenous administration. *Eur. J. Pharm. Biopharm.* **2011,** *77* (3), 407-416.

(258) Chen, C. C.; Li, J. J.; Guo, N. H.; Chang, D. Y.; Wang, C. Y.; Chen, J. T.; Lin, W. J.; Chi, K. H.; Lee, Y. J.; Liu, R. S.; Chen, C. L.; Wang, H. E., Evaluation of the biological behavior of a gold nanocore-encapsulated human serum albumin nanoparticle (Au@HSANP) in a CT-26 tumor/ascites mouse model after intravenous/intraperitoneal administration. *Int. J. Mol. Sci.* **2019,** *20* (1).

(259) Powell, J. J.; Faria, N.; Thomas-McKay, E.; Pele, L. C., Origin and Fate of Dietary Nanoparticles and Microparticles in the Gastrointestinal Tract. *J. Autoimmun.* **2010,** *34* (3), J226-J233.

(260) Hillyer, J. F.; Albrecht, R. M., Gastrointestinal Persorption and Tissue Distribution of Differently Sized Colloidal Gold Nanoparticles. *J. Pharm. Sci.* **2001,** *90* (12), 1927-36.

(261) Jong, W. H. D.; Burger, M. C.; Verheijen, M. A.; Geertsma, R. E., Detection of the presence of gold nanoparticles in organs by transmission electron microscopy. *Materials* **2010,** *3* (9), 4681-4694.

(262) Parker, G. A.; Picut, C. A., Liver immunobiology. *Toxicol. Pathol.* **2005,** *33* (1), 52-62.

(263) Sleyster, E. C.; Knook, D. L., Relation between localization and function of rat liver Kupffer cells. *Lab Invest.* **1982,** *47* (5), 484-490.

(264) Nam, H. Y.; Kwon, S. M.; Chung, H.; Lee, S. Y.; Kwon, S. H.; Jeon, H.; Kim, Y.; Park, J. H.; Kim, J.; Her, S.; Oh, Y. K.; Kwon, I. C.; Kim, K.; Jeong, S. Y., Cellular uptake mechanism and intracellular fate of hydrophobically modified glycol chitosan nanoparticles. *J. Control. Release* **2009,** *135* (3), 259-267.

(265) Donahue, N. D.; Acar, H.; Wilhelm, S., Concepts of Nanoparticle Cellular Uptake, Intracellular Trafficking, and Kinetics in Nanomedicine. *Adv. Drug Deliv. Rev.* **2019,** *143*, 68-96.

(266) Hui, Y.; Yi, X.; Wibowo, D.; Yang, G.; Middelberg, A. P. J.; Gao, H.; Zhao, C. X., Nanoparticle elasticity regulates phagocytosis and cancer cell uptake. *Sci. Adv.* **2020,** *6* (16), eaaz4316.

(267) Rennick, J. J.; Johnston, A. P. R.; Parton, R. G., Key Principles and Methods for Studying the Endocytosis of Biological and Nanoparticle Therapeutics. *Nat. Nanotechnol.* **2021,** *16* (3), 266-276.

(268) Kuhn, D. A.; Vanhecke, D.; Michen, B.; Blank, F.; Gehr, P.; Petri-Fink, A.; Rothen-Rutishauser, B., Different endocytotic uptake mechanisms for nanoparticles in epithelial cells and macrophages. *Beilstein J. Nanotechnol.* **2014,** *5*, 1625-1636.

(269) Sarkar, K.; Kruhlak, M. J.; Erlandsen, S. L.; Shaw, S., Selective Inhibition by Rottlerin of Macropinocytosis in Monocyte-Derived Dendritic Cells. *Immunology* **2005,** *116* (4), 513-524.

(270) Phanse, Y.; Lueth, P.; Ramer-Tait, A. E.; Carrillo-Conde, B. R.; Wannemuehler, M. J.; Narasihan, B.; Bellaire, B. H., Cellular Internalization Mechanisms of Polyanhydride Particles: Implications for Rational Design of Drug Delivery Vehicles. *J. Biomed. Nanotechnol.* **2016,** *12* (7), 1544-52.

(271) MacLean-Fletcher, S.; Pollard, T. D., Mechanism of Action of Cytochalasin B on Actin. *Cell* **1980,** *20* (2), 329-41.

(272) Liu, M.; Li, Q.; Liang, L.; Li, J.; Wang, K.; Li, J.; Lv, M.; Chen, N.; Song, H.; Lee, J.; Shi, J.; Wang, L.; Lal, R.; Fan, C., Real-Time Visualization of Clustering and Intracellular Transport of Gold Nanoparticles by Correlative Imaging. *Nat. Commun.* **2017,** *8* (1), 15646.

(273) Nguyen, V. H.; Lee, B. J., Protein Corona: A New Approach for Nanomedicine Design. *Int. J. Nanomedicine* **2017,** *12*, 3137-3151.

(274) Salvati, A.; Pitek, A. S.; Monopoli, M. P.; Prapainop, K.; Bombelli, F. B.; Hristov, D. R.; Kelly, P. M.; Åberg, C.; Mahon, E.; Dawson, K. A., Transferrin-functionalized nanoparticles lose their targeting capabilities when a biomolecule corona adsorbs on the surface. *Nat. Nanotechnol.* **2013,** *8* (2), 137-143.

(275) Mizuhara, T.; Saha, K.; Moyano, D. F.; Kim, C. S.; Yan, B.; Kim, Y.-K.; Rotello, V. M., Acylsulfonamide-Functionalized Zwitterionic Gold Nanoparticles for Enhanced Cellular Uptake at Tumor pH. *Angew. Chem. Int. Ed.* **2015,** *54* (22), 6567-6570.

(276) Wu, S.; Zhang, D.; Bai, J.; Zheng, H.; Deng, J.; Gou, Z.; Gao, C., Adsorption of serum proteins on titania nanotubes and its role on regulating adhesion and migration of mesenchymal stem cells. *J. Biomed. Mater. Res. A* **2020,** *108* (11), 2305-2318.

(277) Souza, P. C. T.; Alessandri, R.; Barnoud, J.; Thallmair, S.; Faustino, I.; Grünewald, F.; Patmanidis, I.; Abdizadeh, H.; Bruininks, B. M. H.; Wassenaar, T. A.; Kroon, P. C.; Melcr, J.; Nieto, V.; Corradi, V.; Khan, H. M.; Domański, J.; Javanainen, M.; Martinez-Seara, H.; Reuter, N.; Best, R. B.; Vattulainen, I.; Monticelli, L.; Periole, X.; Tieleman, D. P.; de Vries, A. H.; Marrink, S. J., Martini 3: a general purpose force field for coarse-grained molecular dynamics. *Nat. Methods* **2021,** *18* (4), 382-388.

(278) Zhang, X.; Ma, G.; Wei, W., Simulation of nanoparticles interacting with a cell membrane: probing the structural basis and potential biomedical application. *npg Asia Mater.* **2021,** *13* (1), 52.

(279) van Meer, G.; Voelker, D. R.; Feigenson, G. W., Membrane lipids: where they are and how they behave. *Nat. Rev. Mol. Cell Biol.* **2008,** *9* (2), 112-124.

(280) Tieleman, D. P.; Marrink, S.-J., Lipids out of equilibrium: energetics of desorption and pore mediated flip-flop. *J. Am. Chem. Soc.* **2006,** *128* (38), 12462-12467.

(281) Wong-Ekkabut, J.; Baoukina, S.; Triampo, W.; Tang, I. M.; Tieleman, D. P.; Monticelli, L., Computer simulation study of fullerene translocation through lipid membranes. *Nat. Nanotechnol.* **2008,** *3* (6), 363-368.

(282) Dasgupta, S.; Auth, T.; Gompper, G., Shape and orientation matter for the cellular uptake of nonspherical particles. *Nano Lett.* **2014,** *14* (2), 687-693.

(283) Huang, C.; Zhang, Y.; Yuan, H.; Gao, H.; Zhang, S., Role of nanoparticle geometry in endocytosis: laying down to stand up. *Nano Lett.* **2013,** *13* (9), 4546-4550.

(284) Frey, F.; Ziebert, F.; Schwarz, U. S., Dynamics of particle uptake at cell membranes. *Phys. Rev. E* **2019,** *100* (5), 052403.

(285) Yang, K.; Ma, Y.-Q., Computer simulation of the translocation of nanoparticles with different shapes across a lipid bilayer. *Nat. Nanotechnol.* **2010,** *5* (8), 579-583.

(286) Lin, J.; Miao, L.; Zhong, G.; Lin, C.-H.; Dargazangy, R.; Alexander-Katz, A., Understanding the synergistic effect of physicochemical properties of nanoparticles and their cellular entry pathways. *Commun. Biol.* **2020,** *3* (1), 205.

(287) Lunnoo, T.; Assawakhajornsak, J.; Puangmali, T., In silico study of gold nanoparticle uptake into a mammalian cell: interplay of size, shape, surface charge, and aggregation. *J. Phys. Chem. C* **2019,** *123* (6), 3801-3810.

(288) Harayama, T.; Riezman, H., Understanding the diversity of membrane lipid composition. *Nat. Rev. Mol. Cell Biol.* **2018,** *19* (5), 281-296.

(289) Jensen, C.; Teng, Y., Is it time to start transitioning from 2D to 3D cell culture? *Front. Mol. Biosci.* **2020,** *7* (33).

(290) Edmondson, R.; Broglie, J. J.; Adcock, A. F.; Yang, L., Three-dimensional cell culture systems and their applications in drug discovery and cell-based biosensors. *Assay Drug Dev. Technol.* **2014,** *12* (4), 207-218.

(291) Jolliffe, I. T.; Cadima, J., Principal component analysis: a review and recent developments. *Philos. Trans. R. Soc. A* **2016,** *374* (2065), 20150202.

(292) Najafabadi, M. M.; Villanustre, F.; Khoshgoftaar, T. M.; Seliya, N.; Wald, R.; Muharemagic, E., Deep learning applications and challenges in big data analytics. *J. Big Data* **2015,** *2* (1), 1.

(293) Hinton, G. E.; Osindero, S.; Teh, Y. W., A fast learning algorithm for deep belief nets. *Neural Comput.* **2006,** *18* (7), 1527-1554.

(294) Bryda, E. C., The mighty mouse: the impact of rodents on advances in biomedical research. *Mo. Med.* **2013,** *110* (3), 207-211.

(295) Silva Lima, B.; Videira, M. A., Toxicology and biodistribution: the clinical value of animal diodistribution studies. *Mol. Ther. Methods Clin. Dev.* **2018,** *8*, 183-197.

(296) Mendoza, M. C.; Er, E. E.; Blenis, J., The Ras-ERK and PI3K-mTOR pathways: cross-talk and compensation. *Trends Biochem. Sci.* **2011,** *36* (6), 320-8.

(297) Cao, Z.; Liao, Q.; Su, M.; Huang, K.; Jin, J.; Cao, D., AKT and ERK dual inhibitors: the way forward? *Cancer Lett.* **2019,** *459*, 30-40.

(298) Pawula, M.; Altintas, Z.; Tothill, I. E., SPR detection of cardiac troponin T for acute myocardial infarction. *Talanta* **2016,** *146*, 823-830.

(299) Chon, H.; Lee, S.; Yoon, S. Y.; Lee, E. K.; Chang, S. I.; Choo, J., SERS-based competitive immunoassay of troponin I and CK-MB markers for early diagnosis of acute myocardial infarction. *Chem. Commun.* **2014,** *50* (9), 1058-1060.

(300) Jo, H.; Her, J.; Lee, H.; Shim, Y.-B.; Ban, C., Highly sensitive amperometric detection of cardiac troponin I using sandwich aptamers and screen-printed carbon electrodes. *Talanta* **2017,** *165*, 442-448.

(301) ThermoFisher, **2020,** Cardiac troponin I (TNNI3) human ELISA kit. https://www.thermofisher.com/elisa/product/Cardiac-Troponin-I-TNNI3-Human-ELISA-Kit/EHTNNI3.

(302) MilliporeSigma, **2020,** MILLIPLEX MAP human cardiovascular disease (CVD) magnetic bead panel 1 - cardiovascular disease multiplex assay. https://www.emdmillipore.com/US/en/product/MILLIPLEX-MAP-Human-Cardiovascular-Disease-CVD-Magnetic-Bead-Panel-1-Cardiovascular-Disease-Multiplex-Assay,MM_NF-HCVD1MAG-67K?CatalogCategoryID=#.

(303) Koerbin, G.; Tate, J. R.; Hickman, P. E., Analytical characteristics of the Roche highly sensitive troponin T assay and its application to a cardio-healthy population. *Ann. Clin. Biochem.* **2010,** *47* (Pt 6), 524-528.

(304) Payne, R.; Halik, L.; Ma, J.; Zhang, H.; Zhang, J.; Conklin, J.; Gaylord, M.; Yokoyama, K.; Bahrainy, Y.; Ozgen, N.; Balderson, J.; Chase, A.; Gorman, R.; Plouffe, B.; Deflippi, C., Performance evaluation of the Siemens ADVIA centaur high sensitivity troponin I assay. *Eur. Heart J.* **2017,** *38* (suppl_1).

(305) Masotti, S.; Musetti, V.; Prontera, C.; Storti, S.; Passino, C.; Zucchelli, G.; Clerico, A., Evaluation of analytical performance of a chemiluminescence enzyme immunoassay (CLEIA) for cTnI using the automated AIA-CL2400 platform. *Clin. Chem. Lab. Med.* **2018,** *56* (7), e174-e176.